A Thesis Submitted for the Degree of PhD at the University of Warwick

Permanent WRAP URL:

http://wrap.warwick.ac.uk/108906

Copyright and reuse:

This thesis is made available online and is protected by original copyright.

Please scroll down to view the document itself.

Please refer to the repository record for this item for information to help you to cite it.

Our policy information is available from the repository home page.

For more information, please contact the WRAP Team at: wrap@warwick.ac.uk

warwick.ac.uk/lib-publications

THE BRITISH LIBRARY
BRITISH THESIS SERVICE

Magnetic Properties of Gd-Lu Alloys, Er and a $Ho_{90}Er_{10}$ Alloy.

TITLE ..

AUTHOR ....
Roger Soulsby Eccleston

DEGREE ....
University of Warwick.

AWARDING BODY
DATE ....
December 1991.

THESIS
NUMBER ....

THIS THESIS HAS BEEN MICROFILMED EXACTLY AS RECEIVED

The quality of this reproduction is dependent upon the quality of the original thesis submitted for microfilming. Every effort has been made to ensure the highest quality of reproduction.

Some pages may have indistinct print, especially if the original papers were poorly produced or if the awarding body sent an inferior copy.

If pages are missing, please contact the awarding body which granted the degree.

Previously copyrighted materials (journal articles, published texts, etc.) are not filmed.

cms	1	2	3	4	5	6

REDUCTION X **12**

CAMERA **3**

No. of pages

Magnetic Properties of Gd-Lu Alloys, Er and a $Ho_{90}Er_{10}$ Alloy.

Roger Soulsby Eccleston   BSc. (CNAA).

Submitted for the degree of Doctor of Philosophy
at the University of Warwick.

Department of Physics,
University of Warwick.

December 1991.

Contents

Acknowledgments

Many people have contributed to the work described in this thesis either directly, through technical assistance or guidance or indirectly, simply by giving me encouragement, friendship or making Warwick the pleasant place to work that it has proven to be. I would like to take this opportunity to thank a few of those people.

It is very unlikely that I would have embarked on a PhD. in the first place were it not for the encouragement of Dr Chick Wilson and Professor Bruce Forsyth at R.A.L. and Dr Mike Boyle at Sheffield City Polytechnic. I am grateful to them for that initial impetus and for their continued interest in my progress.

I would like to thank my supervisor Professor Stuart Palmer for his guidance and encouragement, and for his diligent proof reading of this thesis.

My periods at the I.L.L. were made all the more pleasant thanks to the efforts of Dr Richard Melville who introduced me to the more salubrious restaurants and watering holes, and to Drs Mary Vrtis and Gary McIntyre who were both invaluable for their help and advice regarding the experiments and for their agreable company. I am particularly grateful to Valerie Brückel who surrendered her mother for two weeks for the sake of large portions of chapters 4 and 6.

I would like to thank Dr David Fort at Birmingham University for growing all the Gd-Lu crystals and for being so prompt in delivering them. I am also grateful to Dr Jakob Bohr for the loan of the $Ho_{90}Er_{10}$ crystal.

The automated ultrasonic measurement system was developed by Manuel Salguiero da Silva at the Universidade do Porto, Portugal, and I am grateful to him for his efforts in setting up the system at Warwick.

I was privileged to have been a Solid State Boy and am very grateful to the others for their much valued and continued friendship. In their own individual way each of my office mates have made a substantial contribution to the enjoyable life I have had over the past three years and in this respect I would like to thank Steif, Greg, Adrian, Alun, A.C., New Chap, John and Chris. I would also like to extend my thanks to Don and Boothers for their friendship and advice on all matters from neutron scattering to desk top publishing, and their tolerance over the past few

weeks when, nominally in their employ, I devoted much time to the completion of this thesis.

I am very grateful to Elizabeth for applying her artistic flair to the production of some of the diagrams in this thesis, but above all, for being the light at the end of the tunnel and providing the greatest motivation for getting this thesis finished.

However, by far my greatest debt of gratitude is to my parents without whose encouragement and support (both pecuniary and otherwise) throughout my protracted education and before, I would not be in the position I am happy to find myself in today.

R.S.E., December, 1991.

Declaration

The work contained in this thesis is my own except where specifically stated otherwise, and was based in the Department of Physics, University of Warwick from Ocotber 1988 to December 1991. No part of this work has been previously submitted to this or any other academic institution for admission to a higher degree. Some of the work has appeared in the form of publications which are listed in the final section.

Abstract

Two quite different facets of rare earth magnetism have been studied using neutron elastic scattering and ultrasound velocity and attenuation measurements. A new automated ultrasound measurement system gives an improvement in precision on other measurement techniques and has been shown to be well suited to the measurement of both the temperature and magnetic field dependence of ultrasonic elastic constants and their associated attenuation coefficients.

The zero field magnetic phase diagram of the Gd-Lu alloy system has been studied in the vicinity of the multicritical region. New detail has been added to the existing phase diagram. Ultrasound data provides strong evidence for the existence of a ferro-I phase, which displays a net moment along the c-axis while being apparently paramagnetic in the basal plane. A helical antiferromagnetic phase exists for those samples with a Lu concentration of greater than 23.5%. The turn angle of the helix appears to decrease continuously on cooling and tends to zero as the transition to a canted ferromagnetic phase is approached. The transition comes about as ferromagnetic domains grow out of antiferromagnetic domain walls.

The behaviour of a $Gd_{76.0}Lu_{24.0}$ alloy in an applied magnetic field has been studied, permitting the construction of applied field-temperature phase diagrams relating to fields applied parallel to the a-axis and parallel to the c-axis. Both reveal several unexpected features particularly in the ferro-I region.

The ultrasonic elastic constants of erbium show anomalous behaviour as a result of the formation of high order commensurate structures made up of spin-slips. Those commensurate structures which display a net ferromagnetic moment are seen by neutron diffraction to become stable over limited temperature ranges, in good agreement with previous X-ray data. Both the neutron scattering and the ultrasound data show evidence of a subtle change in the magnetic structure immediately above T_C.

The temperature dependence of the ultrasonic elastic constants of the random alloy $Ho_{90}Er_{10}$ have been measured. A limited neutron diffraction experiment shows that the addition of 10% Er produces quite considerable departures from the magnetic behaviour of pure Ho.

Ultrasonic measurements performed on Er in a c-axis applied magnetic field permit the construction of a tentative phase diagram which shows that the commensurate phases with a net ferromganetic moment become more stable. Two conical ferromagnetic cone phases are observed, in addition to the cone phase observed in zero field.

Chapter 1

Introduction;

The Magnetic Properties of the Rare Earths.

The Rare Earth, or Lanthanide, metals display a wide range of magnetic properties, including a bewildering variety of complex magnetic structures.

The electronic configuration of the atoms is a xenon core with outer shell $4f^n5d^16s^2$ where n increases from 0 for lanthanum to 14 for lutetium. The chemical properties are very similar being determined by the 5d and 6s valence electrons. The magnetic behaviour is governed by the 4f electrons and consequently varies across the period.

While the chemical similarity of the rare earths permit alloying, increasing the variety of magnetic properties, it also hampers efforts to produce samples of sufficient purity to provide the experimental information required for a detailed understanding of their magnetic properties. It was the production of high purity samples at Iowa State University and the Ames Laboratory by Spedding and Legvold in the late 1950s, and their magnetisation, susceptibility, heat capacity and resistivity measurements

which pioneered research in the field. However, the most powerful probe for studying these materials is undoubtedly neutron scattering, the initial experiments being performed at Oak Ridge by Koehler (1965,1967) and co-workers.

Since the 1960s the rate of research has been dictated by improvements in the production of high purity samples. In addition, the development of increasingly powerful measurement techniques have revealed a plethora of interesting effects and opened new avenues for research. Indeed, the high resolution ultrasound measurements of Patterson (1986) may be considered to have provided the initial impetus for the current interest in spin-slip structures of holmium and erbium which forms the basis for chapter 6 and 7, and although the investigation of the magnetic behaviour of alloys of gadolinium with non-magnetic diluents was started as long ago as the 1950s (Thoburn, 1958) recent improvements in crystal growing techniques have provided higher purity samples which exhibit subtle effects not observed in the earlier studies.

This study has two separate goals: (i) to investigate the magnetic phase diagram of the gadolinium lutetium alloy system in the light of previous studies on the similar systems Gd-Y (Bates, 1985) and Gd-Sc (Melville, 1989), and (ii) the observation of spin-slip structures in erbium and a $Ho_{90}Er_{10}$ alloy. The principle probes employed are neutron elastic scattering and ultrasound velocity and attenuation measurements. Complementary information has been provided by resistivity and magnetoresistance measurements carried out at the Universidade do Porto, Portugal.

Within the scope of this thesis only a brief introduction to the electronic structures and magnetic properties is possible. Many good texts now exist which offer comprehensive accounts, amongst them Coqblin

(1977) and Jensen and Mackintosh (1991). In this chapter, only the fundamental principles necessary for an understanding of the following text is given.

1.1 Gadolinium, Holmium and Erbium

Gadolinium, holmium and erbium lie within the subgroup known as the heavy rare earths, those with a half or more filled 4f shell. The 4f shell is highly localised for all the rare earths (figure 1.1) and is shielded by the 5s and 5p electrons, with the 5d and 6s electrons being lost to the conduction band. As a consequence of the shielding of the 4f electrons, the ground state is well described by Hund's rules. The splitting between the ground state and first excited state is large, ~0.5eV in Ho, ~0.8eV in Er and ~3.5eV in Gd, consequently only the ground states are filled at room temperature and below.

Gadolinium, with a half filled 4f shell is the only S state rare earth. The spin angular momentum is S=7/2 and, because the 4f charge cloud is spherical, the spin angular momentum L is zero. The saturation magnetic moment is given by $\mu = g\mu_B J$, where g is the Landé splitting factor and J=L+S when the 4f shell is more than half filled, and is calculated to be $7\mu_B$, however the observed value (Roeland, 1975) is $7.63\mu B$ with the discrepancy being accounted for by the polarisation of the conduction electrons.

Holmium and erbium, in common with the other heavy rare earths apart from gadolinium, exhibit highly aspherical 4f charge clouds. For holmium, with 10 electrons in the 4f shell, Hund's rules give L=6, S=2, J=8 and the calculated saturation moment is $10\mu_B$ with an observed value of $10.34\mu_B$. Erbium has 11 electrons in the 4f shell and the ground state is

3
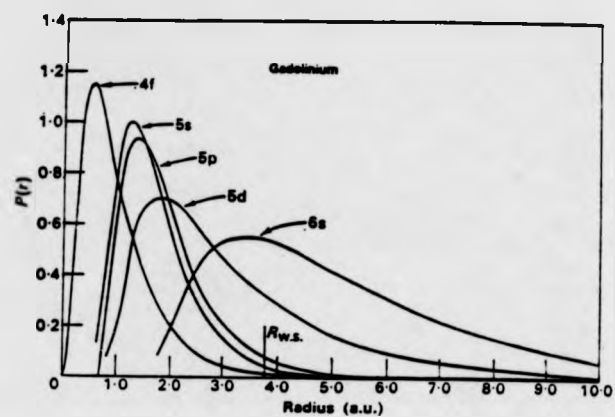
Fig. 1.1 The relative outer radii of the atomic electrons in Gd.

$10.34\mu_B$. Erbium has 11 electrons in the 4f shell and the ground state is described by L=6, S=3/2, J=15/2. The saturation magnetic moment is calculated to $9\mu_B$ but again the polarisation of the conduction electrons has a small contribution and the observed value is $9.1\mu_B$.

Gadolinium, holmium and erbium all condense into an HCP structure (figure 1.2) with a c/a ratios slightly below the ideal value of $\sqrt{\frac{8}{3}}$, with Gd 1.59, Ho 1.57 and Er 1.569.

A discussion of the band structure and the Fermi surfaces of the heavy rare earths is surplus to requirements for this thesis, however, one feature of the Fermi hole surface is critically important for understanding the formation of periodic structures in the rare earths. The calculation of the paramagnetic energy bands by Dimmock and Freeman (1964) and later with relativistic effects by Keeton and Lourks (1968) revealed a webbing feature in the Fermi hole surface between the toes near the zone boundary, which was supported by the positron annihilation experiments of Williams and Mackintosh (1968). Figure (1.3) shows the Fermi hole surface for Tb although the same feature is observed in Ho, Er, Y and Lu. In contrast the Fermi hole surface of Gd (figure 1.4) displays no such webbing feature, which lends weight to the argument that the webbing feature is responsible for the periodic structures, since Gd is the only rare earth not to display periodic behaviour. It is believed that the webbing feature gives rise to a peak in the conduction electron susceptibility, which determines the Q-vector which characterises the periodic structure. Indeed the conduction electron susceptibility $\chi(q)$ has been calculated for Gd, Er and Lu (Liu, 1971) revealing peaks for Er and Lu but not Gd.

4
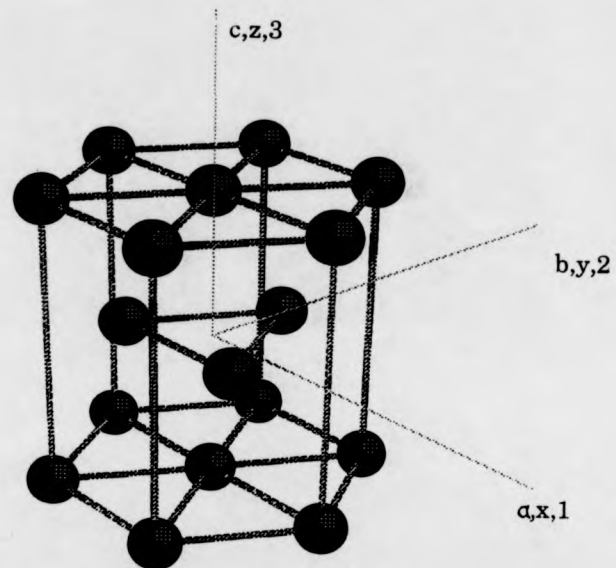
Fig. 1.2 The HCP structure
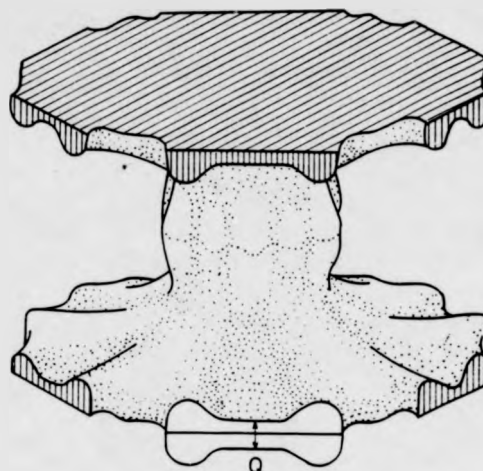
Fig 1.3 The hole Fermi surface of paramagnetic terbium,
showing the webbing feature.
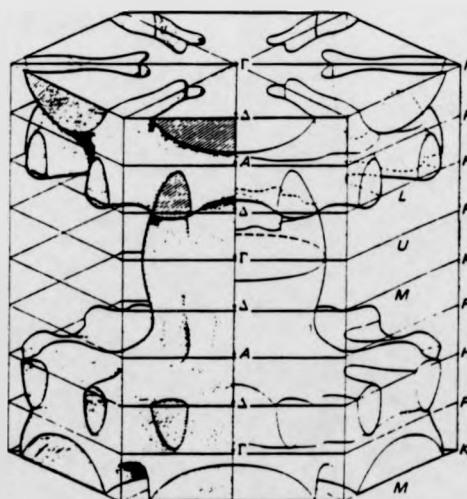
Fig. 1.4 The hole Fermi surface of paramagnetic gadolinium.

1.2 Magnetic Interactions

Because of the high degree of shielding and the highly localised nature of the 4f electrons, there is no overlap of the 4f wavefunctions, and the magnetic ions do not interact directly. As a consequence, the magnetic interactions of the rare earths may be conveniently divided into two categories. Two-ion interactions, in which the ions interact via polarisation of the conduction electrons, and the single ion interaction in which the aspherical 4f charge cloud on each atom interacts independently with its surroundings, unaffected by the magnetic state of it's neighbours. The coupling of the magnetic system to the crystal lattice introduces magnetostrictive strains which may be as large as 1% and will be seen to introduce an additional anisotropy, principally single ion in origin, but in some cases arising from two ion interactions.

Of the two ion interactions, the most important is the indirect exchange or RKKY interaction first proposed by Ruderman and Kittel (1954) and Kasuya (1956) and Yosida (1957). The coupling, H_{sf}, of the 4f spin S_i on site i with the conduction electrons may be written (following Jensen and Mackintosh, 1991)

$$H_{sf} = -\frac{2}{N} \int I(\mathbf{r}\text{-}\mathbf{R}_i)\mathbf{S}_i.\mathbf{s}(\mathbf{r})d\mathbf{r} \qquad (1.1)$$

where $\mathbf{s}(\mathbf{r})$ is the conduction electron spin density, N is the number of ions and $I(\mathbf{r}\text{-}\mathbf{R}_i)$ is the exchange integral which is determined by the overlapping of the 4f and conduction electron charge clouds. In effect, the conduction electrons are polarised by the magnetic field produced by the spin at site i and in turn interact with the spin at site j. Thus the Hamiltonian for the

interaction between spins at sites i and the spins at sites j, H_{ff} may be written

$$H_{\text{ff}} = -\frac{1}{2}\sum_{ij} J_{\text{s}}(ij)\mathbf{S_i}.\mathbf{S_j}. \qquad (1.2)$$

The exchange interaction is more usefully written as the Fourier transform of $J_{\text{s}}(ij)$. Thus

$$J_{\text{s}}(\mathbf{q}) = \frac{V}{N\mu_B{}^2}\,|\,I(\mathbf{q})\,|^2\chi(\mathbf{q}) \qquad (1.3)$$

where V is the volume and $\chi(\mathbf{q})$ is the conduction electron susceptibility. The importance of the peaks in $\chi(\mathbf{q})$ caused by the webbing of the Fermi hole surface to the formation of periodic structures now becomes clearer.

Because of the spin-orbit coupling, $\mathbf{J}$ is a better quantum number than $\mathbf{S}$. Consequently, using the projection of $\mathbf{S}$ on $\mathbf{J}$ ($\mathbf{S}$=(g-1)$\mathbf{J}$) 1.2 becomes

$$H_{\text{ff}} = -\frac{1}{2}\sum_{i} J(ij)\mathbf{J_i}.\mathbf{J_j} \qquad (1.4)$$

and

$$J(\mathbf{q}) = (g-1)^2[J_{\text{s}}(\mathbf{q}) - \frac{1}{N}\sum_{\mathbf{q'}} J_{\text{s}}(\mathbf{q'})]. \qquad (1.5)$$

The quantity $J(\mathbf{q}) - J(0)$ may be deduced from spin-wave dispersion measurements and the values for Gd, Ho and Er are plotted on figure 1.5. Ho and Er have peaks at non-zero q whereas Gd has not, in good agreement

6
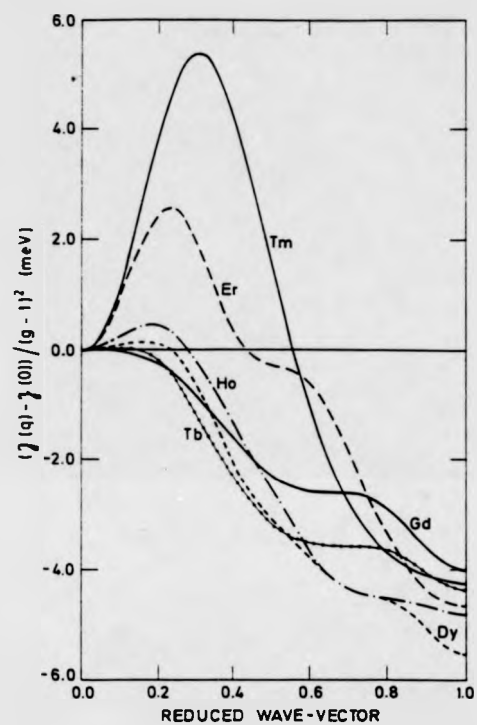
Fig. 1.5 The exchange interaction $J_s(\mathbf{q})$ - $J_s(0)$, determined
experimentally in the magnetic heavy rare earth metals.

with the predictions made on the basis of the shape of the Fermi hole surface. Because the peaks in $J(\mathbf{q}) - J(0)$ are a function of the band structure rather than the crystal structure the periodicity of magnetic structures arising from the RKKY interaction will usually not be commensurate with the crystal lattice.

Because of the strong coupling of the conduction electrons, the polarisation and consequently the RKKY interaction is very long range. While the RKKY interaction dictates the periodicity of the magnetic structure, in terms of the directional orientation of the moments it is isotropic in that it has no bearing upon the direction of the moments. However, other two-ion interactions may give rise to anisotropy.

Usually, two ion anisotropic interactions are dependent upon the orbital angular momentum and may arise through spin-orbit coupling of the conduction electrons, dipolar coupling and magnetoelastic coupling. These effects are well summarised by Levy (1969) and Jensen, Houmann and Bjerum Møller (1975). The dependence on the orbital angular momentum would seem to exclude Gd from these effects. However, Kaino and Kasuya (1981) have pointed out that a non-linearity in the s-f coupling to the conduction electrons (equation 1.1) will lead to two ion anisotropy in Gd. The Hamiltonian for the anisotropic part of the two ion interaction may be written generically as

$$H_{JJ} = -\frac{1}{2} \sum_{ij} \sum_{ll'mm'} \kappa_{ll'}^{mm'}(ij) O_l^m(\mathbf{J}_i) O_{l'}^{m'}(\mathbf{J}_j). \quad (1.6)$$

The coefficient $\kappa_{ll'}^{mm'}$ will vary according to the nature of the coupling giving rise to the anisotropy. O_l^m are Stevens' operators which are operator equivalents of spherical harmonics and describe in effect the quadrupole,

7

octapole, etc. moments of the 4f charge cloud. They relate the anisotropy to the symmetry of the crystal lattice.

The single ion interactions are by their nature short range, tending to align the magnetic moment along crystallographic directions. The local charge environment produces an electric field reflecting the local point symmetry which acts on the highly aspherical 4f charge cloud producing a torque. The resulting anisotropy is very large, and hundreds of Tesla may be required to alter significantly the orientation of the moment. The single ion or crystal field Hamiltonian is generally written as

$$H_{cf} = \sum_i \sum_{lm} B_l^m O_l^m(\mathbf{J_i}) \qquad (1.7)$$

where O_l^m is the Stevens operator described above and B_l^m is the crystal field parameter. B_l^m is a simplification including the Stevens' factor which is dependent upon the anisotropy of the ionic charge cloud and an additional term reflecting the distribution of the external charge. The representation of the local electric field by the Stevens' operators is an approximation and is only valid when the crystal field interaction is considerably weaker then the spin-orbit coupling as in the case of the heavy rare earths.

The formative paper on the effects of magnetostriction is that by Callen and Callen (1965). Because the elastic energy is quadratic in strain and magnetoelastic energy is linear, competition between the two may lead to equilibrium deformations of the lattice. Such deformations will modify both single ion and two ion interactions, however, the most significant effects are on the crystal field and consequently the single ion anisotropy. Magnetostrictive deformations may be divided into three categories, α strains which are symmetry preserving dilations, γ strains which distort

8

the basal plane and ε strains which distort the c-axis. Each type of strain will have a different contribution to the magnetoelastic Hamiltonian, however the form of the Hamiltonian, H_{ME}, will be similar to that of the crystal field (eqn. 1.7), with the crystal field parameter being replaced by the magnetoelastic coupling coefficient.

There does exist some coupling between the 4f moment and the nuclear spin, but it is a very small effect and in the cases of Gd, Er and Ho it does not play a role in the magnetic ordering.

Thus, we have described, albeit in very simple terms, the principal interactions which give rise to ordered magnetic structures in the rare earths at zero field. When considering structures in an applied magnetic field the Zeeman term must also be considered.

$$H_z = - \sum_i \mu_i . \mathbf{B}_i \qquad (1.8)$$

where μ_i is the magnetic moment on the ith ion and $\mathbf{B}_i$ is the magnetic field experienced by that ion.

In summary, the magnetic structures displayed by the heavy rare-earths arise as the result of the five interactions outlined in this section. Thus the overall Hamiltonian is written

$$H = H_{ff} + H_{JJ} + H_{cf} + H_{ME} + H_Z \qquad (1.9)$$

1.3 Magnetic Structures

The wide range of magnetic structures displayed by the rare earths all arise as a result of the competition between the interactions described in the previous section.

The long-range isotropic exchange interaction in all the heavy rare earths bar Gd give rise to structure in which the magnetic moments are modulated periodically. These periodic structures may be divided into two categories; either helices or longitudinal structures. Longitudinal structures have their moments confined to the c-axis as a result of high axial anisotropy such as Er and Tm and the c-axis component of the magnetisation on site i may be written as

$$M_{iz} = M\cos\mathbf{Q}.\mathbf{R}_i \qquad (1.9)$$

where Q is the wavevector of the modulation, and may be translated into lattice planes by multiplication of it's reciprocal by 2π. The magnetisation in the helical structures is confined to the basal plane, with each atomic layer having all the moments aligned ferromagnetically. The adjacent atomic layers have the moments similarly aligned, however, with the magnetisation rotated by a turn angle φ. Ho and Dy display helical antiferromagnetic structures. The basal plane components of the magnetisation may be written

$$M_{ix} = M\cos\mathbf{Q}.\mathbf{R}_i \qquad (1.10)$$

$$M_{iy} = M\sin\mathbf{Q}.\mathbf{R}_i. \qquad (1.11)$$

While the single ion anisotropy will tend to align the magnetisation along crystallographic directions, the two ion anisotropy may, or may not depending upon the nature of the coupling from which it arises.

The magnetostrictive effect will tend to stabilise ferromagnetic structures which brought about the deformation of the lattice, the "clamping effect" referred to by Cooper (1967). The magneto-elastic energy is higher for antiferromagnetic structures than for ferromagnets, the difference depending, at least to the fourth power, on the magnetisation. Consequently the difference will be very small close to the initial ordering temperature, but much larger at lower temperatures (Evenson and Liu, 1969).

As temperature increases, anisotropy and magnetostrictive effects will tend to dominate, favouring ferromagnetic structure. This arises as a result of the increase in the anisotropy and also because of a decrease in the size of the peak in $J(\mathbf{q}) - J(0)$. Since, the periodic structures are usually incommensurate with respect to the crystal lattice, the magnetic order introduces an additional periodicity which is experienced by the conduction electrons via the s-f interaction and causes a modification of the Fermi surface (Mackintosh, 1962).

1.4 Preview of this work.

This thesis presents experimental work performed on two different rare earth systems: i) Alloys of Gadolinium with non-magnetic metals, principally lutetium and ii) spin-slip structures in erbium and an alloy of holmium and erbium.

Gadolinium, as has been stated, is the only S state rare earth, and as such does not exhibit any crystal field anisotropy. There is however, an

11

anisotropy arising from dipolar coupling and a second, competing, anisotropy which originates in the spin-orbit coupling of the conduction electrons. Gadolinium is also the only heavy rare earth which does not display any periodic antiferromagnetic order. However when diluted with Lu, Y, Sc or La, helical, and in the case of Gd-Sc conical, structures will be adopted. The competition between the anisotropies and the tendency of the more dilute alloy to order antiferromagnetically produces complex phase diagrams exhibiting a wide range of magnetic structures including an unusual ferromagnetic phase referred to as ferro-I, which displays a net ferromagnetic moment along the c-axis while appearing to be paramagnetic in the basal plane.

Ultrasound, neutron scattering and resistivity measurements have been made on single crystals of Gd-Lu with five different compositions. New detail has been added to the phase diagram and the nature of the transition from helical antiferromagnet to canted ferromagnet has been considered in some detail. Measurements have also been made in an applied magnetic field, allowing the construction of two applied field-temperature phase diagrams and providing an insight into the nature of the magnetic phases observed in zero field.

Competition between the exchange and the crystal field anisotropy gives rise to modulated structures, which are perturbed as the moments are drawn close to crystallographic directions by the anisotropy. The structure assumes a compromise which may be described by a spin-slip model (Vigren, 1976) and in some circumstances structures which are commensurate with the crystal lattice develop. When these structures display a net ferromagnetic moment the magnetostrictive energy will play an important role and may cause the propagation vector to lock- in at commensurate values producing a devil's staircase (Bak, 1982). X-ray and

12

neutron scattering studies, which will be reviewed in the relevant chapters, have shown the suitability of the spin-slip model to the structures of Ho and Er. The zero field behaviour of the magnetic structures of erbium and $Ho_{90}Er_{10}$ has been studied by ultrasound and neutron scattering measurements paying particular attention to the formation of commensurate phases, and the behaviour of the propagation vector in their vicinity. Ultrasound measurements have been made with a magnetic field applied along the c-axis which is seen to stabilise the commensurate phase and enhance the devil's staircase.

References

Bak P., Rep. Prog. Phys 45 587 (1982).

Bates S., PhD Thesis, University of Hull (1985).

Callen E.R., Callen H.B., Phys Rev 139 A 455 (1965).

Cooper B.R., Phys Rev Letts 19 900 (1967).

Coqblin B., "The Electronic Structure of Rare-Earth Metals and Alloys: the
   Magnetic Heavy Rare-Earths.", Academic Press (1977).

Dimmock J.O., Freeman A.J., Phys Rev Letts 13 750 (1964).

Evenson W.E., Liu S.H., Phys Rev 178 2 (1969).

Jensen J., Houmann J.G., Bjerrum Møller H., Phys Rev B 12 303 (1975).

Jensen J., Mackintosh A.R., "Rare Earth Magnetism, Structures and
   Excitations." Oxford Science Publications (1991).

Kaino K., Kasuya J. J Phys F 11 883 (1981).

Kasuya T., Prog Theor Phys (Japan) 16 45 (1956).

Keeton S.C., Loucks T.L., Phys Rev 1683 672 (1968).

Koehler W.C., J App Phys 36 3 1078 (1965).

Koehler W.C., Metallurgical Society Conference, 43, Gordon and Breach
Science Publishers, pp99 (1967).

Levy P.M., Phys Rev 177 2 509 (1969).

Liu S.H., Gupta R.R., Sinha S.K., Phys Rev B 4 4 1100 (1971).

Mackintosh A.R., Phys Rev Letts 9 90 (1962).

Melville R.J., PhD Thesis, University of Warwick (1989).

Patterson C., PhD Thesis, University of Hull (1986).

Roeland L.W., Cock G.J., Muller F.A., Moleman A.C., McEwen K.A.,
Jordan R.G., Jones D.W., J Phys F: Met Phys 5 L233 (1975).

Ruderman M.A., Kittel C., Phys Rev 96 99 (1954).

Thoburn W.C., Legvold S., Spedding F.H., Phys Rev 110 1298 (1958).

Vigren D.T., Solid State Commun. 18 1599 (1976).

Williams R.W., Mackintosh A.R., Phys Rev 168 679 (1968).

Yosida K., Phys Rev 106 893 (1957).

Chapter 2

Neutron Elastic Scattering in Rare-Earth Elements and Alloys.

Introduction

Neutron diffraction is still the most powerful probe for magnetic structure determination despite recent advances in magnetic X-ray scattering. The neutron mass of 1.675×10^{-27} kg results in a deBroglie wavelength of the order of interatomic distances in solids, giving rise to interference effects. The fact that the neutron is uncharged allows it to penetrate deep in to the bulk of a material and it's interaction with the nucleus via the strong force and unpaired electrons by virtue of it's own magnetic moment means that diffracted neutrons yield information about the crystal and magnetic structure of the scatterer. The apparent paradox of a neutral particle possessing a magnetic moment is explained in terms of a non-symmetrical distribution of quarks within the neutron.

The purpose of this chapter is to provide a brief introduction to the theory of the aspects of neutron scattering relevant to this study, and to describe the experimental techniques employed.

2.1 Theoretical Background

A detailed account of the theory of neutron diffraction is beyond the scope of this thesis. What follows will be kept as simple as possible by restricting the discussion to elastic scattering and, in the case of magnetic diffraction, only considering the use of unpolarised beams, while providing a comprehensive background for the experimental work described later. For further information the reader is referred to any one of a number of good text books available including Squires (1978), Lovesey (1984) and Izyumov and Ozerov (1970).

2.1.1 The Differential Cross Section

The geometry of any neutron scattering experiment is shown in figure 2.1. The quantity that is measured is the fraction of neutrons with incident energy E that are scattered per second into the solid angle Ω in the direction θ, ϕ with final energy between E' and E'+dE'. This quantity is known as the partial differential cross section and is written

$$\frac{d^2\sigma}{d\Omega dE'}$$

where σ is the total scattering cross section (the total number of neutrons scattered per second) and ϕ is the flux of incident neutrons.

In structure determination experiments such as those described here the distribution of final energies is sharply peaked about the incident energy. Consequently dE' is very small and the quantity we measure is the integral of
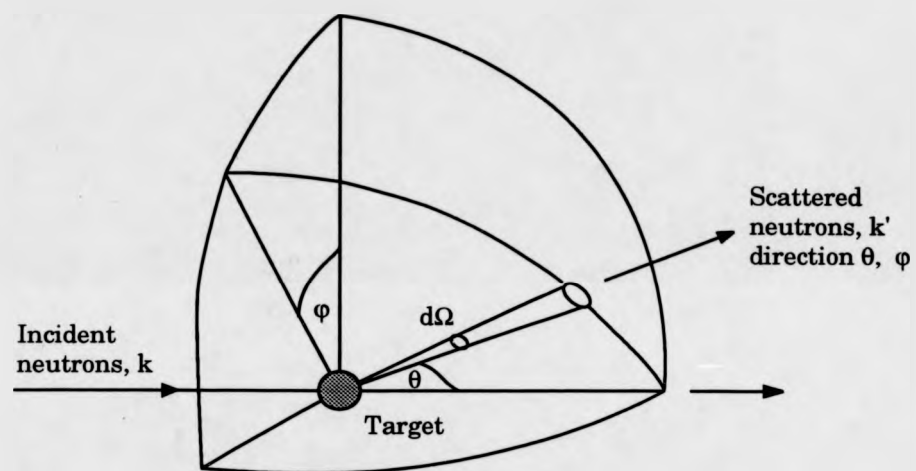
17

Figure 2.1 The geometry of a neutron scattering experiment.

the partial differential cross section over all final energies, thus we define the differential cross section as

$$\frac{d\sigma}{d\Omega} = \int_0^\infty \left(\frac{d^2\sigma}{d\Omega dE'} \right) dE'.$$

2.1.2 Nuclear Neutron Elastic Scattering

A single neutron incident on a single immobile nucleus will result in a spherical symmetrical scattered wave characterised by the wavefunction

$$\Psi_{sc} = -\frac{b}{r} \exp(-i\mathbf{k}\mathbf{r})$$

where r is the position of the scattered neutron, $\mathbf{k}$ is the wavevector of the neutron and b is a constant known as the scattering length which characterises the intensity of the scattered wave and at this stage may be considered to be approximately equal to the nuclear radius. We may assume the scattered wave to be spherical because of the large wavelength of the neutron in comparison to the radius of the nucleus and the weakness of the neutron nucleus interaction.

If we now describe the incident and scattered neutron by the wavevectors $\mathbf{k}$ and $\mathbf{k'}$ respectively, the differential cross section can be written in terms of the number of transitions from the incident to the scattered state per second $W_{k \rightarrow k'}$, which in turn is given by Fermi's golden rule. Hence

$$\left(\frac{d\sigma}{d\Omega} \right) = \frac{1}{\phi} \frac{1}{d\Omega} \sum_{k'} W_{k \rightarrow k'} \qquad (2.1)$$

18

$$\sum_{k'} W_{k\text{-}>k'} = \frac{2\pi}{\hbar} \rho_{k'} \mid <\mathbf{k'} \mid V \mid \mathbf{k}> \mid^2 \qquad \text{(Fermi's golden rule)}$$

where V is the potential of the interaction between the neutron and the nucleus and $\rho_{k'}$ is the density of the final scattered states $\mathbf{k'}$.

Using a technique known as box normalisation (Squires, 1978) $\rho_{k'}$ and ϕ may be evaluated and equation (2.1) may be written

$$\left(\frac{d\sigma}{d\Omega} \right) = \left(\frac{m}{2\pi\hbar^2} \right)^2 \mid <\mathbf{k'} \mid V \mid \mathbf{k}> \mid^2. \qquad (2.2)$$

We will now turn our attention to the nature of the interaction potential V which must be such that, as we have said, the scattering is isotropic. A convenient representation of a potential which gives weak isotropic scattering is the Fermi pseudopotential and is written

$$V(r) = \frac{2\pi\hbar^2}{m} b\delta(\mathbf{r}\text{-}\mathbf{R}) .$$

where $\mathbf{R}$ is the position of the nucleus.

As a consequence of the delta function in the Fermi pseudopotential the nucleus may be considered to be a point scatterer and as such an equivalent of the form factor used in X-ray scattering to account for the spatial distribution of the scatterers is not required.

If we now introduce the scattering vector κ such that $\kappa=\mathbf{k'}\text{-}\mathbf{k}$ the differential cross section becomes

$$\left(\frac{d\sigma}{d\Omega} \right) = b^2 \mid \int \exp(i\kappa.\mathbf{R}) \mid^2 . \qquad (2.3)$$

19

2.1.3 Scattering from a Crystal Lattice

If we consider a unit cell with sides defined by $\mathbf{a_1}$, $\mathbf{a_2}$ and $\mathbf{a_3}$ the lattice vector l is given by

$$\mathbf{l} = \mathbf{a_1} + \mathbf{a_2} + \mathbf{a_3}$$

and the cell volume $v_0 = \mathbf{a_1} . [\mathbf{a_2} \mathbf{x} \mathbf{a_3}]$.

The reciprocal lattice is defined by the vectors

$$\tau_1 = \frac{2\pi}{v_0} [\mathbf{a_2} \mathbf{x} \mathbf{a_3}]$$

$$\tau_2 = \frac{2\pi}{v_0} [\mathbf{a_3} \mathbf{x} \mathbf{a_1}]$$

$$\tau_3 = \frac{2\pi}{v_0} [\mathbf{a_1} \mathbf{x} \mathbf{a_2}].$$

If we first consider the case of a Bravais lattice with one atom per unit cell, the positions of the scatterers are now described by the lattice vector l. By making this substitution into equation 2.3 and performing the summation it can be shown (Lovesey,1984) that for a large Bravais lattice the result is

$$| \sum_l \exp(i\kappa.l) |^2 = N \frac{(2\pi)^3}{v_0} \sum_\tau \delta(\kappa - \tau). \quad (2.4)$$

Now generalising for a non-Bravais lattice by introducing the vector $\mathbf{d}$ which describes the positions of the atom j within the unit cell, the differential cross section may now be written as

20

$$\frac{d\sigma}{d\Omega} = N \frac{(2\pi)^3}{v_o} \sum_\tau \delta(\kappa - \tau) |F_N(\tau)|^2 \qquad (2.5)$$

where
$$F_N(\tau) = \sum_j \exp(i\tau.\mathbf{d})b_j \qquad (2.6)$$

and is referred to as the nuclear structure factor. The physical meaning of this result is that scattering is sharply peaked at the points where the scattering vector is equal to a reciprocal lattice vector. In practice the nuclear scattering peak does have a width which is inversely proportional to the number of scattering centres involved in the scattering process. The exponential term may be replaced by the geometrical structure factor G_{hkl} so 2.6 becomes

$$F_N(\tau) = bG_{hkl}. \qquad (2.7)$$

The indices hkl refer to the specific reciprocal lattice point defined by

$$\tau = h\tau_1 + k\tau_2 + l\tau_3.$$

2.1.4 Magnetic Neutron Elastic Scattering

When considering the scattering of neutrons from the magnetic structure of a solid we will return to the differential cross section for nuclear scattering, but now V is the interaction potential for the neutron moment and the magnetic electrons, and we should make allowances for the initial and final spin states of the neutron, σ and σ' respectively. Thus 2.2 becomes

21

$$\left(\frac{d\sigma}{d\Omega}\right) = \left(\frac{m}{2\pi\hbar^2}\right)^2 |<\sigma'\mathbf{k}'|V|\sigma\mathbf{k}>|^2. \qquad (2.8)$$

Since no polarisation analysis was performed in the work described here we shall neglect σ and σ' in the following discussion.

The neutron has a magnetic moment operator related to the spin by

$$\mu_n = -\gamma\mu_n\sigma$$

where γ is the gyromagnetic ratio, σ is the Pauli spin operator and μ_n is the nuclear magneton

$$\mu_n = \frac{e\hbar}{2m_p}.$$

The corresponding operator for the magnetic dipole moment of the electron is

$$\mu_e = -2\mu_B\mathbf{s}$$

where $\qquad \mu_B = \dfrac{e\hbar}{2m_e}$

the Bohr magneton and $\mathbf{s}$ is the spin angular momentum operator.

The neutron magnetic moment experiences a magnetic field $\mathbf{B(R)}$ created by the electron. $\mathbf{B(R)}$ contains a spin $\mathbf{B_s}$ and an orbital $\mathbf{B_L}$ contribution.

$$\mathbf{B_s(R)} = \frac{\mu_0}{4\pi} \text{ curl } \frac{\mu_e \times \hat{\mathbf{R}}}{|R|^2} \qquad (2.9)$$

22

$$B_L(R) = -\frac{\mu_0}{4\pi} \frac{2\mu_B}{\hbar} \frac{p \times \hat{R}}{|R|^2} \qquad (2.10)$$

where $\hat{R}$ is a unit vector parallel to R the position of the neutron with respect to the electron. The potential V may now be written as

$$V = -\mu_n.B = \frac{\mu_0}{4\pi} \gamma \mu_n 2\mu_B \sigma (W_s + W_L) \qquad (2.11)$$

where

$$W_s = \text{curl} \left(\frac{s \times \hat{R}}{|R|^2} \right) \qquad (2.12)$$

$$W_L = \frac{1}{\hbar} \frac{p \times \hat{R}}{|R|^2} \qquad (2.13)$$

It can be shown that

$$\sum_i \langle k' | W_{si} + W_{Li} | k \rangle = 4\pi q(\kappa) \qquad (2.14)$$

where $q(\kappa)$ is related to the magnetisation of the scattering system and is given by

$$q(\kappa) = \sum_i \exp(i\kappa.r)\{\hat{\kappa} \times (s_i \times \hat{\kappa}) + \frac{i}{\hbar\kappa} (p \times \hat{\kappa})\}. \qquad (2.15)$$

If, for the sake of simplicity, we consider only the spin part of q we may define a spin magnetisation operator $M_s(r)$ by

$$M_s(r) = -2 \mu_B \sum_i \delta(r-r_i)s_i \qquad (2.16)$$

23

and consequently a spin magnetisation vector $\mathbf{q_S}$ which is effectively the Fourier transform of $\mathbf{M_S(r)}$

$$\mathbf{q_S} = -\frac{1}{2\mu_B}\int\mathbf{M_S(r)}\exp(i\kappa.\mathbf{r})d\mathbf{r} \qquad (2.17)$$

and is related to $\mathbf{q}$ by $\qquad \mathbf{q} = \hat{\kappa}\;\mathrm{x}\;(\mathbf{q_S}\;\mathrm{x}\;\hat{\kappa}) \qquad\qquad (2.18)$

Although the calculation for the orbital part is more complicated, $\mathbf{q_L}$ has the same form as $\mathbf{q_S}$, and consequently the spin and orbital terms are easily combined to give a total magnetisation vector $\mathbf{q_M}$ such that

$$\mathbf{q_M} = \mathbf{q_S} + \mathbf{q_L} = -\frac{1}{2\mu_B}\int\mathbf{M(r)}\exp(i\kappa.\mathbf{r})d\mathbf{r}. \qquad (2.19)$$

Now from equation 2.18 $\quad \mathbf{q} = \hat{\kappa}\;\mathrm{x}\;(\mathbf{q_M}\;\mathrm{x}\;\hat{\kappa})$

which is more conveniently written in the form

$$\mathbf{q} = \mathbf{q_M} - (\mathbf{q_M}.\hat{\kappa})\hat{\kappa} \qquad\qquad (2.20)$$

The important results are that a neutron scattering experiment provides information about Fourier components of the magnetisation density and that scattering will only take place if there is a component of the magnetisation vector perpendicular to the scattering vector.

For the case of neutron nuclear scattering we were able to consider the nuclei as point scatterers, however this is obviously not the case for unpaired electrons so we must define a form factor f to account for their spatial distribution

$$f(\kappa) = \int \rho(\mathbf{r})\exp(i\kappa.\mathbf{r}) \qquad (2.21)$$

where $\rho(r)$ is the normalised density of the unpaired electrons.

The scattering of neutrons from ions with both spin and unquenched orbital angular momentum is very complicated (Johnston (1966)) so for this treatment we will simply quote the differential cross section assuming LS coupling, however before doing so it is useful to reduce the constants from equations 2.8,2.11 and 2.14.

$$\frac{m}{2\pi\hbar^2} \cdot \frac{\mu_0}{4\pi} \cdot \gamma \cdot \frac{e\hbar}{2m_p} \cdot 2\frac{e\hbar}{2m_e} \cdot 4\pi = \gamma r_0 \frac{m}{m_p} \approx \gamma r_0$$

and to introduce the magnetic scattering length **p** such that

$$\mathbf{p} = \frac{\gamma r_0}{2} f(\kappa) g \mathbf{J}$$

thus we have the magnetic differential cross section

$$\frac{d\sigma}{d\Omega} = \mathbf{p}^2 |\mathbf{q}|^2 \mid \int \exp(i\kappa.\mathbf{r}) \mid^2 . \qquad (2.22)$$

2.1.5 Scattering from a Ferromagnet

For a simple 3D ferromagnet the position vector of the magnetic moments is equal to those of the nuclear lattice, consequently equation 2.5 and 2.6 are easily rewritten for the ferromagnetic case as

$$\frac{d\sigma}{d\Omega} = N \frac{(2\pi)^3}{v_0} \sum_\tau \delta(\kappa-\tau) |F_M(\tau)|^2 \qquad (2.23)$$

where
$$F_M(\tau) = \sum_j \exp(i\tau.\mathbf{d})p \, \mathbf{q}_j. \qquad (2.24)$$

Consequently magnetic scattering appears as an additional contribution to the nuclear peaks.

Since the majority of the neutron scattering experiments presented here were performed in a zero applied magnetic field we must be aware of the existence of domains and that **q** in the differential cross section must be averaged over all the possible domain orientations to give **<q>**. We will discuss the form of **<q>** in a following section.

2.1.6 Scattering from Modulated Antiferromagnetic Structures

Modulated antiferromagnetic structures are a principle feature of rare-earth magnetism and in the following study we will encounter modulated structures where the moments are confined to the basal plane, forming a helix, and structures where the moments are aligned along the c-axis. First we will derive the differential cross section for a modulated structure and then discuss the importance of the orientation of the moments.

If we define a propagation vector for the modulation, *q* and a vector η which represents the spin at position **r**, we may write η as a Fourier series expansion with n components

$$\eta = \sum_n A_n \exp(in\mathbf{q}.\mathbf{r}). \qquad (2.25)$$

By simply convolving the Fourier series with the magnetic differential cross section (2.22) we get   .

$$\frac{d\sigma}{d\Omega} = p^2 |\,\mathbf{q}\,|^2 \; |\; {\textstyle\int} \exp{(i(\kappa \pm n\mathbf{q}).\mathbf{r})}\,|^2 \; . \qquad (2.26)$$

If we perform the summation as before the differential cross section for a modulated structure becomes

$$\frac{d\sigma}{d\Omega} = N \frac{(2\pi)^3}{v_0} \sum_{\tau} \delta((\kappa \pm n\mathbf{q})\text{-}\tau) p^2 \mathbf{q}^2 |\sum_{n} \sum_{j} A_n \exp(i(n\mathbf{q} \pm \kappa).\mathbf{r})|^2 \quad (2.27)$$

Thus the diffraction pattern consists of n "satellite" reflections at positions n$\mathbf{q}$ away from the nuclear peak along the reciprocal lattice direction which corresponds to the propagation direction of the modulation. The intensities of the satellite peaks will depend upon the amplitudes of the respective Fourier components. In the most simple case the modulation is that of a pure sinusoid and satellites are observed a distance q either side of the nuclear peak. It is still the case that scattering will only be observed if there is a component of the magnetisation vector perpendicular to the scattering vector, and it is this property which will allow us to differentiate between the two types of modulated structure described above. This may be explained more clearly once we have discussed the form of the reciprocal lattice and the types of scans undertaken to observe these satellite peaks.

2.2 Special Considerations for Gd, Lu, Er and Ho

2.2.1 Scattering from The HCP Structure

Before we can describe further the determination of magnetic structure by neutron diffraction and the experimental techniques employed in this study we must discuss the form of the reciprocal lattice for the HCP structure and the geometrical structure factor G_{hkl} which dictates the intensity of the scattering for specific reciprocal lattice points.

We have already defined the reciprocal lattice in section 2.1.3 now we must apply this definition to the HCP system. In the basal (a*b*) plane (figure 2.2) the reciprocal lattice has six-fold symmetry, the a* and b* reciprocal lattice directions being separated by 60°. The a*c* plane of the reciprocal lattice is shown in figure 2.3.

A construction which we will find useful later is the Ewald sphere, which has been drawn on both diagrams of the reciprocal lattice. The Ewald sphere is centred on the sample position and has radius $|\mathbf{k}|$. The reciprocal lattice is centred upon the intersection of $\mathbf{k}$ with the circumference of the sphere. Clearly, the diffraction condition occurs at the point where a reciprocal lattice crosses the Ewald sphere.

The geometrical structure factor (equation 2.7) allows for the fact that the HCP is not a Bravais lattice, and accounts for the scattering from the atom within the unit cell. The positions of both atoms in the unit cell are defined by

$$\mathbf{d_1} = (0,0,0),$$
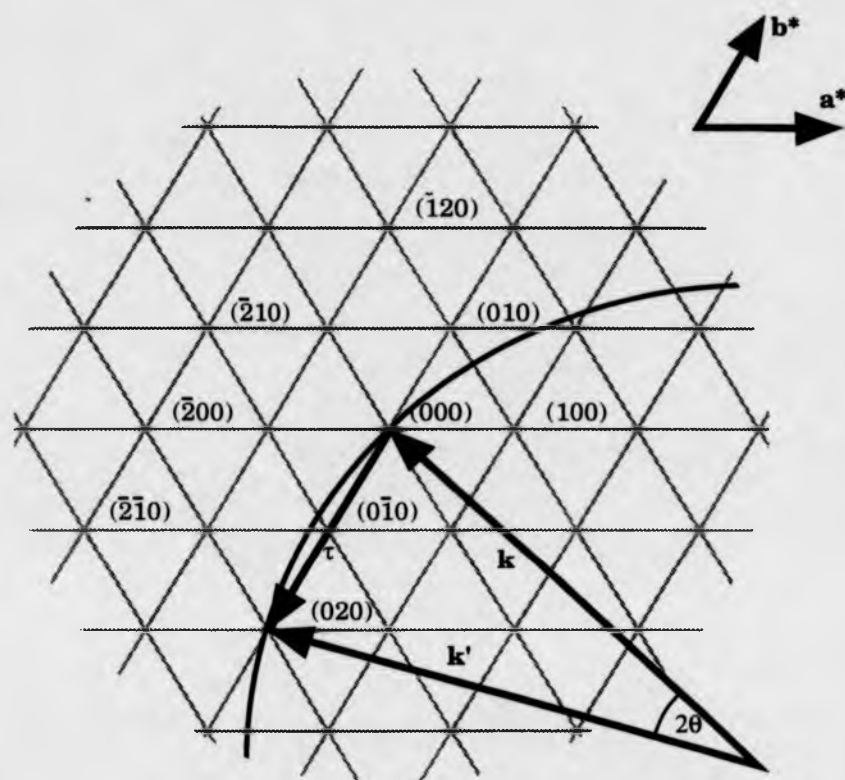
$$\mathbf{d_2} = (\frac{2}{3},\frac{1}{3},\frac{1}{2})$$
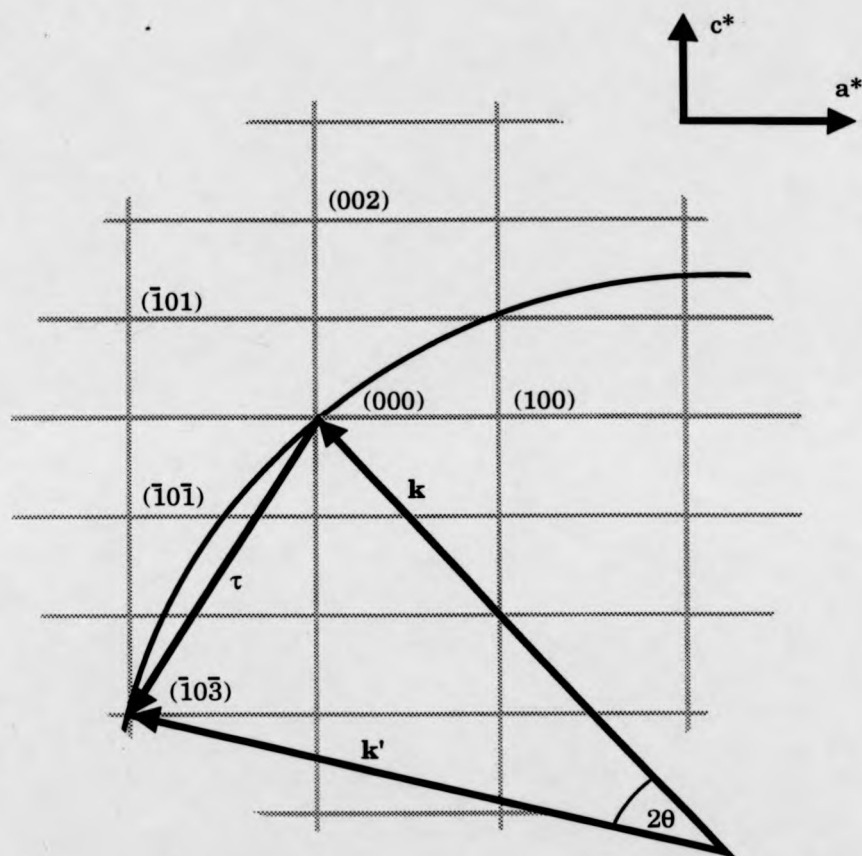
Figure 2.2 The a*b* plane of the HCP reciprocal lattice

Figure 2.3 The a*c* plane of the HCP reciprocal lattice.

Thus summing the scattering from both atoms we have

$$G_{hkl} = 1 + \exp\left(i(\tfrac{2}{3}h, \tfrac{1}{3}k, \tfrac{1}{2}l)\right)$$

Due to the presence of the interlayer, reflections with indices 001 where l is odd are absent. G_{hkl}^2 for some of the most commonly used reflection are tabulated (table 2.1).

2.2.2 The Neutron Scattering Length b

Previously we described the scattering length simply in terms of an impact parameter which we have assumed to be independent of the wavelength of the incident neutron. While on the whole this is a valid assumption, those isotopes, Gd and Lu amongst them, which have a (n,γ) capture resonance in the energy range of thermal neutrons display quite dramatic changes in b as a function of wavelength.

The scattering length is a complex quantity with the imaginary part corresponding to the absorption, usually to form a compound nucleus with the associated emission of a γ. For most cases the imaginary part is negligible, however as the energy of the incident neutron approaches that of a resonance it becomes more important. It is very useful to have some understanding of the behaviour of the scattering length as a function of wavelength not least so the most suitable choice of wavelength for an experiment may be made.

A reasonably reliable way of modelling the behaviour of both parts of the scattering vector in the region of the resonance is to assume a single

Table 2.1 G^2 for some low angle reflections

Reflection (hkl)	G^2_{hkl}
001	0
002	4
100	1
101	3
102	1
103	3
104	1
200	1
110	4
120	1
111	0
201	3
202	1

resonance level in the compound nucleus (Breit and Wigner, 1936). Thus b may be expressed as

$$b = R + \frac{\frac{1}{2}\Gamma_n |k|^{-1}}{(E-E_r) + \frac{1}{2}i\Gamma} \qquad (2.28)$$

where R is the nuclear radius (approximated by $1.5\text{x}10^{-13}\sqrt[3]{A}$ cm), E_r is the (n,γ) resonance energy and E is the energy of the incident neutron. $\Gamma = \Gamma_a + \Gamma_n$ which are the resonance widths for absorption and re-emission of the incident neutron respectively. If we separate b into it's real and imaginary parts we have

$$b' = R + \frac{\Delta E \, \Gamma_n |k|^{-1}}{2\Delta E^2 + \frac{1}{2}\Gamma^2} \quad \text{(real)} \qquad (2.29)$$

$$b'' = \frac{\Gamma_n \Gamma \, |k|^{-1}}{4\Delta E^2 + \Gamma^2} \quad \text{(imaginary)} \qquad (2.30)$$

$$b = \sqrt{b'^2 + b''^2}$$

$$\Delta E = E - E_r$$

We may assume that Γ_a will remain constant while Γ_n is proportional to $|k|$.

Bates (1985) has modelled the behaviour of b for natural Gd near resonance using the following parameters

$$\Gamma_n \approx 1.65 \times 10^{-15} \, |k| \; \text{(eV)}$$
$$\Gamma \approx \Gamma_a \approx 0.108 \; \text{(eV)}.$$

While these parameters are only approximate the calculated values of b are in good agreement with the observed values. Plots of b', b" and b are shown in figure 2.4.

Following the same method b' and b" have been calculated for natural Lu. This necessarily involves averaging over both isotopes By fitting equation 2.29 to the observed value at 1.8Å (Sears,1984) a value for Γ_n was obtained. The value for Γ_a is taken from Lovesey (1984).

$$\Gamma_n \approx 3.97 \text{ x } 10^{-16} \mid k \mid \text{ (eV)}$$
$$\Gamma \approx \Gamma_a \approx 0.063 \pm 0.005 \text{ (eV)}$$

The calculated values are plotted (figure 2.5). The most striking feature is the sharpness of the peak in b" at the resonance, in comparison to the broad effect seen in Gd. Another feature of interest is that by using wavelengths of 0.5Å or lower, serious absorption effects will be avoided in both elements.

Since Gd-Lu is a random alloy, the scattering length will vary throughout the sample, from element to element, isotope to isotope. It is only the mean scattering length, b_{alloy}, which will give rise to coherent scattering.

$$b_{alloy} = \sum_{\varepsilon} c\varepsilon \, b\varepsilon,$$

where $b\varepsilon$ is the mean scattering length and $c\varepsilon$ is the concentration of the εth element.
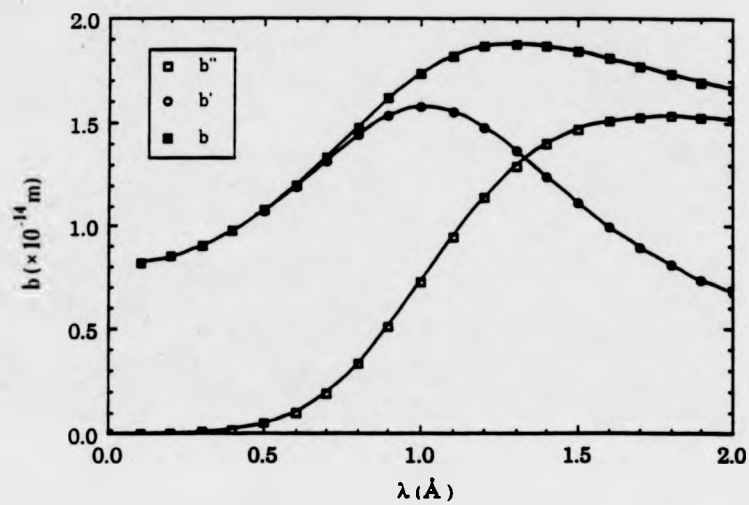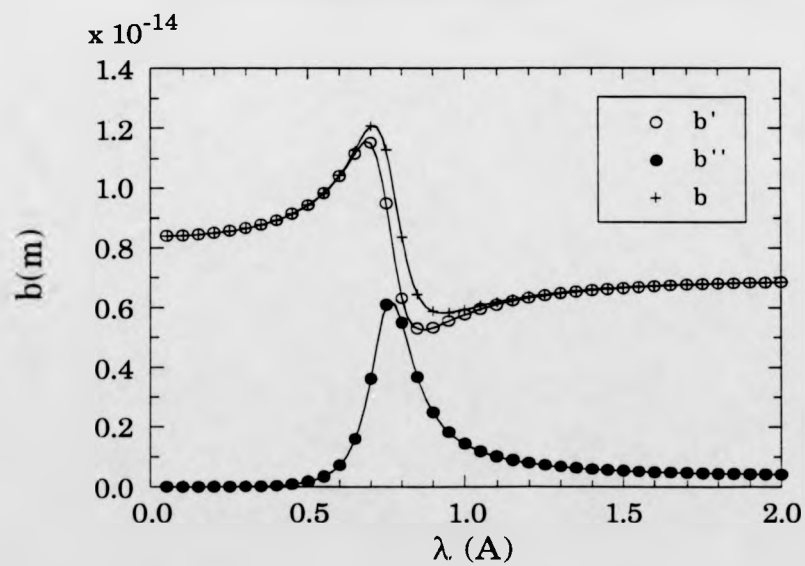
Fig.2.4 The scattering length, b vs λ for Gd.

Fig. 2.5 Scattering length, b, vs. λ for Lu.

2.3 Experimental Techniques

The techniques employed in an elastic neutron scattering experiment must be geared to maximising resolution, and to minimising or at least catering for problems arising from the single crystal sample, such as absorption, extinction and multiple scattering, or from the instrument, such as $\lambda/2$ contamination.

The nature of the experiment obviously also depends upon the information one expects to obtain. To this end the experimental procedure must be carefully considered.

In this section the causes and effects of instrumental resolution will be discussed. The two diffractometers employed in this study will be described, and a brief account of their modus operandi will be given.

The procedure for data collection and analysis, and the corrections applied to the data will be discussed.

2.3.1 Instrumental Resolution

Instrumental resolution is dependent upon four parameters, to wit; beam divergence, crystal mosaic, detector resolution and wavelength bandwidth (Schoenborn, 1983).

The effects of all these parameters bar crystal size and detector resolution may be clearly described using the Ewald construction (fig. 2.6).

The effects of the divergence of the neutron beam is well represented by the Ewald diagram (2.6a) with two Ewald spheres representing the two limiting cases. The result is a smearing of intensity which we assume to be Gaussian in both 2θ and ω and and when represented on a map of ω-2θ space appears as a line at 45° to the axes.
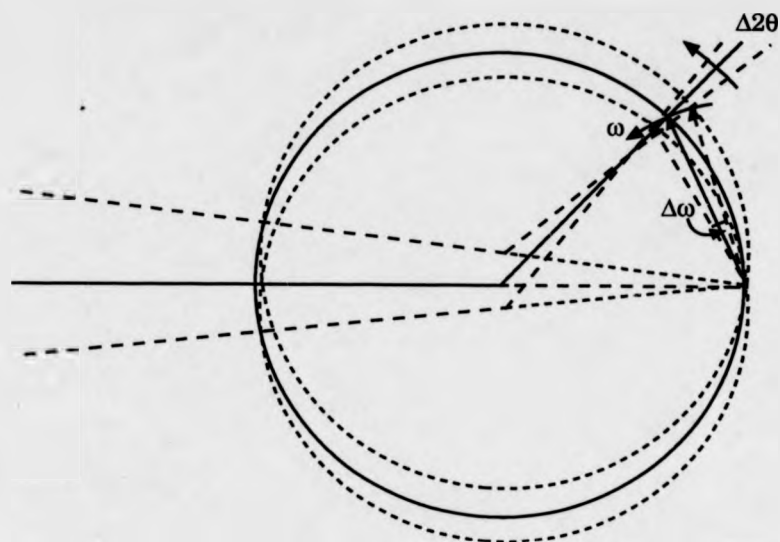
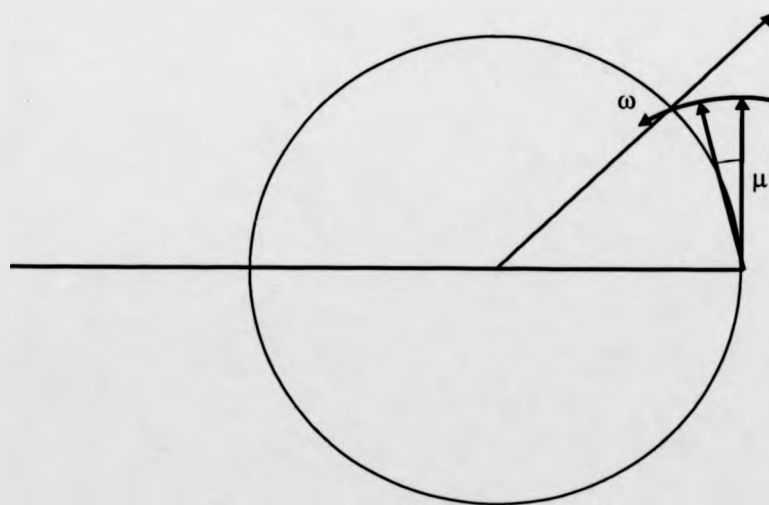Fig. 2.6a Ewald Construction for a Divergent Beam

Fig 2.6b Ewald Construction for a crystal of Mosaic spread μ

If the crystal has a mosaic spread characterised by $\mu°$, the crystal will remain in the reflecting geometry throughout a change $\Delta\omega=\mu$ in ω (fig. 2.6b). Thus a smearing in ω, also assumed to be Gaussian, will be observed.

Because the neutron beam has a divergence and the monochromator will have some mosaic a bandwidth $\Delta\lambda$ will be introduced. If we consider the differentiation of Braggs law we will arrive at equations for the two limiting cases referred to a λ_{min} and λ_{max}.

$$\Delta\lambda = \lambda\varepsilon\cot\theta_m$$

Thus,

$$\Delta\lambda_{min} = \lambda(1-\Delta\theta\cot\theta_m)$$
$$\Delta\lambda_{max} = \lambda(1+\Delta\theta\cot\theta_m)$$

where θ_m is the monochromator angle and ε is the divergence of the neutron beam. The overall effect can be seen in figure 2.6c. Clearly a smearing in both 2θ and ω is produced. One point that is of interest is that two reflections which are Friedel pairs may have differing resolutions with respect to ω as a result of the asymmetric effects of the wavelength bandwidth.

The detector resolution will introduce a Gaussian distribution of intensity along the 2θ direction.

Crystal size will also play a major role in the resolution of measurements. The resolution ellipsoid generated by the parameters described must be superimposed on the crystal at each and every point, this is best achieved by performing a convolution of the resolution ellipsoid with a square wave along 2θ. If the sample is asymmetric in shape there may also be some smearing of intensity in the ω direction.
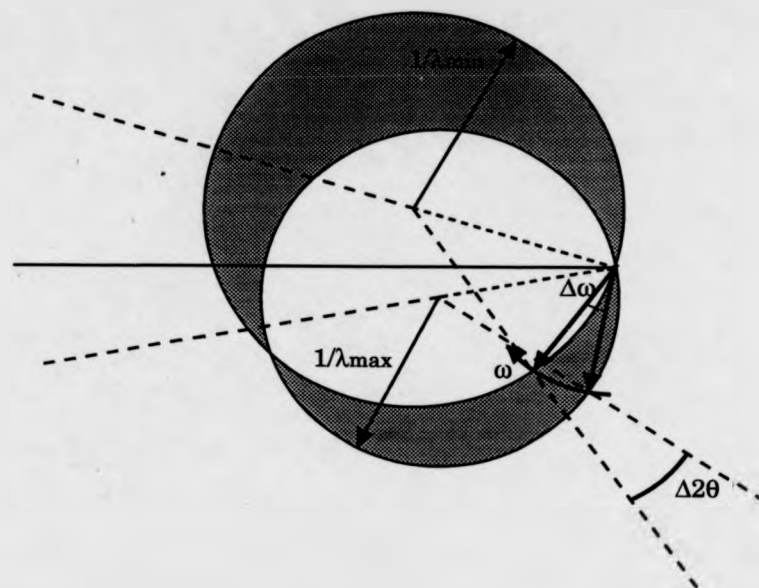
33

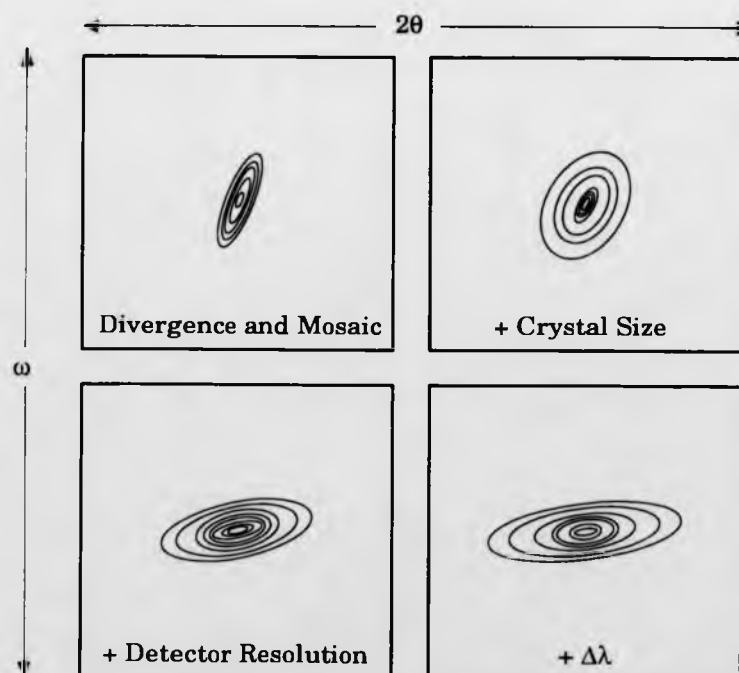Fig 2.6c Ewald construction for a beam with bandwidth $\Delta\lambda$

Fig. 2.7 The effects on the ω-2θ profile of the five
parameters which dictate resolution.

On a map of 2θ against ω the combined effects of all these parameters become evident (fig2.7). The beam divergence and the crystal mosaic produces an ellipse with its major axis at 45° to the ω axis. The detector resolution introduces an additional broadening along the 2θ direction, and usually the ellipsoid is enlarged when crystal size is taken into account. Obviously the scan of highest resolution is that which takes the shortest route through the resolution ellipsoid. To a crude approximation, this is an ω scan. The D10 diffractometer performs ω-xθ scans where x is a function calculated on the basis of the resolution criteria described above, so measurement scans are always performed at the maximum resolution. The D9 diffractometer is equipped with a multidetector and performs scans through diffraction points solely in the ω direction.

2.3.2 The D9 and D10 Diffractometers

Two instruments have been employed in the neutron scattering part of this study, both at the Institut Laue-Langevin in Grenoble, France. D9 is a four circle diffractometer on a hot beam line, while D10 may be operated as a four circle diffractometer or as a triple axis spectrometer and is situated on a thermal beam line. Thermal neutrons are in equilibrium with a D_2O moderator at 300K which produce a maxwellian distribution which peaks at 1.2Å. The thermal neutrons are modified on the hot beam line by a graphite moderator at 2400K which enhances the neutron intensity in the range 0.4Å to 0.8Å. Both instruments are briefly described below.

The schematic diagram of the D9 diffractometer is given (fig. 2.8). The whole body of the instrument is mounted on air-cushioned pads which allow its easy movement around the monochromator permitting continuous variation of the incident wavelength in the range 0.35Å to 0.85Å. The

HOT
SOURCE

10m

MONOCHROMATOR
(Cu 220)

$2\theta_m$

2.29m

Pre-Sample Slit

70mm

70mm

SAMPLE

2θ

Post-Sample Slit

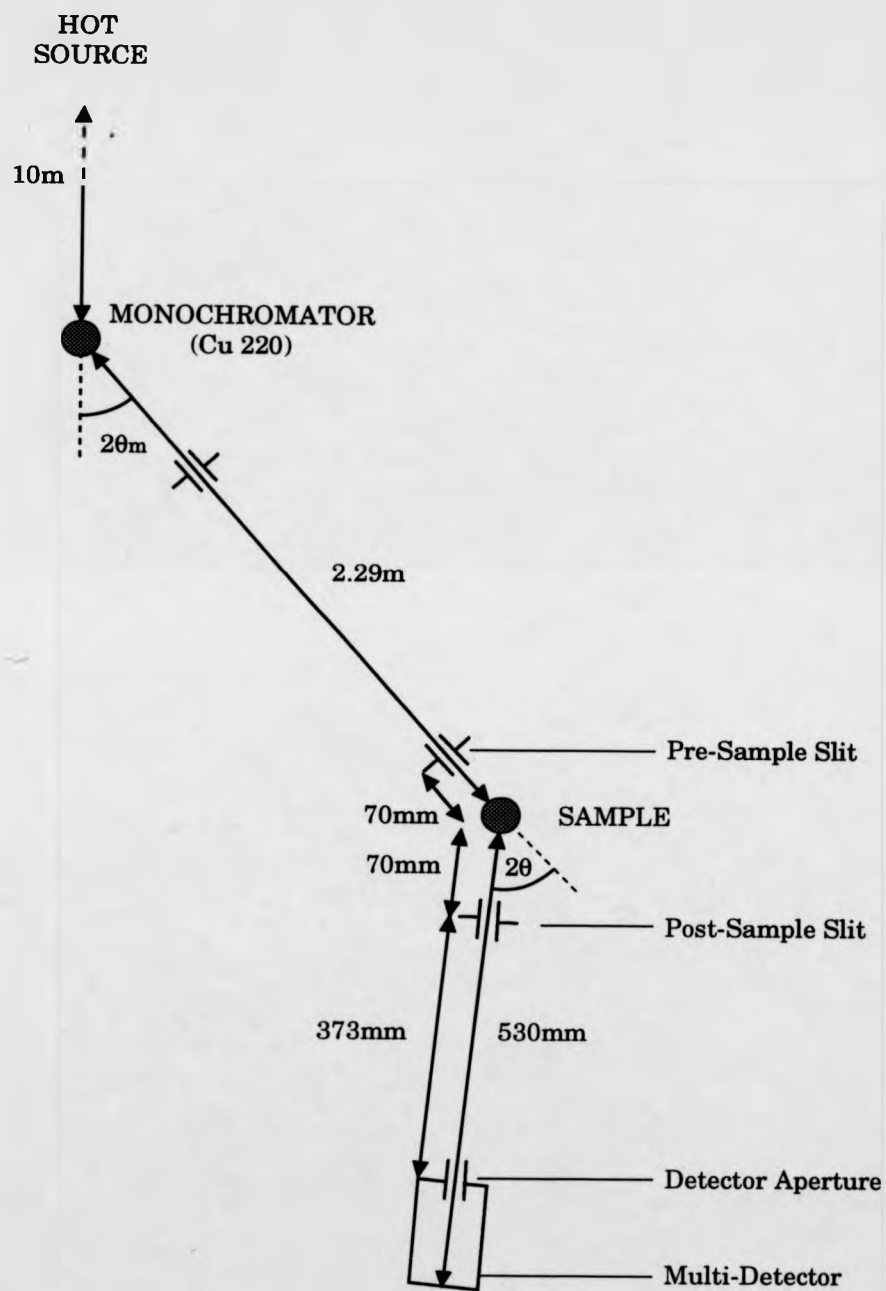373mm

530mm

Detector Aperture

Multi-Detector

Figure 2.8 Plan Schematic of the D9 Diffractometer

monochromator is a Cu crystal aligned to reflect off the (220) plane. Several resonant filters are fitted to suppress higher order contamination at wavelengths of 0.48Å, 0.55Å, 0.70Å and 0.84Å.

D9 is computer controlled by a Micro Vax II. A Displex cryostat permits full four circle access in a temperature range of 300K to 14K with temperature stable to ±0.1K and with an absolute accuracy of ±1K.

D10 is a more versatile instrument, which may be operated in four modes; as a standard four circle, as a four circle with energy analyser, as a 2 axis, or as a 2 axis with energy analyser. The first two configurations are the only ones employed for this work, the standard four circle configuration being well suited to initial surveys of complex diffraction pattern, and the addition of the energy analyser providing improved resolution.

A schematic of the instrument is given in figure 2.9. Two vertically focussing monochromators, one of pyrolytic graphite which produce continuously variable radiation in the range 1.8Å to 6Å and another of Copper reflecting off the (200) plane giving wavelengths in the range 1.8Å to 2.6Å. The energy analyser crystal is pyrolytic graphite.

Complete computer control is provided by a PDP 11/33. A He flow cryostat offers temperature control down to 1.6K. Both detectors are of the ^{3}He type.

2.3.3 Experimental Procedure

The experimental procedure for both instruments is very similar and will be described below in general terms. Samples are mounted with both the scattering vector and the magnetic modulation vector in the equatorial plane, becausue of the poor out of plane resolution of both instruments. Aluminium sample pins are used and the samples are stuck on using "Kwikfil" prior to

Monochromator

10' Collimator

SAMPLE

10' Collimator

^{3}He Detector
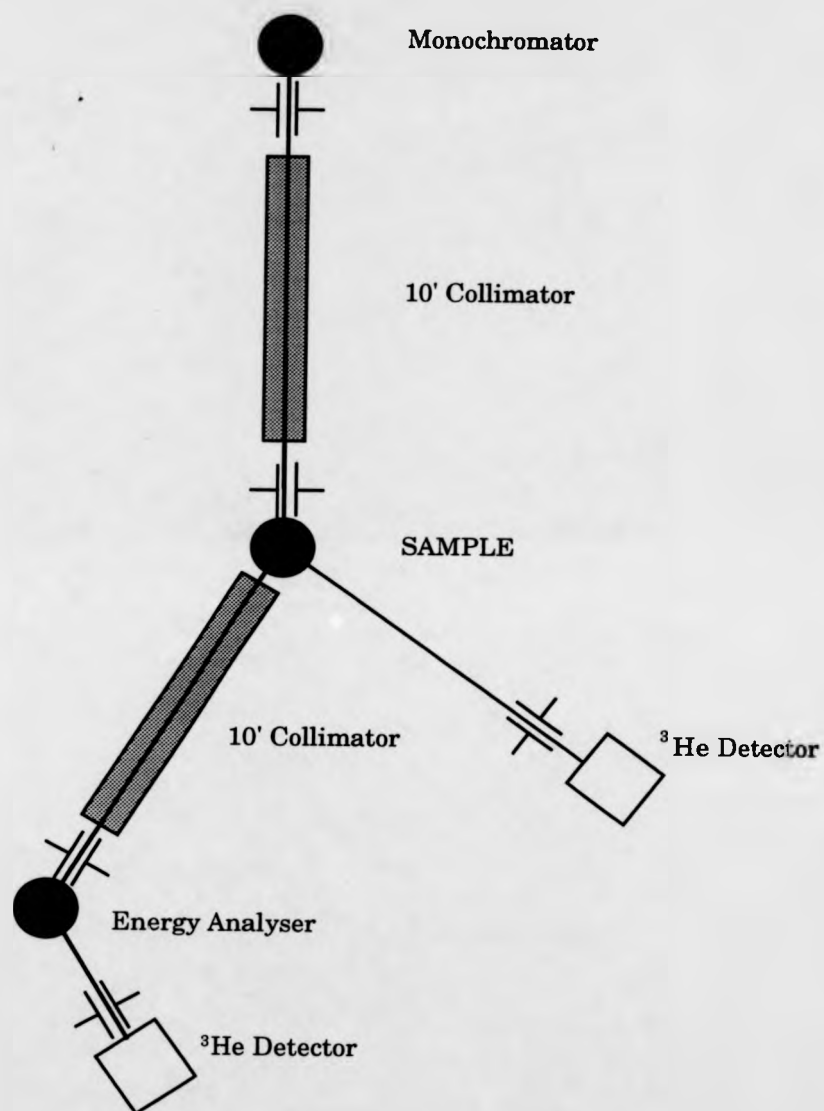
Energy Analyser

^{3}He Detector

Fig. 2.9 The D10 Diffractometer

mounting onto the diffractometer. D9 is equipped with an optical telescope and an XYZ translation at the base of the Displex head which makes the positioning of the sample in the centre of the neutron beam easy. D10 is slightly less cooperative and great care must be taken to ensure that the sample is accurately positioned centrally on the pin. Polaroid photographs are used to ensure that the mounted sample is in the centre of the beam.

Background limiters and detector apertures are set to ensure that the sample is bathed in neutrons, but the background is kept to a minimum. Beam collimators were used on D10 to improve resolution and their use is referred to in chapter 6.

Before the cryostat is put in place and sealed, several strong reflections are identified and centred. This procedure is made considerably easier if the sample has distinct morphology and the scattering vector of a strong reflection can be easily identified. The (002) reflection is a common choice for the samples studied in this work because the scattering vector usually corresponds to the long axis of a cuboid. Once three or four non-colinear reflection have been identified the computer will calculate a UB matrix which relates the reciprocal lattice to the diffractometer geometry. At this point, the cryostat is usually sealed up and the temperature is lowered to approximately 20K above the initial ordering temperature when the UB matrix and diffractometer offsets are refined using a larger set of reflections.

Once the sample is "centred" as described above, a large set of nuclear reflections are measured. Once corrected for Lorentz and absorption (both are explained in the next section) a nuclear refinement is performed which provides parameters for the corrections which must be performed prior to data analysis.

For the collection of magnetic scattering data for structure determination two types of scan are employed; (i) a MES scan in which the intensity of a nuclear peak is measured using an ω or ω-xθ scan as described

earlier and allows determination of the ferromagnetic contribution to the scattering. and .(ii) a Q scan in which a scan is performed along the direction of the propagation vector of a periodic structure in an investigation of satellites and higher order reflections. When performing Q scans, one must bear in mind the orientation of the resolution ellipsoid and choose a scan which will afford the highest possible resolution. In all these systems the propagation vector lies along the c direction however, an $(00l)$ scan through the (002) lattice point is almost entirely a scan in 2θ and as a consequence resolution is so poor that the satellites are often assimilated into the nuclear peak. A far more productive scan, in spite of the lower intensity, would be a $(10l)$ scan across the (101) or (100) points which would be largely scans in ω and of far superior resolution.

When using a multidetector, as on D9, non-uniformities in the response of the elements of the multidetector must be corrected for. These corrections, are made by normalising the data to the response of the detector to a homogeneous beam of neutrons such as scattering from a perspex plate (fig2.10) from the collected data.

2.3.4 Corrections for Real Crystals

In passing through the crystal the neutron beam will undergo several interactions both elastic and inelastic which will cause a deviation from the true intensity of the beam at the detector, in addition the geometry of the diffractometer itself will cause some errors in intensity measurements. By and large five corrections are applied to the collected data:

    i) The Lorentz correction

    ii)The absorption factor, A
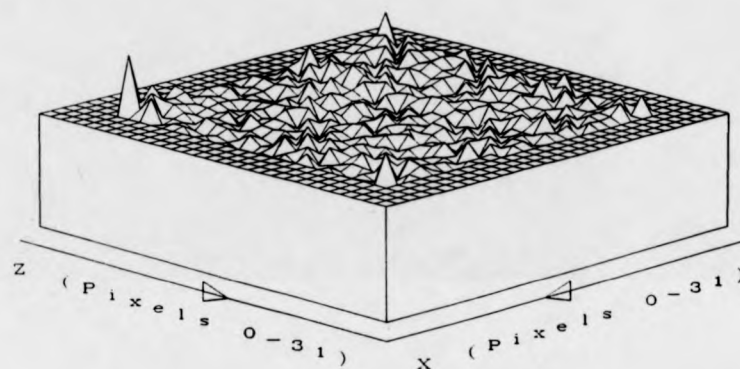
Fig. 2.10 Mulidetector response to incoherent scattering from perspex, used to perform α corrections.

iii) The Debye-Waller factor, e^{-2W}

iv) The thermal Diffuse Scattering correction, α

v) Nuclear and Magnetic extinction corrections, Y_s and Y_m.

The Lorentz correction accounts for the differences in the speed at which the reflection pass through the reflection condition. The data collected on the D9 diffractometer are corrected for the Lorentz effect by running the ADV program whose prime purpose is to extract accurate intensities from multidetector data. The other corrections, however, must be made separately. The observed intensity I' corrected only for the Lorentz factor is given by

$$I' = IAe^{-2W} (Y_s + \alpha)$$

where I is the corrected intensity.

Absorption corrections are performed using the ILL DATAP program prior to the structure refinement. For the calculation of the spontaneous magnetic moment, normalised structure factors are used, consequently absorption effects are assumed to be negligible.

The Debye-Waller factor and thermal diffuse scattering are both inelastic processes. Debye-Waller causes a reduction in peak intensity as the energy of the neutron is altered as a result of interaction with a phonon. W varies with $(\sin\theta/\lambda)^2$, but the refinement showed that the error arising from Debye-Waller would be no more than 3% for the reflection measured.

Thermal vibrations of the lattice will also give rise to diffuse scattering (T.D.S.) in the vicinity of a reciprocal lattice point. While TDS can produce dramatic effects, previous studies have shown that for Gd based alloys the TDS factor is likely to be much less than 1% and may be reduced by fitting a linear background when calculating the integrated intensity of the peak.

The most important correction for magnetic structure determination is extinction. Extinction may be considered as being of two types; primary extinction in which the beam undergoes secondary reflection within a mosaic block, thus weakening the reflected beam, and secondary extinction in which the secondary reflection takes place in another grain. Primary extinction is usually restricted to samples of exceptionally good quality, consequently it is assumed that secondary extinction is of overriding importance in single crystals of rare-earths. Nuclear extinction factors Y_n were calculated by G.J.McIntyre at the I.L.L. with the UPALS program using the data collected above the initial ordering temperature. However, for ferromagnetic reflections, the total extinction including magnetic contributions is a complex function of the total intensity. The total extinction factors have been calculated using a bespoke program ran on the Micro-Vax at the University of Warwick. A more detailed account of the extinction calculation and a listing of the program are included as appendices A and B respectively.

The final confirmation that corrections have been performed properly and that the assumed model for the magnetic structure is correct is the good agreement between the spontaneous magnetic moment collected from the data and a standard Brillouin function normalised to the saturated magnetic moment.

2.3.5 Calculation of the Average Spontaneous Magnetisation

From equation 2.7 and 2.24 the normalised structure factor may be written

$$\frac{F_M}{F_N} = \frac{pqG_{hkl}}{bG_{hkl}} = \frac{\gamma r_o f(\kappa) gJ\mathbf{q}}{2b}$$

Thus,

$$\left(\frac{I_{total}-I_{nuc}}{I_{nuc}}\right) = \frac{F_M{}^2}{F_N{}^2} = \frac{\gamma r_o{}^2 f(\kappa)^2 M(\mathbf{q})^2}{4b^2}$$

and the spontaneous magnetisation $M(\mathbf{q})$ may be calculated. If we expand the expression for q for the (002) reflections, the spontaneous magnetisation giving rise to scattering on the (002) peak may be written

$$M_{(002)}(\mathbf{q})^2 = M^2 \sin^2\theta = M_b{}^2.$$

Where θ is the angle between the magnetisation vector and the c-axis. Thus the component of the magnetisation in the base plane can be calculated solely from the (002) reflections.

For basal plane reflections we shall assume that when the magnetic structure is averaged over all the domains, the overall symmetry remains hexagonal. This would, of course, not be the case if a magnetic field was applied to the sample. Expanding $\mathbf{q}$ for the (100) reflections

$$M_{(100)}(\mathbf{q})^2 = \frac{M\sin^2\theta}{2} + \cos^2\theta$$

and the magnetisation calculated from the basal plane reflection will contain information about the c-axis and basal plane components as follows

$$M_{(100)}{}^2 = M_c{}^2 + \frac{M_b{}^2}{2}.$$

40

Clearly from a data set containing c-axis and basal plane reflections both components of the magnetisation may be calculated allowing models for the magnetic structure to be confirmed, and for canting angles and the total spontaneous magnetisation to be calculated.

References

Bates S. PhD Thesis, University of Hull (1985).

Becker P.J., Coppens P., Acta Cryst. A30 129 (1974).

Breit G., Wigner E. Phys. Rev. 49 519 (1936).

Izyumov Y.A., Ozerov R.P. "Magnetic Neutron Diffraction", Plenum
        Press, New York (1970).

Johnston D.F. Proc. Phys. Soc. 88 37 (1966).

Lovesey S.W. "Theory of Neutron Scattering from Condensed Matter. Vols. 1
        and 2", Clarendon Press, Oxford, (1984).

Melville R.J. PhD Thesis, University of Warwick, (1989).

Schoenborn B.P. Acta Cryst A**39** 315-321 (1983).

Squires G.L. "Introduction to Thermal Neutron Scattering", Cambridge
        University Press (1978).

Zachariasen W.H., Acta Cryst. **23** 558 (1967).

Chapter 3

Ultrasonic Studies of Rare Earth Magnetic Systems

Introduction

The propagation characteristics of an ultrasonic stress wave travelling through a solid provide information about any property of that solid which is sufficiently coupled to the crystal lattice. The coupling of the spin system to the crystal lattice via the magneto-elastic interaction means that the magnetic properties of the solid will give rise to anomalous behaviour in the elastic constant, C, (which is calculated from the ultrasound wave velocity) and the attenuation coefficient α.

We shall see that the magnetic interactions, which give rise to the wide range of magnetic structures displayed by the Rare Earths, have different effects on the crystal lattice and consequently the ultrasonic wave. As a result, the critical behaviour of both C and α as a function of temperature and applied magnetic field is useful, not only in the delineation of magnetic phases, but also for identifying the predominant magnetic interaction which is responsible for the magnetic ordering.

43

The equilibrium behaviour of C and α also provides an insight into the symmetry of the magnetic structure and the nature of the magnetic domains formed within the sample.

3.1 Stress Waves in a Solid

The derivation of expressions for the single crystal elastic constant is reasonably straight forward but a little lengthy, consequently the following discussion is condensed to the point where it serves the purpose of providing a background for the results presented later, but is by no means rigorous or complete. For a fuller account the reader is referred to Truell(1969), Musgrave(1970) or Kittel (1971).

We consider the passage of the ultrasonic wave as giving rise to a small deformation of the atomic position s such that

$$s = x' - x. \tag{3.1}$$

Following Truell, we will assume that the deformation and their derivatives are small enough so as to make the higher order terms negligible and write the strain tensor ε_{jl} as

$$\varepsilon_{jl} = \frac{1}{2}\left(\frac{\delta s_l}{\delta x_j} + \frac{\delta s_j}{\delta x_l}\right). \tag{3.2}$$

The geometrical meaning of ε_{jl} is easily understood; ε_{jl} where $j = l$ is the change in unit length of a straight line parallel to the x_j axis, ε_{jl} ($j \neq l$) is half the change in the angle between the x_j and x_l axes.

44

The equilibrium behaviour of C and α also provides an insight into the symmetry of the magnetic structure and the nature of the magnetic domains formed within the sample.

3.1 Stress Waves in a Solid

The derivation of expressions for the single crystal elastic constant is reasonably straight forward but a little lengthy, consequently the following discussion is condensed to the point where it serves the purpose of providing a background for the results presented later, but is by no means rigorous or complete. For a fuller account the reader is referred to Truell(1969), Musgrave(1970) or Kittel (1971).

We consider the passage of the ultrasonic wave as giving rise to a small deformation of the atomic position s such that

$$s = x' - x. \tag{3.1}$$

Following Truell, we will assume that the deformation and their derivatives are small enough so as to make the higher order terms negligible and write the strain tensor ε_{jl} as

$$\varepsilon_{jl} = \frac{1}{2}\left(\frac{\delta s_l}{\delta x_j} + \frac{\delta s_j}{\delta x_l} \right). \tag{3.2}$$

The geometrical meaning of ε_{jl} is easily understood; ε_{jl} where $j = l$ is the change in unit length of a straight line parallel to the x_j axis, ε_{jl} ($j \neq l$) is half the change in the angle between the x_j and x_l axes.

44

The deformation s may be considered to be made up of three components relating to rigid body translation, rigid body rotation and local deformation. When considering the effect of the magnetic system on the crystal lattice we are only concerned with small local deformations of the lattice, consequently only the last term is important, thus we may write 3.1 as

$$s_1 = \varepsilon_{11}x_1 + \varepsilon_{12}x_2 + \varepsilon_{13}x_3$$
$$s_2 = \varepsilon_{21}x_1 + \varepsilon_{22}x_2 + \varepsilon_{23}x_3$$
$$s_3 = \varepsilon_{31}x_1 + \varepsilon_{32}x_2 + \varepsilon_{33}x_3. \tag{3.3}$$

We can now define the elastic constant, C_{ikjl}, in terms of the stress strain relationship

$$\sigma_{ik} = C_{ikjl}\varepsilon_{jl} \tag{3.4}$$

where σ_{ik} is the stress tensor, i denotes the direction of the normal to the plane on which the stress component acts and k denotes the direction of the stress component.

There are nine equation 3.4s each with nine coefficients giving a total of 81 coefficients in total. However, due to the absence of turning moments $C_{ikjl} = C_{kijl} = C_{iklj}$ and these coefficients are reduced to 36. This symmetry property also permits a simplification of the tensor notation, by giving each pair of indices one value thus

Tensor notation	11	22	33	23,32	13,31	12,21
Reduced tensor notation	1	2	3	4	5	6.

Because the system is elastic ie. the strain energy is a function of state and not dependent on the path by which the state was reached C_{ikjl} and C_{jlik} are equivalent and a further reduction to 21 coefficients is possible. By invoking the symmetry of the HCP lattice we arrive at the allowed elements of C for HCP crystals which are $C_{11} = C_{22}$, $C_{12} = C_{21}$, $C_{13} = C_{31} = C_{23} = C_{32}$, C_{33}, $C_{44} = C_{55}$ and $C_{66} = \frac{1}{2}(C_{11} - C_{12})$.

3.2 The Elastic Constants of the HCP System

We are now in a position to discuss the elastic constant in terms of the nature of the ultrasonic wave and its interaction with the crystal lattice.

If we consider the forces acting on a small volume within the crystal, by resolving all the forces and equating them to the acceleration components the following equation of motion is obtained (Kolsky, 1953)

$$\frac{\delta \sigma_{ij}}{\delta x_j} = \rho \ddot{s}_i \qquad (i = 1,2,3). \qquad (3.5)$$

where the indices run through the orthonormal directions (fig. 3.1).

Combining the equation of motion with the stress strain relationship (3.4) we have

$$C_{ijkl} \frac{\delta \varepsilon_{kl}}{\delta x_j} = \rho \ddot{s}_l$$

where

$$\frac{\delta \varepsilon_{kl}}{\delta x_j} = \frac{1}{2} \left(\frac{\delta s_l^2}{\delta x_k \delta x_j} + \frac{\delta s_k^2}{\delta x_l \delta x_j} \right).$$
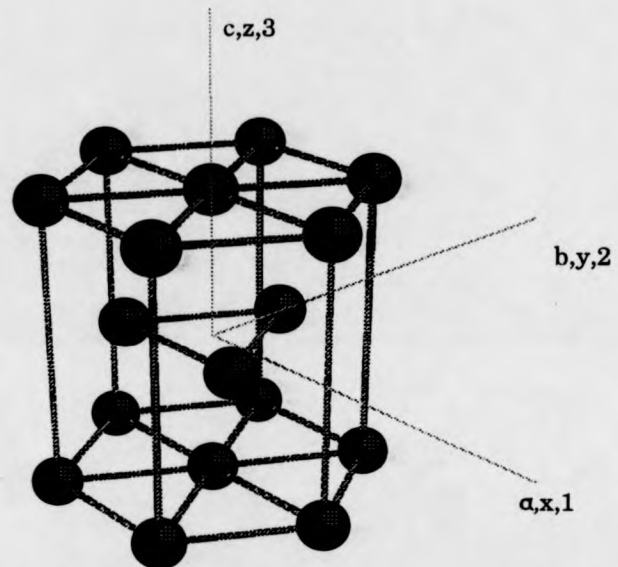
Fig. 3.1 The HCP structure showing the directional indices.

By invoking the $C_{ijkl} = C_{ijlk}$ symmetry condition the equation of motion may be written as

$$C_{ijkl}\frac{\delta s_l^2}{\delta x_k \delta x_j} = \rho \ddot{s}_i. \qquad (3.6)$$

If we consider the ultrasonic wave as a plane wave with wave vector **k** and define a unit vector **n**(n_1, n_2, n_3) in the same direction as **k** the wave equation is

$$s_l = s_{0l} \text{expi}(\omega t - \mathbf{k.r})$$

and

$$\frac{\delta s_l^2}{\delta x_k \delta x_j} = n_k n_j s_{0l} \left(\frac{\omega^2}{v^2}\right) \text{expi}(\omega t - \mathbf{k.r}).$$

Equation 3.6 may be written

$$C_{ijkl}\, s_{0l} n_k n_j = \rho v^2 s_{0i}. \qquad (3.7)$$

By substituting the allowed element of C for the HCP structure given earlier into (3.7) and using the reduced tensor notation we can first consider a wave propagating along the c axis (ie $n_1 = n_2 = 0$, $n_3 = 1$). The following solutions are obtained

$$(C_{44} - \rho v^2)s_{01} = 0 \qquad\qquad C_{44} = \rho v^2 \text{ (shear poln. along a)}$$

$$(C_{44} - \rho v^2)s_{02} = 0 \qquad\qquad C_{44} = \rho v^2 \text{ (shear poln. along b)}$$

$$(C_{33} - \rho v^2)s_{03} = 0. \qquad\qquad C_{33} = \rho v^2 \text{ (longitudinal)}$$

47

where the directions a,b and c are given in figure 3.1. Thus the C_{33} elastic constant may be calculated from the velocity of a longitudinal wave propagating parallel the c axis and C_{44} from the velocity of a shear wave polarized in any direction in the basal plane propagating along the c axis.

Similarly for propagation along a ($n_1=1$ $n_2=n_3=0$) we have

$$(C_{11} - \rho v^2)s_{01} = 0 \qquad C_{11} = \rho v^2 \text{ (longitudinal)}$$

$$\left(\frac{1}{2}(C_{11} - C_{12}) - \rho v^2 \right)s_{02} = 0 \qquad C_{66} = \rho v^2 \text{ (shear poln. along b)}$$

$$(C_{44} - \rho v^2)s_{03} = 0 \qquad C_{44} = \rho v^2 \text{ (shear poln. along c)}.$$

3.3 Magnetoelastic Effects

The interactions between the ultrasound wave and the magnetic structure via the crystal lattice are generically referred to as magnetoelastic effects. For the sake of simplicity we may divide them into two categories. In the case of the equilibrium state we are concerned with the effects on the propagation of the ultrasound wave caused by the strains induced in the lattice by the magnetic order. In the vicinity of phase transitions, it is the dynamic coupling between the magnetic excitations (magnons) and the lattice excitations (phonons) which are predominant.

3.3.1 Symmetry Dependence of the Elastic Constant

If we bear in mind that the ultrasonic wavelength is very large (~0.2mm) in comparison to the size of the unit cell, we may consider the ultrasonic wave to be a homogeneous strain field. In terms of a local site magnetisation $M(r)$ the free energy of the coupled magnetic/crystal system can be written as

$$F(r) = F_M(M(r)) + E_{ME}(M(r),\varepsilon) + E_E(\varepsilon) \qquad (3.9)$$

where F_M is the magnetic free energy density and E_E is the elastic energy which has no dependence on the magnetisation. E_{ME} is the magneto-elastic energy given by (Turov, 1983)

$$E_{ME} = \sum_{ijkl} B_{ijkl}\varepsilon_{ij}M_k(r)M_l(r) \qquad (3.10)$$

where B_{ijkl} is the magneto-elastic coupling tensor whose elements are defined by the crystal symmetry and consequently the allowed elements are the same as those for the elastic constant. The indices ijkl run through the directions described earlier (figure 3.1)

Magnetic order will induce a distortion of the crystal lattice which is compatible to the symmetry of the magnetic structure (magnetostriction). The strains created in this way may be included into the free energy expression by a renormalisation to the energy densities (Turov, 1983). If we now consider the strain in the lattice caused by the ultrasonic wave to have caused a small perturbation in the magnetic structure, this new magnetic structure may be derived by minimising the free energy density with respect

49

to the magnetisation along the three cartesian co-ordinates ($M_x(r)$, $M_y(r)$ and $M_z(r)$).

This derivation has been performed by Bates (1988), however it will be useful later to have quoted one expression from this derivation when considering the coupling of the various modes of the elastic constants to particular structures. Adopting the reduced tensor notation for C and B

$$\Delta Cab = - \sum_{PP'} \sum_{ijkl} B_{aij} M^0_i(P) \chi_{jl}(M^0(P), M^0(P')) M^0_k(P') B_{bkl}. \quad (3.11)$$

P and P' are the positions of a site of local magnetisation and the nearest neighbour and M^0 is the magnetisation prior to the distortion by the strain field. However, the most interesting term is the susceptibility χ_{jl}. From inspecting this expression one can see that the C_{44} mode, for instance, couples to the out-of-plane susceptibility while C_{66} couples to the in-plane susceptibility.

Describing the magnetic structure by the magnetic tensor T_{ijkl} equation 3.11 may be written

$$\Delta C_{ab} = - \sum_{ijkl} B_{aij} T_{ijkl} B_{bkl} \quad (3.12)$$

thus formalising the relationship between the symmetry of the magnetic structure and that of the crystal lattice.

When the symmetry of the magnetic structure breaks the crystal symmetry, magnetic domains will be formed. The magnetic tensor for the different possible domain orientations (T_{mnop}) may be formed by simply

to the magnetisation along the three cartesian co-ordinates ($M_x(r)$, $M_y(r)$ and $M_z(r)$).

This derivation has been performed by Bates (1988), however it will be useful later to have quoted one expression from this derivation when considering the coupling of the various modes of the elastic constants to particular structures. Adopting the reduced tensor notation for C and B

$$\Delta Cab = - \sum_{PP'} \sum_{ijkl} B_{aij} M^0_i(P) \chi_{jl}(M^0(P), M^0(P')) M^0_k(P') B_{bkl}. \quad (3.11)$$

P and P' are the positions of a site of local magnetisation and the nearest neighbour and M^0 is the magnetisation prior to the distortion by the strain field. However, the most interesting term is the susceptibility χ_{jl}. From inspecting this expression one can see that the C_{44} mode, for instance, couples to the out-of-plane susceptibility while C_{66} couples to the in-plane susceptibility.

Describing the magnetic structure by the magnetic tensor T_{ijkl} equation 3.11 may be written

$$\Delta C_{ab} = - \sum_{ijkl} B_{aij} T_{ijkl} B_{bkl} \quad (3.12)$$

thus formalising the relationship between the symmetry of the magnetic structure and that of the crystal lattice.

When the symmetry of the magnetic structure breaks the crystal symmetry, magnetic domains will be formed. The magnetic tensor for the different possible domain orientations (T_{mnop}) may be formed by simply

applying the rotational matrices a_{ij} to the magnetic tensor of the primary domain T_{ijkl}.

$$T_{mnop} = \sum_{ijkl} a_{mi} a_{nj} a_{ok} a_{pl} T_{ijkl}$$

and thus 3.11 becomes

$$\Delta C_{ab} = - \sum_{mnop} B_{amn} \left(\sum_{ijkl} a_{mi} a_{nj} a_{ok} a_{pl} T_{ijkl} \right) B_{bop} \qquad (3.13)$$

By summing over the allowed elements of B expressions for the single crystal elastic constants may now be derived, the sum over all the possible domains for all the allowed elements of T_{ijkl} must then be performed in order to evaluate the changes in the elastic constants for a particular structure.

3.3.2 Sound Propagation in the Vicinity of Magnetic Phase Transitions

The interaction of the ultrasound wave with the spin system via the crystal lattice in the vicinity of magnetic phase transitions is governed by the magnetic interaction which is driving the phase transition. In the case of disorder-order transitions for example, the predominant interaction is the long range exchange interaction which is dependent on the ionic separation. The coupling of the ultrasound to the magnetic structure arises as a result of the strain modulation of the interaction which causes the whole spin-wave spectrum to become soft giving rise to large fluctuations of the order

parameter leading to singularities in the velocity and attenuation of the ultrasound wave. This coupling is referred to as either volume magnetostrictive or two magnon-one phonon coupling. Order-order transitions such as spin re-orientations are driven by the magnetocrystalline anisotropy of the magneto-elastic effect. Such transitions cause a softening in only a small portion of k space, consequently fluctuations in the order parameter are small and the dominant interaction between the soft mode and the ultrasonic wave will be a resonant one (Gorodetsky, 1971). The coupling is of the linear magnetostrictive type (one magnon-one phonon).

Depending on the type of coupling between the soft mode and the ultrasonic wave the elastic constant and attenuation coefficients will respond in different ways to the magnetic phase transition.

3.3.2.1 Order-Disorder Transitions

As the magnetic phase transition is reached from the paramagnetic region critical behaviour will be observed in the elastic constant well above the transition due to short range spin correlations. The critical behaviour of the ultrasound velocity is described by the exponent ξ (Luthi, 1970) such that

$$\frac{\Delta v}{v} \, \alpha \, -\left(\frac{(T-Tc)}{Tc} \right)^{-\xi}.$$

There appears to be no dependence of the critical exponent on the relaxation

time of the critical fluctuations, so we may assume that the critical behaviour will be the same irrespective of the type of magnetic ordering.

It has been shown (Pollina, 1969 and Luthi, 1968) that the critical behaviour of the ultrasound attenuation coefficient of the heavy rare earths at the initial ordering transition is well described by a model in which only volume magnetostrictive coupling is taken in to account.

If we assume that the decay time of the spin fluctuations is very small in comparison to the time period of the ultrasound wave the critical attenuation may be described (Luthi, 1970) by

$$\alpha \ \alpha \ \ \tau_c \omega^2 \sqrt{\chi}$$

where χ is the spin susceptibility and τ_c is the decay time of the critical fluctuations.

If we visualise the two ion volume magnetostrictive interaction in terms of the ultrasonic stress wave interacting with the long range interaction by introducing a small perturbation to the ionic separation it is reasonable to assume and has been shown (Pollina 1969) that longitudinal waves will display anomalous behaviour as a result of volume magnetosrictive coupling while shear waves will not .

3.3.2.2 Order-Order Transitions

We can start our discussion of the effects of linear magnetostrictive coupling on the propagated wave by considering the free energy of the system (3.9).

It is the nature of the magneto-elastic interaction energy E_{ME} which will govern the effect of the transition on C and α; if E_{ME} has terms which are quadratic in the order parameter we would expect step-like discontinuities in the corresponding elastic constant, however, if E_{ME} has terms linear in the order parameter typical soft mode behaviour will be observed (Gorodetsky, 1971).

The resonant interaction between the magnetic spin system and the ultrasound wave which is the predominant interaction for linear magnetostrictive coupling is manifest in a mixing of the magnon and phonon dispersions forming "quasiphonons" and "quasimagnons" (Kittel, 1958, Turov, 1983). As shown in figure 3.2 mode mixing effects will occur at finite q and will obviously have no effect on the ultrasound wave. The magnetic order will cause a magnetostrictive deformation of the lattice along the direction of magnetisation and introduce an effective anisotropy. Thus, the quasimagnon gap at low q is due to anisotropy energy and the anisotropy arising from the deformation of the lattice. At a spin reorientation transition the anisotropy energy will go to zero softening the quasimagnon branch. Because of the coupling between the the two branches of the dispersion the quasiphonon mode will also be deformed giving rise to an increase in the attenuation and a decrease in the velocity of the ultrasonic wave (figure 3.3).

3.4 Experimental Techniques

The measurement of the ultrasonic attenuation and velocity provides a powerful probe for the delineation of magnetic phases by virtue of critical
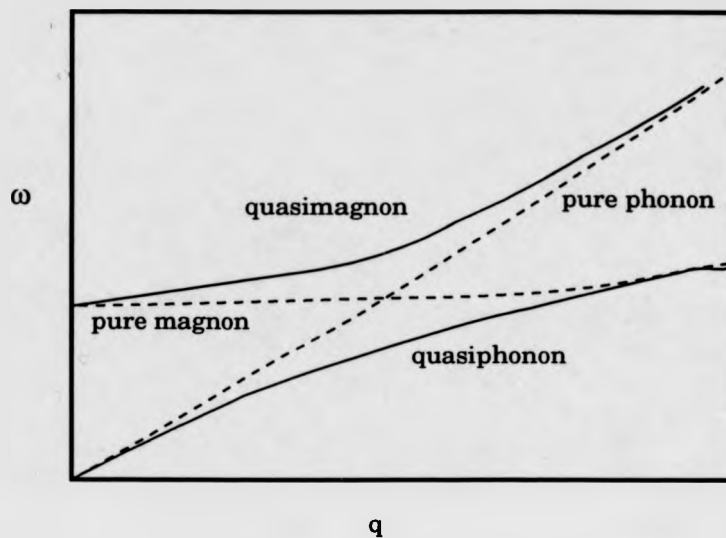
Fig 3.2 Mode mixing caused by a resonant interaction
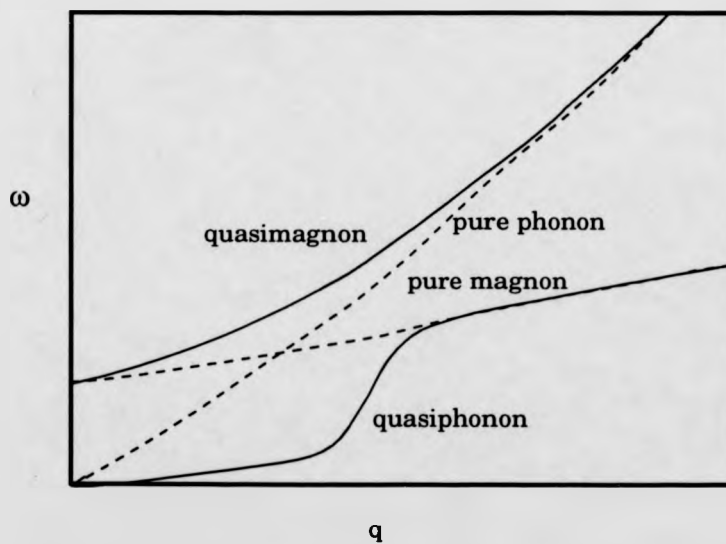
Fig 3.3 Mode mixing at a soft mode

coupling at phase transitions. The behavior of the elastic modulus and the attenuation coefficient provides some insight into the nature of phase transitions, and their equilibrium behaviour permits some predictions about the magnetic structures exhibited. Many of the effects displayed by the systems studied in this work exhibit small coupling to the ultrasonic wave, consequently good point to point precision is required in data collection, while absolute accuracy is a dispensible luxury. Equally, low heating and cooling rates are required over long periods making manual measurements time consuming, susceptible to human error and often very monotonous. Thus, the specifications for the most suitable method for performing ultrasonic measurements on magnetic systems are good point to point precision and automation.

A wide variety of techniques have been developed for the accurate measurement of changes in ultrasonic velocity and attenuation with changes in time, temperature, magnetic field and pressure. Proven techniques include pulse interference (McSkimin, 1961), the sing-a-round system (Whitehead (1979), the long pulse (McSkimin, 1950) and pulse-echo overlap (PEO) (Hellier, 1975) techniques. The PEO has been found to be the most convenient technique for the measurement of ultrasonic velocity changes, where point to point precision is of more importance than absolute accuracy. Changes in the elastic constant of the order of 0.001% may be detected, although great care has to be taken in aligning the appropriate oscillations within the ultrasonic echoes as an error of a single oscillation could introduce an absolute error of 2-3%.

The principal drawback of the technique has been the difficulty in automating the data logging process. While a microcomputer may be used to record the temperature and the time interval between echoes by

the thermocouple DVM and the frequency synthesizer to the micro, an operator is required to adjust the frequency synthesizer to maintain the coincidence of the high frequency peaks.

The measurement of the ultrasonic attenuation usually involves the use of a comparator to fit an exponential function to the decaying echo train. While the technique is reasonably accurate, it is slow and, again, difficult to automate. The attenuation coefficient $\alpha(T)$ in $dBcm^{-1}$ may be calculated (Wallace, 1986) by

$$\alpha(T) = \frac{-20}{(m\text{-}n)2L} \log_{10}\left(\frac{Vm(T)}{Vn(T)}\right) \qquad 3.10$$

Where m and n are the echo numbers and L is the length of the sample in cm. Because the calculation only includes the amplitude of two echoes this method is susceptible to errors caused by unusual echo shapes arising from sidewall reflection and non-parallelism.

3.4.1 The Measurement System

The automatic data logging process used in this study allows measurement of ultrasound velocity and, simultaneously, attenuation. The accuracy and sensitivity of the velocity data is comparable to that of the data collected using the PEO technique, however the increase in speed which is inherent in the automation has led to improved temperature resolution. The attenuation data are calculated by the method outlined by equation 3.10 and suffer from the consequential errors although these may be minimised by careful choice of the relevant parameters.

A schematic of the hardware is given in figure 3.4. The principal components are an r.f. pulse generator, a Hewlett-Packard HP54201A digital oscilloscope and a 16 bit IBM compatible PC fitted with a National Instruments IEEE interface card and a hard disk for data storage. The HP54201A has the advantage that it may be programmed from the computer via the IEEE connection using English-like commands to carry out instructions such as changing the instrument setup, automatic waveform measurements and waveform data and parameter output. Waveform measurements are computed internally, eliminating the need to transfer raw data to the PC and thus reducing data transfer and computing time. Thermocouple and Hall magnetometer output voltages are monitored using IEEE compatible digital voltmeters allowing calculations of sample temperature and applied magnetic field to be carried out in real time. The temperature of the sample is controlled by means of a continuous flow cryostat, temperature controller and sweep generator. An absolute accuracy of $\pm$ 1K in a range of 10 to 300K is possible. Typical sweep rates vary between 0.5 to 2 K per minute. An electromagnet capable of producing up to 1.7T is used both to provide a constant field and is linked to a sweep generator allowing isothermal field scans.

3.4.3 Experimental Procedure

A 15MHz quartz transducer, which is either x-cut to produce a longitudinal wave or y-cut for a shear wave, is bonded to the sample by either vacuum grease or epoxy resin. Vacuum grease overcomes the problem of

57
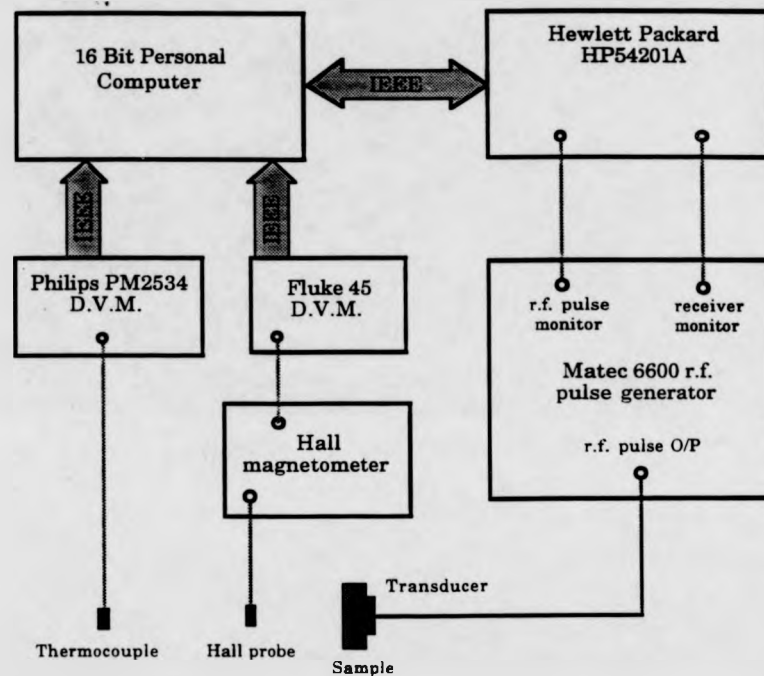
Fig. 3.4   A schematic of the automated ultrasound measuring system.

the bond breaking due to the thermal change of the sample size, but is only effective down to approximately 130K.

An r.f. pulse from the generator excites the transducer to launch an ultrasonic pulse into the sample. A coincident monitor pulse triggers the oscilloscope which displays the echo train. Measurements are usually made with only two successive echoes displayed in the oscilloscope time window where the signal is digitized into 1000 points. For a longitudinal wave propagating across a sample of length 5mm a time base of 5µs is used to fit both echoes on the screen. When digitized to 1000 points this provides a precision of 5ns, two orders of magnitude less than that provided by the PEO technique. However, this shortfall in precision is eliminated by interpolating between digitized points and averaging over several pairs of corresponding high frequency cycles within each echo wave packet.

An arbitrary number of high frequency cycles are selected from each echo, the choice of the number of cycles to be used is determined by the shape of the echoes and the fact that the shape of the echoes may alter as temperature changes. The time separation (ΔT) of the echoes is determined by taking the mean separation between the points at which the positive slopes (and sometimes the negative slopes) of the corresponding cycles in the two echoes cross the V=0 line (fig.3.5). The calculation of the attenuation (α) is equally simple using the mean of the relative amplitudes of corresponding cycles in successive echoes.

Immediately after the waveform data is read into the PC, ΔT and α are calculated, the thermocouple, and if required Hall magnetometer output voltages are read vie the IEEE connections and the temperature and applied field are calculated. Each complete measurement (ΔT, α, temperature and applied magnetic field) usually takes one to two seconds.

58
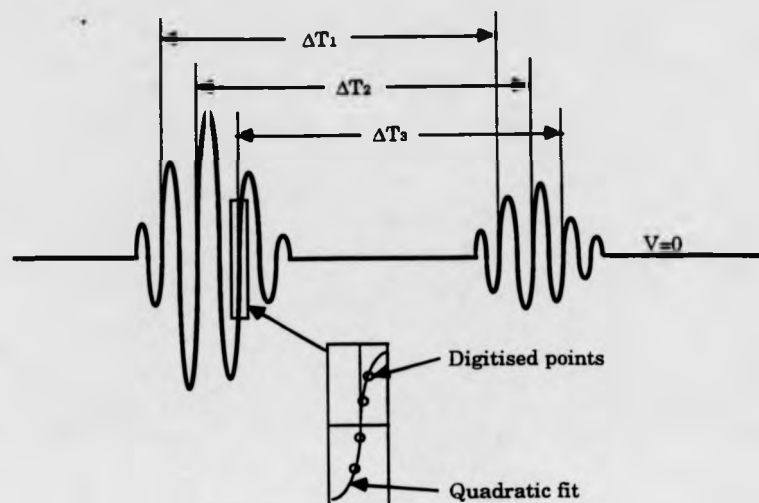
Fig. 3.5 Fitting of one cycle intwo consecutive echoes for the
calculation of Δt.

A flow chart of the software algorithm is given in figure 3.6 for the case of measuring ultrasound velocity and attenuation as a function of temperature in a constant magnetic field. However, isothermal magnetic field scans are performed in very much the same way.

Usually two successive echoes are used for the measurement. Any increase in accuracy afforded by increasing the time difference by selecting widely separated echoes is offset by the effect of having less digitized points in each cycle. The cycles to be used are selected using the oscilloscope cursors positioned as close as possible to the V=0 line on the positive slope of the first cycle in each of the two echoes. The oscilloscope is then interrogated by the PC and the scale parameters, which are required to translate point positions into meaningful values of time and voltage, and cursor positions are read into the PC. This allows an initial estimation of the time separation between the two echoes and identifies the high frequency cycles to be used in the calculation of ΔT.

For both positive and negative slope of each of the high frequency cycles chosen, an arbitrary number of points (four has been found to be ideal for most cases) in the vicinity of the intercept with V=0 are selected from the waveform array. A quadratic fit is made to these points allowing a more accurate determination of the time at which the high frequency cycle intersects V=0. Figure 3.5 shows only the case for the positive slope for the sake of clarity. By averaging over both slopes of as many corresponding high frequency cycles as possible a precision of 0.002% is obtained. The calculation of the attenuation is achieved by averaging the amplitudes of corresponding high frequency cycles.
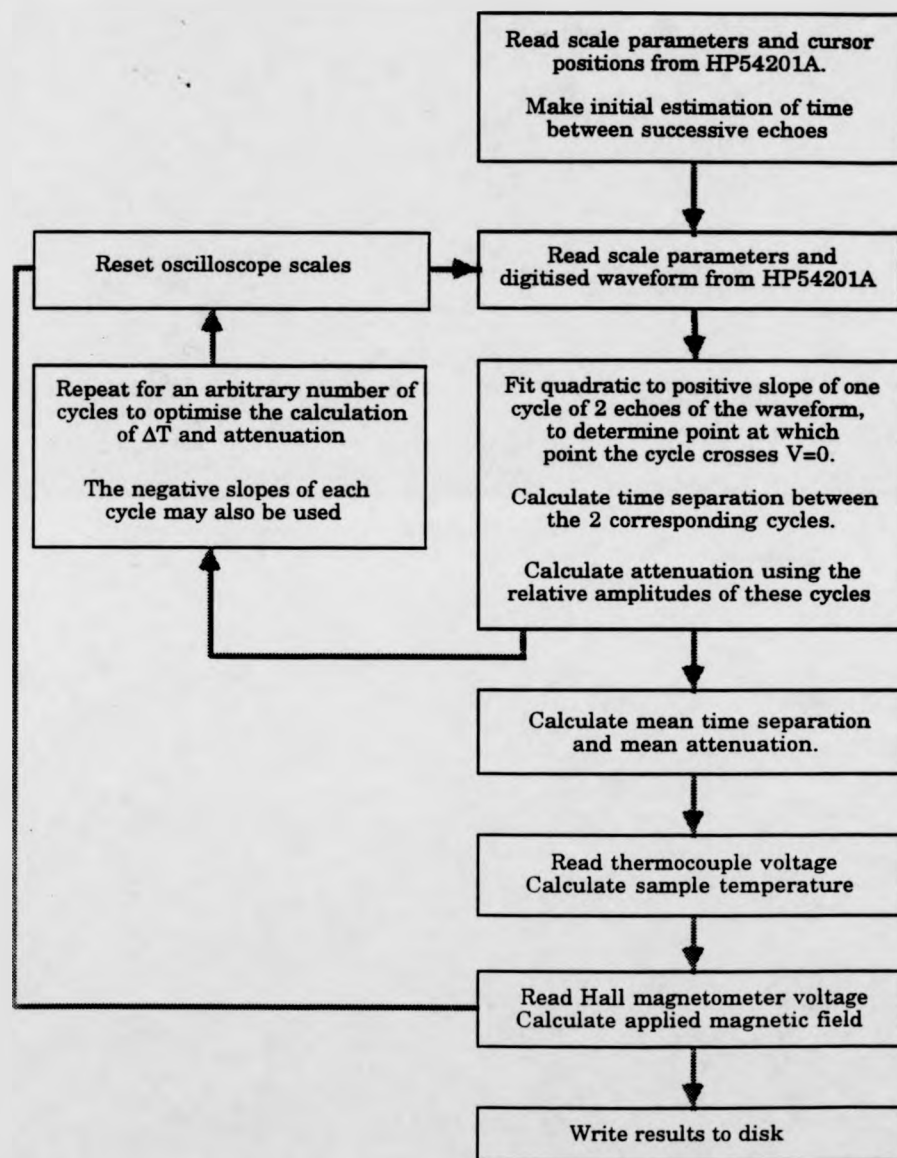
Fig. 3.6 Flow chart of the algorithm for the automated
measurement system.

The ultrasonic signal may be attenuated as temperature changes. Rescaling of the oscilloscope is necessary in the course of a temperature scan and is carried out automatically after each measurement.

The calibration data for both the thermocouple and the Hall magnetometer are stored within the software. The temperature of the sample and the value of the applied magnetic field are calculated for each measurement point and written to the datafile simultaneously with ΔT and α.

3.5 Conclusion

The measurement of ultrasound velocity and attenuation provide powerful probes for the delineation of magnetic phases and reveal subtleties of the magnetic structure and the nature of magnetic phase transitions.

The automated measurement system has maintained the accuracy of the PEO technique while having several inherent advantages, such as being able to follow large and rapid changes in attenuation, increased sample throughput and more thorough temperature scans by virtue of its higher speed of operation.

References

Bates S., Patterson C., McIntyre G.J., Palmer S.B., Mayer A., Cowley
        R.A., Melville R.J. J.Phys C. Solid State Phys. 21 4125 (1988).

Gorodetsky G., Lüthi B.,Moran T.J. Intern. J. Magnetism 1 295 (1971).

Hellier A.G., Palmer S.B., Whitehead D.G. J.Phys E8 352 (1975).

Kittel C. "Introduction to Solid State Physics (4th Ed.)", Wiley, New York,
        (1971).

Kittel C. Phys Rev 110 386 (1958).

Kolsky H. "Stress Waves in Solids", Clarendon Press, Oxford, (1953).

Lüthi B., Moran T.J. Pollina R.J. J.Phys Chem Solids 1741 (1970).

Lüthi B., Pollina R.J. Phys Rev 1672 488 (1968).

McSkimin H.L. J.Acoust Soc. Am. 22 413 (1950).

McSkimin H.L. J.Acoust. Soc Am. 33 12 (1961).

Musgrave M.J.P. "Crystal Acoustics", Holder-Day, (1970).

Pollina R.J., Lüthi B. Phys Rev 117 2 841 (1969).

Truell R., Elbaum C., Chick B.B. "Ultrasonic Methods in Solid State
        Physics", Academic Press, (1969).

Turov E.A., Sharov V.G. Sov. Phys USP. 26(7) 593 (1983).

Wallace P.W., Garland C.W. Rev. Sci. Inst. 57 3085 (1986).

Whitehead D.G., Palmer S.B. IEEE Trans. Instrumn. Meas. 28 220 (1979).

Chapter 4

The Zero Field Magnetic Phase Diagram of the Gd-Lu Alloy Series.

Introduction, Review of Previous Work

Gadolinium is unique amongst the heavy rare earths in that it does not exhibit any periodic antiferromagnetic structures, ordering at 293K into a c-axis ferromagnet then undergoing a spin re-orientation transition at 235K to a canted ferromagnetic structure. The cant angle changes from a maximum of 71° at 130K down to approximately 40° at low temperatures (Cable and Koehler, 1982).

The anisotropies which give rise to the ferromagnetic easy direction are both of two ion origin. Because the c/a ratio is not ideal the dipole-dipole interaction forms a contribution to the anisotropy along the c-axis, which is very long range (Jensen and Mackintosh, 1991). Another, competing, anisotropy arises as a result of the spin-orbit coupling of the conduction electrons, which constrains the rotation of the spins relative to the lattice. The indirect exchange interaction is then responsible for similarly

constraining the other spins (Kasuya and Kaino, 1981, Jensen and Mackintosh, 1991).

On dilution with non-magnetic metals such as scandium, yttrium and lutetium more complicated structures are observed. The phase diagrams display helical and conical antiferromagnetic phases in addition to a novel ferromagnetic structure which will be referred to as ferro-I.

Y, Sc and Lu all crystallise into the same HCP structure as Gd. The atomic volume of Y is very similar to that of Gd at $19.95cm^3mol^{-1}$ compared to $19.91cm^3mol^{-1}$ for Gd. Sc is considerably smaller at $15.03cm^3mol^{-1}$ while Lu is intermediate at $17.8cm^3mol^{-1}$. The relative atomic volumes seem to play an important role in the magnetic ordering of these alloys, by virtue of their perturbing effect on the Fermi surface.

The study of alloys of Gd with non-magnetic metals may be traced back to the magnetisation measurements on polycrystalline samples of Gd-La and Gd-Y by Thoburn et al (1958). They observed the existence of antiferromagnetic order in Gd-Y samples with Y concentration > 40% and in some Gd-La samples. However, a more thorough understanding of the magnetic structures was not possible until neutron scattering experiments had been completed, revealing the existence of periodic antiferromagnetic structures such as helices in the rare-earths. See for example the review article by Koehler (1967).

One of the most interesting features of these studies, and of the continued magnetisation and resistivity measurements (Smidt and Daane, 1963) was the effect of the dilution on the initial ordering temperature and an apparent increase in the saturation magnetic moment as a result of dilution.

The initial ordering temperature of the heavy rare earths was expected to be proportional to the strength of the exchange, and as such to scale with the deGennes factor $G = (g-1)^2J(J+1)$, but Bozorth and Gambino

63

(1966) and Koehler (1965) showed that a scaling with $G^{2/3}$ was more correct, when G was averaged over the constituents of the alloy.

The excess saturation magnetic moment was seen by Legvold et al (1977) to be inversely proportional to the c/a ratio, but paradoxically there appeared to be no correlation between the c/a ratio and the initial ordering temperature.

These problems were tackled by Lindgård (1977) whose mean field approach based on a concentration dependent exchange interaction produced good quantitative agreement with the phase diagrams of heavy rare earths diluted with non-magnetic metals. The behaviour of Gd-Lu and Gd-Y alloys was very similar with the ordering temperature increasing in a convex manner with the parameter $X = c(g-1)^2 J(J+1)$ where c is the concentration of Gd and g and J have their usual meanings. Gd-Sc alloys however, increased in a concave manner. This difference in behaviour was attributed to the small conduction electron susceptibility arising from the low density of states at the Fermi surface which was a consequence of the low atomic radius of Sc.

While this approach provided a good explanation of the scaling of the ordering temperature to $G^{2/3}$, the relationship between the c/a ratio and the excess saturation magnetic moment was not well understood. Legvold and co-workers (1977 and 1979) took a slightly different approach. While preparing a review article they found that the ordering temperature for the heavy rare earths and their alloys scaled with S(S+1) as opposed to J(J+1), in good agreement with a Heisenberg exchange. There were two considerable departures from this behaviour; alloys of Gd-Y and Gd-Sc. The former having consistently higher transition temperatures, the latter lower. They also noticed a linear relationship between residual resistivity and the suppression of the ordering temperature. The resistivity was

64

highest for Gd-Sc alloys and lowest for Gd-Y alloys, the relationship between the atomic volumes of the diluents and the resistivity was clear.

These results were interpreted as arising from two separate processes. 1) the scattering of the conduction electrons by the diluent atoms which reduces the mean free path length, consequently weakening the exchange and suppressing the transition temperature. This effect will be greater the larger the discrepancies between the solute atoms and the host. 2) the enhancement of the magnetic moment arises as a result of the polarisation of the 5d conduction electrons. The second effect will have most dramatic consequences on the magnetic moment, however, the increased moment will strengthen the exchange and increase the ordering temperature. Indeed, the addition of Sc and Lu are also seen to enhance the moment, but the knock on effect on the ordering temperature is offset by scattering effects.

More recently a third, and with hindsight simple approach, was taken by Young (1983) who pointed out that if the conduction electron mean free path is applied to the RKKY interaction and included in the calculation of the deGennes factor, most heavy rare earths and their alloys, including Gd based alloys, will have transition temperatures which scale with the deGennes factor.

Further studies of Gd based magnetic alloys concentrated in the multicritical region. The proposal, by Hornreich (1975), of a multicritical point, known as a Lifshitz point, at which helical antiferromagnetic (HAF), ferromagnetic and paramagnetic phases co-exist with the propagation vector of the helix becoming zero at the transition prompted theoretical discussion (Michelson, 1977) and a concerted experimental search in the multicritical region of several alloy systems (Legvold, 1980). Although ultimately fruitless the search unearthed several interesting features the most noteworthy being the observation of a novel ferromagnetic phase. This

65

phase, known as ferro-I, was first observed in a $Gd_{70}Y_{30}$ single crystal by Legvold et al (1980) and appears to have a component of the magnetisation along the c-axis while being paramagnetic in the basal plane. It has also been observed in Gd-Sc alloys (Melville, 1989) and Gd-Lu alloys (Ito, 1984). Initially it was assumed that any phase with a disordered component would be stabilised by the addition of diluents with a smaller atomic volume which would reduce the exchange as described earlier. However, the ferro-I phase displayed by Gd-Sc alloys is considerably smaller than that displayed by Gd-Y alloys. Some success in stabilising the ferro-I region appears to have been made with tertiary alloys of Gd-Y-Sc (Ito, 1988) and Gd-Y-Lu (Ito, 1984), however, a recent neutron scattering experiment on a single crystal of $Gd_{75.0}Y_{17.5}Sc_{7.5}$ suggests that the enhanced ferro-I region observed in resistivity, magnetisation, thermal expansion and specific heat measurements does have a basal plane component of the magnetisation (Eccleston, 1990).

Several models have been proposed for the ferro-I region and these will be discussed in full in the light of the data presented hereafter.

Although a Lifshitz point has not been observed, Bates et al (1986) added more detail to the phase diagram of Gd-Y which shows a multicritical point at which HAF, ferromagnetic and ferro-I phases co-exist, with turn angle of the helix tending to zero, essentially a Lifshitz point in two dimensions. The thorough study of the Gd-Y system (Bates, 1985, Melville, 1989) raised interesting questions about the nature of the transition between the HAF phase and the canted ferromagnetic phase, with q for the HAF phase becoming zero at the transition . There is no a priori reason why the disappearance of the propagation vector of the helix should be coincident with the development of an out of plane component of the magnetisation. If the symmetry of the basal plane is assumed to be 3-fold rather than 6-fold, an additional term in the Landau free energy is

66

produced which couples the basal plane magnetisation to that of the c-axis and rules out an intermediate phase in which the moments are ferromagnetically aligned in the basal plane (Mukamel, 1989). However, such a coupling should give rise to third order modulations of the c-axis moment which have not been observed experimentally despite a thorough search (Melville,1991).

The phase diagram of the Gd-Sc alloy system displays a conical ferromagnetic phase between the HAF and the canted ferromagnetic phases. The propagation vector of the helix, although it appears to decrease as the transition is approached, remained finite throughout and locked in to apparently incommensurate values prior to the transition (Melville,1989).

The multicritical region of Gd-Lu has been studied by Legvold (1980) who drew up a partial phase diagram which seems to rule out the existence of a Lifshitz point. Ito et al (1984) have observed a ferro-I region in a $Gd_{80}Lu_{20}$ single crystal which was stable over a temperature range of only 2K, surprising considering the similarities in the atomic radii and the character of Lu and Y.

It is the aim of this study to add new detail to the partial phase diagram of Legvold et al, and in doing so to provide new insight into the problems posed by the studies of the Gd-Y and Gd-Sc alloy systems.

4.1 Ultrasound Investigation

In the absence of crystal field anisotropy, all the magnetic phases exhibited by Gd-Lu alloys have their origins in the 2 ion interaction, which is sensitive to the interatomic distance. As a consequence, those elastic constants which correspond to compressional waves, particularly a compressional wave propagated along the c-axis, are those which couple

most strongly to the magnetic order. Indeed, the results show that while a compressional wave propagated along the c-axis (C_{33}) shows very distinct features in each of the different magnetic phases, shear waves, and compressional waves propagated across the basal plane only exhibit very small effects if any. The C_{33} elastic constant and α_{33}, the associated attenuation coefficient, have been measured for all of the samples, the other modes have only been measured for the $Gd_{76.0}Lu_{24.0}$ sample. Measurements of those modes which require the transducer to be bonded to the a or b faces of the crystal are hampered by the high magnetostriction which causes bonding problems. These may be overcome to some extent by the use of vacuum grease which provides a reasonable bond down to approximately 170K.

4.1.1 Coupling of C_{33} to Anticipated Magnetic Structures

In the light of the previous work discussed in the introduction, we expect to observe HAF, canted ferro and ferro-I structures in the phase diagram of Gd-Lu. From section 3.4 and particularly equation 3.13 the relative softening of C_{33} as a result of the formation of the anticipated structures may be estimated.

For each magnetic structure the rotational matrix which describes the different possible domain orientations, a_{ij}, will be a unitary diagonal matrix, thus equation 3.13, for C_{33}, may be written

$$-\Delta C_{33} = 4((B_{33}T_{33}B_{33} + 2B_{13}(T_{13} + T_{23})B_{33} + B_{13}(T_{13} + T_{22} + 2T_{12})B_{13}). \qquad (4.1)$$

68

For a helical structure, with no component of the magnetisation out of the basal plane, all matrix elements with an index of 3 will be zero. In addition, since the helix is incommensurate we may assume circular symmetry, so $T_{11} = T_{22}$. Thus 4.1 becomes

$$-\Delta C_{33} = 8B_{13}(T_{11} + T_{12})B_{13}. \qquad (4.2)$$

For a canted ferromagnet, the situation is more complicated since each domain will have monoclinic symmetry. However, in the absence of an applied field an average over all domains yields the hexagonal symmetry and the anomalous softening of C_{33} is given by equation 4.1. Since the basal plane anisotropy is negligible, and assuming that the canted ferro phase is an artefact of the exchange along the c-axis there will be no preferred orientation with respect to the basal plane. Consequently we may assume the terms T_{11} and T_{22} are equal. Thus, the softening in the canted ferro phase is given by

$$-\Delta C_{33} = 4(B_{33}T_{33}B_{33} + 4B_{13}T_{13}B_{33} + 2B_{13}(T_{11} + T_{12})B_{13}). \qquad (4.3)$$

The behaviour of C_{33} in the ferro-I phase is difficult to predict. If we accept the random cone model the expression above applies. If, however, we assume the structure to have some Gd atoms with moments ordered along the c-axis and others where the moments remain disordered, the expression for a c-axis ferromagnet is more correct. This expression arises as a result of disregarding all the matrix elements which correspond to a basal plane component of the magnetisation and is written

$$-\Delta C_{33} = 4B_{33}T_{33}B_{33}. \qquad (4.4)$$

69

Clearly, the behaviour of C_{33} may be easily interpreted in term of the symmetry of the magnetic structure. The lower the symmetry of the structure, the higher the anomalous softening will become, thus C_{33} is softer in the HAF region than in the canted ferromagnetic region. The interpretation of ultrasound data however remains qualitative, it being easier to predict the behaviour of the elastic constant for a magnetic structure than to deduce the magnetic structure from the ultrasound data.

Domain relaxation is another mechanism by which the formation of certain magnetic structures may bring about a softening of the elastic constant (Bates, 1985). Certain magnetic structures will have domain orientations which are energetically more favourable than others under the influence of the ultrasound wave. Consequently energy is lost from the ultrasound wave as these domains are reoriented. However the absence of basal plane anisotropy and the resulting high symmetry of all the structures considered here means that the elastic constant couples equally to all possible domain orientations and domain relaxation may be neglected.

4.1.2 Experimental Results

The behaviour of a sample of composition $Gd_{76.0}Lu_{24.0}$ has already been studied by magnetisation measurements (Legvold, 1980). Consequently, it was the first to be studied to permit comparison.

The temperature dependence of the C_{33} elastic constant is shown in figure 4.1. The concave reduction of C_{33} starts above room temperature, and arises as a result of two ion spin correlations possibly extending no further than next nearest neighbours. Prior to the minimum one would normally associate with the onset of magnetic order at 221.5K(indicated as

Fig. 4.1 C_{33} vs. temperature for $Gd_{76.0}Lu_{24.0}$.
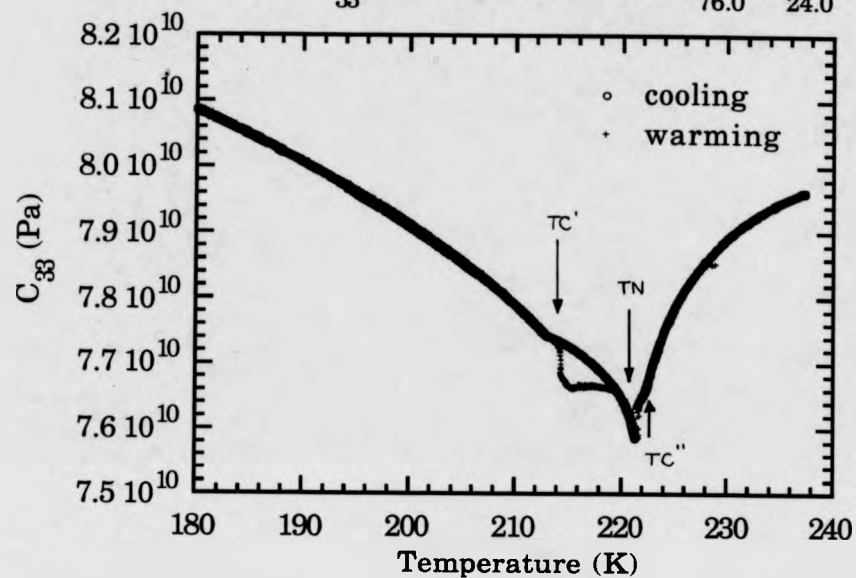
Fig 4.2 α_{33} vs. temperature for $Gd_{76.0}Lu_{24.0}$.
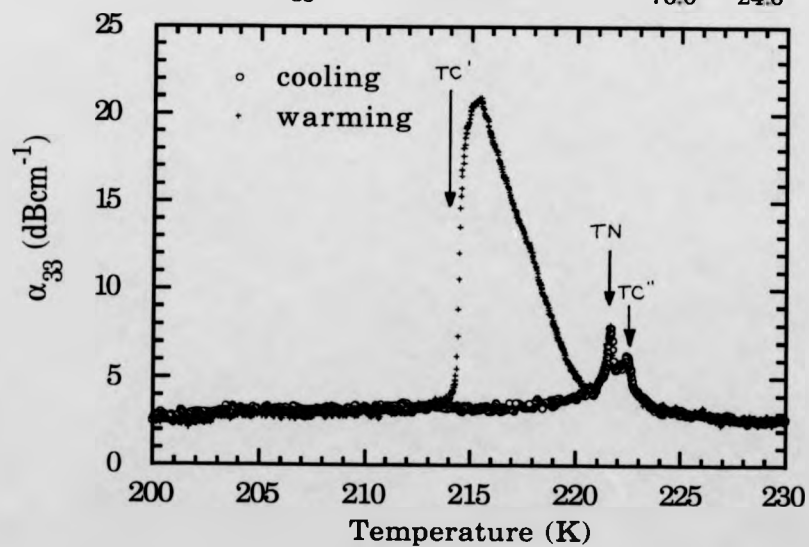
T_n), there appears to be a small inflection at 222.5K (indicated as T_c"), providing the first evidence of the existence of a ferro-I phase. While the softening of C_{33} in this region is much less than that observed by Bates in the ferro-I regions of the Gd-Y samples, it is very similar to that observed by Melville in a single crystal of composition $Gd_{75}Sc_{25}$. The large hysteresis in C_{33} is characteristic of a HAF phase.

On cooling from 221K to 212K, coupling to the HAF phase appears to be very small, showing only a small inflection at the transition to canted ferromagnetic order at 213K (T_c'), however, on warming the softening at 214K is far more dramatic.

The attenuation data (fig. 4.2) exhibits equally dramatic hysteresis, with the attenuation rising dramatically on the formation of the helix, when measurements were made with increasing temperature. Two peaks appear, corresponding to the inflection at T_c" and the minimum at T_n in C_{33}. The peaks are both characteristic of two ion, volume magnetostrictive coupling. Both the C_{33} and α_{33} data suggest that T_c" corresponds to the onset of some magnetic order, however the second peak in α_{33} at T_n and the continued concave softening of C_{33} in the intermediate region suggests that the phase has some disordered component and that it is completely decoupled from the subsequent phase.

The large hysteresis in the HAF phase is the result of difference in the formation of helical chirality domains on warming and cooling (Palmer, 1975). On cooling from the paramagnetic phase into the HAF region chirality domains form at random, seeded on crystal imperfections. However, on warming from a ferromagnetic phase with some component of the magnetisation in the basal plane, domains form as stripes perpendicular to the c-axis because they have grown out of the Bloch walls. This mechanism has been clearly illustrated by neutron topography in Tb and MnP (Baruchel, 1981, Drillat, 1981). Tachiki (1968) has studied the

71

interaction of an ultrasound wave with a helical structure and showed that the ultrasound stress wave causes an increase in the exchange energy which is dissipated by a change in the helical turn angle, thus removing energy from the ultrasound wave. The random domains formed on cooling will have complicated intermeshed domain walls which will provide a mechanism for pinning the helix and remaining stiff. The striped domains on the other hand, will permit the turn angle to vary and thus be softer with respect to the ultrasound wave. While explaining the presence of the hysteresis, this in itself, does not explain the fact that the attenuation appears to decrease steadily as the temperature is increased from just above the lower temperature transition to the helical structure. The extent to which the ultrasound wave is attenuated may be related to a parameter of the HAF structure which varies with temperature, the obvious one being the turn angle or q.

The domain wall energy is related to the helical turn angle (Drillat, 1981), the domain walls having higher energy at high q than at low q. Considering the two extremes, at low q changes in q will result in small changes in the domain wall energy, however at high q changes in q will increase the domain wall energy which will act as if to pin q, consequently the damping effects are approximately invariant with q.

If we consider the thickness of the domain wall however, it becomes clear that smaller turn angles (lower q) will be more attenuating than high q helices. The domain walls are assumed to be ferromagnetic regions of several atomic layers in thickness. At low turn angles, only a small change in turn angle will be necessary to bring the moments on those atoms close to the domain wall into alignment with the ferromagneticaly aligned atoms of the domain wall, thus increasing the domain wall thickness. At high q, however, a large change in q will realise only a modest increase in the domain wall thickness. Consequently energy is lost

72

from the ultrasound wave as the domain wall thicknesses vary in response to the ultrasonic strain.

Topography measurements (Pearce, 1991) have shown that, within the HAF phase, striped domains may break up to form random domains in response to small thermal cycling. It may be that during the period that the measurements are made domains are breaking up in this manner and reducing the attenuation of the ultrasound wave.

The neutron data which show the thermal evolution of $\mathbf{q}$ will be presented later.

The C_{44} elastic constant (fig. 4.3) shows very little coupling to the magnetic structure, with only a small inflection in the initial ordering region. α_{44} shows no coupling whatsover. The measurement of C_{11} and C_{66} were hampered by the bonding problems outlined earlier, C_{11} (fig. 4.4) showed a small inflection at 222K (T_n) and what appears to be a quite dramatic softening of some 0.4% at 212K which corresponds to the HAF-canted ferro transition (T_c'). At first sight, the sharp dip in C_{11} could be interpreted as being brought about by the onset of the canted ferro phase, however the sharp increase in the attenuation (fig. 4.5) and the poor signal at lower temperatures indicate that it arises as a result of the deterioration of the coupling between the sample and the transducer caused by a change in the dimensions of the crystal. Araldite Rapide and vacuum grease were both used as couplants neither surviving the transition and preventing measurements below T_c'.

The C_{66} data show no distinct coupling to the magnetic order.

The failure of all the measured elastic constants bar C_{33} to couple to the magnetic ordering reinforces the view that various forms of the two ion exchange along the c-axis are responsible for all the magnetic structures observed. Only C_{33} was measured for the remaining samples.

Fig 4.3 C_{44} vs. temperature for $Gd_{76.0}Lu_{24.0}$.
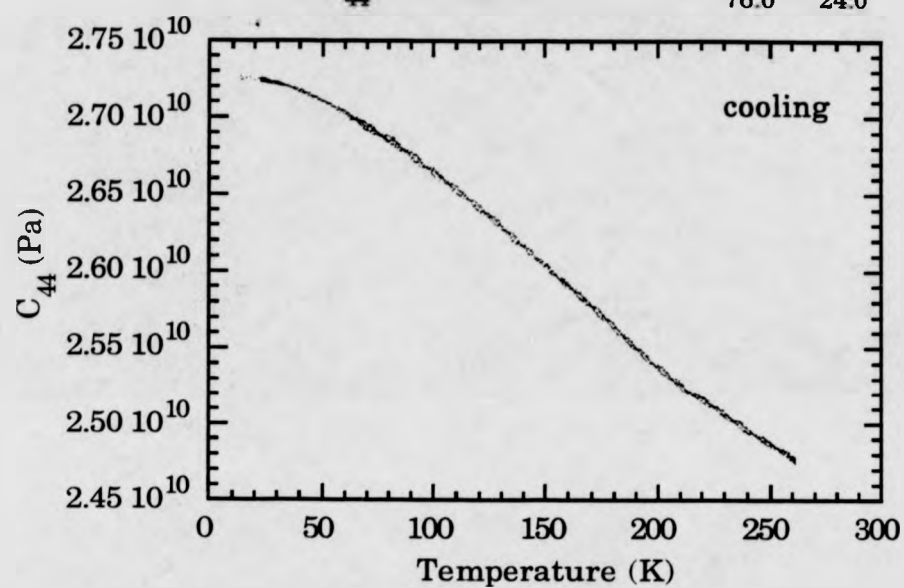
Fig. 4.4 C_{11} vs. Temperature for $Gd_{76.0}Lu_{24.0}$ on cooling.
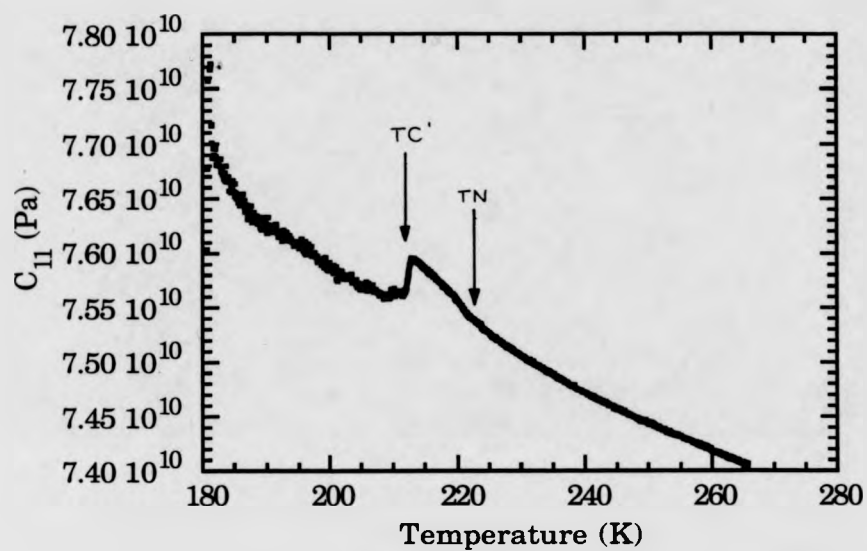
Fig. 4.5 α_{11} vs. Temperature of $Gd_{76.0}Lu_{24.0}$ on cooling.
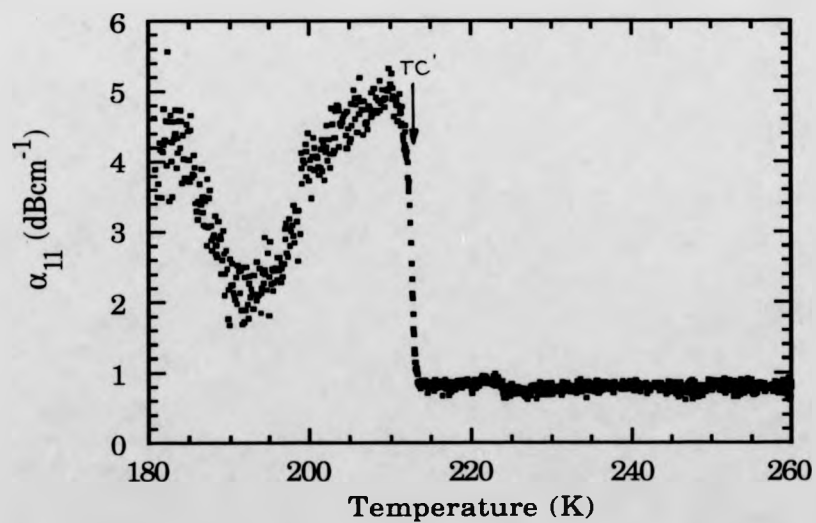
The $Gd_{76.3}Lu_{23.7}$ and $Gd_{75.7}Lu_{24.3}$ data show very similar characteristics to the $Gd_{76.0}Lu_{24.0}$ sample. The $Gd_{76.3}Lu_{23.7}$ sample (figs. 4.6 and 4.7) displays a ferro-I phase which exists over 2K and HAF phase between 222K and 218K. By contrast the $Gd_{75.7}Lu_{24.3}$ sample (figs. 4.8 and 4.9) has a much smaller ferro-I phase with a bigger HAF phase existing from 221K to 211K.

$Gd_{76.5}Lu_{23.5}$ (figs. 4.10 and 4.11) shows no evidence of a HAF region, but has an enhanced ferro-I region. No samples with a higher Gd concentration were available although Ito et al have seen evidence of a ferro-I phase in the resistivity measurements on a $Gd_{80}Lu_{20}$ sample.

The $Gd_{75.3}Lu_{24.7}$ sample (figs. 4.12 and 4.13) appears to have no ferro-I region and a HAF region between 219K and 206K.

On the basis of the ultrasound data, new detail has been added to the partial phase diagram of Legvold et al (fig4.14). The principle refinements being the new detail added to the multicritical region and the observation of the ferro-I phase. It should perhaps be mentioned that Legvold and co-workers did comment on the broadness of what they took to be the initial ordering transition which they attributed to statistical fluctuations in the relative concentrations in their polycrystalline sample. It is probably the use of high purity single crystals in this study which has revealed the existence of this phase.

The phase diagram is also printed on the folded sheet behind fig4.14 which the reader may find convenient to fold out in order to facilitate easy reference throughout the ensuing discussion of the neutron scattering investigation of the phase diagram.

Fig. 4.6 C_{33} vs. temperature for $Gd_{76.3}Lu_{23.7}$.
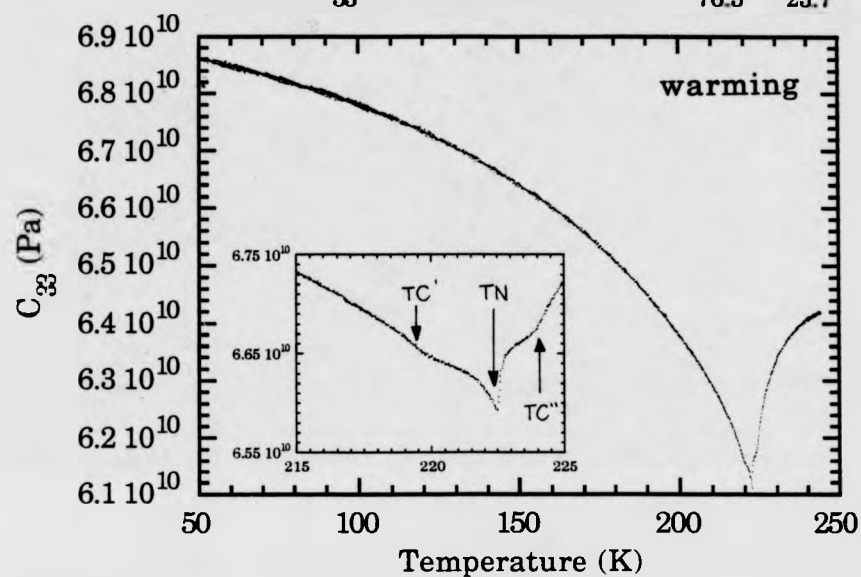
Fig. 4.7 α_{33} vs. temperature for $Gd_{76.3}Lu_{23.7}$.
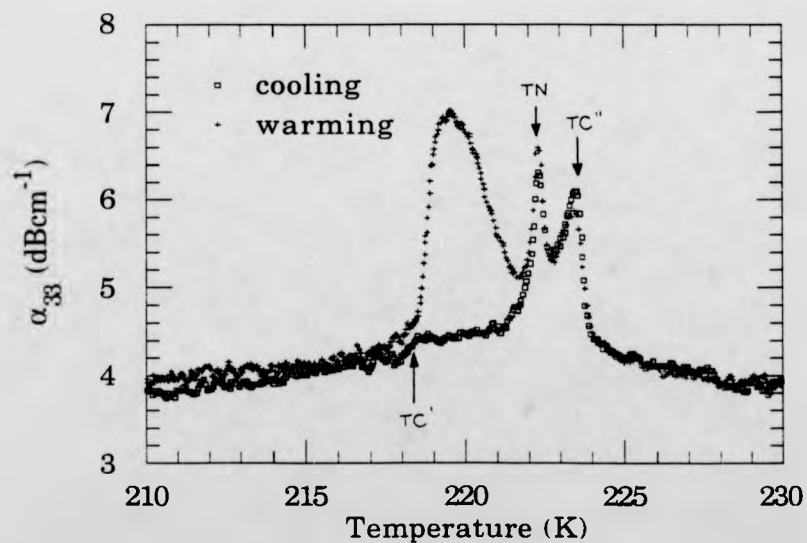
Fig. 4.8 C_{33} vs. temperature for $Gd_{75.7}Lu_{24.3}$.
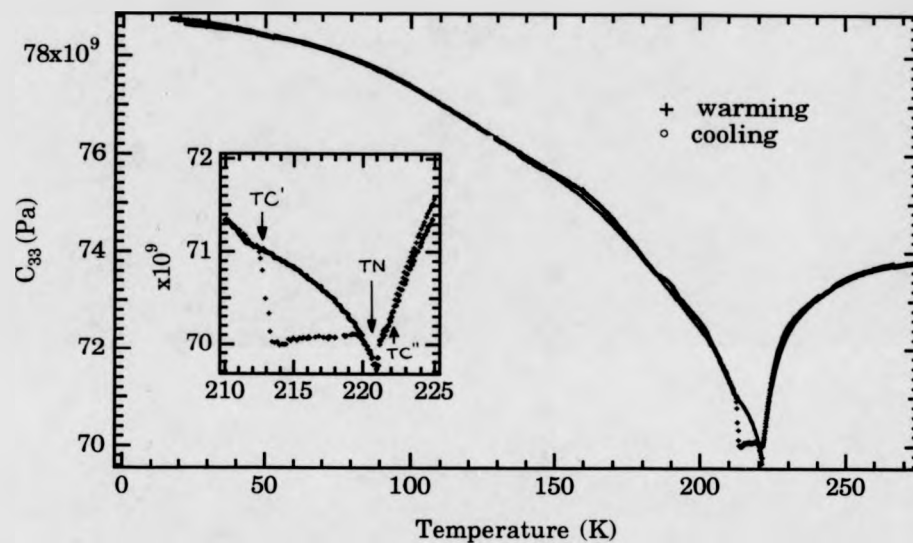
Fig. 4.9 α_{33} vs temperature for $Gd_{75.7}Lu_{24.3}$.
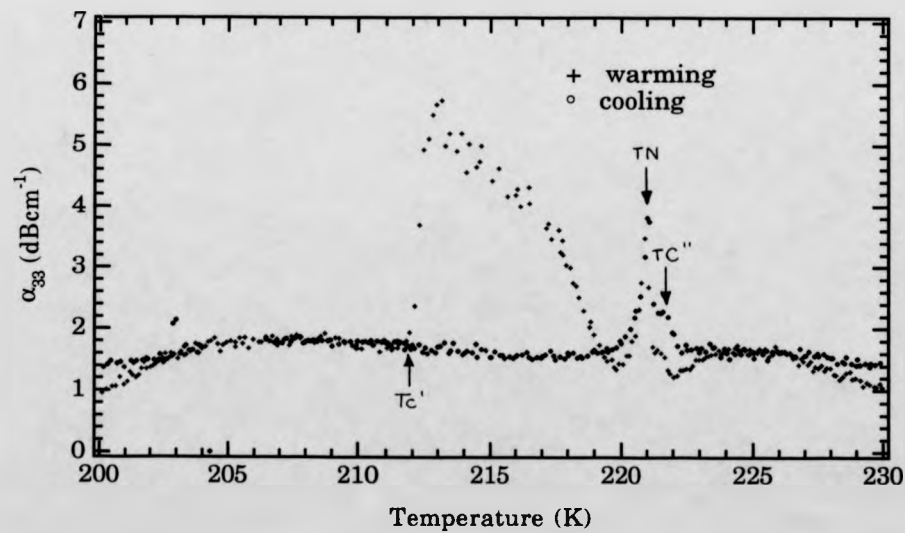
Fig. 4.10 C_{33} vs. temperature for $Gd_{76.5}Lu_{23.5}$.
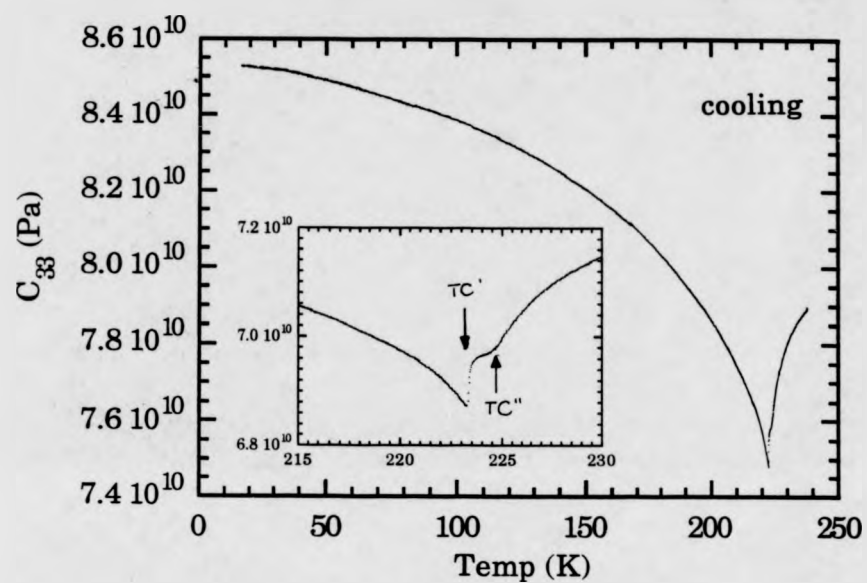
Fig. 4.11 α_{33} vs. temperature for $Gd_{76.5}Lu_{23.5}$.
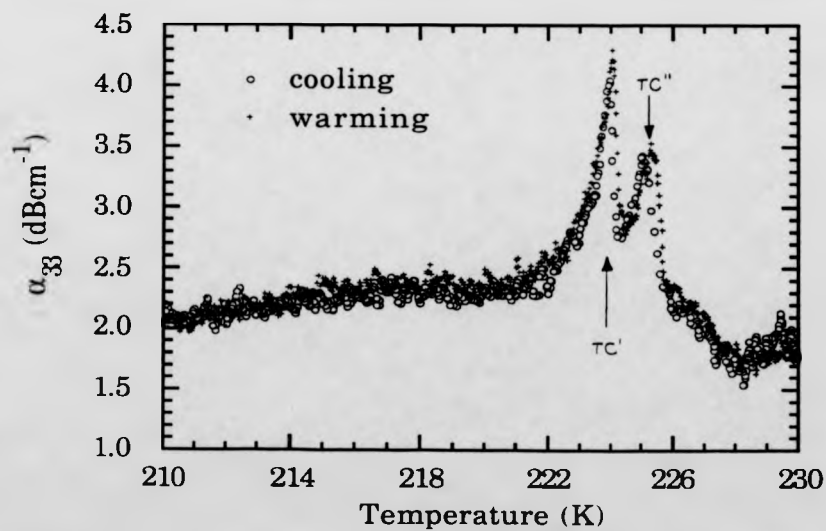
Fig. 4.12 C_{33} vs. temperature for $Gd_{75.3}Lu_{24.7}$.
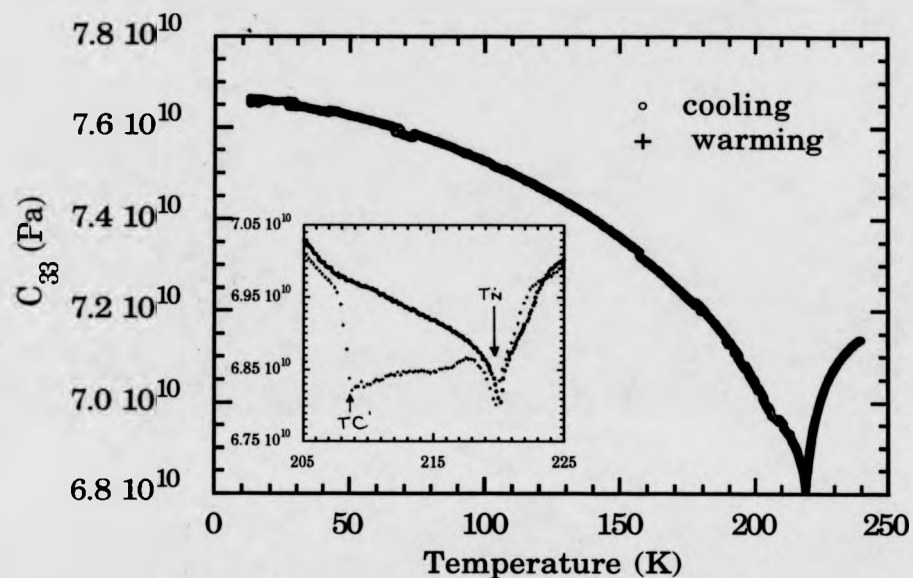
Fig. 4.13 α_{33} vs. temperature for $Gd_{75.3}Lu_{24.7}$.
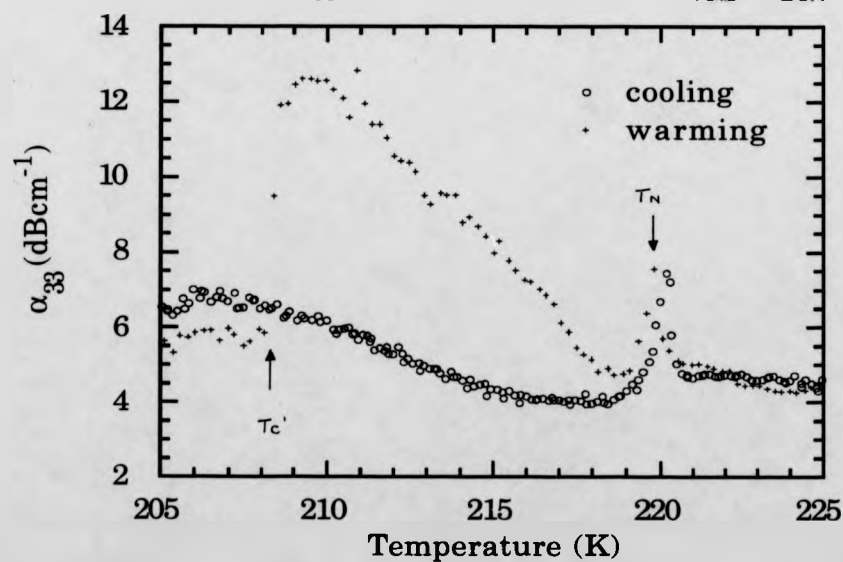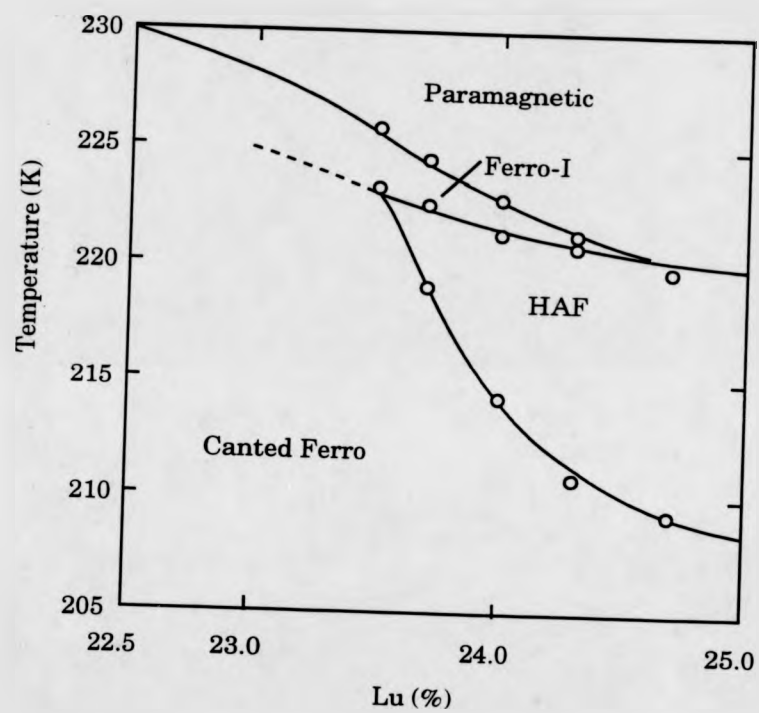
Fig. 4.14 Partial phase diagram of the Gd-Lu alloy system.

4.2 Neutron Scattering Studies

The neutron data presented here were all collected on the D9 diffractometer at the I.L.L. using a wavelength of 0.48Å to avoid the high capture resonance of Gd-Lu alloys at thermal wavelengths. All the samples were mounted with the a*c* plane in the equatorial plane so as to maximise the resolution along the c-axis. Extinction and absorption corrections have been performed in the manner described in chapter 2.

After an initial survey, involving the three samples with the lowest concentrations of Lu, the apparent reliability of the phase diagram constructed by the ultrasound data has provided the freedom to use the neutron study to concentrate on interesting points arising from the phase diagram. For this reason the discussion of the neutron data will not be conducted sample by sample, but rather discussing particular features of the phase diagram. The most detailed study of the HAF region was performed on the $Gd_{75.3}Lu_{24.7}$ sample, and the most thorough study of the ferro-I region on the $Gd_{76.5}Lu_{23.5}$ sample.

The use of the multidetector fitted to D9 has been discussed earlier, however, the ability to step through the Bragg spot facilitated the 3D representation of the spot which gives a good evaluation of the quality of the crystal. Figure 4.15 show such a picture of the 100 reflection for $Gd_{75.3}Lu_{24.7}$. This is the worst case of the samples studied and the existence of a small single peak suggests that the crystal contains additional crystallites. Unfortunately this will introduce inevitable errors in the fitting of the peak, and the calculation of the integrated intensity however, extinction will be reduced.

The experimental results of the neutron investigation are presented below phase by phase. A detailed interpretation of the results is given in the discussion and conclusions section at the end of this chapter.
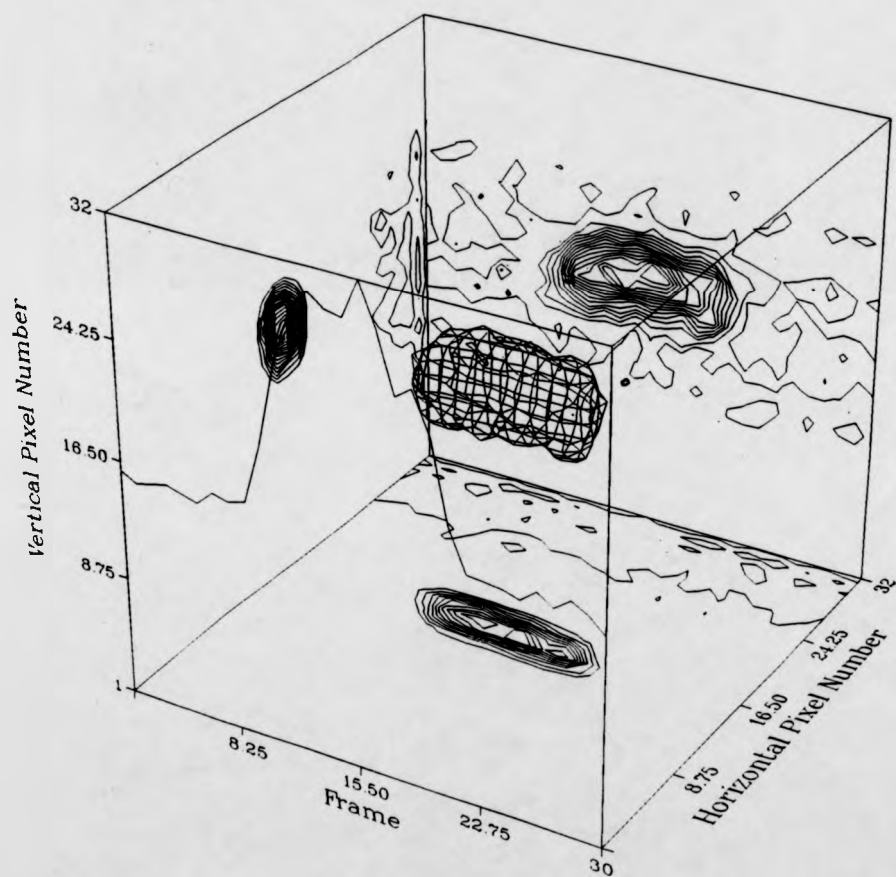
Fig. 4.15 The (100) Bragg spot of Gd$_{75.3}$Lu$_{24.7}$ imaged by the multidetector.

4.2.1 The Helical Antiferromagnetic Phase

Throughout the HAF phase, as delineated by the ultrasound measurements, scans were made along the c-axis across the 101 and 100 lattice points, initially extending to one quarter of a Brillouin zone either side of the Bragg peak, but once the behaviour of the satellites became clear the search was limited to an area of 0.1 reciprocal lattice units either side of the Bragg peak. Several searches were conducted across full Brillouin zones so as to rule out the existence of higher order satellites. For all the samples studied except $Gd_{76.5}Lu_{23.5}$ magnetic satellites were observed as predicted by the ultrasound measurements. The agreement of the transition temperatures is good, both the ultrasound and neutron scattering data showing a hysteresis of approximately 2K in T_c'.

The isometric plots in fig. 4.16 show a vivid representation of the thermal evolution of the satellites for the $Gd_{75.3}Lu_{24.7}$ sample. The satellites continuously approach the nuclear peak as the temperature decreases, before becoming assimilated into the nuclear peak. The base of the nuclear peak appears to remain broad below the transition to the canted ferro phase indicating that long range order is not fully established.

Figures 4.17a and 4.17b show two q scans through the (101) lattice point together with the fitting of the satellites. The former is for the $Gd_{75.3}Lu_{24.7}$ sample and shows the attempts to overcome the problem of the additional crystallite by fitting the distorted nuclear peak with two Gaussians. The latter illustrates the fitting of satellites down to the lowest measurable turn angles where in order to derive a reliable value for q the widths of the satellites were frozen.

X: steps of 0.000 0.000-0.003
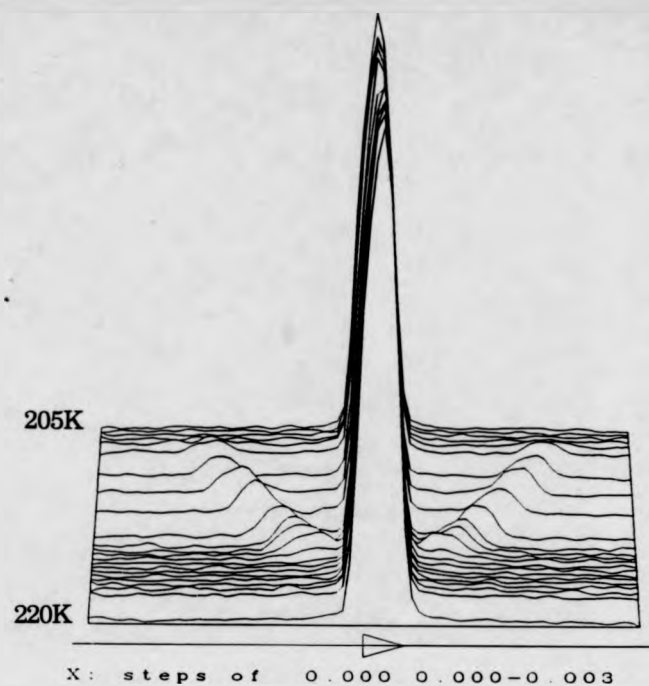
Fig. 4.16 Isometric plot of (10l) scans performed across the (101)
peak from 220K to 205K.

X: steps of 0.000 0.000 0.005
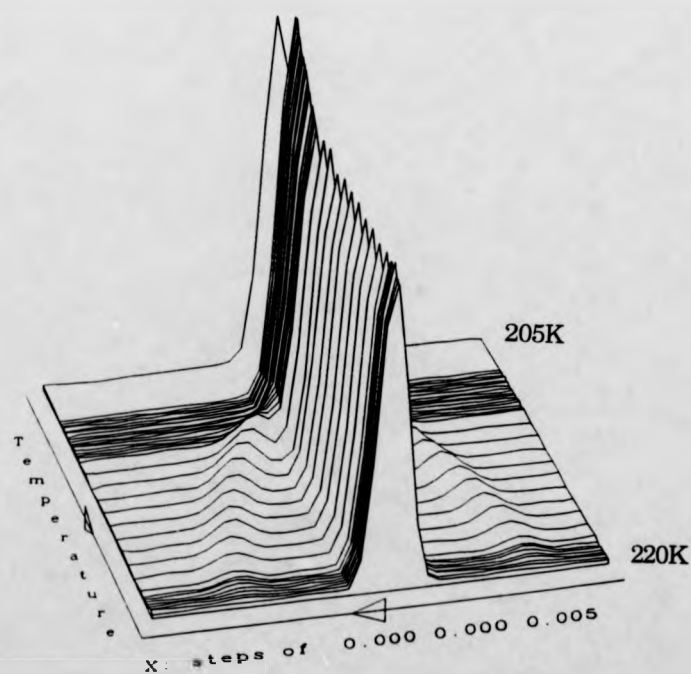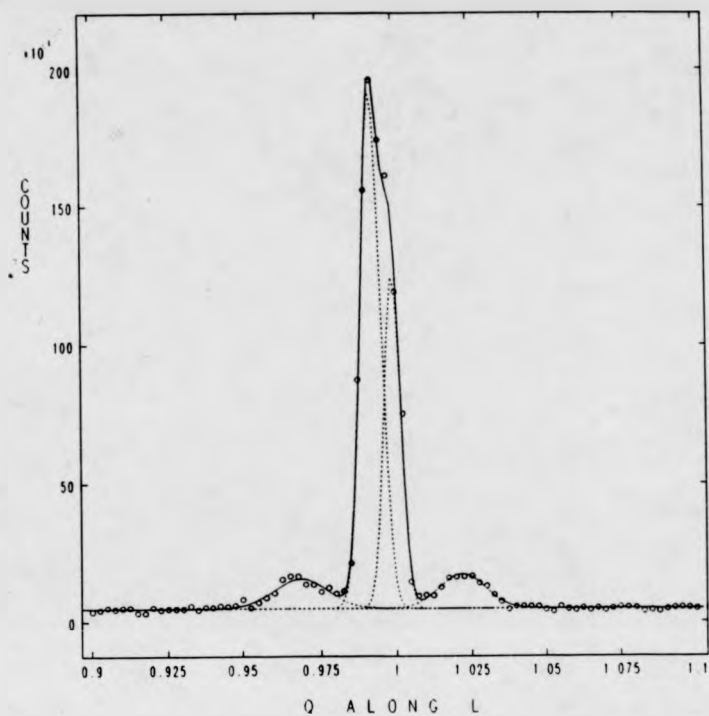
Fig. 4.17 a and b (10*l*) scans across the (101) lattice point.
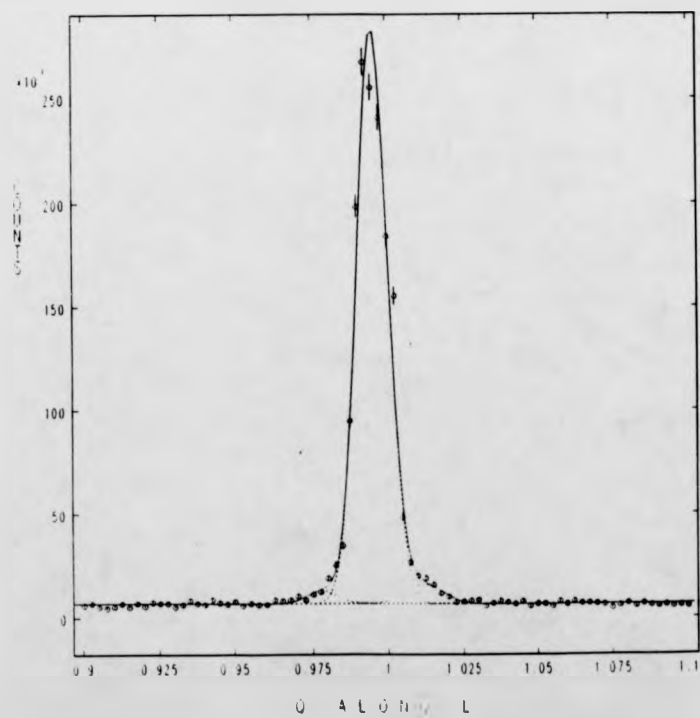
The interlayer turn angle of the helix is given by $\varphi^\dagger = \pi\mathbf{q}$ and has been calculated for the three samples in which satellites were observed and the results are presented as a function of temperature (figure 4.18). The lowest measurable interlayer turn angle is 3° at which point the satellite intensity had died away.

None of the samples exhibited appreciable hysteresis in the turn angle, however there does appear to be some hysteresis in the emergence of the satellites at T_c'. There is no reason why this should be the case, indeed, in the rare earth elements where there is hysteresis in the onset of the helix there is also hysteresis in the turn angle, the initial turn angle on warming being equal to the final turn angle on cooling despite hysteresis. The fact that the HAF-canted ferro transition comes about as the turn angle approaches zero is also unusual as described in the introduction.

Further information about the transition at T_c' (206K) is provided by the relative intensities of the nuclear and satellite intensities (fig.4.19). The data have only been corrected for the Lorentz effect. The satellite intensities are liable to scatter as a result of small fitting errors but the overall trend is clear. The increase in the nuclear peak at nearly 2K above the transition might possibly be attributed to critical scattering, however, when one sees that, at the same time, the satellite intensities are rapidly dying away, it becomes clear that the transition is broad with the ferromagnetic contribution to the peak increasing as the antiferromagnetic intensity falls. The most plausible explanation is that, as the transition is approached from the HAF phase, ferromagnetic domains grow out of the walls between chirality domains causing the slow break up of the helix. Equally on warming, HAF domains form out of the Bloch walls. This hypothesis may

---

$\dagger$ The interlayer turn angle is often given the symbol ω, φ has been chosen in this instance to avoid confusion with the sample rotation angle.
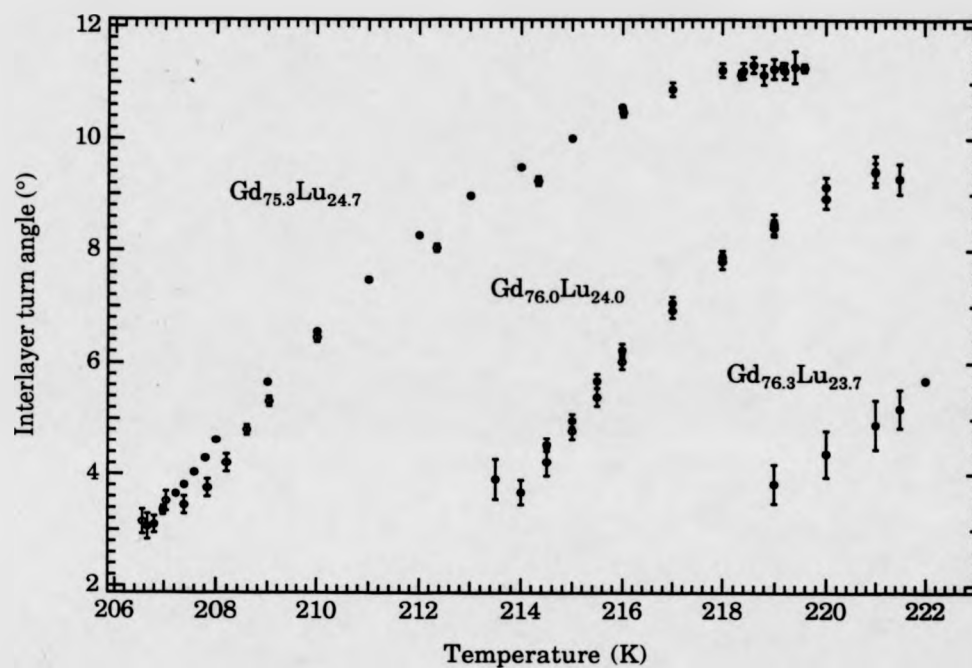
Fig.4.18 Interlayer turn angle vs. temperature.
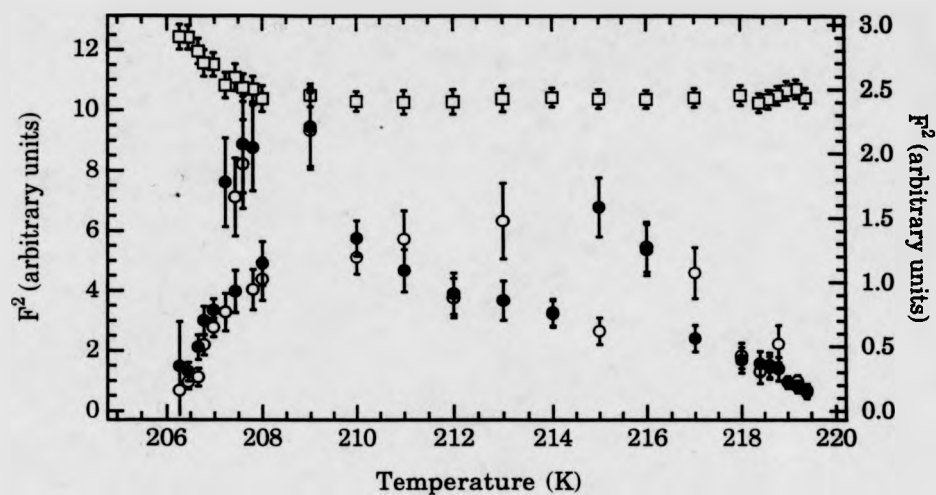The filled symbols represent data collected whilst cooling.

Fig 4.19 Structure factor squared for the (101) peak (squares and left hand axis) and the $(101)^+$ and $(101)^-$ satellites (filled and open circles respectively and right hand axis).
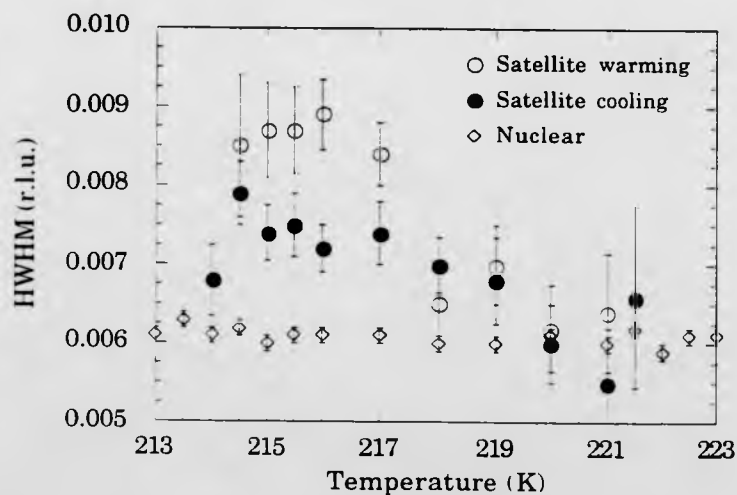

Fig. 4.20 HWHM of the nuclear and magnetic peaks vs. temperature for $Gd_{76.0}Lu_{24.0}$.

be supported by the behaviour of the satellite peak widths which provide some insight into the correlation length of the magnetic structure.

Figure 4.20 shows the HWHM vs temperature of the satellites and the (100) nuclear peak in the HAF phase of $Gd_{76}Lu_{24}$. The nuclear width is assumed to be resolution limited with a width of 0.012 which corresponds to a correlation length of approximately 80 atomic planes. Any structure which is correlated over that distance or more will appear as a resolution limited peak. The satellites on the other hand are broader particularly prior to the HAF-canted ferro transition and correspond to correlation lengths as short as 55 atomic layers. Similar behaviour has been observed in the studies of Bates and Melville. There is also some hysteresis in the antiferromagnetic correlation lengths which may be attributed to the formation of the striped or random HAF domains described in section 4.1.2.

4.2.2 The Ferromagnetic Phases

Extinction and absorption corrections were performed on the data and the basal plane and c axis components of the magnetisation (Mb and Mc) respectively were calculated in the manner outlined in chapter 2. Basal plane reflections were averaged over at least three equivalents (four in the case of the $Gd_{75.3}Lu_{24.7}$ data) and the Mb calculation is based in the average of the {002} reflections. The form factors used are those measured for Gd^{160} by Moon et al (1972). Both components are plotted as a function of temperature for $Gd_{75.3}Lu_{24.7}$, $Gd_{76.0}Lu_{24.0}$ and $Gd_{76.5}Lu_{23.5}$ (figures 4.21, 4.22 and 4.23 respectively). The unusual behaviour of the {002} reflection in the HAF phase is the result of the antiferromagnetic satellites falling within the resolution ellipsoid of the {002} reflections and appearing as additional scattering. A second experiment was performed on the

Fig. 4.21 Mb and Mc vs. temperature for $Gd_{75.3}Lu_{24.7}$.

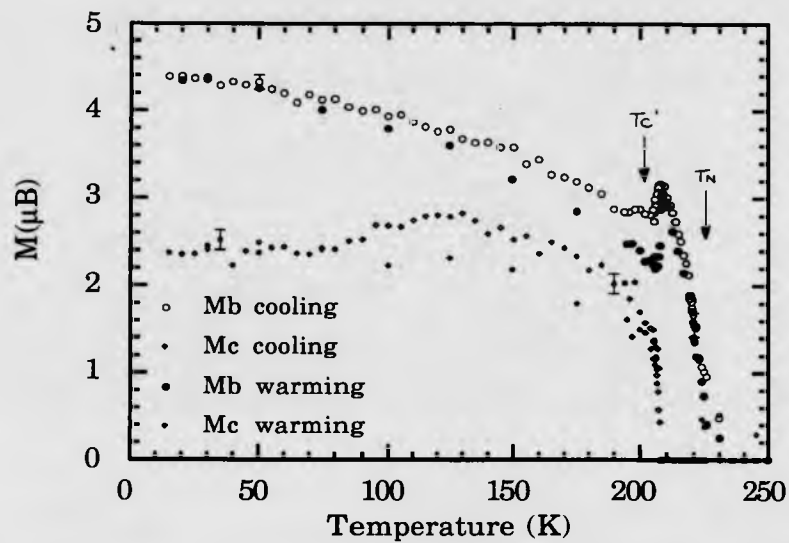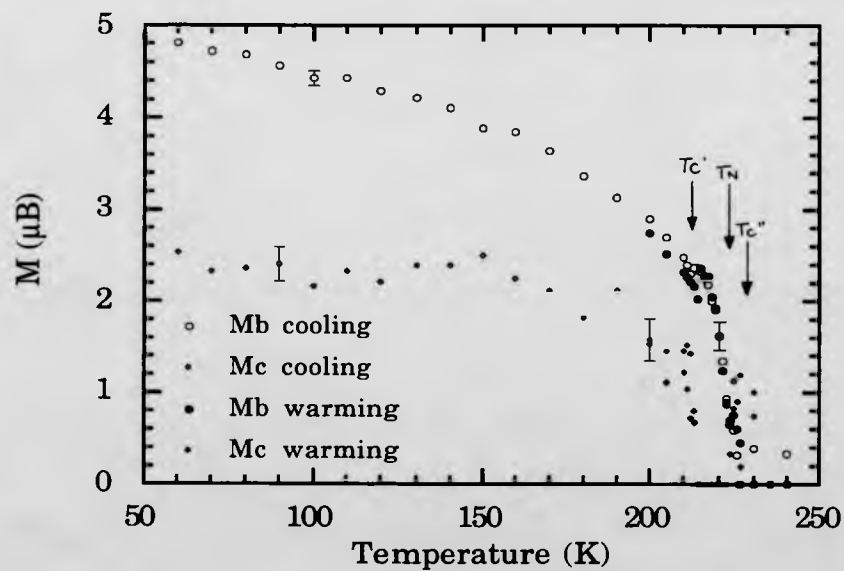Fig. 4.22 Mb and Mc vs. temperature for $Gd_{76.0}Lu_{24.0}$.

Fig. 4.23 Mc and Mb vs. temperature for $Gd_{76.5}Lu_{23.5}$ (1990).

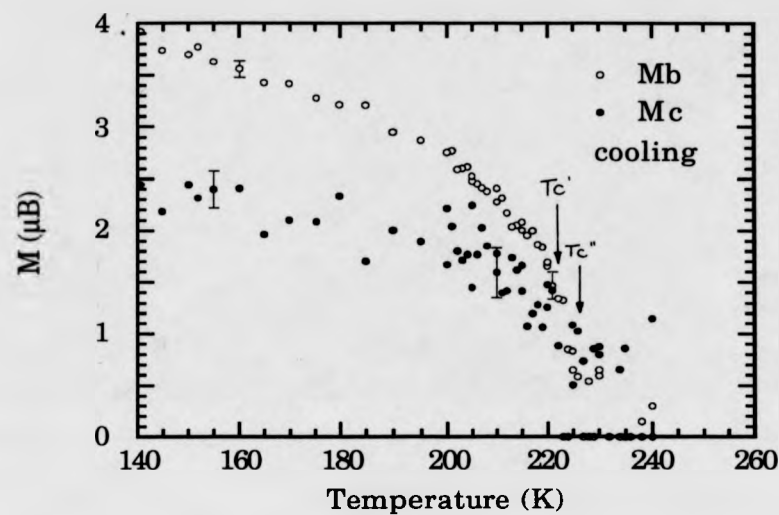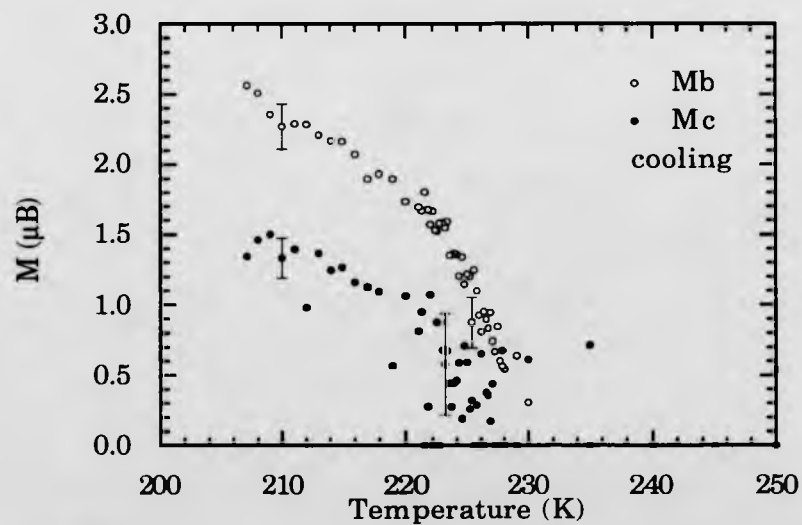

Fig. 4.24 Mb and Mc vs. temperature for $Gd_{76.5}Lu_{23.5}$ (1991).

$Gd_{75.5}Lu_{23.5}$ crystal using longer count times in an attempt to improve statistics and provide more information in the ferro-I region. Unfortunately these data (fig 4.24) do not show an improvement on the existing data. A study of the $Gd_{76.3}Lu_{23.7}$ crystal was also carried out, but the scatter in the intensities is so great (fig. 4.25) that a reasonable analysis of the data is not possible.

4.2.2.1 The Canted Ferromagnetic Phase

The fact that the antiferromagnetic satellites contribute to the intensity measured on the {002} peaks makes the calculation of Mb and Mc misleading. However, when the ferromagnetic cant angle is calculated and plotted as a function of temperature, it does provide a graphic representation of the way the moments rotate out of the basal plane at the transition from the HAF to canted ferro phase.

The ferromagnetic cant angle (the angle between the magnetisation vector and the c-axis) has been plotted for three samples (figures 4.26, 4,27, 4,28 and 4.29). $Gd_{75.3}Lu_{24.7}$ shows the magnetisation rotating out of the basal plane to assume a cant angle of approximately 60°. The data suggests that the cant angle tends to a slightly lower value at higher temperatures on cooling but remains constant on warming. However, the plot of Mb and Mc against temperature (fig. 4.21) shows that both Mc and Mb appear to be consistently lower on warming through the canted ferro region, than on cooling. It is unusual that both Mb and Mc are reduced and it is unlikely to be the result of hysteresis in the cant angle. The most plausible explanation is that the cooling of the sample has increased the magnetic domain size and that, as a result, magnetic extinction is greater on warming than on

79

Fig.4.25 Intensity vs. temperature for Gd$_{76.3}$ Lu$_{23.7}$

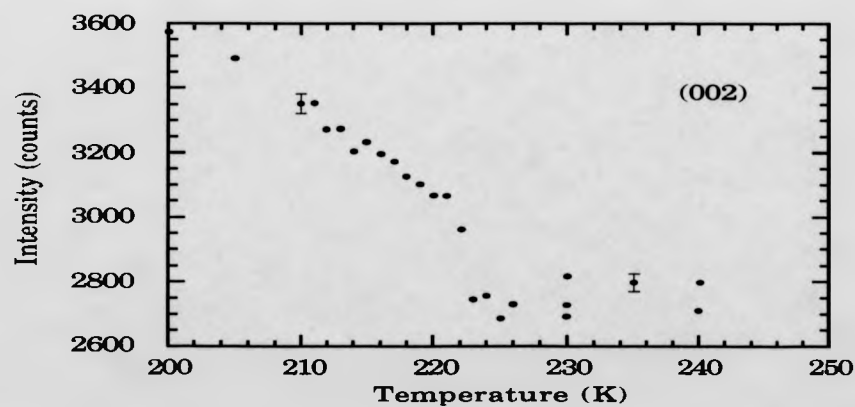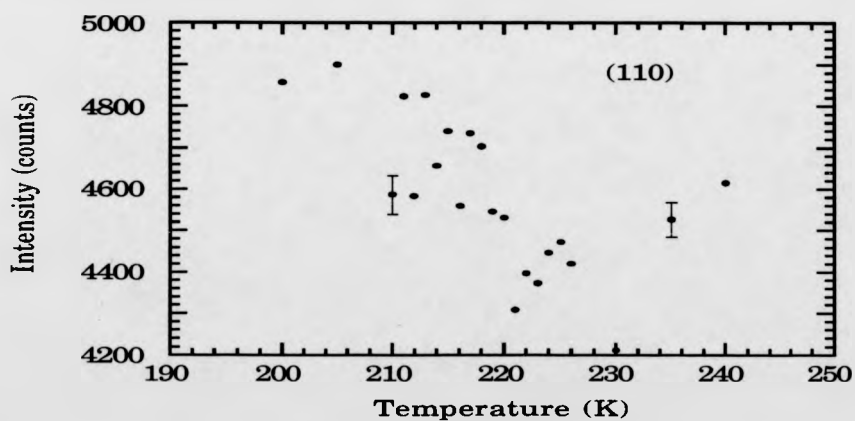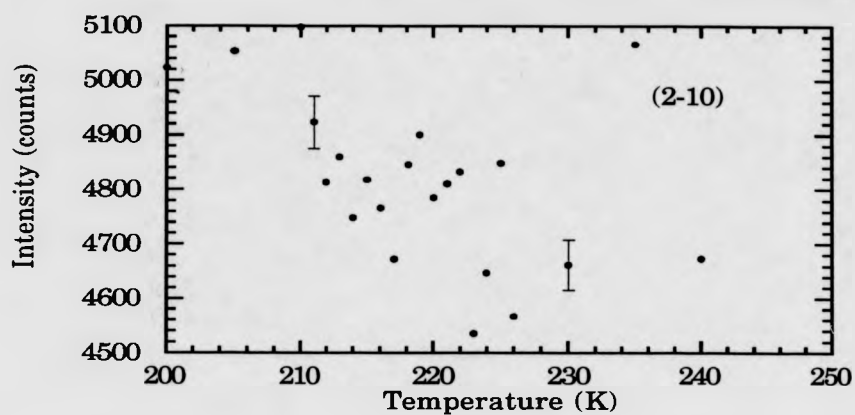Fig. 4.26   Cant angle vs. temperature for $Gd_{75.3}Lu_{24.7}$.

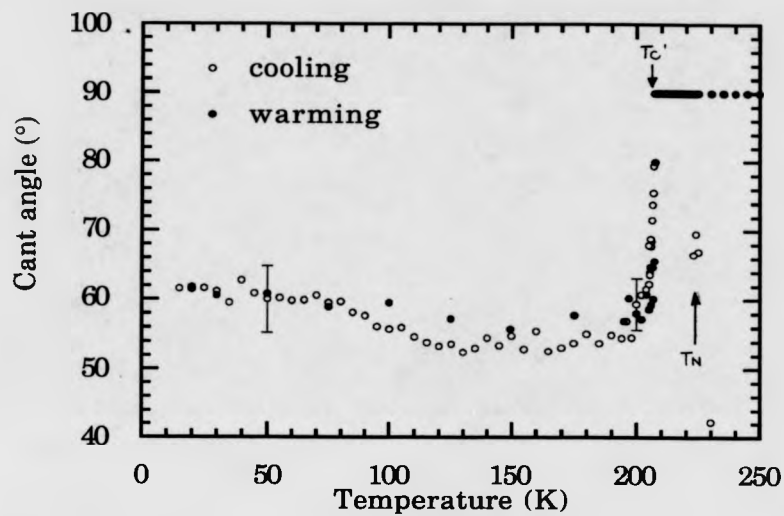
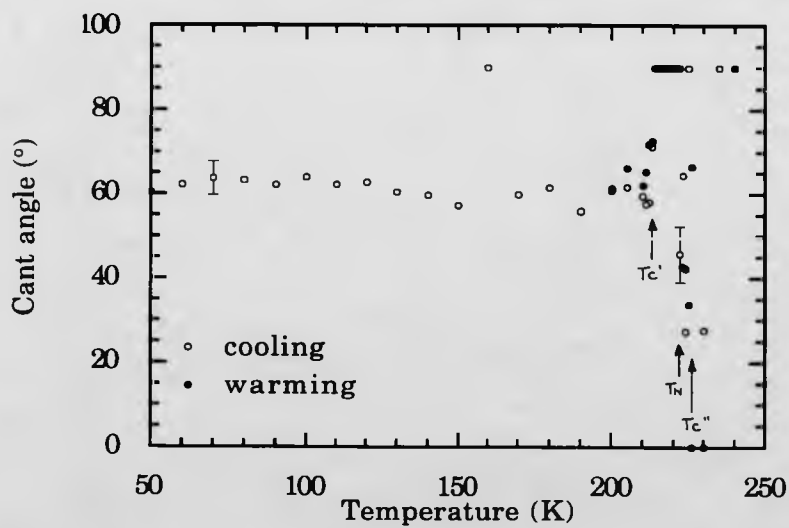Fig. 4.27   Cant angle vs. temperature for $Gd_{76.0}Lu_{24.0}$.

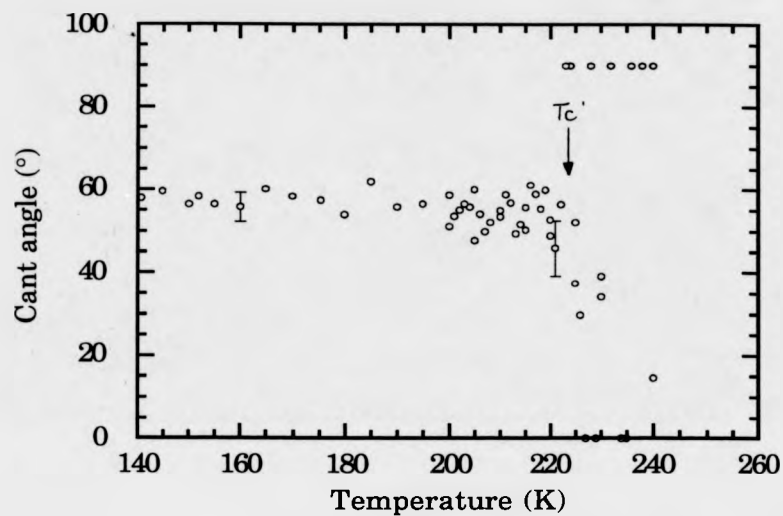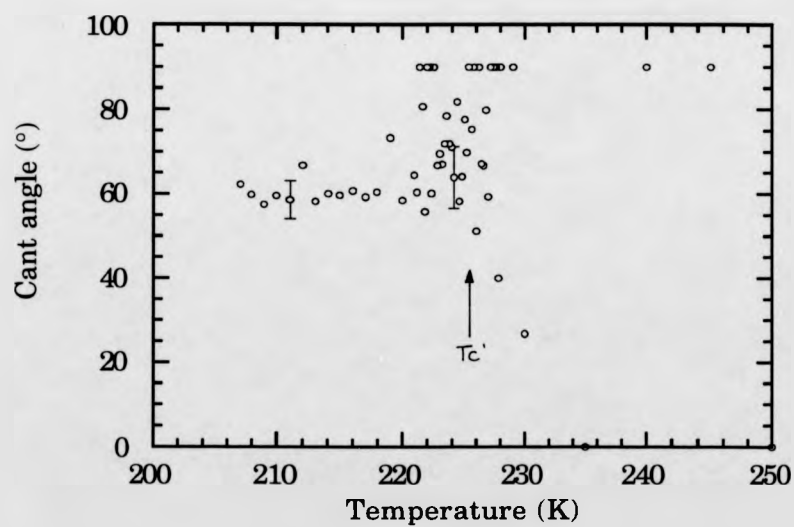Fig. 4.28 Cant angle vs. temperature for $Gd_{76.5}Lu_{23.5}$(1990)

Fig. 4.29 Cant angle vs. temperature for $Gd_{76.5}Lu_{23.5}$ (1991).

cooling. The magnetic extinction corrections performed were based on a simple approximation and cannot cater for a change in domain size.

Another unusual feature in the $Gd_{75.3}Lu_{24.7}$ data is the step in Mb below T_c'. This feature is not accompanied by a coincident anomaly on Mc which would seem to rule out a spin re-orientation. At present this feature remains unexplained.

The behaviour of the cant angle for $Gd_{76.0}Lu_{24.0}$ (fig. 4.27) is very similar to the exhibited by $Gd_{75.3}Lu_{24.7}$. The magnetisation is seen to rotate out of the basal plane at the HAF-canted ferro transition. However, above the T_n, there is some evidence of a phase with a component along the c-axis. This is the first neutron evidence of a ferro-I phase in this sample, but in view of the low intensities the cant angle data in this region must be viewed with some caution.

$Gd_{76.3}Lu_{23.5}$ unlike the other two samples discussed does not exhibit a HAF phase. On the basis of the ultrasound data, only a ferro-I phase which exists over a range of approximately 2K and a canted ferro phase were anticipated. The evidence supporting the existence of the ferro-I phase (which will be discussed in the next section) is modest, however the behaviour of the cant angle does suggest that the moment is aligned along the c-axis before rotating away to assume a cant angle of approximately 60° as with the previous samples. Again the low intensity in the initial ordering region means that the cant angle calculations must be viewed with caution close to the initial ordering temperatures

4.2.2.1 Ferro-I

Of the samples for which reasonable neutron scattering data is available only $Gd_{76.0}Lu_{24.0}$ and $Gd_{76.5}Lu_{23.5}$ were expected to exhibit a

ferro-I phase. The ultrasound data suggested that the ferro-I phase in these samples would be stable for no more than 2K. Returning to the plots of the two components of the magnetisation against temperature for these two samples, it is clear that the small thermal range of the ferro-I phase and the low spontaneous moment just below the ordering temperature makes an accurate study of the phase very difficult. Indeed scattering on the {002} reflections arising from short range order may be enough to obscure the existence of the ferro-I phase entirely.

The $Gd_{76.0}Lu_{24.0}$ data (plotted over a narrower temperature range in fig. 4.30) do show scattering on the basal plane reflections between T_c" and T_n as would be expected from a c-axis ferromagnet and in good agreement with the ultrasound results. Additional scattering is also observed above the initial ordering temperature at T_c", which may correspond to short range correlations. The difference between scans at 240K and 225K has been calculated because short range correlations would be expected to give rise to a broad Lorentzian contribution to the nuclear peak. The difference between the two scans was very small, although the available range may have been too small to prevent the broad feature being lost in the background.

Initial measurements on the $Gd_{76.5}Lu_{23.5}$ sample performed in steps of 1K did show some scattering on the basal plane reflections concurrent with a c-axis ferromagnet.

On the basis of these results a more thorough investigation of the ferro-I phase was conducted on the $Gd_{76.5}Lu_{23.5}$ sample which according to the ultrasound measurements displays the largest ferro-I phase. With hindsight this decision was somewhat misguided because the absence of a HAF phase makes separation of the ferro-I phase from the canted ferro phase difficult. The longer count times do not appear to have reduced the scatter of the data. The small temperature range and the low

Fig. 4.30 Mb and Mc vs. temperature for $Gd_{76.0}Lu_{24.0}$.
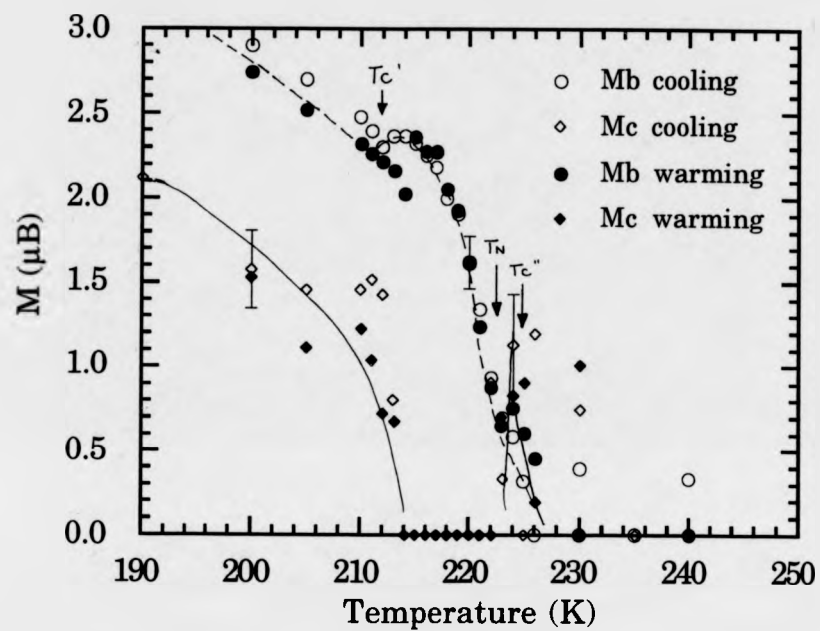
magnetisation will cause inevitable errors in the calculation of the mean ionic moment and make the two-tier magnetisation plot characteristic of the ferro-I phase impossible to identify without ambiguity.

To draw this section on the neutron scattering data to a close, the spontaneous moment per Gd ion has been calculated from all the data collected and is plotted for comparison with a theoretical Brillouin function (figs. 4.31, 4,32, 4.33 and 4.34). this has been normalised to a saturated moment of $7\mu_B$ because the contribution from the itinerant conduction electrons will not be detected by these neutron measurements since the form factor dies away very rapidly. The agreement is good and appears to validate the assumptions made in the data analysis and demonstrates that the necessary real crystal corrections were performed correctly.

4.3 Resistivity Measurements

In addition to the cubic samples prepared for the ultrasound measurements, needles of approximate dimensions (1x1x10)mm3 were cut from the same boule, to be used in resistivity measurements. To date, only resistivity measurements on the $Gd_{76.0}Lu_{24.0}$ and $Gd_{76.3}Lu_{23.7}$ sample have been performed, at the Universidade do Porto, Portugal, and they provide interesting evidence corroborating and challenging the interpretation of the ultrasound and neutron data.

Lutetium, in common with the other non-magnetic rare-earths has a finite "residual" resistivity at 0K, and displays a linear increase in resistivity with temperature. The others however display considerable structure below the ordering temperature, after which the resistivity
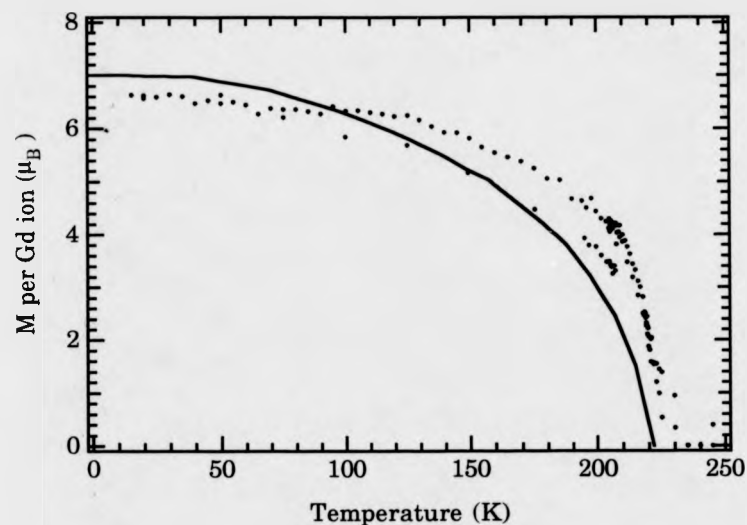
Fig. 4.31 Spontaneous magnetisation per Gd ion vs. temperature for
$Gd_{75.3}Lu_{24.7}$. The points represent the experimental data,
the solid line a theoretical function.
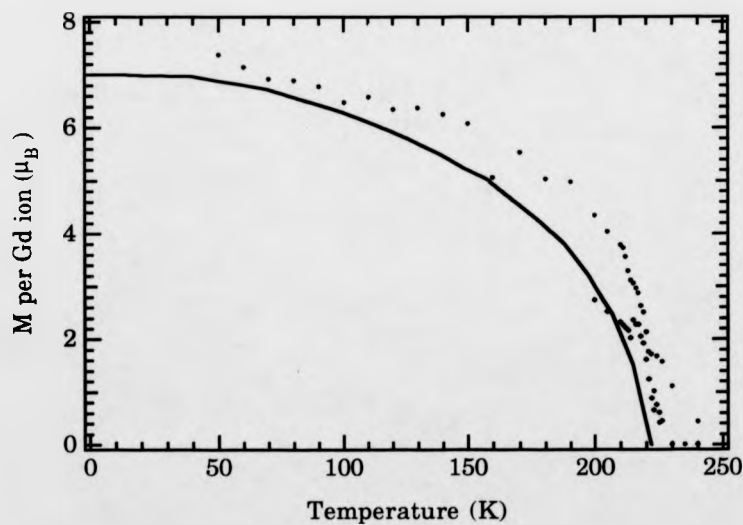

Fig. 4.32 Spontaneous magnetisation per Gd ion vs. temperature for
$Gd_{76.0}Lu_{24.0}$. The points represent the experimental data,
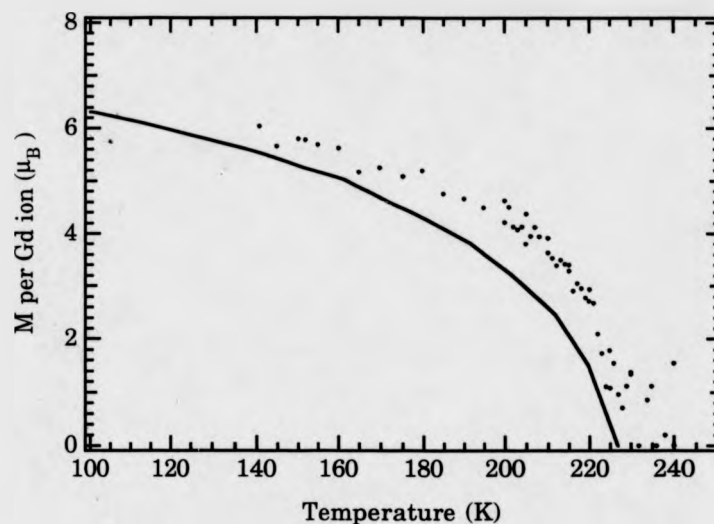the solid line a theoretical function.

Fig. 4.33 Spontaneous magnetisation per Gd ion vs. temperature for
Gd$_{76.5}$Lu$_{23.5}$. The points represent the experimental data,
the solid line a theoretical function.
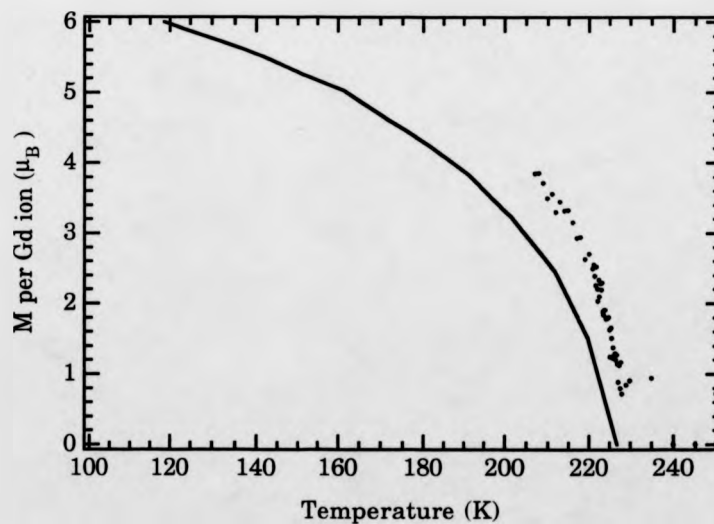

Fig. 4.34 Spontaneous magnetisation per Gd ion vs. temperature for
Gd$_{76.5}$Lu$_{23.5}$. The points represent the experimental data,
the solid line a theoretical function.

increases linearly above the Debye temperature. The total resistivity may be considered as arising from three components, the residual resistivity ρ_{res}, the resistivity arising from phonon scattering, ρ_{ph} and the magnetic contribution, ρ_m. Thus,

$$\rho(T) = \rho_{ph}(T) + \rho_{res}(T) + \rho_m(T).$$

The behaviour of the magnetic contribution, $\rho_m(T)$, is dictated by the magnetic order, and as such displays characteristic features at magnetic phase transitions, especially in the case where the conduction electrons play a significant role in the ordering mechanism. Critical fluctuations will also produce dramatic effects in both $\rho(T)$ and its temperature derivative $\frac{d\rho(T)}{dT}$.

By and large the formation of ferromagnetic order leads to a reduction in ρ_m after critical effects have subsided. The formation of incommensurate periodic structures ($q \neq 0$) will cause the formation of energy gaps in the conduction band. These gaps will effectively reduce the number of carriers and consequently increase the resistivity as the temperature decreases and the helical order becomes more stable.

Needles of $Gd_{76.0}Lu_{24.0}$ and $Gd_{76.5}Lu_{23.5}$ have been studied with the measurements being made parallel to the a and c-axes, the study is however made difficult by the limited extent of the ferro-I region and the low turn angle of the helix.

The plots of ρ against temperature for $Gd_{76.0}Lu_{24.0}$ with the measurement made parallel to the c-axis (fig. 4.35) show a concave approach to the initial ordering temperature as the temperature is lowered, once again hinting at correlations along the c-axis prior to the initial ordering temperature. Once order is established ρ decreases continuously.

83

Figs. 4.35 a&b. Resistivity and its derivative (dρ/dT) vs. temperature
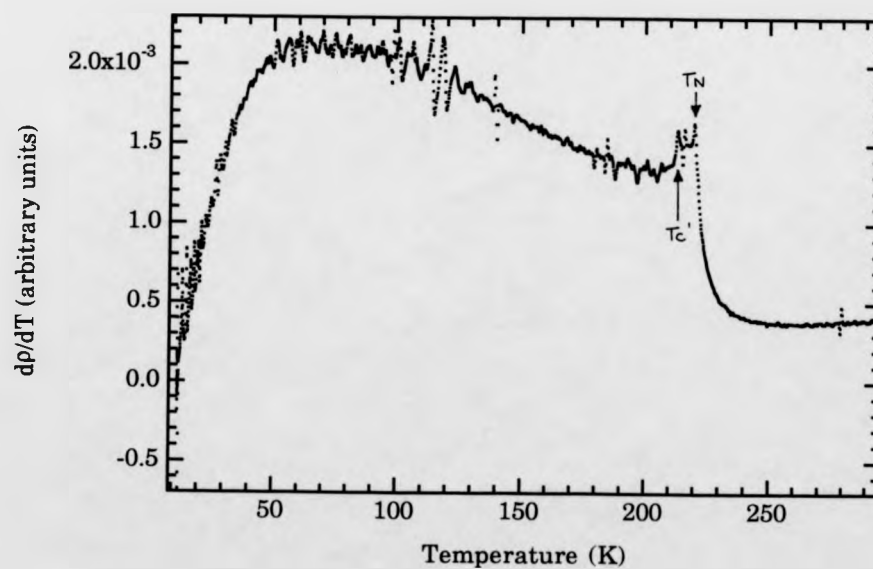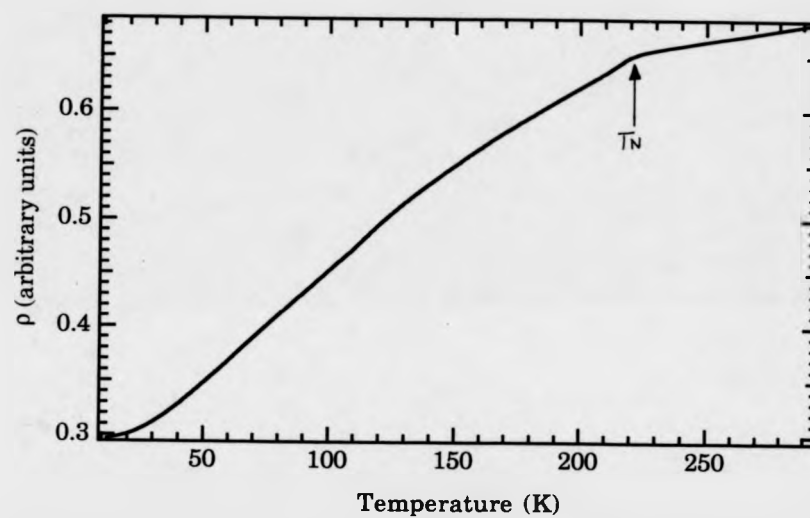for $Gd_{76.0}Lu_{24.0}$. Current flowing along the c-axis.
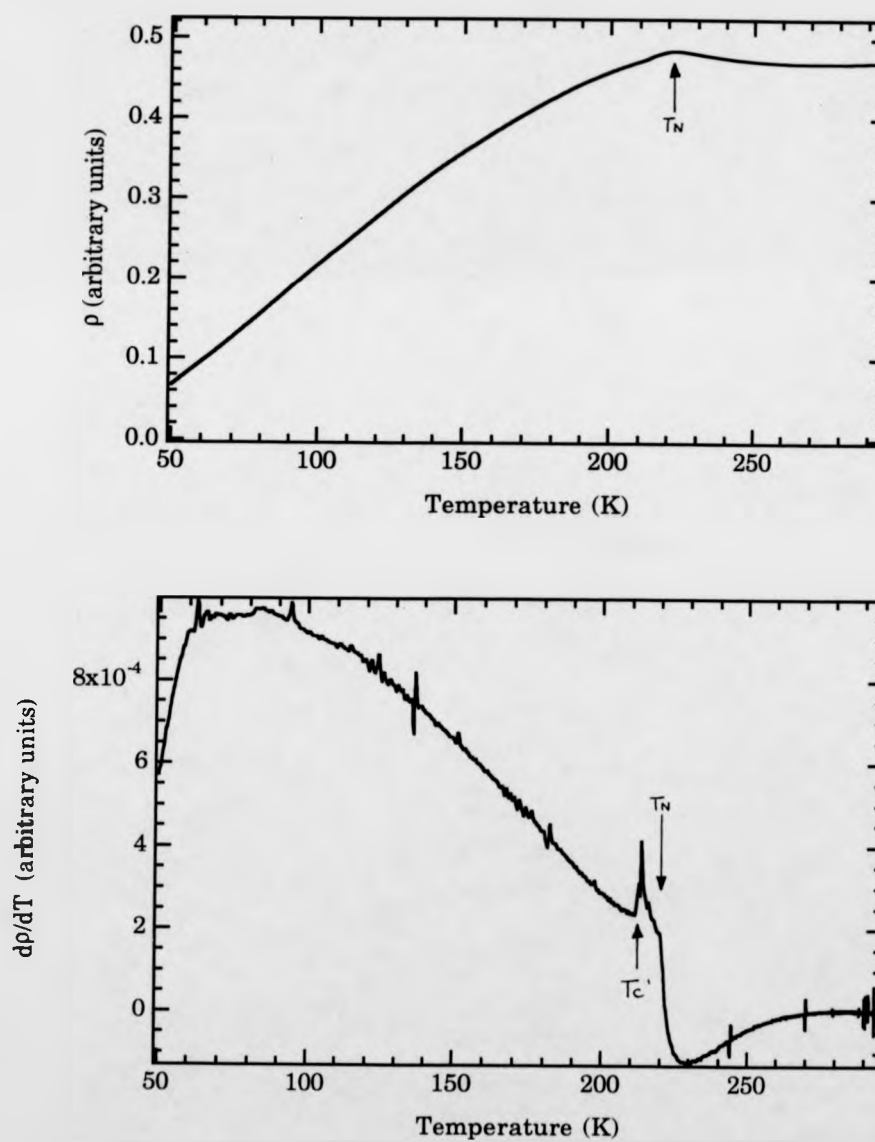
The measurements of ρ parallel to the a-axis (fig.4.36) show a knee at the initial ordering temperature (T_c").

The temperature derivative of resistivity shows considerably more detail, particularly the rise in $\frac{d\rho}{dT}$ in the HAF region. The differentiation was performed using a slide rule technique which is liable to cause spikes in the $\frac{d\rho}{dT}$ as a result of the random scatter in the data. Smoothing was applied to the raw data in order to reduce this effect, but this was done cautiously so as not to obscure the real features of the data. The c-axis measurement exhibits a dramatic increase in the HAF region with T_c' distinguished by a distinct step. The a-axis measurements are less distinct showing spikes at the upper and lower transitions. In any atomic layer in the HAF phase all the moments are aligned ferromagnetically, consequently the conduction electron and hence $\frac{d\rho}{dT}$ behave in the same manner as in a ferromagnetically ordered structure.

The data collected from the $Gd_{76.5}Lu_{23.5}$ needles (figs. 4.37 and 4.38) are very similar to those collected for $Gd_{76.0}Lu_{24.0}$ and illustrate the diminished HAF region. Indeed the a-axis data does not appear to couple to the lower temperature transition.

While the resistivity data corroborates much of the neutron and ultrasound data the most disappointing exception is the failure of the resistivity measurement to confirm the existence of a ferro-I phase. Other needles of different compositions have been produced and are presently being studied by the Oporto team. In addition to the resistivity measurements, magnetoresistance measurements will also be made.

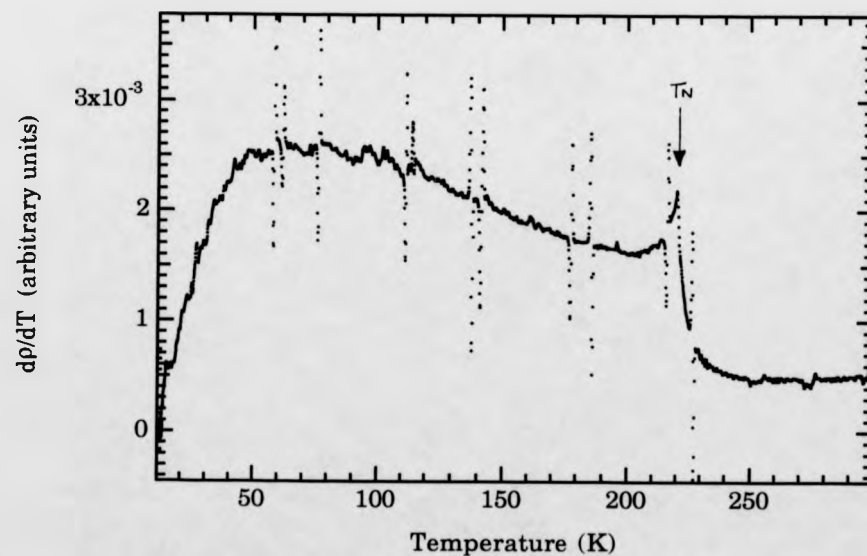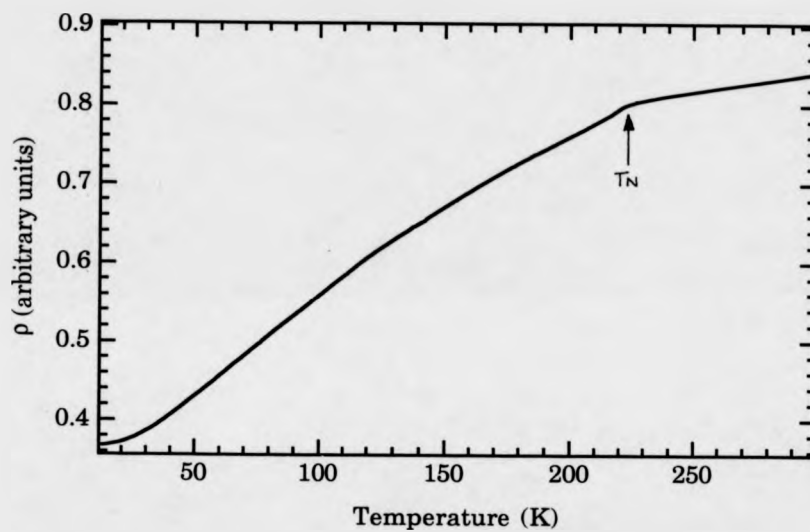Figs. 4.36 a&b Resistivity and its derivative ($d\rho/dT$) vs. temperature for $Gd_{76.0}Lu_{24.0}$. Current flowing along the a-axis.

Figs. 4.37 a&b Resistivity and its derivative (dρ/dT) vs. temperature for $Gd_{76.3}Lu_{23.7}$. Current flowing along the c-axis.
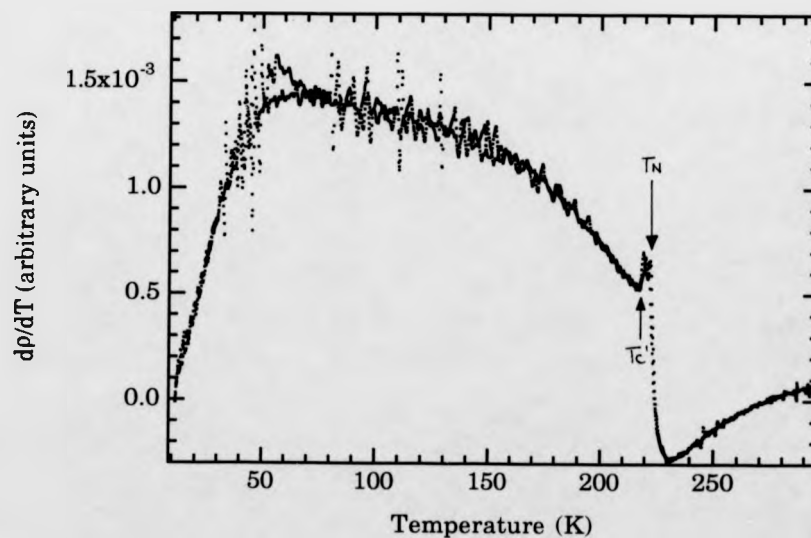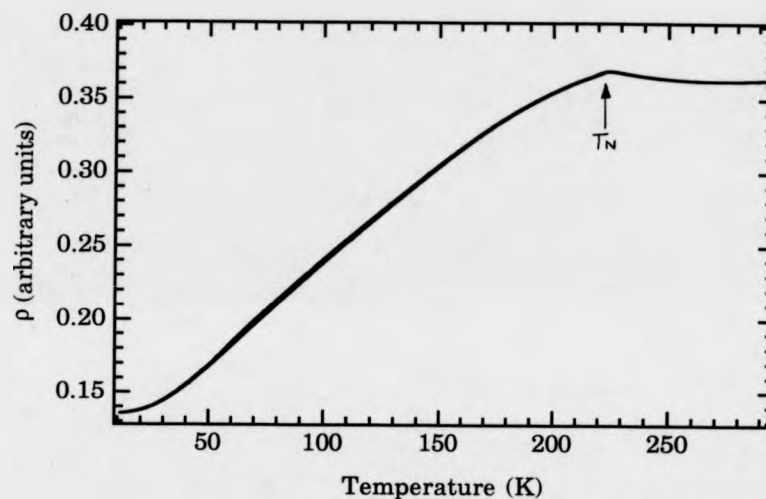
Figs. 4.38 a&b Resistivity and its derivative (dρ/dT) vs. temperature for $Gd_{76.3}Lu_{23.7}$. Current flowing along the a-axis.

4.4 Discussion and Conclusions

By and large the agreement between the three techniques employed for the study of the phase diagram is good. The one feature which must be regarded with some scepticism is the existence of the ferro-I phase which is solely supported by the ultrasound data. The observation of a ferro-I phase in a $Gd_{80}Lu_{20}$ crystal by Ito et al (1984) lends more credibility to the phase diagram presented here but more supportive evidence would ideally be required.

The failure of the neutron data to provide unequivocal evidence may be attributed to the small temperature range of the phase, and critical scattering problems. The size of the sample used for the experiment ($125mm^3$ cube) may cause some problems with the accurate calculation of the spontaneous magnetisation, because the absorption corrections are prone to inaccuracy. These problems are magnified with such absorbing samples, because most of the scattering will undoubtedly take place close to the surface.

The failure of the resistivity measurements on the other hand are more difficult to explain, since the formation of the ferro-I phase has shown quite dramatic effects in other samples (Ito, 1984).

The ultrasound evidence however, is substantial showing good agreement to other ultrasound measurements made on Gd-Y samples (Bates,1985) in which a ferro-I phase has been observed by neutron diffraction. Measurements detailed in the following chapter present additional evidence to support the existence of the ferro-I phase, consequently a more detailed discussion of this phase will be left until later.

In the HAF region the observed behaviour of Gd-Lu is very similar to that of Gd-Y. The transition from HAF to canted ferromagnet would appear to take place as the antiferromagnetic domain walls between

domains of different chirality grow to become ferromagnetic domain walls, and ferromagnetic Bloch walls grow into helical domains. The domain wall energy is related to the turn angle (Drillat, 1981) and, qualitatively speaking it is possible to understand how a reduction in the turn angle could allow an increase in the domain wall size big enough to bring about the transition. While this series of events would seem to explain the behaviour of the scattering intensities and the hysteresis in the transition, there is still no reason why an out of plane component of the magnetisation should develop coincident with this transition. Undoubtedly the balance between the anisotropy which gives rise to the canted ferromagnetic phase and the domain wall energy which is effectively an anisotropy is complex. The results suggest that the canted ferro region is formed continuously during the transition without an intermediate basal plane ferromagnetic phase.

The modelling of the transition, particularly the break up of the helix into the ferro domains, would provide a more quantitative argument and would undoubtedly be a rewarding exercise. However, to do so the exchange energies and anisotropies which drive the two phases must be fully understood in order to draw up an expression for the free energy including the domain wall energy. This calculation is temporarily set aside for further work.

The detail added to the phase diagram of Beaudry et al confirms the assertion that Gd-Lu will not have a Lifshitz point. In this respect Gd-Lu has been shown to be very similar to Gd-Y in that it displays two multicritical points, one of which may be considered to be a two dimensional Lifshitz point, where the ferro-I, canted ferro and HAF regions meet with the turn angle tending to zero.

References

Bak P., Høgh Jensen M., J. Phys. C: Solid State Phys., 13 L881 (1980).

Baruchel J., Palmer S.B., Schlenker M., J de Physique 42 1279 (1981).

Bates S., PhD Thesis, University of Hull, (1985).

Bates S., Palmer S,B., Sousa J.B., McIntyre G.J., Fort D., Legvold S.,

Beaudry B.J., Koehler W.C., Phys. Rev. Letts. 55 27 2968 (1985).

Bozorth R.M., Gambino R.J., Phys. Rev. 147 2 487 (1966).

Cable J.W., Koehler W.C., J. Appl. Phys 53 (3) 1904 (1982).

Drillat A., PhD Thesis University of Grenoble, (1981).

Eccleston R.S., Melville R.J., Griffiths A.R., Palmer S.B., Vrtis M.L. I.L.L.
    Experimental Report 5-32 375 (1990).

Garel T., Doniach S., J. Phys. C: Solid State Phys., 13 L887 (1980).

Hornreich R.M., Marshall Luban, Shtrikman S., Phys. Rev. Letts. 35 23
    1978 (1975).

Ito T., Mizuno K., Ito K., Beaudry B.J., J. de Physique C8 12 49 343 (1988).

Ito T., Oka M., Legvold S., Beaudry B.J., Phys. Rev. 29 11 6276 (1984).

Jensen J. and Mackintosh A.R., "Rare Earth Magnetism, Structures and
    Excitations", Oxford Science Publishers, (1991).

Kaino K., Kasuya J., J. Phys F 11 88 3 (1981).

Koehler W.C. J. Appl. Phys. 36 3 1078 (1965).

Koehler W.C., in "Magnetic and Inelastic Neutron Sbattering of Neutrons
    by Metals", Gordon Breach Science Publishers, (1967).

Legvold S., Harmon B.N., Beaudry B.J., Burgardt P., Younkin D.R., White
    H.W., Phys. Rev. 16 11 4986 (1977).

Legvold S., Ito T., Beaudry B.J., Phys. Rev. Letts. 45 15 1275 (1980).

Legvold S., Phys. Rev. B 19 146 (1979).

Legvold S.,Bugardt P., Beaudry, B.J., Phys. Rev. B 225 2573 (1980).

Lindgård P., Phys. Rev. B 16 5 2168 (1977).

Melville R.J., Eccleston R.S., Griffiths A.R., Palmer S.B., Vrtis M.L.,
     I.L.L. Experimental Report 5-32 376 (1990).

Melville R.J., PhD Thesis, University of Warwick, (1989).

Michelson A., Phys. Rev. B 16 1 577 (1977).

Moon R.M., Koehler W.C., Cable J.W., Child H.R., Phys. Rev. B 53 997
     (1972).

Mukamel D., Phys. Rev. Letts. 46 13 845 (1981).

Palmer S.B., J. Phys. F 5 2370 (1975).

Pearce A.S., Personal communication (1991).

Smidt F.A., Daane A.H., J. Phys. Chem. Solids 24 361 (1963).

Tachiki M., Levy M., Kagiwada R., Lee M.C., Phys. rev. Letts. 21 16 1193
     (1968).

Thoburn W.C., Legvold S.., Spedding F.H., Phys. Rev. 110 1298 (1958).

Young R.C., J.Phys. F: Met. Phys 13 L239 (1983).

Chapter 5

$Gd_{76.0}Lu_{24.0}$ in an Applied Magnetic Field

Introduction

The behaviour of the magnetic structure of $Gd_{76.0}Lu_{24.0}$ with a magnetic field applied either along the c-axis or in the basal plane should be easy to predict. One would expect the canted ferromagnetic structures to become aligned along the field direction as the field is increased. The helical structure under the influence of a basal plane field should collapse via distorted helix and fan phases to a ferromagnetic phase (Cooper 1968). In response to a field applied along the c-axis the formation of a cone phase is likely. However, previous studies of the Gd-Y and Gd-Sc systems (Bessa Sousa, Moriera et al, 1991) have revealed that the H-T phase diagrams of these alloy systems are more complex than may have been anticipated. Transport and ultrasound measurements on $Gd_{64}Sc_{36}$ (Melville, 1989) suggested the presence of a fan phase intermediate between the helix and ferro phases. However this has not been satisfactorily confirmed by neutron diffraction measurements (Melville et al, 1989). In fact, the neutron diffraction results may be interpreted as arising due to the coexistence of ferro and helical phases in much the same way as Baruchel et al (1988) have observed in terbium.

The proposal of a 'helifan' phase by Jensen and Macintosh (1990), in which the distortion of the helix introduces an additional periodicity to the structure, and its subsequent observation in holmium by Cowley et al (1991) raise the possibility that a helifan phase may also be present in those Gd based alloys which exhibit helical phases. Basal plane anisotropy is not considered to be an important factor in the stability of a helifan. However, the small turn angle and limited thermal range of the helical phase would seem to make the observation of a helifan phase in $Gd_{76.0}Lu_{24.0}$ very unlikely.

Thus, a study of the behaviour of $Gd_{76.0}Lu_{24.0}$ may result in the observation of new and unexpected phases and in addition, it will provide some insight in to the nature of the interactions which compete to produce the wide range of magnetic structure observed in zero field.

A neutron diffraction experiment in an applied magnetic field on this sample was not possible before the completion of this thesis, however, the complementary nature of the ultrasound and neutron data at zero field allow for a more detailed picture to be drawn from the ultrasound data than would usually be possible.

To reiterate the salient points from the preceding chapter, $Gd_{76.0}Lu_{24.0}$ exhibits a small ferro-I region between 222.5K and 221.5K below this region a HAF phase exists with an inter-layer turn angle which decreases smoothly from an initial value of approximately 6.5° to 3.5° before the transition to canted ferromagnet at 214K.

5.1 C_{33} Coupling to Anticipated Structures

The coupling of C_{33} to the three magnetic structure exhibited by $Gd_{76.0}Lu_{24.0}$ at zero field has been discussed in the previous chapter. The

anomalous behaviour of C_{33} on the formation of those new structures which are anticipated to occur as the result of the application of a magnetic field are now considered.

In a c-axis ferromagnet there are obviously no matrix terms corresponding to the projection of the moments on the basal plane, consequently the anomalous softening of C_{33} on the formation of this structure may be written

$$-\Delta C_{33} = 4B_{33}T_{33}B_{33}. \qquad (5.1)$$

Similarly, for an a-axis ferromagnet those matrix terms with index 3 become zero, hence

$$-\Delta C_{33} = 4B_{13}(T_{11} + T_{22} + 2T_{12})B_{13}. \qquad (5.2)$$

In the presence of a c-axis magnetic field, helically ordered moments will lift out of the basal plane introducing the terms T_{33}, T_{13}, and $T_{23} = T_{13}$ (the equality being valid because the turn angle of the spiral is not commensurate) to equation 4.2. Thus, in the cone phase we can write

$$-\Delta C_{33} = 4(B_{33}T_{33}B_{33} + 4B_{13}T_{13}B_{33} + 2B_{13}(T_{11} + T_{12})B_{13}). \qquad (5.3)$$

Clearly, the additional matrix elements will produce considerable softening in C_{33}, often to the extent of making the signal immeasurably small.

5.2 c-axis Field

Only the C_{33} elastic constant and α_{33}, the associated attenuation coefficient, have been measured because all three phases may be clearly delineated due to the strong coupling to C_{33}, albeit via different mechanisms. Measurements were performed at a constant field, decreasing and increasing the temperature and at a fixed temperature sweeping the field. Because no magnetisation measurements have been performed on these samples an accurate determination of the internal field is not possible.

5.2.1 Isofield Measurements

The most dramatic representation of the affects of a c-axis field on the magnetic structures of $Gd_{76.0}Lu_{24.0}$ is the waterfall plot showing the attenuation α_{33} at 4 field strengths (fig. 5.1).

Application of a small field (0.1T) appears to be enough to lift the helically oriented moments out of the basal plane forming a cone structure. The out of plane moments, described by the additional matrix terms in equation 5.3, are soft with respect to C_{33} giving rise to considerable attenuation of the signal. Compounded with the hysteretic domain effects outlined in the previous chapter, this means that the signal is not measurable over a region of approximately 3K between 215K and 218K when the sample is warmed from the canted ferro region. The hysteresis is clearly visible on the C_{33} scan (fig 5.2) as is the inflection which was associated with the paramagnetic-ferro-I transition at zero field. The effect of the applied field appears to be to move the initial ordering temperature (T_c") to a slightly higher temperature. The effect of an applied field is usually to reduce
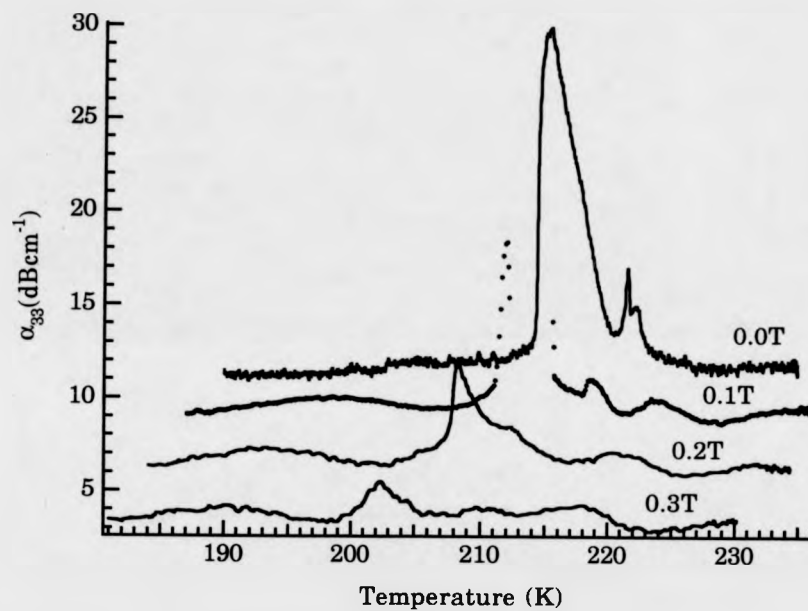
92

Figure 5.1. α_{33} vs. Temperature with increasing temperature for 4 c-axis fields. The scale corresponds to the zero field measurements, succeeding measurents are each offset by 3K.

Figure 5.1. α_{33} vs. Temperature with increasing temperature for 4 c-axis fields. The scale corresponds to the zero field measurements, succeeding measurents are each offset by 3K.

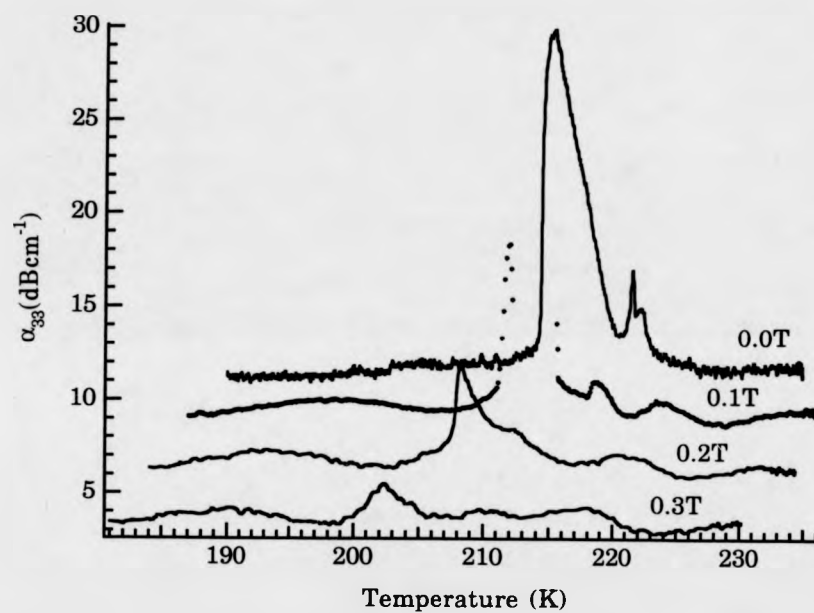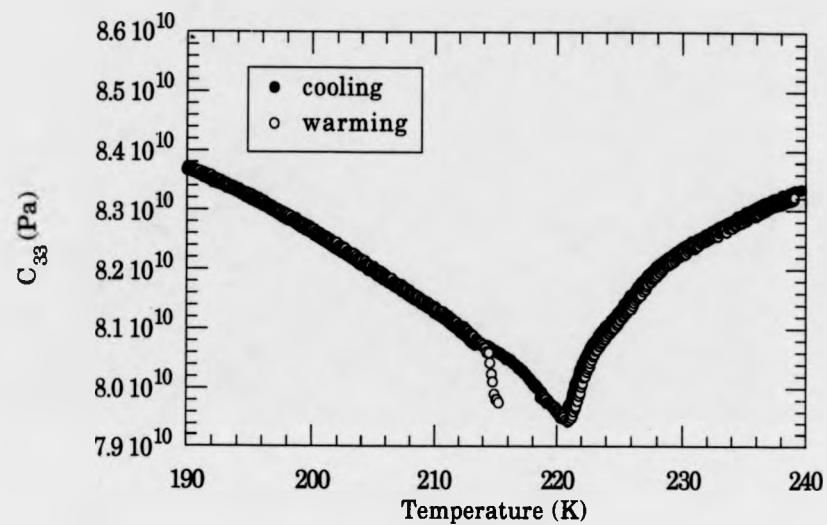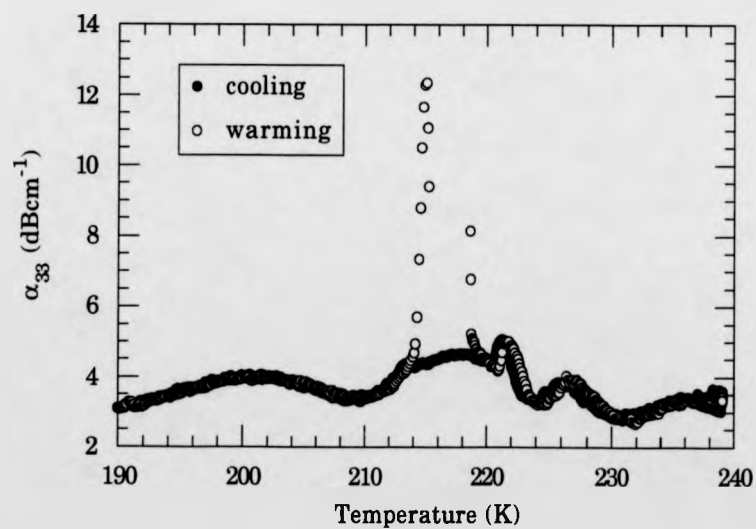Figure 5.2 C_{33} vs. Temperature with 0.1T applied along the c-axis

Figure 5.3 α_{33} vs. Temperature with 0.1T applied along the c-axis.

ordering temperatures, and we assume that the unusual behaviour of C_{33} and α_{33} (fig.5.3) is caused by the development of short range order prior to T_n. It is not clear if this short range order develops out of the ferro-I region. The neutron scattering data showed evidence of short range correlations above Tc" and these may be the precursors of the effects being witnessed in the ultrasound data with a field applied along the c-axis.

One other point which merits comment in the discussion of the 0.1T isofield measurements, is the region between the cone phase and what we will still refer to as ferro-I. The attenuation data on warming show a region between the critical peak originally associated with the ferro-I-helix transition and the steep rise at the onset of the helical phase. For the C_{33} measurements this region is only visible on the warming measurements by virtue of the hysteresis in the cone/HAF region, the gradient being very similar to that in the canted ferromagnetic region. This phase is characterised by a modest hardening of the elastic constant and the absence of any hysteresis in α_{33}. Possibly the elevation of the moments out of the basal plane has overcome the effects of the periodic part of the long range exchange interaction and the structure has assumed a canted ferro structure which is driven by the anisotropic part of the exchange. While this model explains the C_{33} and α_{33} behaviour, it is obviously a very simplistic approach and raises the unlikely prospect of two identical ferro regions being separated by a helical region. Another explanation is that the striped chirality domains which produce the pronounced softening of C_{33} on warming, no longer exist, because of the lifting of the moments out of the basal plane. however, this would imply that the semi-cone angle decreases dramatically as the temperature reduces, which seems to contradict other results. Also, the distinct nature of the transition suggests a phase change rather then a gradual change in the shape and orientation of the domains.

We will leave further discussion of this phase until the isothermal measurement have been reviewed.

With a field of 0.15T applied along the c-axis, the C_{33} behaviour is very similar to that at 0.1T. The inflection associated with the onset of ferro-I or short range order takes place at a higher temperature and the intermediate region, which we have yet to identify definitively has increased at the expense of the conical phase which has reduced to approximately 3K.

The intermediate region appears to be destroyed by an applied field of 0.2T. The inflection in C_{33} (fig. 5.4) at 226K and the broad peak in the attenuation (fig.5.5) at the same temperature corresponds to the onset of short range order. The isofield measurements exhibit no direct evidence of a transition from ferro-I to a c-axis ferromagnetic structure. One would assume that such a transition takes place at a low field of approximately 0.1T but we will rely on isothermal scans to provide more definite information. The region between 225K and 217K is ferromagnetic probably with the moment aligned along the c-axis, however, it is not clear from the data if and when long range order is established above T_n. From 217K to 212K both C_{33} and α_{33} still exhibit the thermal hysteresis and the soft behaviour associated with the conical phase. The hysteresis in the transition temperature from cone to canted ferro is 2K similar to that at zero field with the transitions at 214K on warming and 212K on cooling approximately 0.5K lower than the zero field values.

With an applied field of 0.3T the initial ordering transition is now manifest as broader features on the C_{33} data (fig. 5.6), but the attenuation data (fig. 5.7) reveal little of interest. The conical phase has been completely destroyed and the c-axis ferro and canted ferro transition is visible as the sharp dip in C_{33} at 211K which exhibits hysteresis of no more than 0.3K, which may be attributed to the thermal coupling of the thermocouple to the sample. The behaviour of C_{33} at this transition reflects the changeover in the

94

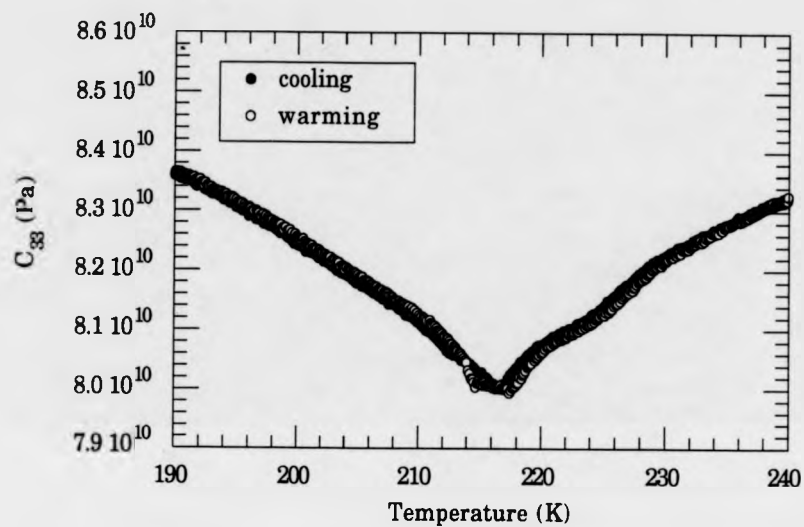Figure 5.4 C_{33} vs. Temperature with 0.2T applied along the c-axis.

Figure 5.5 α_{33} vs. Temperature with 0.2T applied along the c-axis
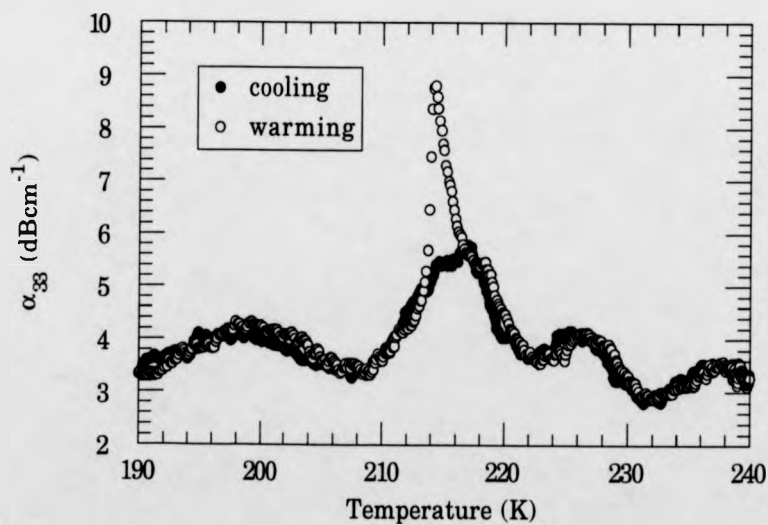
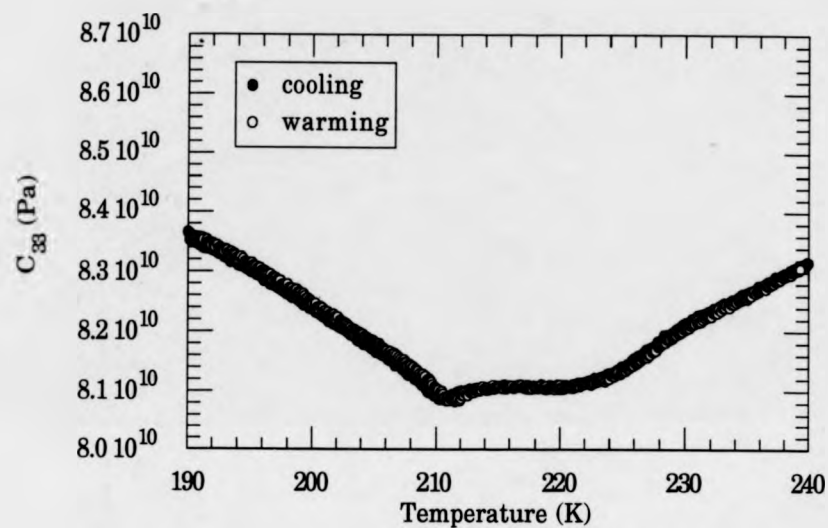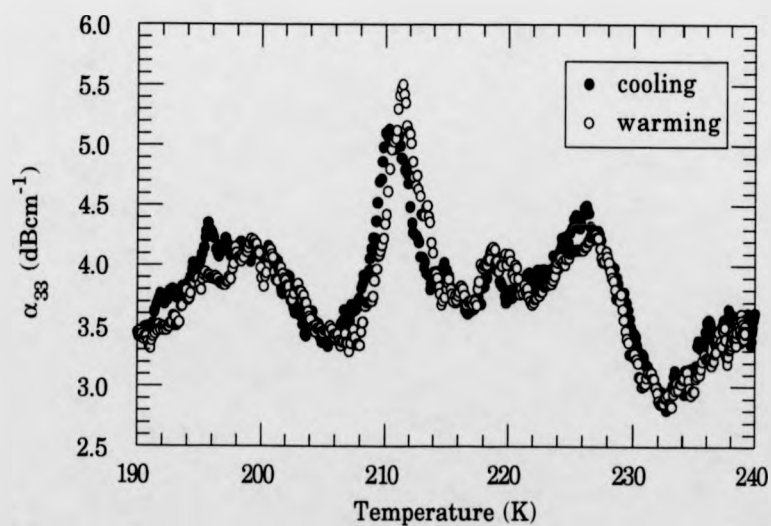Figure 5.6 C_{33} vs. Temperature with 0.3T applied along the c-axis.

Figure 5.7 α_{33} vs. Temperature with 0.3T applied along the c-axis.

interactions which stabilise the two phases. Further increases in the applied field have the effect of moving the transitions to lower temperatures. The feature that had appeared as an inflection at lower fields is now a broad minimum which heralds the onset of c-axis ferromagnetic order. Neither the elastic constant nor attenuation data provide any firm indication of the temperature at which order becomes long range. As the field is increased further the minimum remains broad, centred on approximately 224K.

5.2.2 Isothermal Measurements

Isothermal scans provide information about the effects of an applied field on particular phases and when cross referenced with the isofield scans provide more information from which to draw up a phase diagram. These scans were performed using a sweep generator which varied the field applied parallel to the c-axis continuously from the remnant field of the magnet up to the maximum field of 1.7T in approximately 20 minutes. The temperature was found to be stable to within ±0.2K for the duration of the field sweep. The absolute accuracy of the thermocouple was not thought to be better than ±1K. Consequently, before performing measurements in the ferro-I region for example measurements were made as the temperature was slowly increased or decreased, knowledge of the zero field behaviour allowing identification of the correct phase. Obviously it was essential to allow time for the sample to reach thermal equilibrium before making the measurements.

The first isothermal scan was performed in the paramagnetic region, at 240K well away from the initial ordering transition. C_{33} increased continuously showing no unusual features.

At 223K, 1K above Tc, C_{33} (fig. 5.8) appears to harden as the field is applied indicating that a field of approximately 0.2T is adequate to produce short range alignment of the moments along the field direction. There is some hysteresis, but it is very small and may be attributed to the effect of the ordering on the domain structure. Coupling to α_{33} is very small.

The most dramatic results of the c-axis isothermal scans are those collected in the ferro-I region. On increasing the field C_{33} (fig. 5.9) hardens continuously in much the same way as it did just above Tc, however, as the field is decreased a hardening is observed from approximately 0.8T down. The attenuation data (fig. 5.10) is equally intriguing. On increasing the field there is a pronounced anomalous dip in α_{33} at 0.15T before it increases to 1.8dBcm^{-1}. On decreasing the field the attenuation reduces continuously. This behaviour is most unusual particularly because no thermal hysteresis was observed in the ferro-I region in zero field. In magnetic systems with a random component such as ferro-I the domain walls may be pinned (Natterman, 1991) thereby producing a possible mechanism for the damping of the ultrasound wave. While this proposal may go some way to explaining the hysteresis in C_{33} the unusual behaviour of the attenuation coefficient is more difficult to explain. The most likely explanation is that due to the application of the field, the ferro-I phase has been irreversibly destroyed. This new phase appears to be more ordered, hence the greater stiffness of C_{33} and the lower zero field value of α_{33}. The structure of any new phase arising from the destruction of ferro-I by a field is difficult to predict until the origins of ferro-I are more clearly understood. It is hoped that the data contained in this chapter may complement that taken at zero field and will provide evidence either in favour or against the models for ferro-I discussed in the previous chapter. A further discussion will be left to the end of this chapter.

At 219K, where the isofield measurements suggest that a canted ferro or some other intermediate phase exists between the HAF/cone phase and
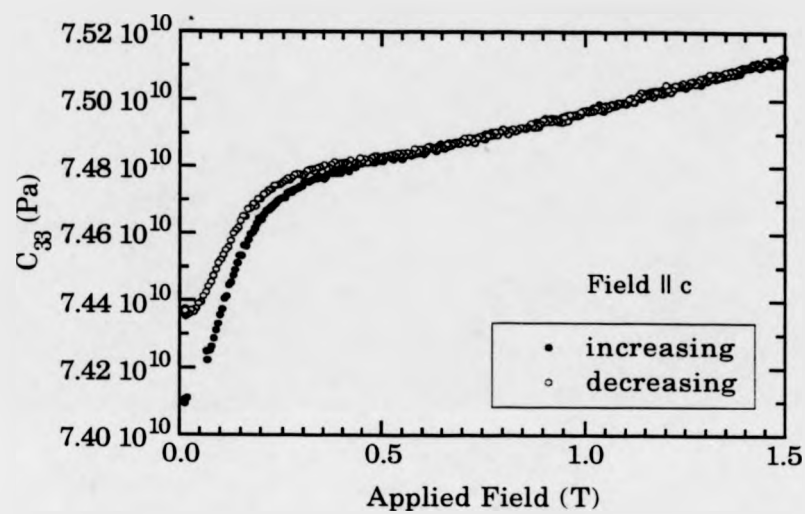
Fig. 5.8 C_{33} vs. applied field at 223K.

Figure 5.9 C_{33} vs Temperature at 221.5K, field applied along the c-axis.
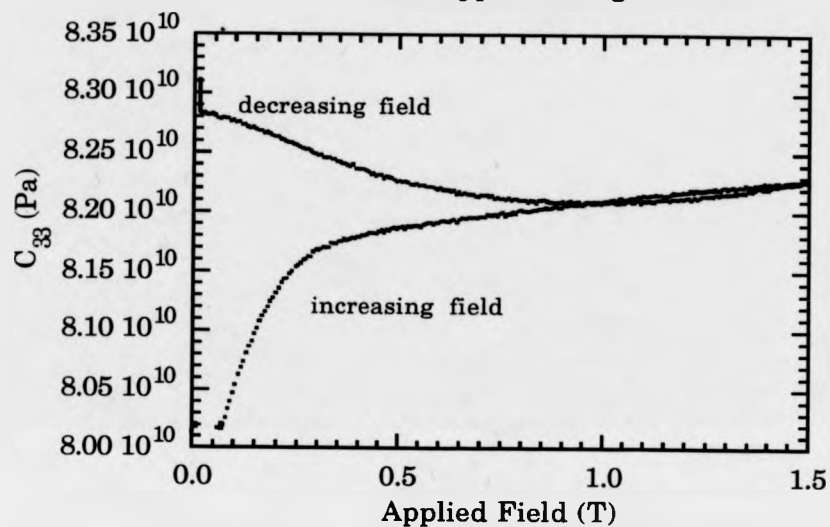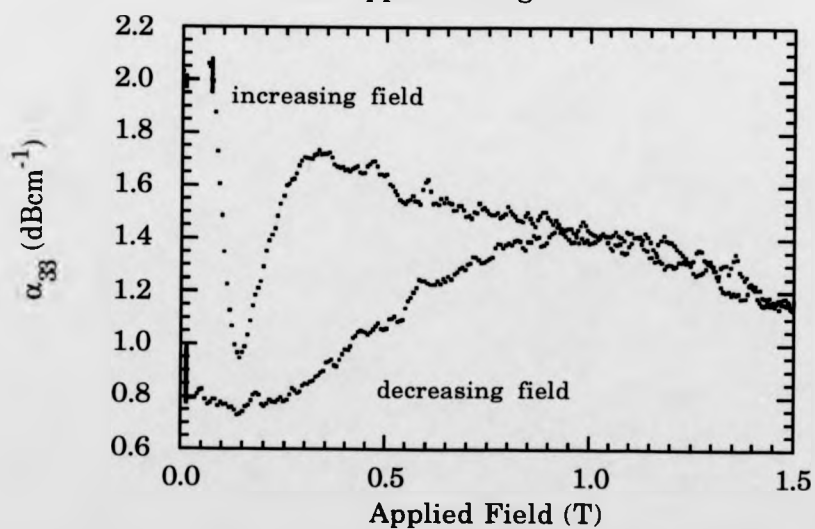

Figure 5.10 α_{33} vs. Temperature at 221.5K, field applied along the c-axis.

the c-axis ferro region, C_{33} (fig. 5.11) exhibits quite considerable hysteresis in the lower field region. The attenuation effects are all of small magnitude but reveal some interesting features (fig. 5.12). The peak associated with the transition to c-axis ferro occurs at 0.15T followed at 0.3T by a broader peak. As the field is increased from the remnant field of the magnet the attenuation rises steadily towards the critical peak, however, on decreasing the field from the c-axis ferro region the attenuation appears to rise between 0.1T and zero field, suggesting that the not only does the cone/HAF region exist between 0.1T and 0T, but that the c-axis ferro-HAF transition takes place via an intermediate ferromagnetic phase with a component in the basal plane. Striped chirality domains will be formed from the ferromagnetic domain walls as they are on warming from canted ferro in zero field and produce the increase in the attenuation.

When the sample is cooled to well within the canted ferro region and then warmed into the HAF region prior to the isothermal scan C_{33} (fig. 5.13) hardens as field is increased until the transition to c-axis ferro at approximately 0.25T whereafter C_{33} exhibits the convex hardening characteristic of the c-axis ferro structure. The attenuation (fig. 5.14) decreases continuously as the semi-cone angle of the cone decreases and the striped shaped chirality domains are destroyed. The small peak in α_{33} at 0.25T correponds to the canted ferro-c-axis ferro transition. On decreasing the field, a peak in α_{33} at 0.25T is the only evidence of the phase transition, since there is no basal plane component of the magnetisation in the ferro phase the HAF chirality domains are formed at random rather than as stripes perpendicular to the c-axis, consequently there is no marked increase in the attenuation on the formation of the cone/HAF phase.

In the canted ferromagnetic region at 200K the canted ferro/c-axis ferro transition exhibits a 2-magnon 1-phonon soft mode transition indicative of the cross over between two ordering mechanisms (fig. 5.15). The

97

Fig. 5.11 C_{33} vs. applied field at 219K, cooled from 240K.

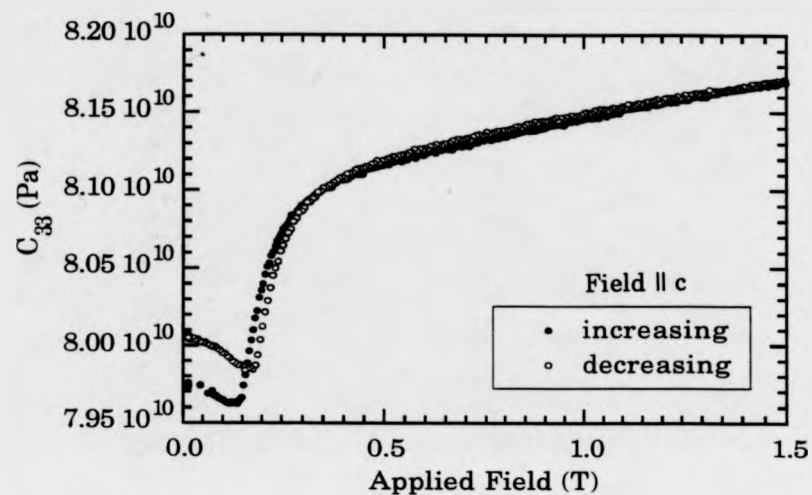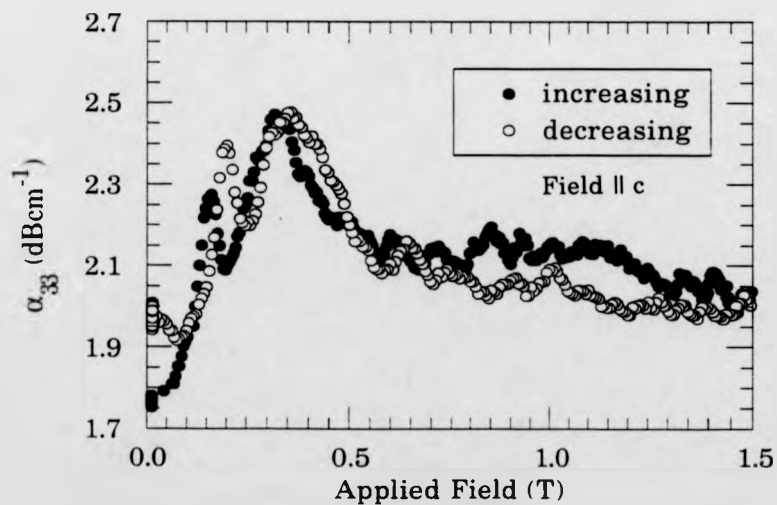Fig. 5.12 α_{33} vs. applied field at 219K, cooled from 240K.

Fig. 5.13 C_{33} vs. applied field at 215K, warmed from 200K.

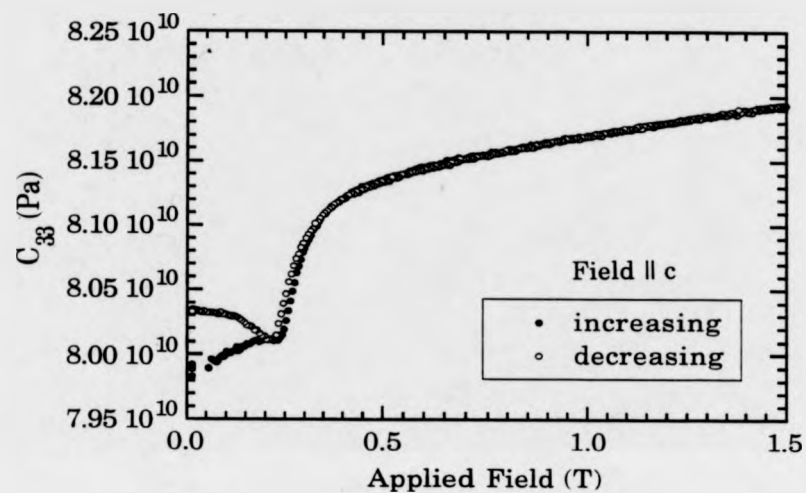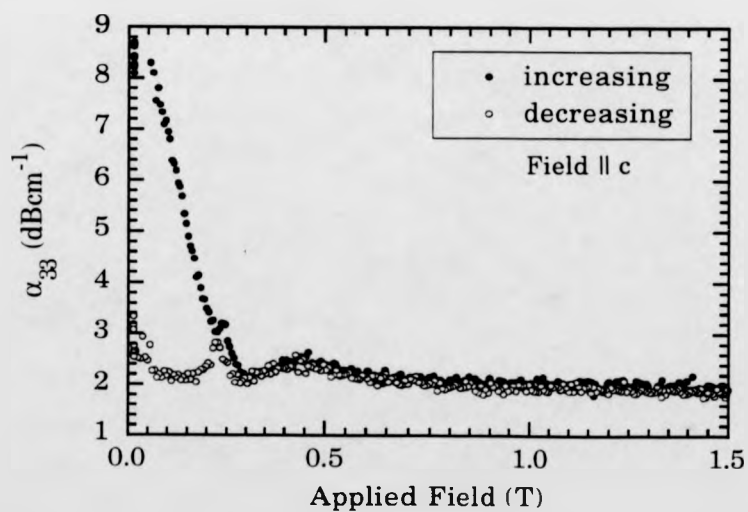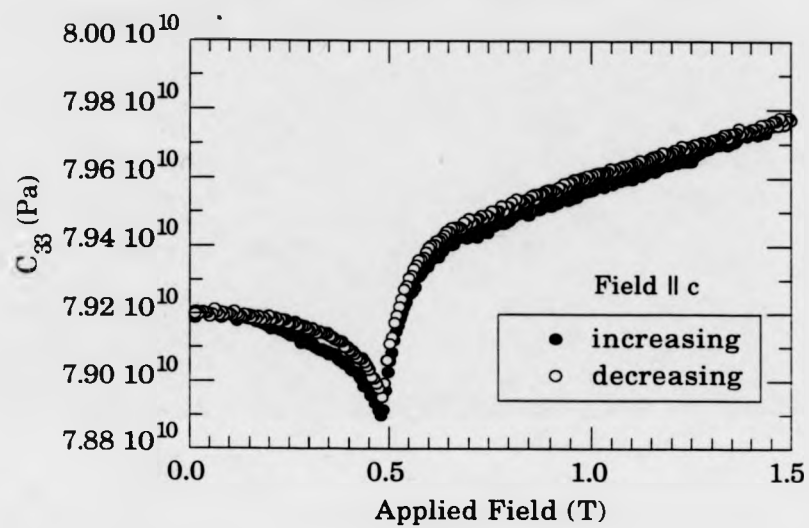Fig. 5.14 α_{33} vs. applied field at 215K warmed from 200K.

Fig. 5.15 C_{33} vs. applied field at 200K.

transition displays no appreciable hysteresis as a function of field. The attenuation displays no distinct features at the transition. An increase in the attenuation is observed at approximately 0.7T when the field is both increased and decreased. The affect is not mirrored in the elastic constant behaviour and may be caused by a change in the domain structure. The elastic constant appears to moderately harden on both sides of the transition when the field is reduced than when it is increased.

5.2.3 The Applied Field-Temperature Phase Diagram for a c-axis Field

In the absence of neutron diffraction data the phase diagram drawn from the ultrasound data is tentative and relies heavily on conjecture. However, the knowledge of the zero field behaviour of this system provides a good basis from which to interpret the applied field measurements.

The phase diagram (fig 5.16) is reasonably straight forward at lower temperatures, but is quite complicated in the region of multicriticality. The results suggest that the transition from HAF to cone is continuous, with the moments lifting up out of the basal plane. Isothermal measurements seem to support the domain model for the high attenuation in the HAF region. The transition from HAF to canted ferro as a function of temperature exhibits hysteresis of a similar order to that seen at zero field (approximately 2K), consequently this phase diagram is only correct for measurement made while warming. The canted ferro-c-axis ferro transition as a function of field has the characteristics of a cross over between two ordering mechanisms.

The intermediate phase which we tentatively refer to as canted ferro is difficult to identify definitively, but provides some insight into the complexity of the interactions which compete to produce the wide range of structures observed.
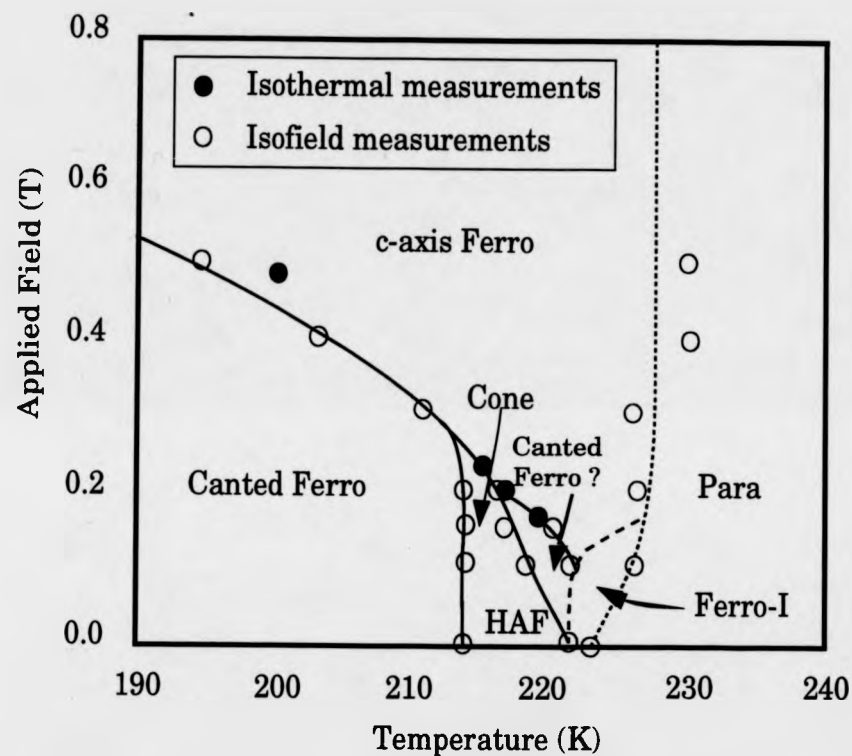
Fig. 5.16 Applied field-temperature phase diagram for Gd(76.0)Lu(24.0)
with the field applied parallel to the c-axis.

5.3 a-axis Field

Again only C_{33} and α_{33} have been measured in the investigation of the H-T phase diagram of $Gd_{76.0}Lu_{24.0}$ with a magnetic field applied along the a-axis. Both, isothermal and isofield measurements were performed, the same sample has been used and as mentioned earlier, demagnetisation corrections have not been made.

5.3.1 Isofield Measurements

The waterfall plot of the temperature dependence of α_{33} (temperature increasing) (fig. 5.17) provides a good overview of the effects of an a-axis field. The most striking feature is perhaps the thermal evolution of the ferro-I phase and evidence for the existence of an additional intermediate phase.

With a field of 0.025T applied along the a-axis the behaviour of C_{33} (fig.5.18) is very similar to that displayed at zero field. α_{33} (fig. 5.19), on the other hand, shows considerably more structure. The two peaks observed in zero field are still visible and in addition, a broad peak is observed at 225K suggesting that some ordering (probably short range) has developed above the nominal Tc.

On the warming α_{33} scan the high attenuation, characteristic of warming into the HAF region, appears to die away at approximately 217K suggesting that the region between 217K and 221K is not a helix, or at least, that the domain structure is different. The lack of any deviation from the zero field behaviour in this region for C_{33} would seem to suggest that the structure in this region is some derivative of the helix. The obvious

99
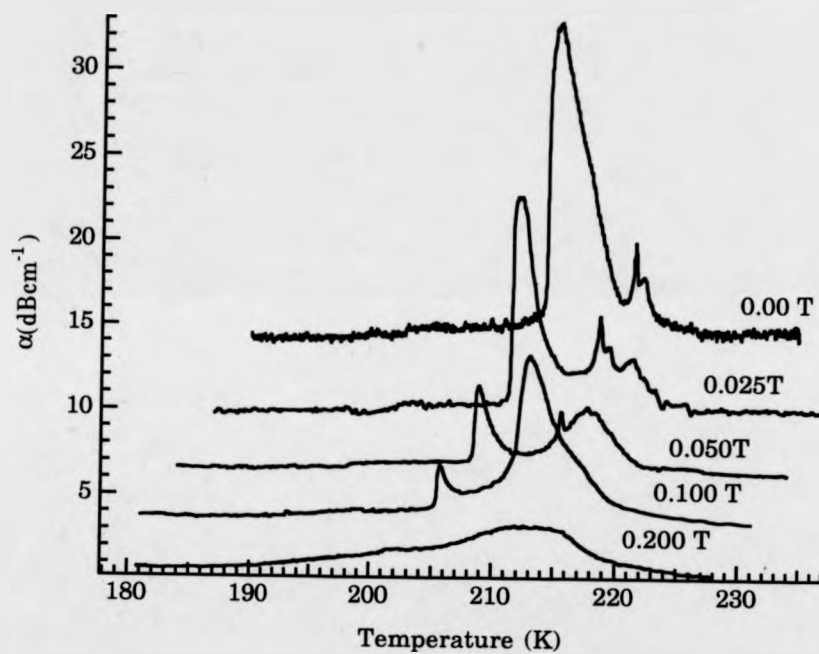
Figure 5.17 α_{33} vs. Temperature with increasing temperature for
        5 a-axis fields. The scales corrspond to the zero field
            measurements, succeeding measurements are are each
        offset by 3K and 3dBcm^{-1}.

Fig. 5.18 C33 vs. temperature with 0.025T applied parallel
to the a-axis. Data collected with increasing temperature.
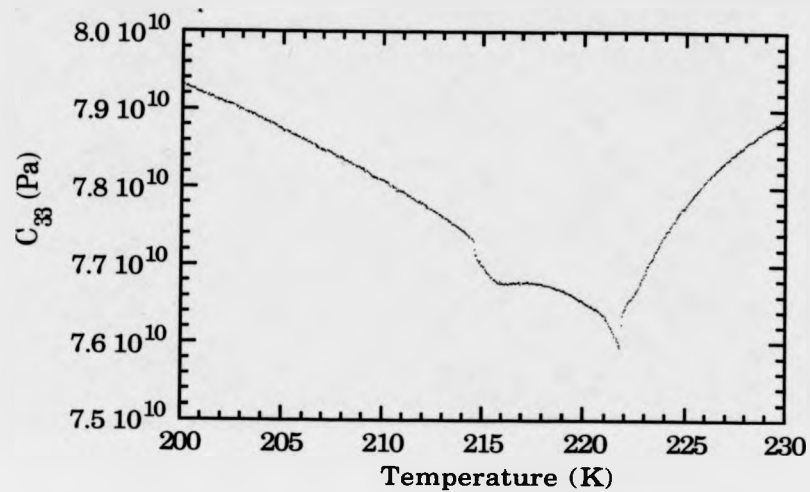
Fig. 5.19 α_{33} vs. temperature with 0.025T applied parallel to
the a-axis. Data collected with increasing temperature.

possibility is a distorted helix or fan phase, however, another perhaps more plausible alternative is that in this region both HAF and a-axis ferro domains co-exist in the manner observed in terbium by Baruchel et al (1988). Their neutron topographs showed that on applying a magnetic field in the basal plane in the helical region, a-axis ferro domains would start to grow out of the domain walls between chirality domains. These domains are assumed to be initially only a few atoms wide, but will be ferromagnetic. As the field increases the f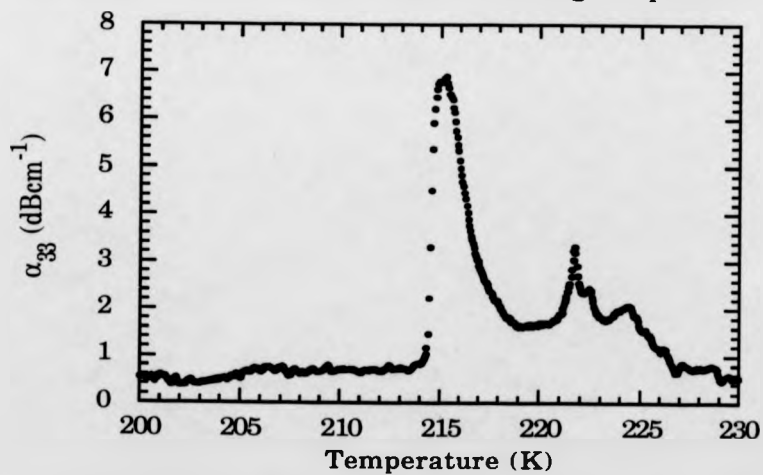erro regions grow forcing the HAF region to the edges of the sample as shown in figure 5.20. One could suppose that this process if more efficient when the domains have formed on warming from the canted ferro region, when the domain walls lie parallel to the field direction. Unfortunately, the absence of any evidence of this effect on the cooling data makes this point impossible to corroborate. A distorted helical phase will form domains in the same way as an undistorted helix, but will probably not have such a dramatic effect on the attenuation data. Domain structure in a fan phase will, however, be considerably different since there can be no such thing as a chirality domain for a fan structure and the concept of domain walls is more difficult to visualise. In the absence of any neutron scattering data, a fan structure cannot be ruled out in this region. The transition from helix to fan is believed to be first order (Cooper, 1968), and as such would probably cause a peak in α_{33}. Such a peak has not been observed.

When the field is increased to 0.05T (figs. 5.21 and 5.22) the region which we will tentatively refer to as undistorted helix, has been reduced to approximately 3K from 218K to 215K, with the intermediate phase growing at its expense. The three peaks observed at 0.025T in the ferro-I region have merged. However the lower temperature peak can be clearly resolved on both the warming and cooling data. Two peaks can just be made out on the warming data, the lower temperature peak corresponding to the inflection in C_{33} normally associated with the initial onset of ferro-I. The C_{33} data are,

Fig. 5.20 The growth of ferromagnetic domains in response to an
applied field along the a-axis.

Fig. 5. 21 C_{33} vs. temperature with 0.05T applied parallel to the a-axis. Data collected with increasing temperature.
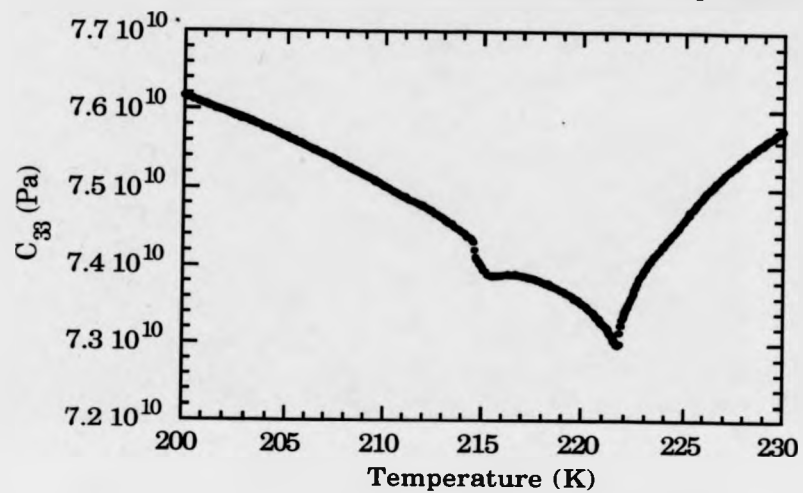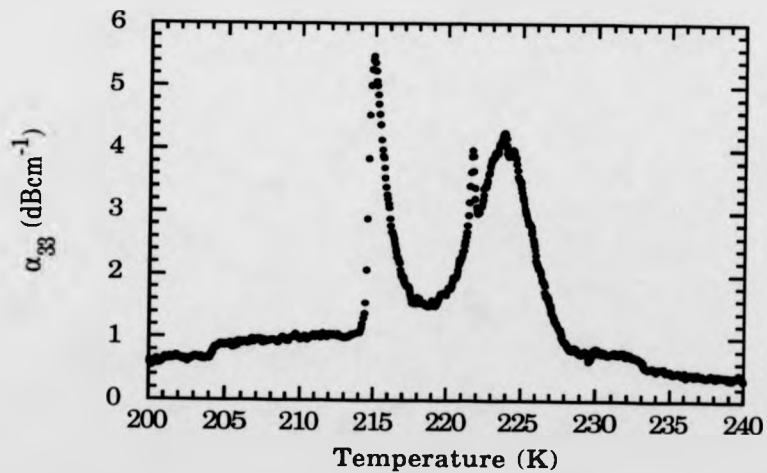

Fig. 5.22 α_{33} vs. temperature with 0.05T applied parallel to the a-axis data collected with increasing temperature.

again, very similar to those at zero field, however, the inflection appears to be slightly less distinct.

When the applied field is doubled again to 0.1T the effects on both C_{33} (fig.5.23) and α_{33} (5.24) are more dramatic. The peaks in the ferro-I region have become one single peak twice the size of its precursors suggesting that the field is causing the moments to fall away from the c-axis towards the basal plane. C_{33} will be softened throughout this process due to a linear coupling between the ultrasound wave and the magnons until the moments are in the basal plane when the coupling will disappear. The convex shape of C_{33} above Tc is somewhat distorted and along with the width of the peak in α_{33} suggest that some short range magnetic ordering has occurred as high as 227K. On both the warming and cooling data C_{33} exhibits a small plateau at approximately 221K. The undistorted helix has been reduced yet further.

With applied fields of 0.2T (fig. 5.25) and above the situation is much simplified, the broad dips in C_{33} and wide features in α_{33} seemingly heralding the transition from paramagnet to a-axis ferromagnet. As was the case with the field applied along the c-axis, the onset of long range order is difficult to identify. One feature that is striking is the fact that there appears to be no coupling to the canted ferro-a-axis ferro transition.

5.3.2 Isothermal Measurements

In the paramagnetic region at 240K the C_{33} becomes slightly softer as the field is increased and the disordered moments are drawn closer to the field direction.

Again, the most dramatic results are attained for measurements in the ferro-I region. The underlying shape in the C_{33} data (fig. 5.26) is that of a straightforward transition to an a-axis ferromagnet via a softmode

Fig. 5.23 C_{33} vs. temperature with 0.1T applied parallel to the a-axis. Data collected with increasing temperature.
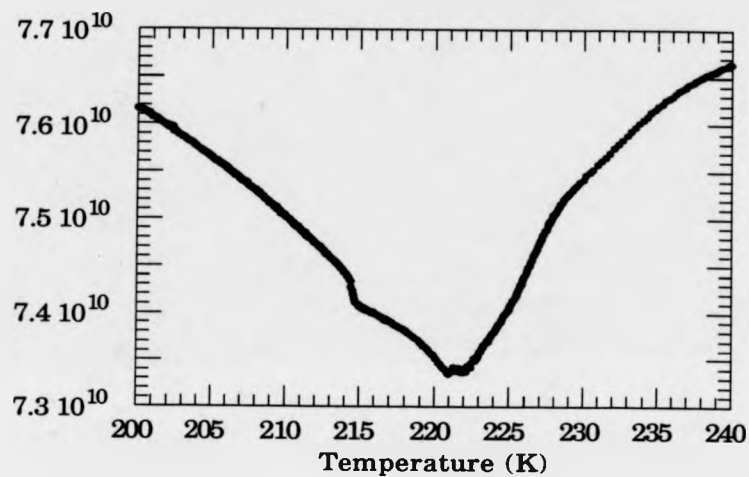

Fig. 5.24 α_{33} vs. temperature with 0.1T applied parallel to the a-axis. Data collected with increasing temperature.
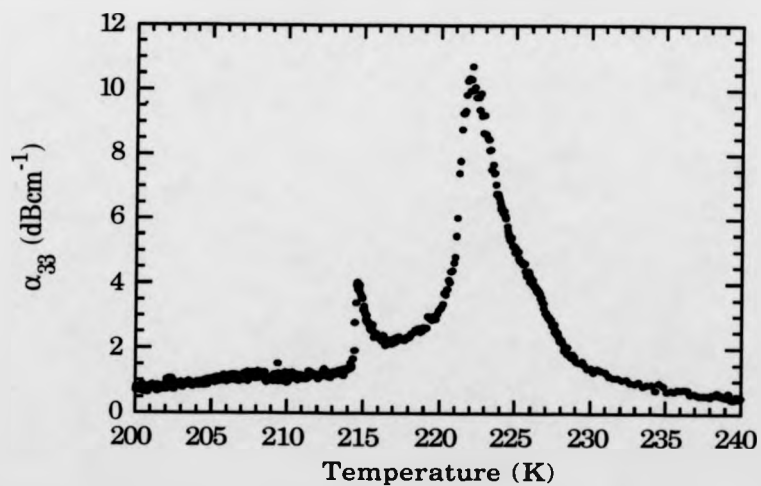
Fig 5.25 C_{33} vs. temperature with 0.2T applied parallel to the a-axis. Data collected with increasing temperature.
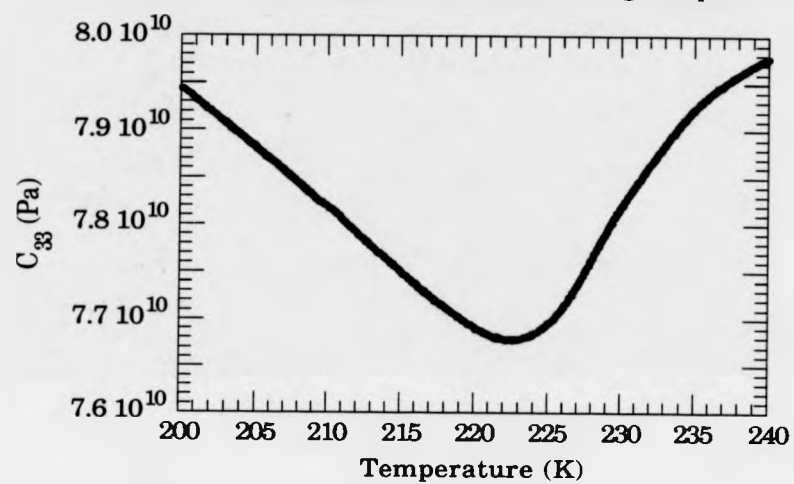
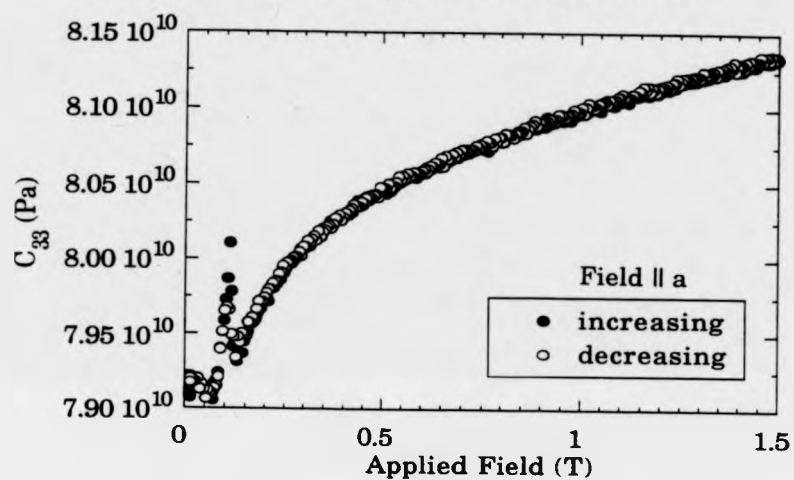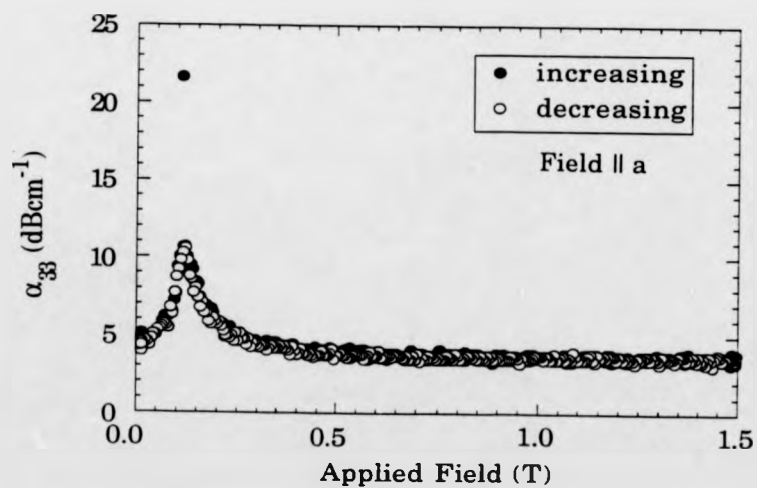Fig. 5.26 C_{33} vs applied field at 222K.

Fig. 5.27 α_{33} vs. applied field at 222K

transition. The change of the elastic constant in this transition compared to the canted ferro-a-axis ferro transition which will be discussed later bears testament to the softness of the ferro-I phase relative to the canted ferro phase. The peak in α_{33} (fig. 5.27) corresponds to this transition. However, a spike appears in C_{33} at 0.1T. The measurement has been repeated many times giving the same result. The behaviour is the same irrespective of thermal history and does not exhibit any appreciable hysteresis. The fact that the transition from ferro-I to a-axis ferromagnet is accompanied by a brief stiffening of the elastic constant is very difficult to explain and precedents in other data have been impossible to find. An initial explanation was that, due to the limited temperature range of the region, some crossing over from one phase to another may be responsible. Consequently, the same measurement was repeated on a crystal of $Gd_{70.2}Y_{29.8}$ which displays a ferro-I region stable over approximately 10K. The phase immediately below ferro-I in $Gd_{70.2}Y_{29.8}$ is not HAF as is the case in $Gd_{76.0}Lu_{24.0}$, but a canted ferromagnetic phase.

When the measurement was performed at 211K after the sample had been cooled from the paramagnetic region (figs. 5.28 and 5.29) the spike was not observed. The result is very similar to the underlying behaviour exhibited by the $Gd_{76.0}Lu_{24.0}$ data. However, when the measurement is repeated at a higher temperature, but still in the ferro-I region (figs. 5.30 and 5.31), a similar spike is observed albeit slightly broader. In this case the spike is also accompanied by a brief drop in the attenuation. The sample was then cooled into the canted ferromagnetic region, warmed back into the ferro-I region, and the measurement repeated. This time no spike was observed.

The obvious first explanation for the spike is that it is an artifact of the phase transition or is caused by a short lived intermediate phase. Domain effects are another possible cause, the onset of order removing some pinning

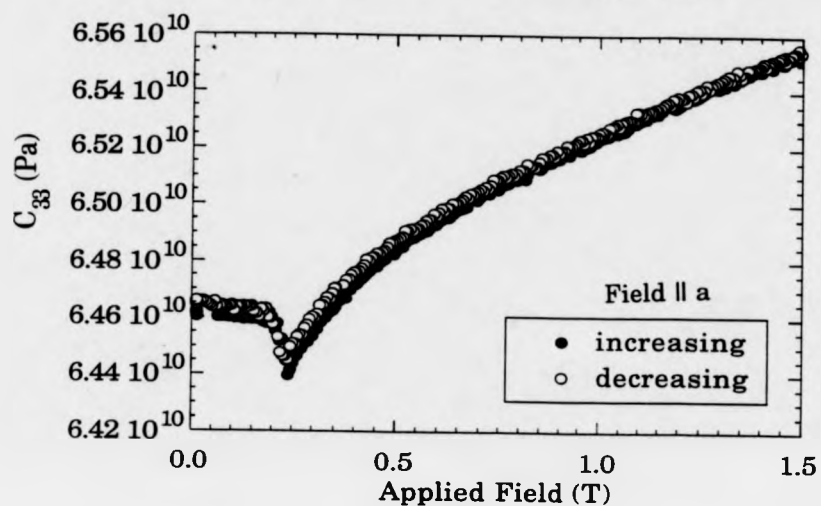Fig. 5.28 C_{33} vs. applied field for $Gd_{70.2}Y_{29.8}$ at 211K.

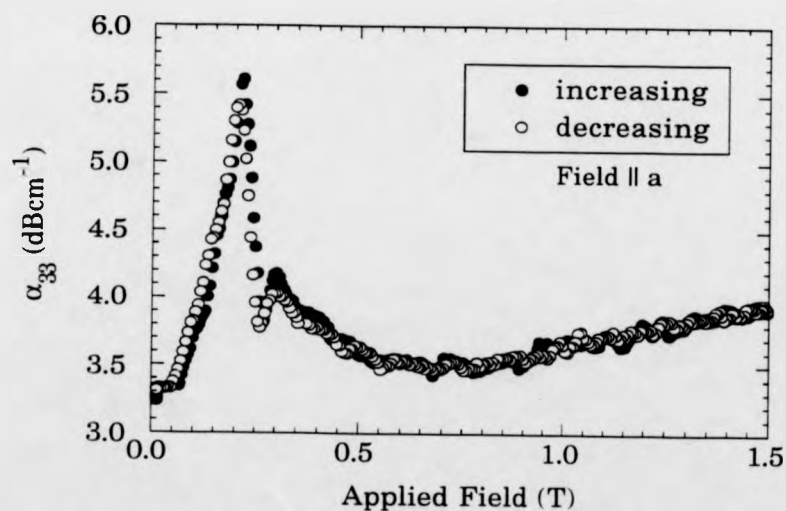Fig. 5.29 α_{33} vs. applied field for $Gd_{70.2}Lu_{29.8}$ at 211K.

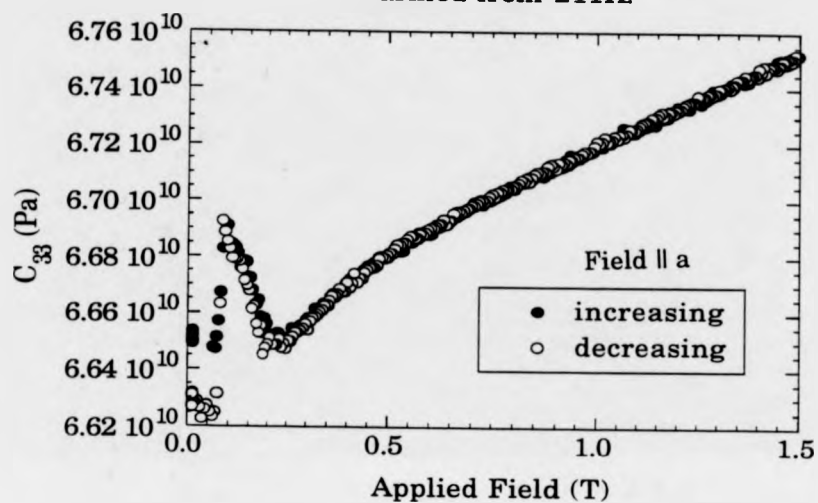Fig. 5.30 C_{33} vs. applied field for $Gd_{70.2}Y_{29.8}$ at 219K, warmed from 211K.

Fig. 5.31 α_{33} vs. applied field for Gd70.2Y29.8 at 219K, warmed from 211K.
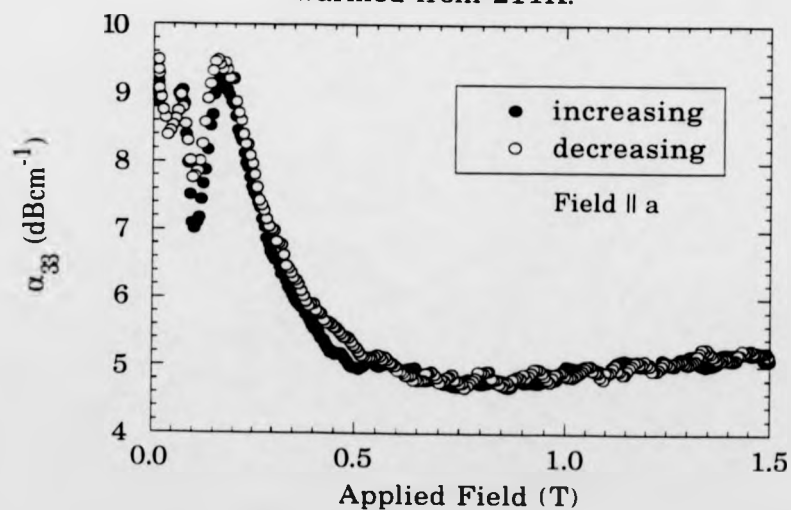
from the domain walls and reducing the damping from the ultrasound wave. This explanation would also account for the dip in the attenuation observed in the Gd-Y sample. However, it fails on the existence of the spike on the decreasing scan when the transition is supposedly from an ordered structure, and raises the prospect of the domains relaxing into a strained state. Fermi surface effects are worthy of consideration (Jensen, 1991) however, the energy corresponding to a field of 0.1T is 0.04meV and would be expected to be smeared out by thermal effects at such high temperatures. At present this effect is not understood.

Isothermal scans in the HAF region underline the effects of chirality domains on the ultrasound wave, but also provide corroborating evidence for the intermediate phase proposed in the previous section. On cooling into the HAF region from the paramagnetic phase the ultrasound signal is strong. As the field is increased the behaviour of C_{33} (fig. 5.32) indicates that the transition to a-axis ferromagnet occurs at 0.2T. The transition is accompanied by a small broad peak in α_{33} (fig. 5.33). On decreasing the field C_{33} appears to be softer below the transition than it was on increasing the field. However, it is not until the field has been reduced to 0.05T that the attenuation rises sharply to the levels that would be expected if the striped domain structure had been assumed. On decreasing the field α_{33} exhibits the same peak at 0.2T which identified the transition. These data would support the hypothesis that the intermediate phase comprises a co-existence of ferro and HAF domains as described earlier.

At 200K the isothermal data (fig. 5.34) indicates that the coupling of the ultrasound wave is very similar for the canted ferro and the a-axis ferro phases. This is not surprising in view of the high cant angle (60°). The start of the convex increase in C_{33} at 0.3T is assumed to be the transition from canted ferromagnet to a-axis ferromagnet. There is no coupling of this transition to α_{33}.

103

Fig. 5.32 C_{33} vs. applied field at 216K cooled from 240K.
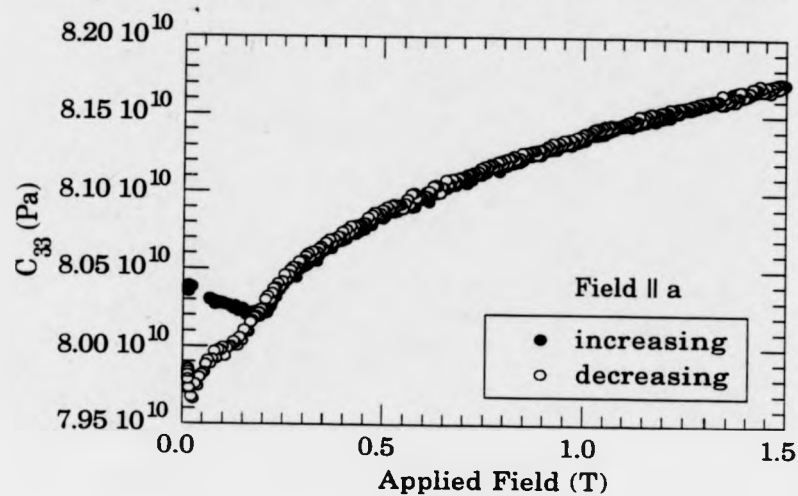
Fig. 5.33 α_{33} vs applied field at 216K cooled from 240K.
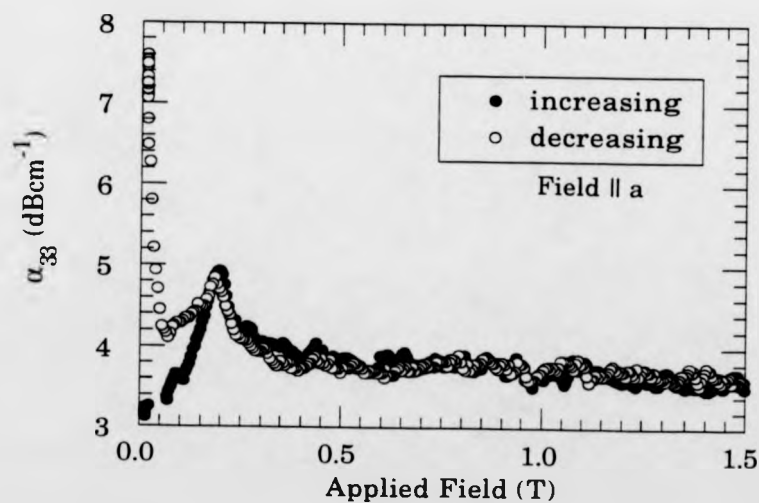
Fig. 5.34 C_{33} vs. applied field at 200K
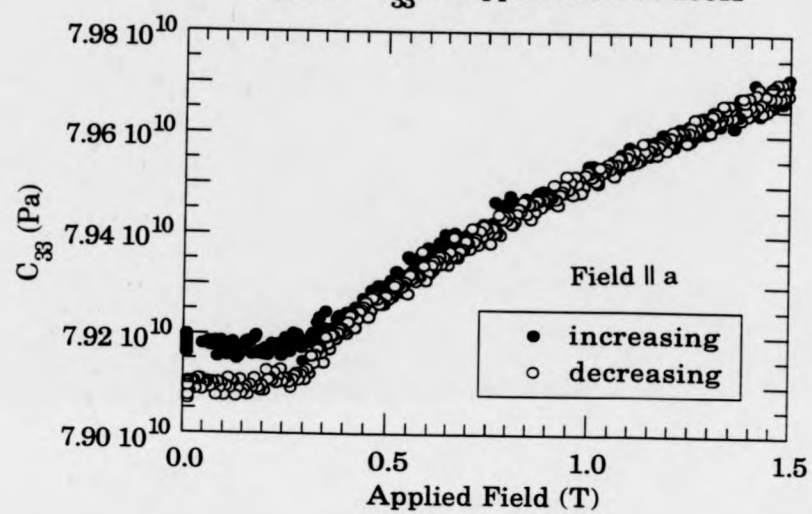
5.3.3 The Applied Field-Temperature Phase Diagram for an a-axis Field.

On the basis of these data the phase diagram (fig5.35) has been constructed. The outstanding problems are the nature of the transitions from the ferro-I phase, and the structure of the intermediate phase.

The data collected in a constant field shows complex behaviour in the initial ordering region. Short range order above Tc couples to α_{33} producing peaks above that originally associated with the onset of ferro-I. The behaviour of the ferro-I structure itself is very difficult to determine. The appearance of the spike in the isothermal measurement of α_{33} has still to be properly explained.

At present, in the absence of neutron scattering data, the most plausible explanation of the ultrasound data is that the intermediate region features a co-existence of ferro and HAF domains. This is especially true with such a large cubic crystal where the internal field is very unlikely to be uniform throughout the sample.

5.4 Discussion and Conclusions.

Both applied field-temperature phase diagrams presented here show several unusual features which are worthy of further investigation using both neutron scattering and ultrasound techniques. The use of other probes such as resistivity, magnetoresistance and specific heat could also be usefully employed in acquiring a more thorough understanding of these systems. However in view of the small temperature ranges of the HAF and ferro-I regions, such studies would be more fruitful on Gd-Y samples which
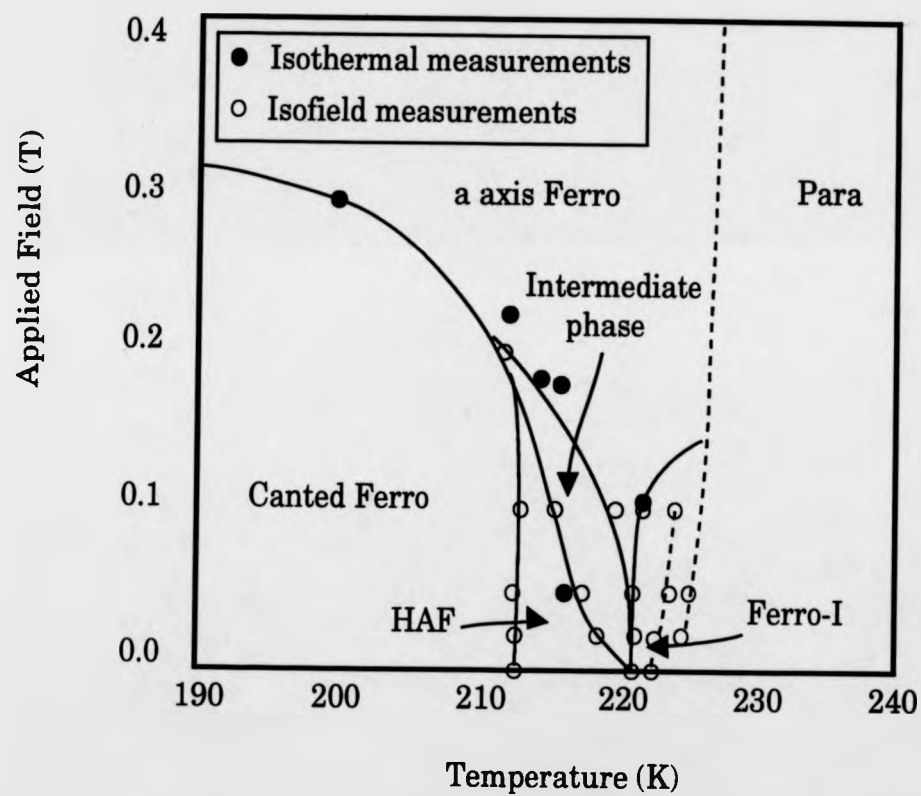
Fig. 5.35 The applied field-temperature phase diagram of
Gd(76.0)Lu(24.0) with the field applied parallel to the a-axis.

exhibit very similar behaviour, but display both the phases mentioned above over larger temperature ranges permitting more exhaustive investigations.

The canted ferromagnetic phase was shown to re-orient into an a-axis ferromagnet continuously on the application of an a-axis field. When the field is applied along the c-axis, however, the data suggested that the transition from canted ferro to c-axis ferro was abrupt, and brought about by a cross over between ordering mechanisms.

The canted ferromagnetic structure is stabilised by two ion anisotropy arising from the spin-orbit coupling of the conduction electrons. The anisotropy which brings about the canted ferromagnetic structure has its origins in the dipole-dipole interaction, and only occurs in HCP structures when the c/a ratio is not ideal. Consequently, the application of a c-axis stress may well induce a phase change from the canted ferro structure to the c-axis ferro structure. Indeed Forgan (1991) has shown that the application of a c-axis stress does induce some very interesting effects, and appears to "make rare earths lighter". Ultrasound and neutron scattering experiments performed as a function of pressure may provide some insight into the competition between the two anisotropies.

The existence of a canted ferromagnetic phase above the HAF phase is very difficult to justify and requires corroboration by other probes. Its presence would, however, provide some indication of the delicate balance between competing interactions which exist in the multicritical region. Again measurements performed on a stressed sample, or as a function of stress may be very enlightening.

The existence of a fan phase in the Gd-Lu system is unlikely, all the data to date point to a phase co-existence. It is not clear why this phase should exist above the HAF phase, but the shape and the position of the phase is reminiscent of the phases in Gd-Sc originally thought to be fan phases, but now thought to be made up of HAF and ferro domains in co-existence. The

105

phase co-existence model would seem to be in good agreement with the zero field behaviour.

The unusual ultrasound results presented in this chapter and the agreement between the measurements performed on $Gd_{76.0}Lu_{24.0}$ and $Gd_{70.2}Y_{29.8}$ provide a strong case for the presence of ferro-I in the multicritical region of Gd-Lu.

The ferro-I phase continues to pose several unanswered questions. There is little doubt from this work and previous measurements on Gd-Y that ferro-I is completely de-coupled from both the canted ferro and HAF phases. Of all the models considered for the phase, the two most plausible remain the ferro cone model (Legvold et al,1980), in which the moments all adopt the same cant angle without a preferred orientation within the basal plane and the competing interactions model of Bates (1985). The latter suggests that, due to the statistical distribution of Gd ion throughout the lattice, some will be predominantly influenced by the long range interaction, while other will be influenced by short range interactions (nearest neighbours). In the ferro-I phase, only those sites influenced by the short range interaction will order, the long range interaction being destroyed by thermal fluctuations.

Both models may be used to explain the unusual data presented here in a qualitative manner, the common thread being the disordered component which may be the cause of the spike in the a-axis data and the hysteresis in the c-axis data. Ultimately the ultrasound data can only delineate phases and indicate regions of interest. Conjecture can only be removed by performing a thorough neutron scattering experiment. A proposal for such an experiment at the I.L.L. had been accepted, but the shut down of the reactor occurred several weeks before the scheduled date.

References

Baruchel J., Sandonis J., Pearce A.s., Phil. Mag. B57 505 (1988).

Bessa Sousa J., Moriera J.M., Personal Communication (1991).

Cooper B.R., Solid State Phys. 21 303 (1968).

Cowley R.A. et al., to be published in Europhys, Letts. (1991).

Forgan E.M., Lee S. ICM91 to be published in J. Magn. Magn Mats. (1991).

Jensen J., Mackintosh A.R., Phys. Rev. Letts. 64 22 2699 (1990).

Jensen J., Personal Communication (1991).

Legvold S., Burgadt P., Beaudry B.J., Phys. rev. B22(5) 2573 (1980).

Melville R.J., Eccleston R.S., Palmer S.B., Vrtis M.L., ILL Experimental
   Report 5-33 (1989).

Melville R.J., PhD Thesis, University of Warwick (1989).

Natterman T., ICM91 to be published in J. Magn. Magn. Mats. (1991).

Chapter 6

Spin-Slip Structures in Erbium and Holmium-Erbium

Introduction

As stated in chapter 1, the wide range of structures exhibited by the rare earth elements and their alloys arise as a result of competition between three principle magnetic interactions. These interactions being the long range exchange interaction which favours long range modulated structures, the magneto-crystalline anisotropy, which favours structures in which the moments are aligned along crystallographic directions, and the magnetoelastic energy which is only important at lower temperatures and may transform antiferromagnetic structures to ferromagnetic structures and stabilise ferromagnetic structures. In the case of the erbium and holmium-erbium alloys the interplay between these three interactions results in a variety of complex magnetic structures. In the first half of this chapter, the magnetic structure of Er is considered in the light of ultrasound and neutron scattering results. Later, the magnetic structure of the random alloy $Ho_{90}Er_{10}$ is discussed.

6.1 Erbium

6.1.1 Review of Previous Work

Three principle phases of magnetic order have been identified by neutron diffraction (Cable, 1965, Atoji 1974, Habenschuss 1974). Below the Néel point ($T_n = 85K$) the magnetic moment is confined to the c-axis and is sinusoidally modulated with a propagation vector of between 7 and 8 atomic layers. At approximately 52K a basal plane moment develops which is modulated with the same propagation vector as the c-axis modulation. Higher order scattering peaks have been observed up to the 17th order at approximately 22K attributed to a gradual "squaring up" of the modulation towards an 8 layer structure with four layers with moment pointing down, four layers with moments pointing up and so on. Below 18K the c-axis becomes ferromagnetic resulting in a cone structure with a propagation vector $\mathbf{q} = \dfrac{5}{21}$.

It is the intermediate phase which has proved to be the most difficult to characterise. Miwa and Yoshida (1961) proposed a structure where the basal plane components of the moments trace out an ellipse. Cable (1965) argued that because of the unimportance of the basal plane anisotropy this structure was not possible, and favoured a structure where the ellipse was tilted out of the basal plane, a theory which was elucidated by Sherrington (1973). The most promising model for the structure of the intermediate phase has been proposed by Jensen (1976) developing, to some extent, from his earlier study of the low temperature phase (1974).

The lock-in value of the $\mathbf{q}$ vector ($\mathbf{q} = \dfrac{5}{21}$) in the ferro-cone phase is not commensurate with the crystal lattice. Jensen (1974) attributed this to the

109

importance of the isotropic part of the long range exchange interaction which is caused by various orbital effects including spin orbital coupling of the conduction electrons, electric multipole interactions and the influence of the ionic orbital moment on the spin exchange matrix elements (Levy, 1969). Jensens' calculations are corroborated by the spin wave data of Nicklow et al (1971).

By extending this discussion to the intermediate phase and using a molecular field approximation, Jensen developed a model in which the moments trace out an ellipse perpendicular to the basal plane when they are drawn to a common origin (figure 6.1). The basal plane moments are clamped to the c-axis moments in such a way that the basal plane moment is a maximum when the c-axis moment is a minimum and vice versa. This model seems to be in good agreement with the neutron diffraction data of Habenschuss (1974).

More recently Gibbs et al (1986) have studied the intermediate phase using magnetic X-ray scattering, and have proposed a spin-slip model for the c-axis components of the magnetisation. As the q-vector decreases from a seven layer to an eight layer structure the structure has commensurate regions corresponding to different arrangements of blocks of four (quartets) and three (triplets) atomic layers. For instance, at approximately 48K when $\mathbf{q}$ corresponds to a 7 layer structure the c-axis moments will assume a structure with one quartet with c-axis moments aligned parallel to the c-axis followed by one triplet with the moments aligned antiparallel. For $\mathbf{q} = \frac{3}{11}$ a structure with 2 quartets per triplet will be assumed and so on. As $\mathbf{q}$ decreases commensurate phases will be encountered with an integer ratio of quartets to triplets until $\mathbf{q} = 0.25$ (the squared-up structure) whereupon the
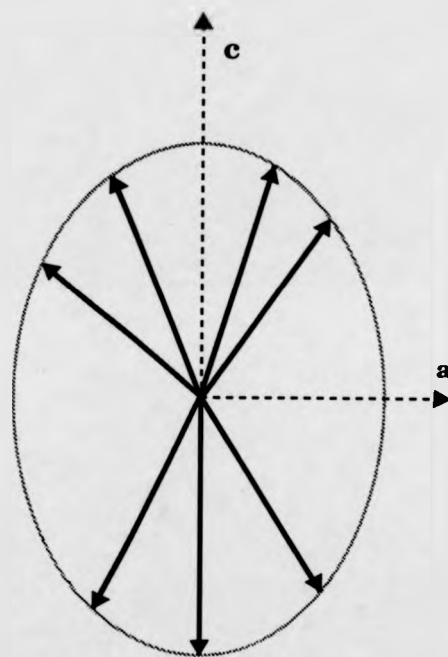
Fig. 6.1 The magnetic structure of Er at 48K q=2/7, b=7
(after Jensen 1991).

structure is simply made up of alternating quartets. The $q=\frac{3}{11}$ structure is shown in figure 6.2 by way of an example.

Gibbs data showed that at several of these commensurate structures the q-vector would lock-in to the same value for temperature ranges of 2 or 3K, reminiscent of a Devils' staircase (Bak, 1982). In total Gibbs et al identified six commensurate structures between 52K and 18K with the following q values (in the order in which they appear on cooling from 52K) $\frac{2}{7}$, $\frac{3}{11}$, $\frac{4}{15}$, $\frac{5}{19}$, $\frac{6}{23}$, and $\frac{1}{4}$. Of these the $\frac{2}{7}$, the $\frac{4}{15}$ and the $\frac{6}{23}$ structures display a net ferromagnetic moment and were seen to exist over the temperature ranges 51.6-48.5K, 34.5-31.5K and 26.5-23K respectively. The $q = \frac{1}{4}$ structure appeared to exist from 23K down to 18K.

Because essentially, the existence of a triplet represents a missing moment, when there is an odd number of quartets to each triplet the directions of the missing moment will be coincident and a net ferromagnetic (strictly ferrimagnetic) moment will exist. Clearly if there are an even number of quartets per triplet the net magnetisation will be antiferromagnetic.

In order to understand the diffraction data more clearly it may be useful to visualise the structure in terms of a spin-slip or soliton model as proposed by Vigren (1976) and successfully applied to holmium by Gibbs (1985) and extended by Cowley and Bates (1988).

For the sake of simplicity we will discuss the case of the $q=\frac{3}{11}$ structure ignoring the existence of a basal plane component of the magnetisation (refer to figure 6.3). The 2 quartets per triplet structure arises as a compromise between the long range exchange interaction which prefers the pure sinusoidal modulation of the moment and the high axial anisotropy which "squares-up" the modulation of the moment. The ideal

↓
↓
↓   1 Quartet
↓

↑
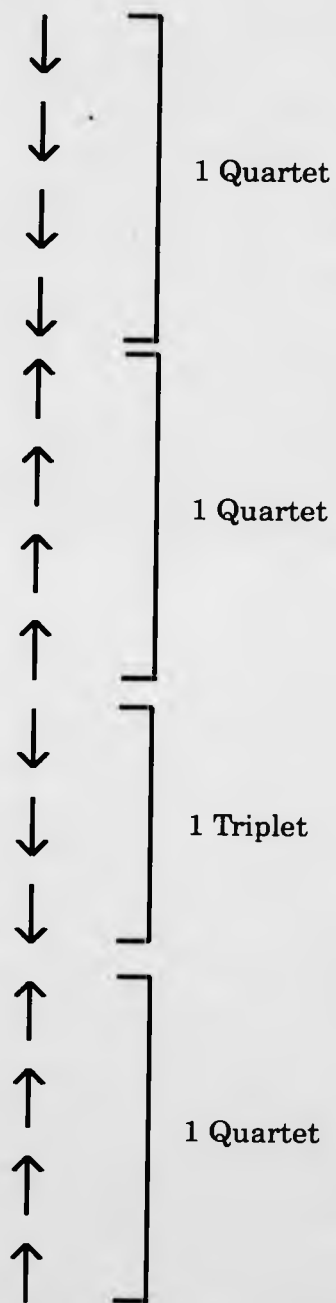↑   1 Quartet
↑
↑

↓
↓   1 Triplet
↓

↑
↑
↑   1 Quartet
↑

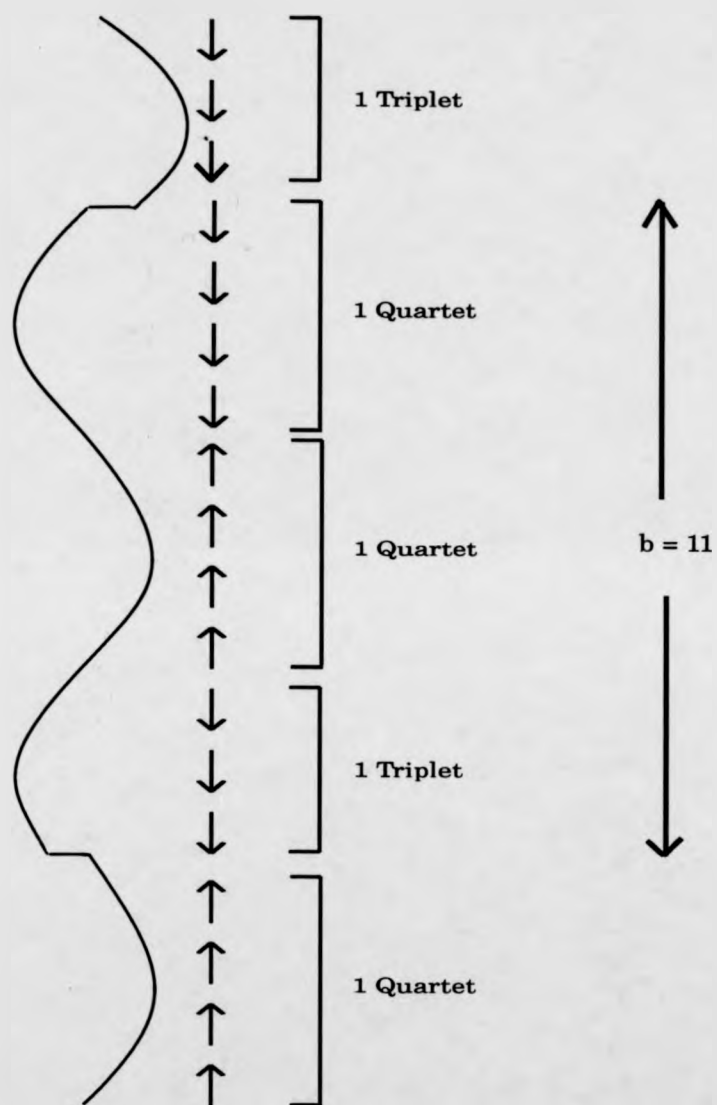Fig. 6.2 Two quartets per triplet making up the q= 3/11, structure

Fig. 6.3 Two quartets per triplet making up the q= 3/11, structure, charcterised by a spin-slip distance b.

value of $\mathbf{q}$ from the point of view the axial anisotropy is $\frac{1}{4}$ that of the squared up structure, and in the regions of the c-axis made up only of quartets this is the value which the structure will assume, however, the difference between this value and the value of $\mathbf{q}$ dictated by the long range interaction ($\frac{3}{11}$) is made up by the omission of one atomic layer from one quartet in three ie. the formation of a triplet. Thus we can consider a triplet as being a step in the pure squared up modulation and we can use three parameters to characterise the structure; $\mathbf{q}$ which is the average propagation vector, $\mathbf{q}_0$ the commensurate propagation vector and b the spin-slip distance, which is the number of atomic layers between steps in the pure $\mathbf{q}{=}\frac{1}{4}$ modulation. For the $\mathbf{q}{=}\frac{3}{11}$ case for example, b=11.

The commensurate structures which may be assumed as $\mathbf{q}$ evolves are tabulated (table 6.1) with the corresponding values of b. The b=13 structure was first proposed by Cowley (1991). The X-ray scattering data of Gibbs et al displays locking in of q at b=7, b=15 and b=23 structures which exhibit a net ferromagnetic moment. This model has been supported by the observation of anomalies in other properties of Er single crystals.

The magnetisation data of Burger et al. (1986) displays anomalies at 27K and 33K in good agreement with the temperature at which Gibbs and co-workers observed lock-ins. Habenschuss et al (1974) observed inflections in the evolution of q in their neutron diffraction data at approximately 33K and 23K. Specific heat measurements (Schmitzer, 1987) only display anomalies at 22K (these measurements were made on increasing temperature and thermal hysteresis accounts for temperature discrepancies). Åstrom and co-workers (1989) observed anomalies in their calometric measurements at 21.6K, 23.3K, 25.3K and 50.8K, however, when they made AC susceptibility measurements on the same sample anomalies

Propagation Vector q	Spin-slip distance, b	Repeat Pattern	Ferro/ Antiferro
2/7	7	4,3	Ferro
3/11	11	4,4,3	Antiferro
7/26	13	4,4,4,3,4,4,3	Antiferro
4/15	15	4,4,4,3	Ferro
5/19	19	4,4,4,4,3	Antiferro
6/23	23	4,4,4,4,4,3	Ferro

Table 6.1 Commensurate Structures of Erbium.

were only observed at 28K and 34K other than the features corresponding to the principle phase transitions (Åstrom, 1990). AC susceptibility measurements were also performed by Ali and Willis (1990) who observed distinct peaks at 51K, 34K and 27K. In addition they measured the magnetisation and observed anomalies at the same temperatures, and weaker anomalies at 40K (the b=11 structure) and 29K (the b=19 structure).

6.1.2 Ultrasound Results

The four single crystal elastic constant C_{33}, C_{44}, C_{11} and C_{66} and their associated attenuation coefficients have been measured in the temperature range 100 to 10K.

The crystal used for this study was cut from a boule grown for Professor Bill Stirling in the Department of Metallurgy and Materials at the University of Birmingham by Dr D.Fort. The crystal has dimensions (4.3 x 5.3 x 4.6)mm and is believed to have a purity of approximately 99.99%. Unfortunately one corner of the cube is shaved off, consequently ultrasound measurements along the b direction are not possible.

The C_{33} elastic constant (fig. 6.4), corresponding to a longitudinal wave propagating along the c-axis, display step-like discontinuities at the three principal phase transitions. The magnitude of the softening accompanying the transitions at 85K and 52K are of a similar magnitude to that observed in previous measurements (Jiles, 1981, du Plessis, 1976) however, the softening at the transition to ferro-cone of approximately 5% is slightly deeper than that of 4% observed by Jiles and 2.5% observed by du
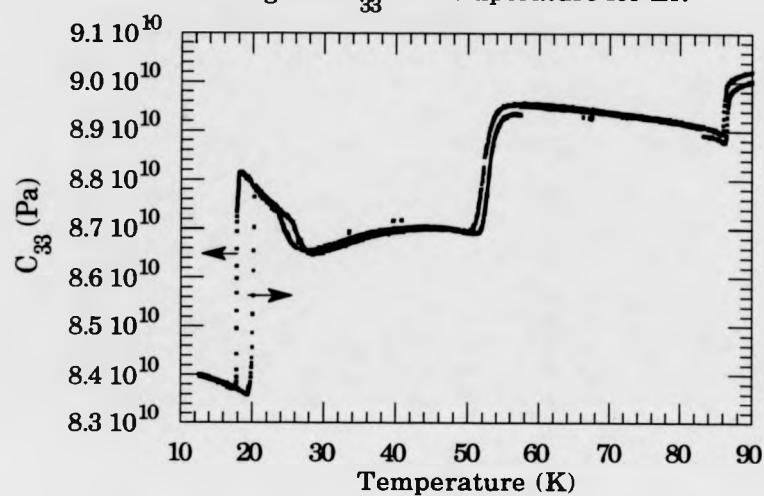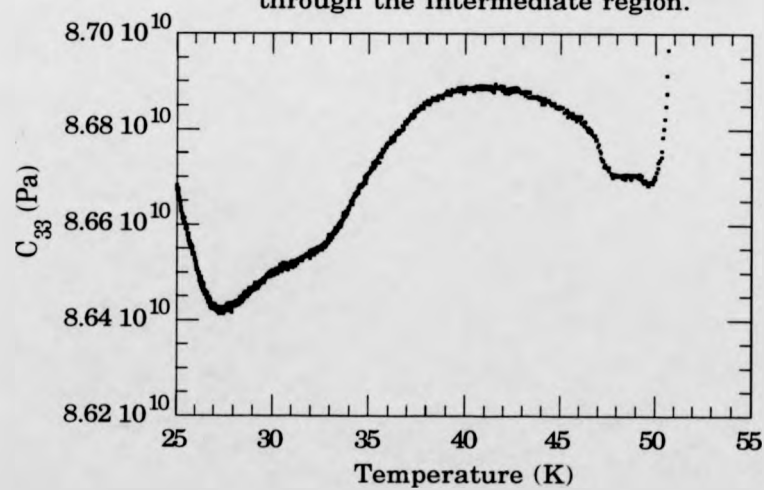
Fig. 6.4 C_{33} vs. temperature for Er.

Fig. 6.5 C_{33} vs. temperature, cooling at 0.05Ks^{-1} through the intermediate region.

Plessis. The hysteresis in the transition temperature is in good agreement with the neutron data of Habenschuss (1974).

A distinct change in the gradient is observed at 24K which may be attributed to the lock-in to the squared-up structure or the formation of the b=23 structure. In contrast, Jiles's measurements show a softening of the elastic constant above the transition to the ferro-cone structure.

A closer inspection of the intermediate region using the slowest cooling speed (0.05 Ks^{-1}) (fig. 6.5) reveals inflections at 48K and 33K, possibly associated with the b=7 and b=15 structures respectively. The hardening of C_{33} commencing at approximately 27K may be attributed to the gradual squaring up of the structure or to the formation of the b=23 structure.

The attenuation coefficient displays critical behaviour at the three principal transitions, but shows no interesting features in the intermediate phase.

The C_{44} elastic constant may be calculated from the velocity of two supposedly equivalent modes, either a shear wave propagating along the c-axis polarised in the basal plane or a shear wave propagating across the basal plane polarised along the c-axis. However both modes were measured and some discrepancies between the two have been observed. The elastic constant behaviour (figs. 6.6 and 6.7) appears to be very similar for both modes, showing small inflections at T_N and the onset of basal plane order. A small anomaly is visible at 24K before the echo train dies away completely at 22K for the b polarised mode and 21K for the c polarised mode making further measurements impossible. At high temperature the corresponding attenuation coefficients (figs. 6.8 and 6.9) are very similar, neither couple to the phase transitions at 52K and 85K. However, a sharp, well defined peak in the attenuation is observed on the c polarised mode followed by a steep

114

Fig. 6.6 C_{44}, corresponding to a shear wave propagated along b, polarised parallel to c, vs. temperature for Er (cooling).
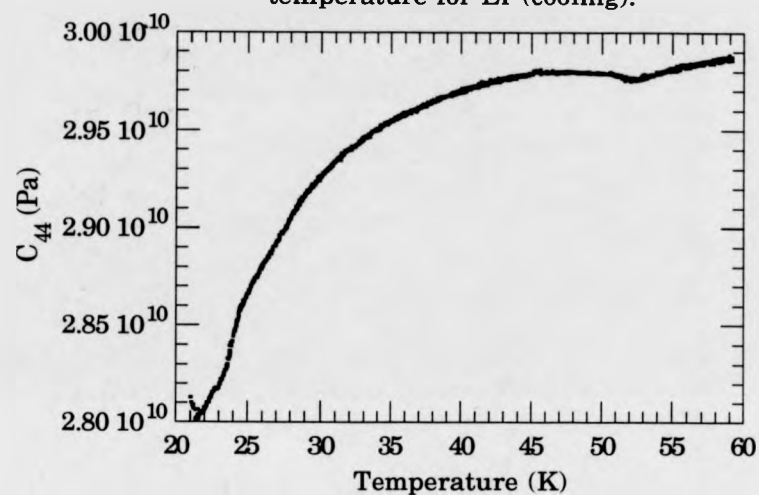

Fig. 6.7 C_{44}, corresponding to a shear wave propagated along c, vs. temperature for Er. Data collected with decreasing temperature.
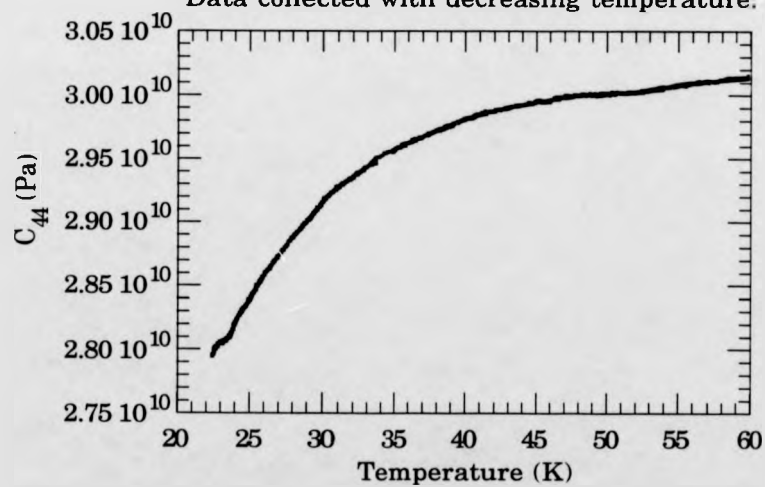
Fig. 6.8 α_{44} vs. temperature for Er (cooling).
Shear wave propagated along b polarised along c
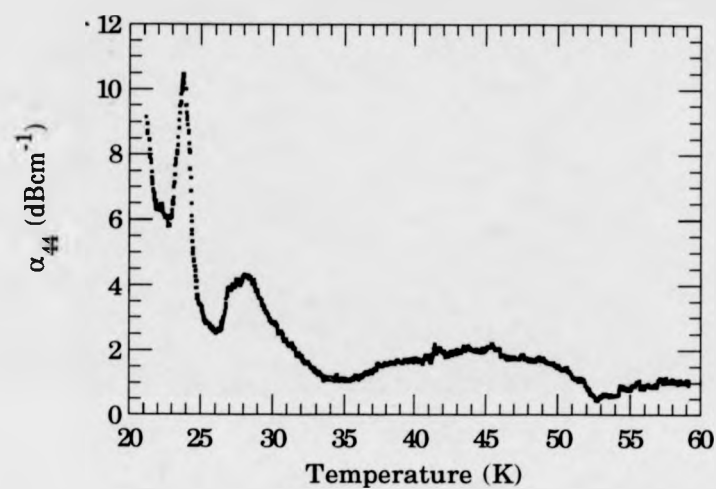
Fig. 6.9 α_{44} vs. temperature for Er (cooling).
Shear wave propagated along c polarised along b
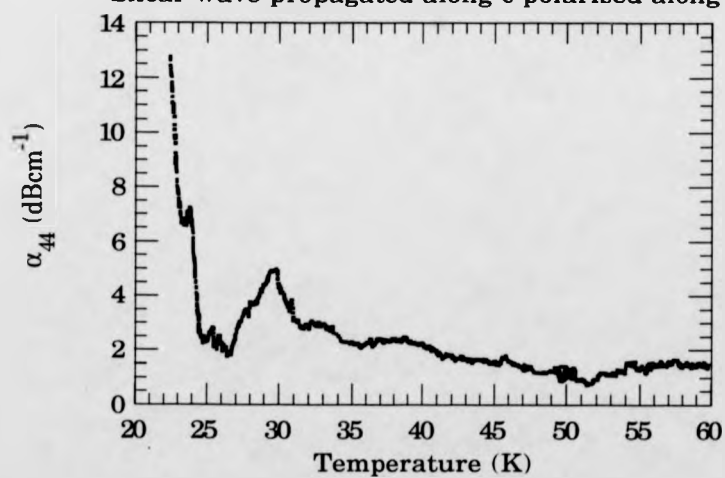
rise in the attenuation at 21K while in the b polarised mode the peak is not as great and is not clearly defined from the increase in attenuation which appears to be centred at approximately 24K.

A difference in apparently equivalent elastic modes has been observed in MnF_3 by Melcher (1976) and was attributed to magnetoelastic or magneto-acoustic birefringence. Such behaviour was first proposed by Kittel (1958) and observed in yttrium-iron-garnet by Matthews and LeCraw (1962) and in magnetite and nickel by Lüthi (1966), and predicted for ferromagnetic structures in the rare-earths by Southern and Gooding (1973).

Kittel pointed out that if the magnon-phonon coupling is sufficiently strong magneto-acoustic birefringence will occur. The nature of the effect will depend on the relative orientation of the polarisation vector, the propagation direction and the direction of magnetisation having the consequence for the HCP case that the two C_{44} modes are no longer equivalent.

From Schlömann (1960) it is clear that the strength of the coupling between the ultrasonic shear wave and the magnetic spin system is dependent on the angle between the magnetisation and the polarisation vector. Bearing in mind the fact that the hexagonal directions are separated by only 60°, it is likely that vibrations along two directions are excited when the b polarised mode is measured. The degree of coupling is likely to be different for each direction thus the ultrasound velocity will also be different hence magneto-acoustic birefringence. The resulting phase difference between the two modes will result in an apparent increase in attenuation of the b polarised shear wave and a distortion of the exponential shape of the echo train (Matthews, 1962).

Southern and Goodings demonstrated that for a ferromagnetic structure the effects of magneto-acoustic birefringence would increase as a function of applied magnetic field, causing a softening of the b polarised mode and a proportional hardening of the c polarised mode.

The broad feature displayed in the c polarised mode of α_{44} may arise as result of the domain structure within the sample. However, without a more detailed knowledge of the magnetic structure, a full discussion of this point is not possible. Another broad feature has been observed in the attenuation of both modes at approximately 30K. The shape of this feature is not repeatable and may arise as a result of domain formation and as such be connected to the formation of a commensurate phase within the sample.

The anomaly at 24K in C_{44} and the corresponding peak in α_{44} may arise as a result of the low temperature limit of the b=23 structure. The attenuation peak is remarkably large bearing in mind that no coupling to the other ferromagnetic structure (b=15) was seen. The anomalies in C_{44} at 32.5K and 40K reported by Jiles have not been consistently observed in this sample.

Between 21K and 18K no measurements of C_{44} or α_{44} were possible because of the high attenuation, however, when the sample was cooled to into the ferro-cone phase, measurements were possible up to the transition at 20K (fig. 6.10).

The high attenuation exhibited by both the C_{11} and C_{66} modes in the intermediate phase made measurements in this region almost impossible. However, measurements of C_{11} (a longitudinal wave propagating across the basal plane) were possible down to 51K and warming from 10K to nearly 20K and C_{66} (a shear wave polarised in the basal plane propagating across the basal plane) were possible down to 47K and warming up to 28K.

116

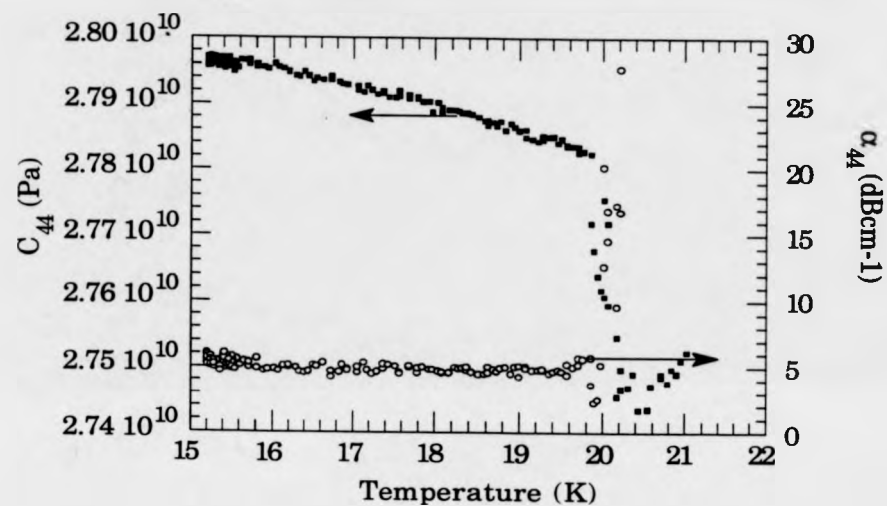Fig. 6.10 C_{44} and α_{44} vs. temperature for Er (warming).

Fig. 6.11 C_{66} vs. temperature for Er.
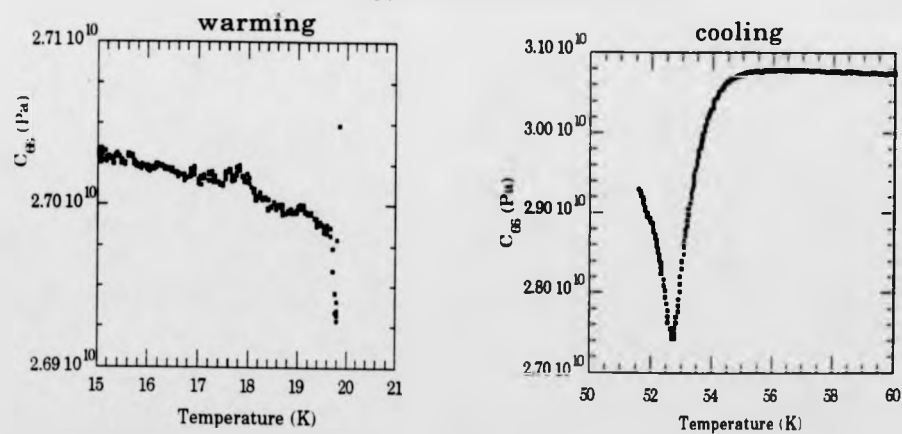
C_{66} (fig. 6.11) yielded very little information the echoes being unmeasurable between the onset of basal plane order and the transition to the ferro-cone structure. In this respect however, these measurement appear to contradict, dramatically, those of Jiles, who observed no coupling to the lower temperature transition, a hardening of the elastic constant at approximately 24K before the signal becomes unmeasurable at approximately 27K.

The C_{11} and α_{11} measurement were, however, more fruitful. On warming from the ferromagnetic phase, C_{11} (fig. 6.12) exhibits a rapid hardening coincident with the transition to the intermediate phase followed by a continuous softening with a slight inflection at approximately 24.5K and a more distinct anomaly at 27K. The attenuation(fig. 6.13) behaved in much the same way displaying a more dramatic feature between 26K and 27K.

Cooling through the transition at 52K to the intermediate phase, the phase change is manifest in the softening of the elastic constant (fig. 6.14). The attenuation increases until further measurements are not possible. A small inflection in C_{11} at 48.5K which is echoed by two small anomalies at 48.5K and 49.5K in the attenuation data may delineate the range over which the b=7 structure exists.

The anomalies observed in the ultrasound measurements are tabulated (table 6.2). All the modes measured bar C_{66} couple to the b=23 structure, C_{44} showed features at 27K and 24K which may correspond to the upper and lower temperature limits of the b=23 phase respectively. While C_{11} and α_{11}, measured while warming, suggested that this structure may be stable from approximately 26K to 28K. The only evidence for a locked in structure at other b values is supplied by α_{11} which showed features at 49.5K

117

Fig. 6.12 C_{11} vs. temperature for Er (warming).
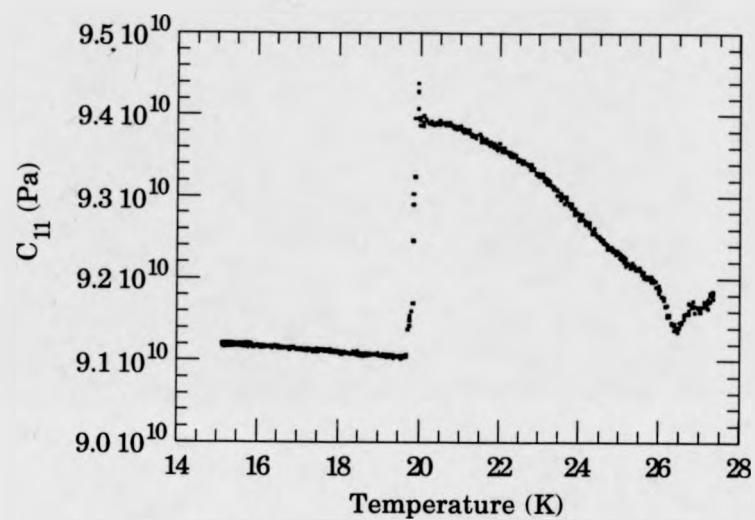
Fig. 6.13 α_{11} vs. temperature for Er (warming).
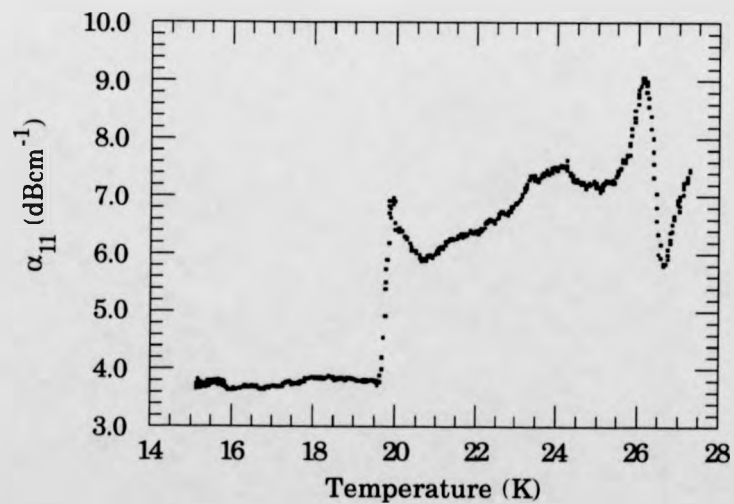
Fig. 6.14 C_{11} and α_{11} vs. tmperature for Er (cooling)
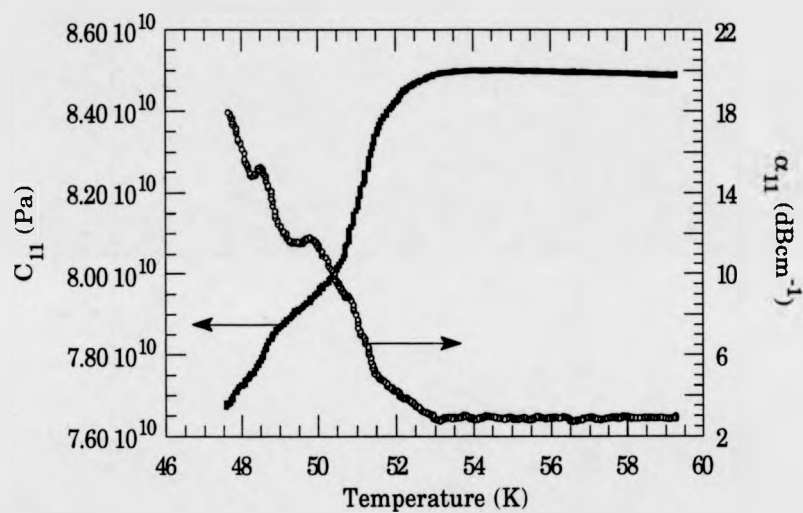
	T_c		b=23	b=15	b=7	T_m	T_n
C_{33}	18/20w		24	33	48	52	85
α_{33}	18					52	85
C_{44}	20w	21.5/22	24			52	85
α_{44}	20w	21.5/22	24-27				
C_{11}	20w		26-28w		48	52	85
α_{11}	20w		26-28w		48.5-49.5	52	
C_{66}	20w					53	85

Table 6.2 Temperatures of anomalies observed in ultrasound data. T_n, T_m and T_c represent the Néel point, the onset of basal plane order and the Curie point respectively. Where appropriate, the b values of the structures which produce the anomalies are given. The anomalies all appear on data collected with decreasing temperature unless indicated otherwise by a w.

and 48.5K which may mark the limits of the b=7 phase. Only C_{33} showed any coupling to the b=15 phase. None of the modes showed any coupling to the b= 11,13 or 19 structure, those which do not display a net ferromagnetic moment. Anomalies were usually only observed when scans were made at cooling rates of ~0.1Ks^{-1} or slower.

The high value of α_{44} between 21K and 18K may caused by the spins adopting a structure in which they are not confined to the a-c plane, thus producing a more circular distribution of the magnetisation on the basal plane.

The large peak in α_{44} at 24K may arise as a result of soft mode behaviour at the low temperature transition from the b=23 structure it is however, reminiscent of the dramatic peak in α_{44} displayed in Ho at 95.5K (Lee, 1975). Tachiki (reported in Lee, 1975) observed that the peak occurred when the helical magnetic structure had a period of eight layers, which would produce a commensurate structure with an angle of 45° between adjacent spins. Of course at 24K erbium is close to adopting an eight layer structure, but comparison between the peak in α_{44} for Ho and that displayed in the Er data is only valid if we assume that the basal plane component of the magnetisation has assumed a helical structure. If we assume that the high attenuation of C_{44} between 21.5K and 18K arises as a result of the spins falling out of the a-c plane it is reasonable to suggest that at this point, the component of the magnetisation on the basal plane is circular and adopts a helical structure.

Lee has thoroughly characterised the 95K peak in Ho by performing measurements as a function of the angle between an applied magnetic field and the a and c axes. Similar measurement on Er would indicate whether the two peaks were of the same origin.

118

The symmetry arguments employed to great effect by Bates et al (1988) to predict the behaviour of the elastic constants of Ho may be used in broad terms to describe the elastic constants of Er. If we consider the intermediate phase as described by Jensen we may define a two-fold symmetry axis along the c axis and another along the b-axis. On the formation of the commensurate structure with a net ferromagnetic moment, only the former will still be valid, and all elastic constants could be expected to show anomalous behaviour.

Recalling equation 3.11, peaks in the magnetic susceptibility will also produce anomalous effects in the elastic constants. Commensurate structures of erbium have been shown to produce large peaks in the susceptibility (Ali, 1990) and will produce additional anomalous behaviour in the elastic constants

6.1.3 Neutron Scattering from a Spin-Slip Structure

The presence of solitons or spin-slips will introduce an additional periodicity to the commensurate modulation and as such will give rise to additional scattering. Following Cowley and Bates (1988) we may consider the spin-slips as domain walls separating domains in which the moments are modulated by the commensurate propagation vector ($q_0 = \frac{1}{4}$). The phase of the modulation within each domain is given by

$$\Phi_d = z'q_0.c$$

where z' is the index of the plane within the domain. The increase in the phase resulting from the spin-slip is likewise

119

$$\Phi_s = m\mathbf{q_0}(b+1).\mathbf{c}$$

where m is the spin-slip number and b is the spin-slip distance referred to in section 6.1. The intensity of the scattering at wavevector transfer Q, will be dictated by both phase functions. Setting the magnetic scattering cross section to unity and ignoring the magnetic form factor

$$I = I_0 \sum_{m=0}^{N-1} \exp(i[\mathbf{c}.(\mathbf{Q} \pm \mathbf{q_0})mb \pm \mathbf{c}.\mathbf{q_0}m]) \sum_{z'=0}^{b-1} \exp[i\mathbf{c}.(\mathbf{Q} \pm \mathbf{q_0})z'].$$

Summing over the spin-slip number, scattering will only be observed for Q given by

$$\mathbf{Q} = \pm \left[\mathbf{q_0} + \left(\frac{1}{b}\right)(\mathbf{q_0} + J\mathbf{c}^*) \right] \tag{6.1}$$

where J is a positive or negative integer. Thus, the diffraction pattern for a spin-slip structure will include a magnetic satellite at $\mathbf{q_0} + \left(\frac{\mathbf{q_0}}{b}\right)$ accompanied by higher order peaks separated by a distance $\frac{1}{b}$.

The two sublattices of the HCP structure which cause the absence of (00l) peaks for l, odd also means that for scans along (00l) only peaks corresponding to even J will be observed.

6.1.4 Neutron Scattering Results

The neutron data described hereafter were collected at the I.L.L. on the D10 diffractometer described in chapter 2. A preliminary experiment was performed on the D15 diffractometer in April 1989, however, the poor

resolution of D15 relative to that of D10 has meant that the data collected there has been superceeded; they will not be discued in this thesis.

Three configurations of the D10 diffractometer were employed based on a compromise between flux and resolution to gain as much information in the available time as possible.

The initial measurement of the thermal evolution of the higher order peak positions was performed with the diffractometer in four circle diffractometer configuration. For the later, more detailed, analysis of the positions and intensities of the higher order peaks, the energy analyser was used, set for zero energy transfer, to improve resolution. A further improvement in resolution was achieved by using 10' collimators before and after the sample, however, this configuration considerably reduced available flux and was only used for scans in commensurate regions at low temperatures where the higher order peaks are almost coincident. All experiments were conducted using a wavelength of 2.3602Å (14meV) unless specifically stated otherwise. The higher wavelength of 4.28Å would have afforded a small improvement in resolution as a result of the smaller Ewald sphere, but at the expense of a considerable reduction in flux.

Several problems are associated with studying higher order peaks with intensities two or three orders of magnitude below those of the Bragg peaks and principle magnetic satellites. Multiple scattering will give rise to additional peaks on a Q scan and, by coincidence, may produce artificially reinforced scattering on other peaks. The crystal must be sufficiently large to produce enough scattering for the higher order peaks to have measurable intensity, unfortunately a large crystal is also more prone to extinction which will produce inaccuracies in the determination of peak intensities. Contamination from half wavelength neutrons scattered by the

monochromater may also produce additional peaks, however, this was reduced by using a pyrolytic graphite filter. Checks for multiple scattering were made by performing scans equivalent to those employed for the collection of the data, but with different scattering geometries. Scans performed at 1.26Å revealed that extinction was not an important factor (extinction falls off rapidly at lower wavelengths).

Scans across the Brillouin zones (100) to (101) and (001) to (002) were performed using the instrument in standard four circle mode over the temperature range 100K down to 10K. The proliferation of higher order peaks observed is dramatically illustrated by the isometric plots (figures 6.15 and 6.16), however, the thermal evolution of the peak positions is more clearly illustrated on the plan plots (figure 6.17 and 6.18). The high order peaks are indexed in terms of multiples of the propagation vector q and the integer J from equation 6.1.

The $(10l)$ scans are reasonably straight forward. Odd integer multiples of **q** up to the 13th order were measured. Magnetic satellites appear above the Néel temperature in accord with the data of Habenschuss et al (1974). They were typically broad indicative of short range order. The over simplification of this method of presenting the data gives the impression that the higher order peaks die away at approximately 25K where in reality this is the point at which they become coincident as **q** approaches $\frac{1}{4}$.

The peaks at 2**q** are not directly caused by the spin-slip structure, but arise as a result of strain modulations of twice the repeat distance of the magnetic modulation (Nourtier, 1973). The $(00l)$ scans display several features which merit comment. The most striking is the presence of a (001) peak which would suggest that the magnetic structure has lifted the
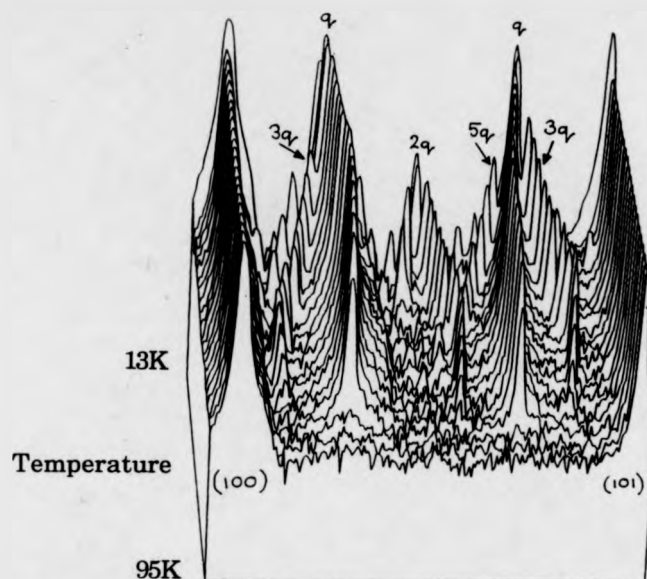
Fig. 6.15 Isometric plot of (10l) scans peformed from 95K to 13K using the detector.
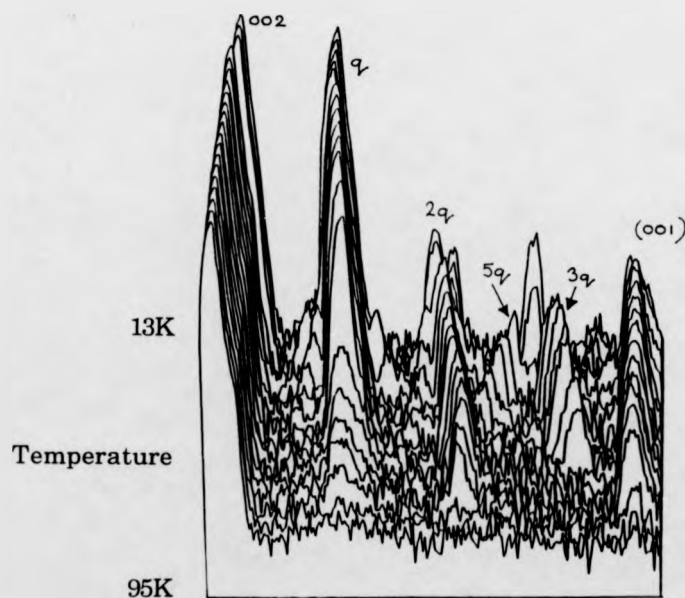

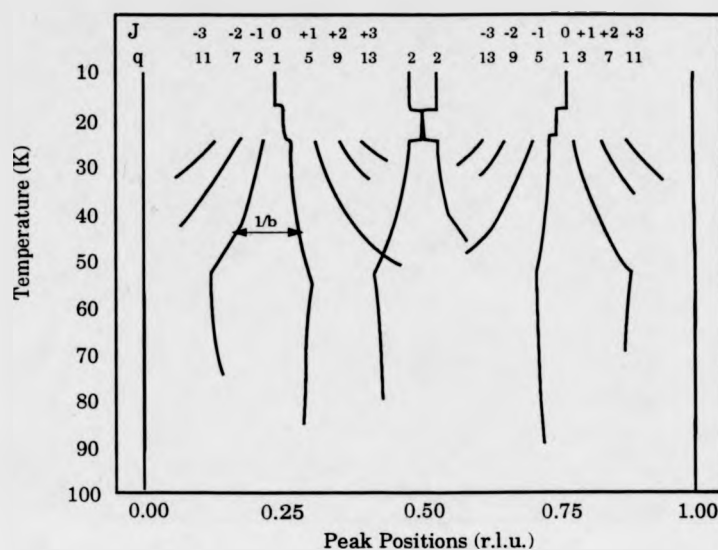Fig. 6.16 Isometric plot of (00l) scans peformed from 95K to 13K using the detector

Fig. 6.17 Thermal evolution of peak positions on a $(10l)$ scan from l=-0.05 to 1.05, data collected with increasing temperature.
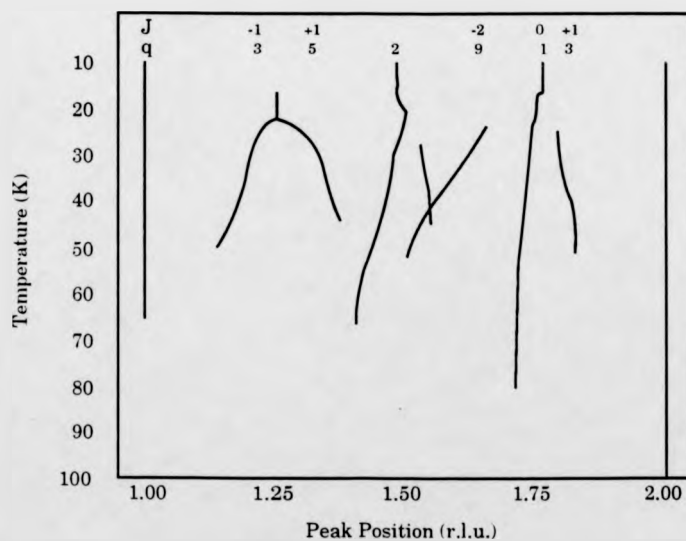

Fig. 6.18 Thermal evolution of peak positions on $(00l)$ scans where l=0.95 to 2.05. Data collected with decreasing temperature.

equivalence of the inter-layer which leads to (00l), where l is odd being absent. The presence of the third and fifth order peaks may be associated with the existence of the (001) peak, however, this is unlikely due to their relatively high intensity and their unusual thermal behaviour. We shall return to these points later in the chapter, for the time being it may be safe to assume that the third and fifth order harmonics of the basal plane modulation do not arise directly from the spin-slip structure.

The higher order peaks on the (10l) scan may be considered to be the result of the squaring up of the c-axis modulation. This is the case, but one must bear in mind that the spin-slip structure arises because the modulation is not commensurate with a squared up structure. As such the two effects are one and the same effect. Thus, from the positions of the peaks on the (10l) scan, the spin-slip distance was calculated as described in the previous section and is plotted as a function of decreasing temperature (fig 6.19).

The temperatures of the high symmetry structures are in good agreement with the data of Gibbs et al and coincident with anomalous behaviour observed in the ultrasound measurements described earlier and those observed by other authors.

Further experimental effort is now concentrated on studying the nature of the high symmetry phases and whether or not there was a locking-in of $\mathbf{q}$ to commensurate wave vectors. The X-ray data of Gibbs et al appear to show evidence of locking-in over ranges of between 3K and 3.5K at the b=7, 11 and 23 structures. However, previous neutron data (Habenschuss) do not corroborate this evidence, but the difference in resolution between the two experiments makes comparison difficult. Any reservations about the validity of the lock-ins observed in the X-ray data are

Fig. 6.19 Spin-slip distance vs. temperature for Er.
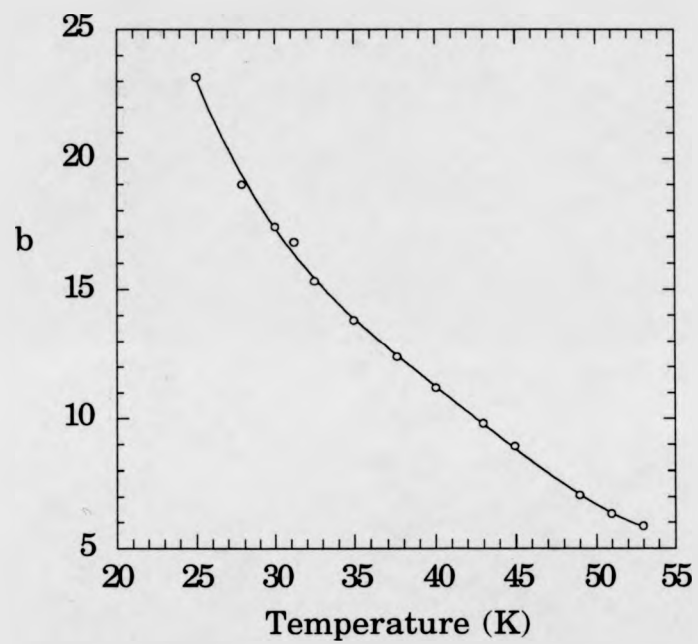
based on the presence of charge scattering peaks which may mask the true behaviour of $\mathbf{q}$.

The use of the analyser set for zero energy transfer permits a substantial improvement in resolution above the standard four-circle permitting a careful monitoring of the thermal evolution of $\mathbf{q}$. The shape of all the magnetic peaks appeared to be slightly non-Gaussian, with a broad Lorentzian like base. This feature is exaggerated when the data are plotted on a logarithmic axis, which is essential when fitting the higher order peaks, and produces error in peak fitting. In order to overcome these problems a broad Gaussian was used to fit the base of the collection of peaks surrounding a primary satellite, and another, narrower Gaussian, in the base of the primary satellite (fig. 6.20). $(10l)$ and $(00l)$ scans were performed as before in steps of 0.2K through the regions where lock-ins were expected. The peaks were fitted in the manner described above and the propagation vector $\mathbf{q}$ was determined and is plotted (figs. 6.21) and (6.22). The use of the fitting technique described above resulted in error bars smaller then the size of the points on figures 6.21 and 6.22. All fitting was performed using the DIFFIT program at the I.L.L..

The data show evidence of a tendency to lock-in to the b=15 phase from 32K to 29K and to the b=23 phase from 27K to 24K. The transition to the $\frac{1}{4}$ phase is not as dramatic in this sample as it appears to be in the data of both Gibbs and Habenschuss. No data was taken in the region of the b=19 structure, however, there does appear to be an inflection in q in that region. A detailed scan performed across the region of the b=11 structure showed no tendency to lock-in.

The scattering intensities measured with the detector are shown in figures 6.23 and 6.24, and show the same general features as Habenshuss et
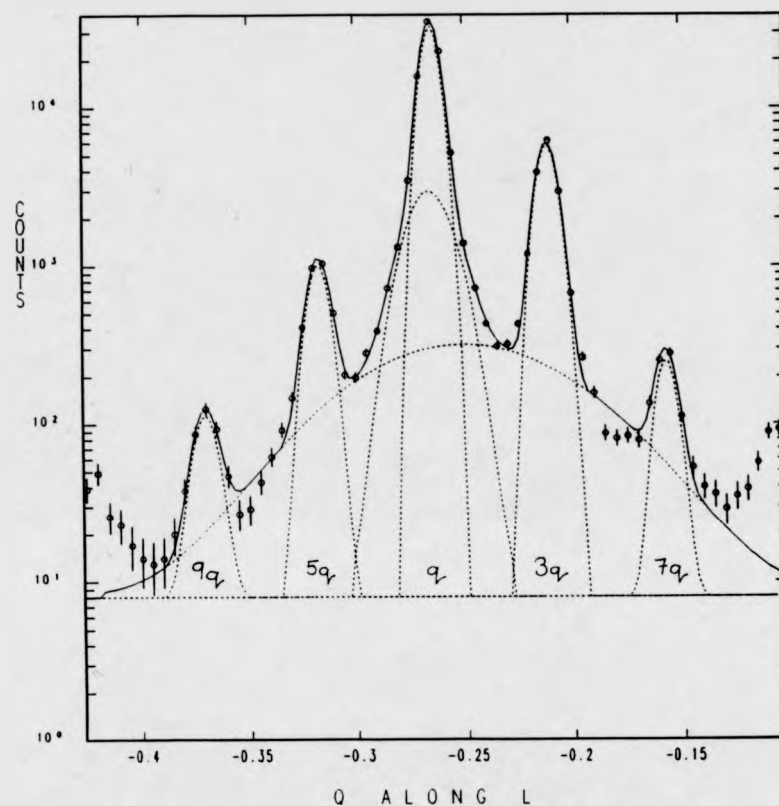
Fig. 6.20 The fitting of the (100-q) satellite and surrounding higher
order peaks at 28K. Data collected using the energy analyser.

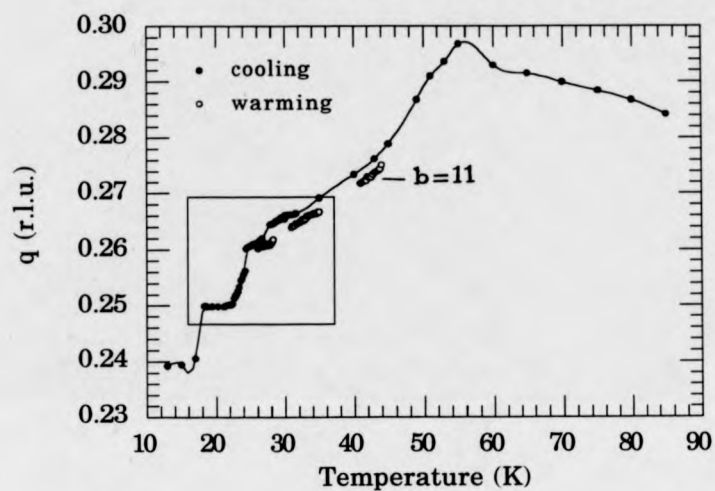Fig. 6.21 q vs temperature for Er.

Fig. 6.22 q vs. temperature for Er from 40K to 20K.
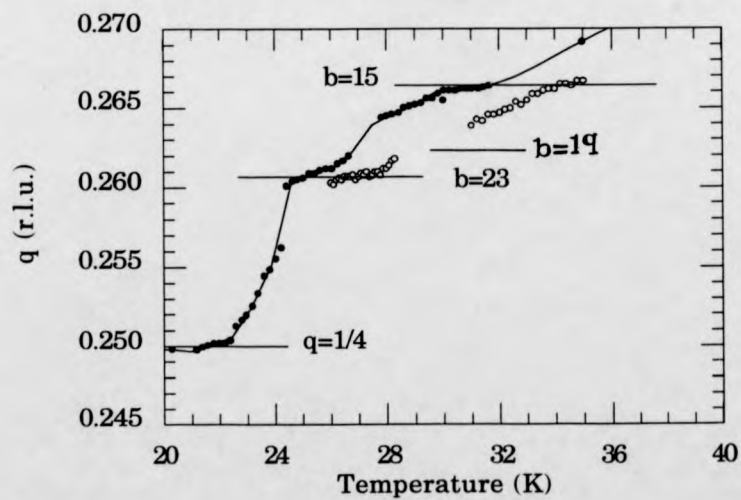
Fig. 6.23 F^2 for (10l) reflections vs. temperature for Er.
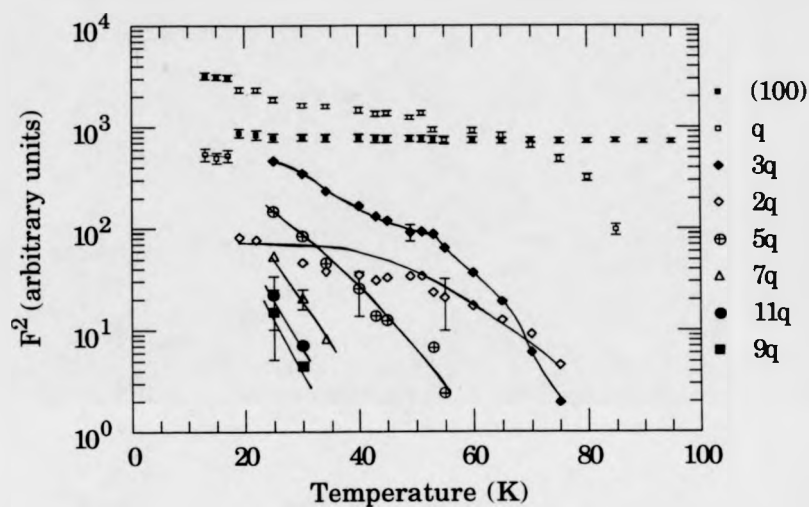
Fig. 6.24 F^2 for (00l) reflections vs. temperature for Er.
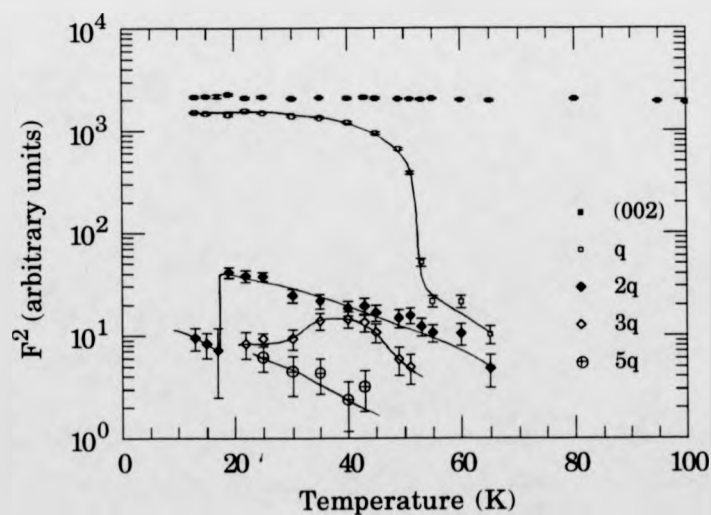
al. On the (10l) scans, the intensities of all the higher order peaks increase steadily as the temperature is reduced, and the structure becomes more squared up, until they become assimilated into the primary satellite on the formation of the $\frac{1}{4}$ structure. The 2**q** peak increases continuously as would be expected until the transition to the ferro-cone structure where it dies away rapidly.

The (00l) data shows very similar behaviour, the only exception being the reduction of the 3**q** peak. This effect was observed by Habenschuss et al and is well accounted for by Jensen's model (1976). (001) peaks and 2**q** peaks were observed on the scans performed with the detector, and those performed using the energy analyser,with the collimators in position. However, they were not observed during the later experiment when the energy analyser was used without collimation. Clearly the peaks arise as a result of multiple scattering. The thermal evolution, suggests a correlation with scattering at q on an (h0l) peak.

The smaller temperature steps and improved resolution of the second experiment, revealed several interesting features which had been overlooked in the initial study of the peak positions. The (10l) scans performed in the region of the b=15 structure (fig.6.25) did not reveal any unusual behaviour. The scattering in all peaks appeared to increase continuously as the temperature was decreased, in good agreement with the initial survey. The scan performed from 27K down to 18K (fig. 6.26), however, show the higher order peaks reduce in intensity before becoming assimilated into the primary satellites. This effect is not very clear on the isometric plot, so the intensities have been plotted as a function of temperature across this region (fig. 6.27) which clearly shows the reduction of the higher order peaks.
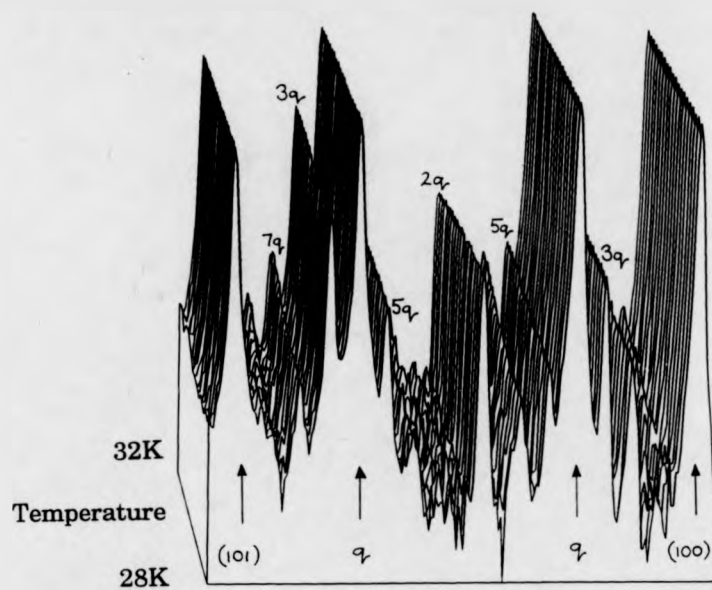
Fig. 6.25 Isometric plot of ($10l$) scans from 32K to 28K.
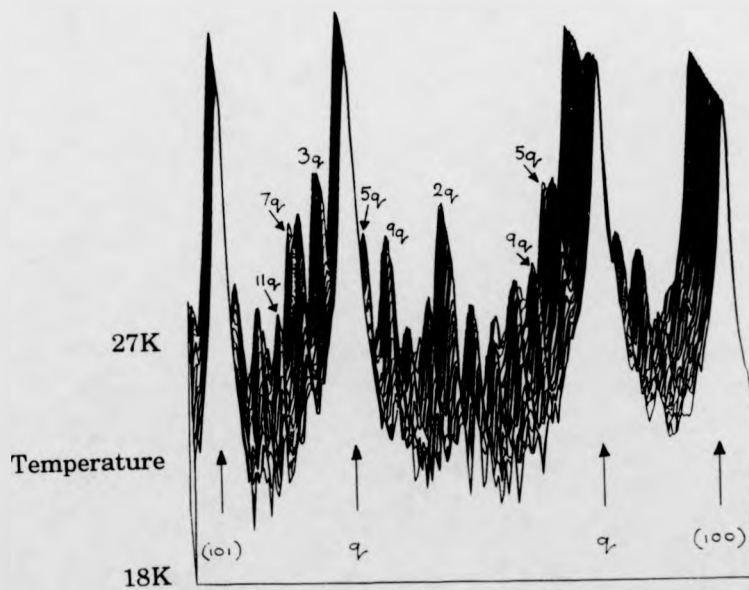
Fig. 6.26 Isometric plot of ($10l$) scans from 27K to 18K.

Fig. 6.27 F^2 vs. temperature for the 3q and 5q , and 7q and 9q (inset) peaks surrounding the (100) peak for erbium. Data collected with decreasing temperature.
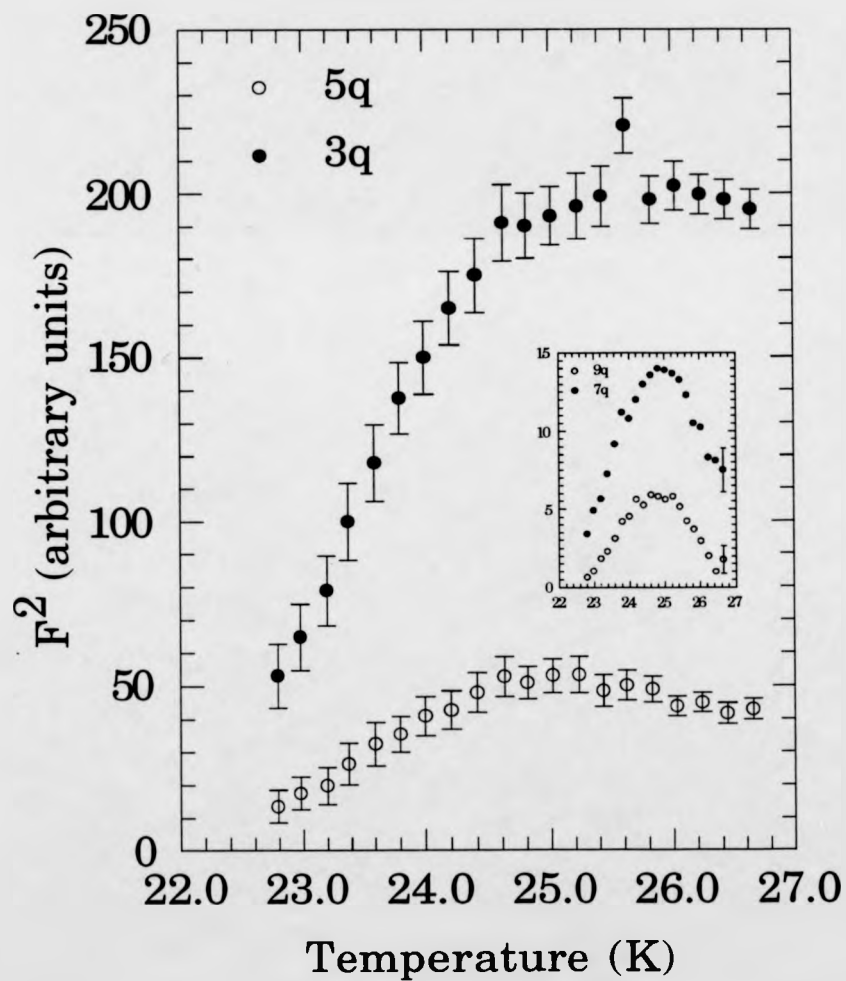
The behaviour of the primary satellite is even more dramatic. A small dip in the intensity of the satellite of the (100) peak is just discernable on the isometric plot (fig. 6.26), with no similar feature being obvious on the satellite of (101), however, when plotted out as a function of temperature (fig. 6.28) a sharp dip is clear in the intensities of both peaks, being more distinct on the satellite of (100). The dip at 24 K is clearly coincident with the lower temperature limit of the b=23 phase (the thermal evolution of **q** has also been plotted in figure 6.28 to allow comparison). A second step-like feature is visible at 22.5K in the (100) data, coincident with the lock in to the $\mathbf{q} = \frac{1}{4}$ structure. This feature is not clearly mirrored on the (101) data. These features undoubtedly arise from changes in the nature of the c-axis modulation because they appear to be less distinct on the (101) data which will be smeared out by an increase in scattering from the basal plane components.

Scattering on the $(00l)$ scans also displays similar features in the vicinity of 24.5K. The isometric plot (fig. 6.29) clearly shows the higher order peaks reducing and disappearing as the temperature is decreased, while scattering at (001) and its primary satellite emerges indicating a lifting of the inter-layer equivalence which forbids the (001) reflection. This behaviour is clearly illustrated by relevant q scans. Figure 6.30 shows data collected at 30.3K. The third, fifth, and ninth order peaks are indicated. The origins of the fourth order peak are not clear at this stage. As the temperature is decreased to 26K (fig. 6.31) the third order peak is dramatically reduced the higher order peaks less so. At 23K, however, (fig. 6.32) a dramatic change has occurred, with the third order peak now all but extinguished, and a satellite appearing at (001-q). By 22.4K (fig. 6.33) the process is almost complete with the other higher order peaks disappearing

126

Fig. 6.28 Intensities of the primary satellites of (100)
and (101) vs temperature (left hand axis) and the
thermal evolution of the propagation vector q. Data
collected simultaneously, with decreasing temperature.
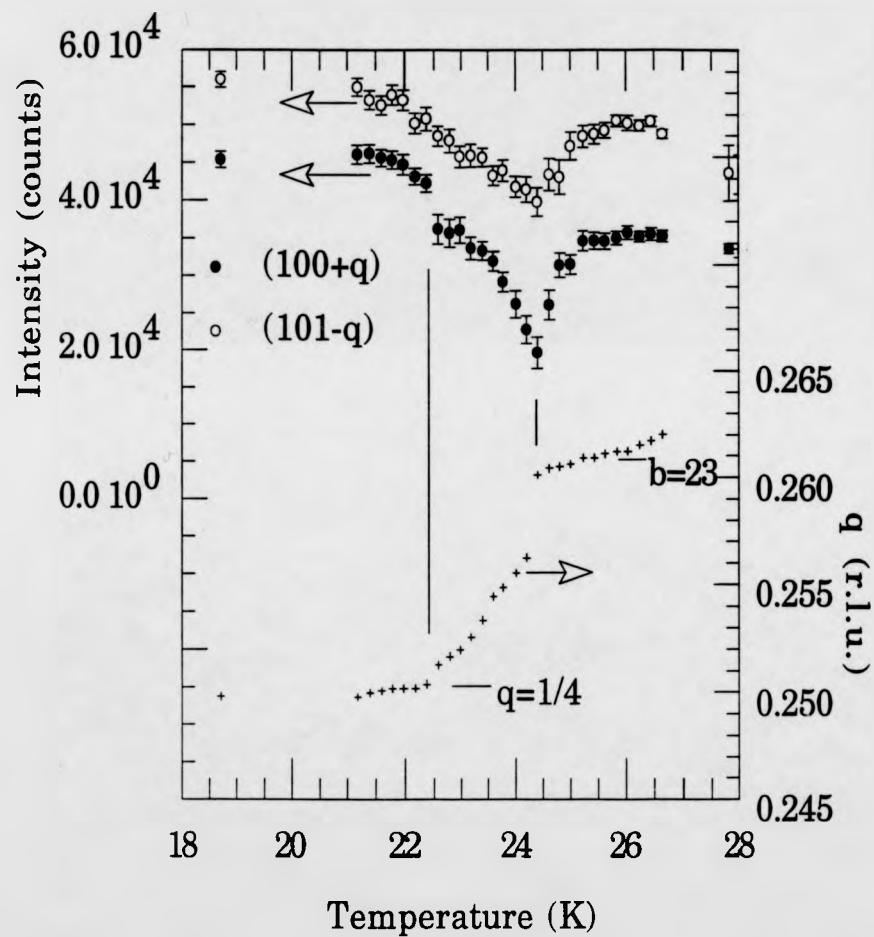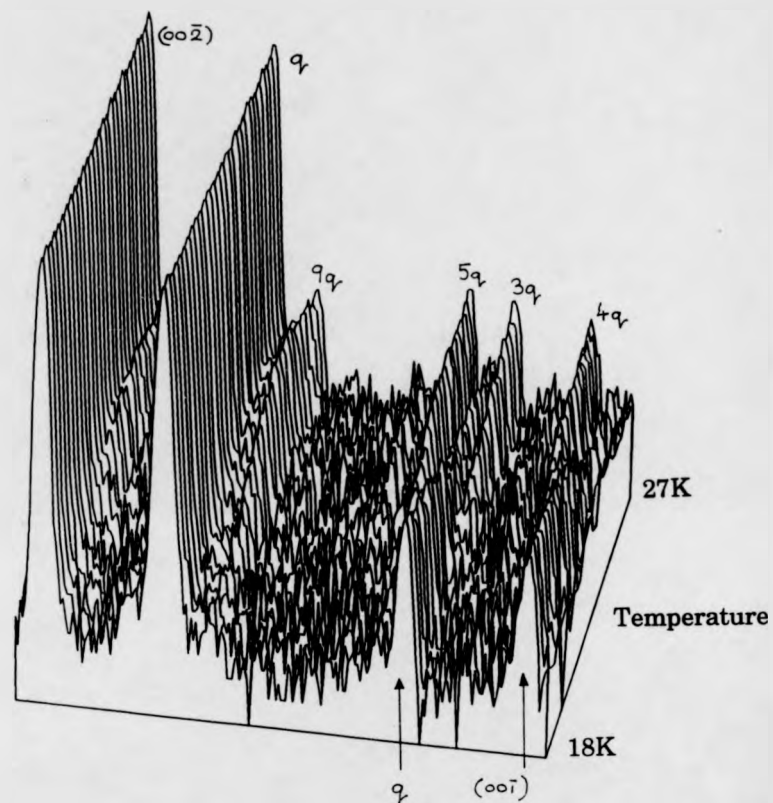
Fig. 6.29 Isometric plot of $(00l)$ scans from 27K to 18K.
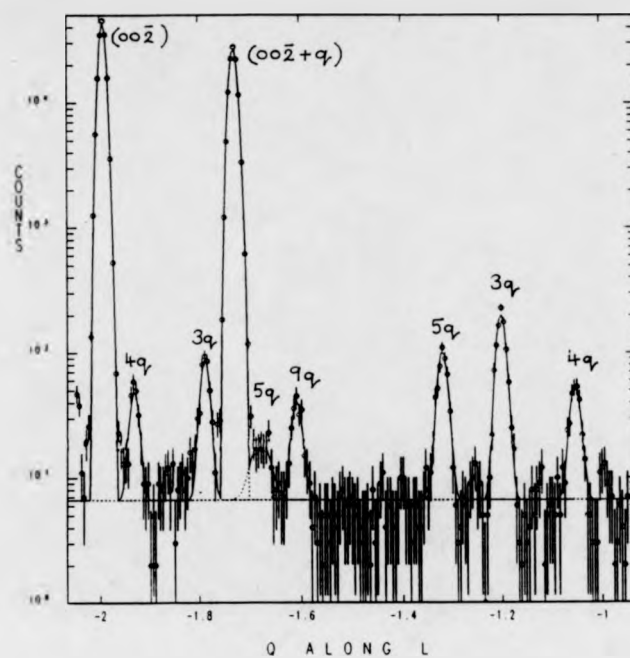
Fig. 6.30 (00*l*) scan at 30K.
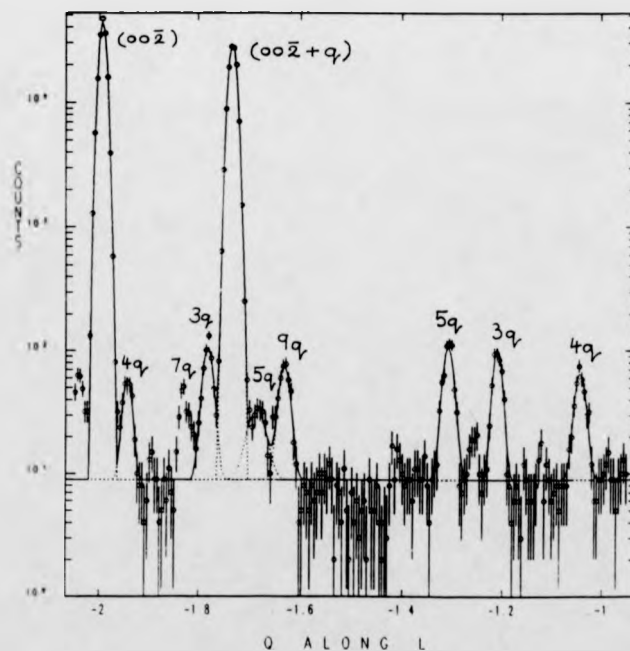
Fig. 6.31 (00*l*) scan at 26K.
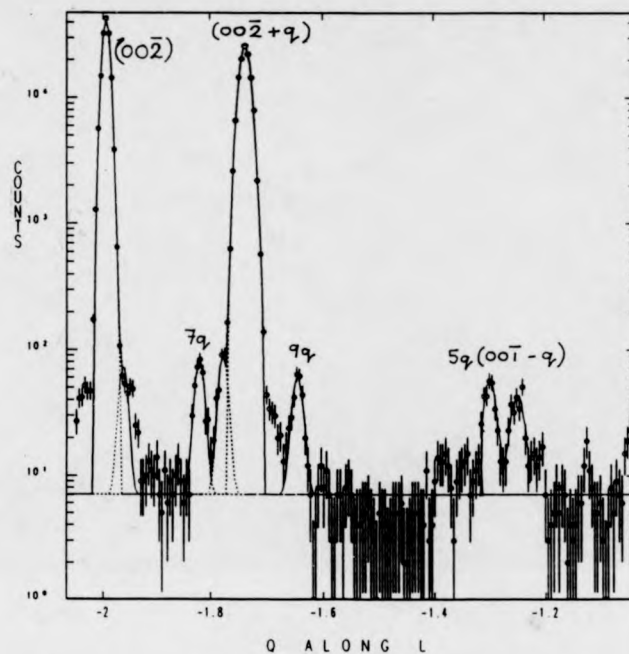
Fig. 6.32 (00l) scan at 23K.
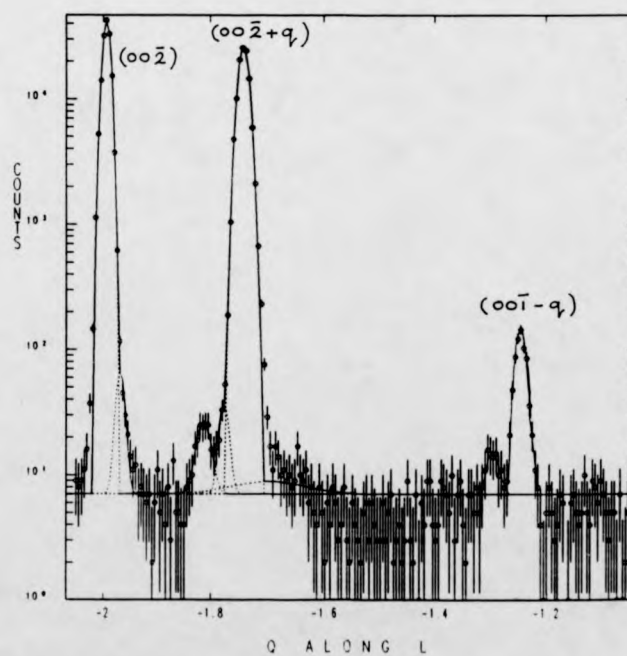
Fig. 6.33 (00l) scan at 22.4K.

into the background. Immediately above T_c at 18.1K (fig. 6.34) only the nuclear peak and two satellites are distinguishable. The lifting of the inter-layer equivalence which permits the (001) reflection will also have the same effect on those peaks arising from the spin slip structure, which have an odd index, J. Thus, the seventh order peak is seen to appear at 26K and disappear along with the other higher order peaks at 22K.

The use of 10' collimators before and after the sample provided a considerable increase in resolution as can be clearly seen from figures 6.35 and 6.36. Both data sets were collected at 25K. Peaks up to the 17th order were indexed on the (h0l) data. The (00l) data shows scattering at 2q unlike the data collected without the collimators. Between the two experiments the crystal was removed and remounted, so the scattering at 2q on these data is probably due to multiple scattering. A second (00l) scan was performed at 21K (fig.6.37) and displayed peaks only at (002), (001), their primary satellite and at 2q. These data are in good agreement with those collected without the collimators, with the exception of the scattering at 2q.

6.1.5 Discussion and Conclusions from the Er data.

The commensurate structures with a net ferromagnetic moment described by the spin-slip parameters b=15 and b=23 have been shown to show a tendency to lock-in over temperature ranges of approximately 31-30K and 26.5-24K respectively. For comparison, Gibbs et al observed lock-ins in their X-ray scattering data between 34.5K and 31.5K and from 26.5K to 23K. The discrepancies may be due to the large charge scattering peaks observed in the X-ray data, however, there may also be some dependence on cooling
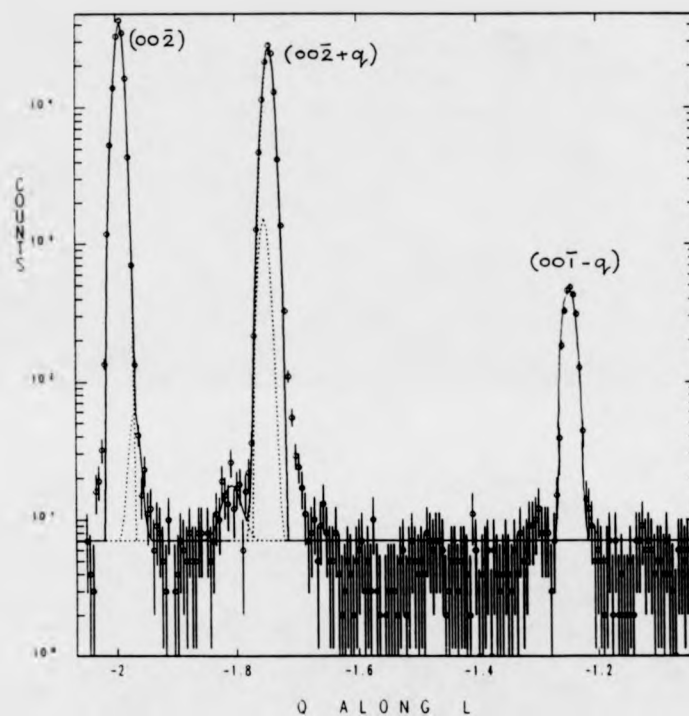
Fig. 6.34 (00l) scan at 18.1K.
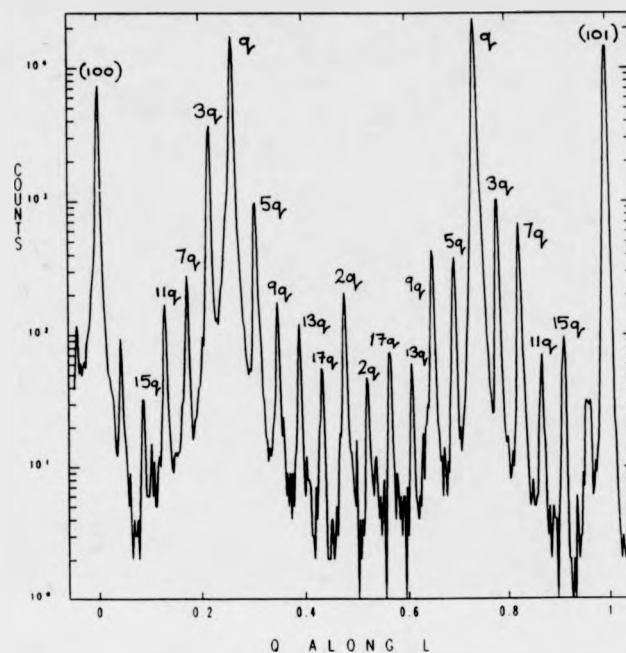
Fig. 6.35 (10l) scan at 25K with 10' collimators before and after the sample.
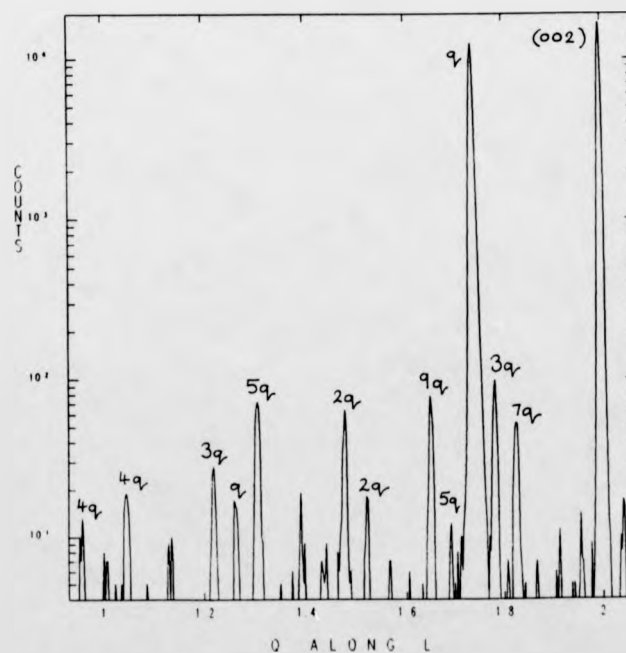
Fig. 6.36 (00l) scan at 25K with 10' collimators before and after the sample.
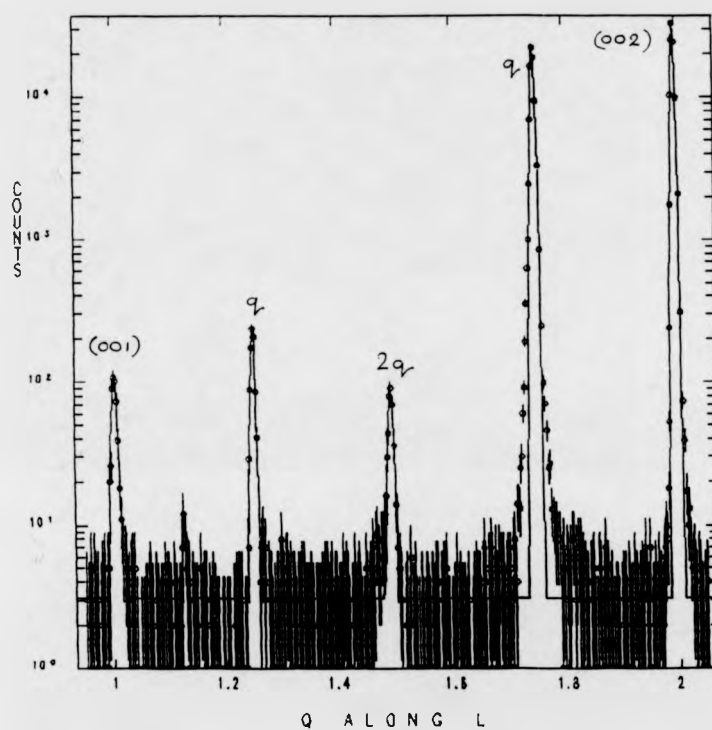
Fig. 6.37 (00*l*) scan at 21K with 10' collimators before and after the sample.

rates and sample purity. The upper temperature limit of the b=15 structure has not been well defined in this study. The proposed lock-in to the b=7 structure has not been studied as thoroughly as the lower temperature ferromagnetic structures, however, there is limited evidence from the ultrasound data of a lock-in from 49.5K to 48.5K.

The agreement between the ultrasound data and the neutron scattering data is good, and the anomalous behaviour of the elastic constants are caused by the formation of commensurate structures.

The high attenuation of the C_{44} modes between 21K and 18K may be caused by the spins falling out of the a-c plane to form something akin to an alternating cone structure. While the neutron scattering intensities do not show any anomalous behaviour in the region of the b=15 commensurate structure, unusual behaviour of both the higher order peaks and the primary satellites in the region of 24K support the view that the magnetic structure is undergoing quite considerable change.

Considering the behaviour of the peaks on the $(00l)$ scans, only those with an even index, J, may be attributed directly to the spin-slip structure. Felcher et al (1976) when considering the magnetisation distribution of Ho identified the third, fifth and seventh order peaks as arising from asphericity in the magnetisation, while only the fifth and seventh order peaks arise as a result of bunching about crystallographic directions. The behaviour of the third order peak has been shown to be in good agreement with Jensen's model (1976). The fifth and seventh order satellite on the other hand will disappear when the projection of the magnetisation on the basal plane becomes circular, and their apparent disappearance at approximately 24K may be caused by the development of a helical component in the basal plane consistent with an alternating cone structure.

Scattering on (001) is unlikely to occur as a result of the formation of an alternating cone structure. Magnetostrictive deformations of the lattice may result in the lifting of the inter-layer equivalence.

The scattering on the (10l) scan is somewhat more complicated. The reduction of the higher order peaks as the $q = \frac{1}{4}$ structure is approached heralds the end of the spin-slip structure as b tends rapidly to infinity, however, if the $q = \frac{1}{4}$ phase is actually fully squared up one would still expect all odd harmonics. The unusual behaviour of the primary satellite intensities at 24.5K, coincident with the lower temperature limit of the b=23 structure and the high absorption of transverse phonons propagated along the c-axis suggests a magnetic phase transition.

The magnetic structure of erbium is still attracting considerable attention and still poses many problems. At the time of writing it was believed that Jensen (1991) and Cowley and McMorrow (1991) were close to publishing work on a new model for the structure of Er which accounts for many of the ambiguities described in this chapter.

6.2 Spin-slip Structures in the Random Alloy $Ho_{90}Er_{10}$.

In chapter four the properties exhibited when a magnetic rare earth is alloyed with a non-magnetic metal diluent were discussed. A new level of complexity is introduced when alloys of two magnetic rare earths are considered, with the possibility that the two constituents will order independently. A recent neutron diffraction experiment by Howard and Bohr (1991), showed that a $Ho_{50}Er_{50}$ alloy displays a conical structure where the semi-cone angle of spins on the Ho sites is different to those on the Er

sites. The elastic constants C_{33}, C_{44} and C_{11} have been measured for a single crystal of $Ho_{90}Er_{10}$ on loan from Dr. Bohr and a limited neutron diffraction experiment has been performed using time remaining after a previous experiment.

From the phase diagram derived by Bozorth and Gambino (1966), $Ho_{90}Er_{10}$ would be expected to order into a basal plane helix at approximately 125K and into a ferro-cone structure at 23K, thereby displaying very similar behaviour to pure Ho.

Holmium has been well characterised, by X-ray (Gibbs, 1985) and neutron scattering techniques (Cowley and Bates, 1988), and the helical magnetic structure has been well described by a spin-slip model. The conical phase however, is still not properly understood. There is some disagreement as to whether or not ferromagnetic scattering is observed on the 100 peak in the conical phase consistent with a ferromagnetic component along the c-axis. On cooling the propagation vector $\mathbf{q}$ decreases from ~0.275 at 133K down to the commensurate propagation vector $\mathbf{q}=\frac{1}{6}$ at 20K when the conical structure is adopted. As $\mathbf{q}$ evolves, the helix is distorted by the basal plane anisotropy and several commensurate structures are encountered, which may be described, again, by a spin-slip distance b.

For the time being we will assume that the anisotropy in the basal plane is strong enough to align the spins along one of the hexagonal directions. In this case the commensurate propagation vector is $\mathbf{q}=\frac{1}{6}$ which corresponds to a helical structure in which two adjacent planes have their spins aligned along one of the hexagonal directions in the basal plane and the next two lattice planes have their spins rotated by 60° to lie along the next easy direction. At higher values of $\mathbf{q}$ the compromise between the

130

exchange and the anisotropy will result in the introduction of a spin-slip into the above structure whereby a single lattice plane will have its spin aligned along a particular direction. The distance between spin-slip is once again referred to as b. Figure 6.38 illustrates the b= 5 structure.

Cowley and Bates (1988) refined this mode by introducing two other parameters; α , which is the angle between the spin and the closest easy direction and a Gaussian Debye-Waller factor, σ, which allows for a change in a for those spins closest to the spin-slip and uncertainties in the position of the spin-slip arising from thermal fluctuations.

The spin-slips will move continuously through the lattice as **q** evolves, and as it does so several high order commensurate structures will evolve (fig.6.39) producing anomalous behaviour in the ultrasonic elastic constants (Bates, 1988). Such structures with an odd values of b will have effective symmetries such as trigonal (b=3) or orthorhombic (b=5) which are easy to visualise. Even values of b will also produce symmetries such as orthorhombic, although they are somewhat more difficult to visualise.

6.2.1 Ultrasound Results

The symmetry arguments used in previous sections to describe the behaviour of ultrasonic elastic constants was derived by Bates (1988) specifically for interpreting the large anomalies observed in ultrasonic measurements on Ho. He showed that C_{44} and C_{66} should couple strongly to the formation of b=2, b=5, b=8 and b=11 structures. C_{33} should only couple to the monoclinic b=11 structure.
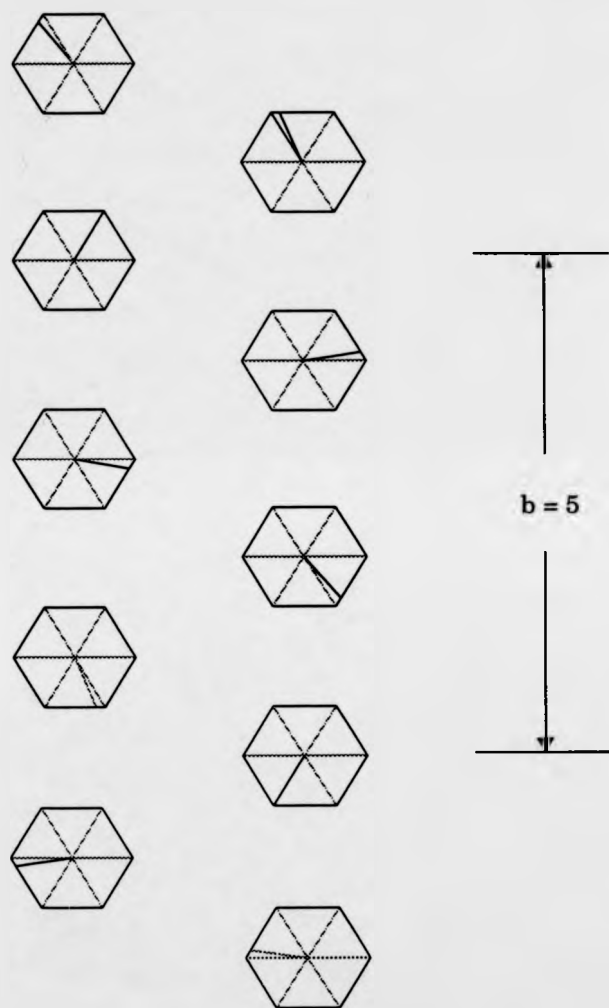
Fig. 6.38 The b=5 spin-slip structure in Ho.

b=5, orthorhombic   b=3, triagonal   b=2, orthorhombic
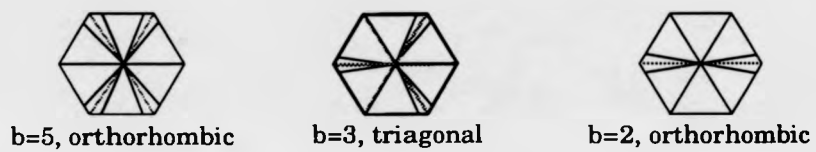
Fig. 6.39 Higher order commensurate structures in Ho.

The elastic constants C_{33}, C_{44} and C_{11} and their associated attenuation coefficients have been measured in the manner described in chapter 3. Attempts to measure C_{66} produced non-repeatable results because the crystal was too narrow to prevent errors arising from sidewall reflections. C_{44} was only measured by propagating a shear wave parallel to the c-axis, because of the narrowness of the crystal along the c direction.

The behaviour of all the elastic constants is very similar to that for pure Ho. C_{33} (fig. 6.40) shows a rapid softening at 126K indicating the initial ordering. Another dramatic step at 25K heralds the transition to the conical phase. There is no evidence of the anomalous behaviour displayed by pure Ho immediately above Tc. The inflection at 85K also appears in the Ho data and cannot be attributed to the independent ordering on the Er sites.

C_{44} (fig.6.41) shows a continuous increase from the Néel point at 126K. The pronounced anomaly at 89K and the corresponding peak in α_{44} is identical to that observed by both Bates and Lee (1975) and attributed by Bates to the formation of the b=2 structure. The knee at 25K is unlike the step feature in Ho which corresponds to Tc.

The C_{11} data (fig 6.42) show a small inflection at T_n and a step at T_c.

The ultrasound data give T_n at 126K and T_c at 26K. No anomalous behaviour is observed apart from the distinct feature at 89K. The difference between the behaviour of C_{44} at T_c for Ho and $Ho_{90}Er_{10}$ suggests some difference in the ordering.

Some of the Ho measurements were repeated in order to asses the sensitivity of the automatic measurement system. All the anomalies observed by Bates et al were clearly visible.

Fig. 6.40 C_{33} vs. temperature fo $Ho_{90}Er_{10}$.
Data collected with decreasing temperature.
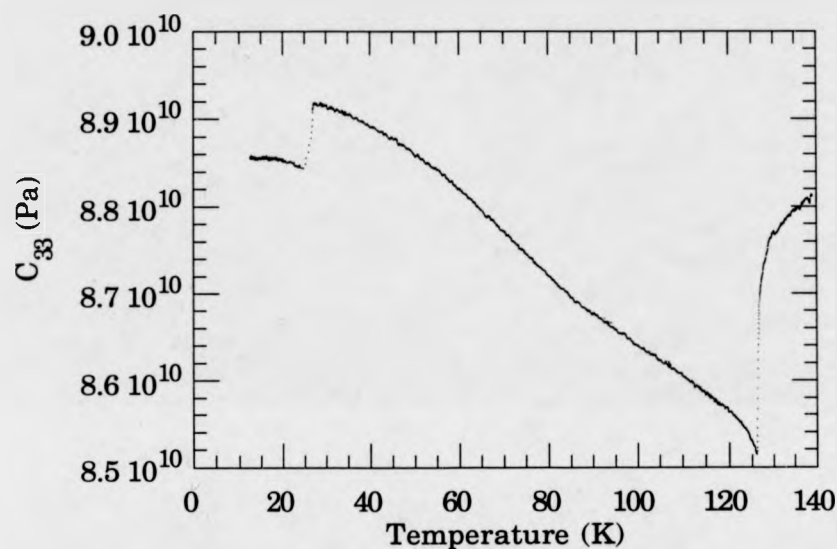
Fig. 6.41 C_{44} vs. temperature for $Ho_{90}Er_{10}$.
Data collected with decreasing temperature.
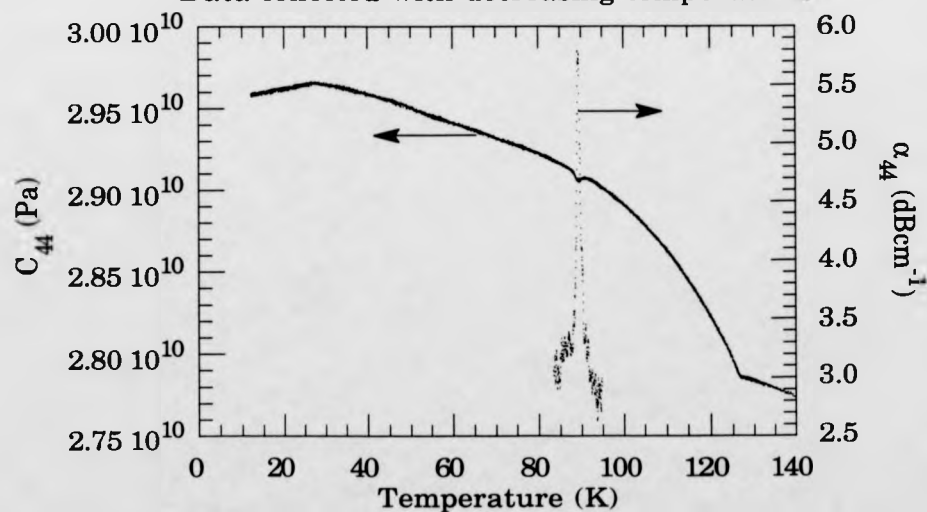
Fig. 6.42 C_{11} vs. temperature for $Ho_{90}Er_{10}$.
Data collected with decreasing temperature.
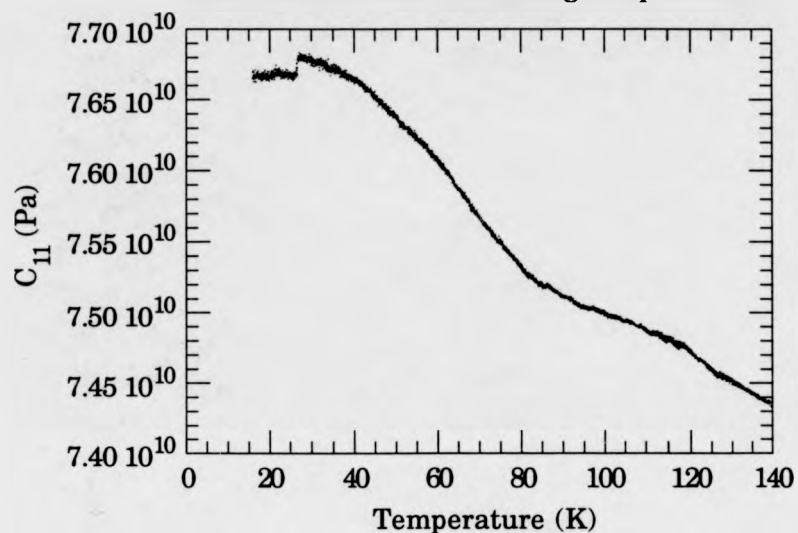
Fig. 6.43 q vs. Temperature for $Ho_{90}Er_{10}$
with decreasing temperature.
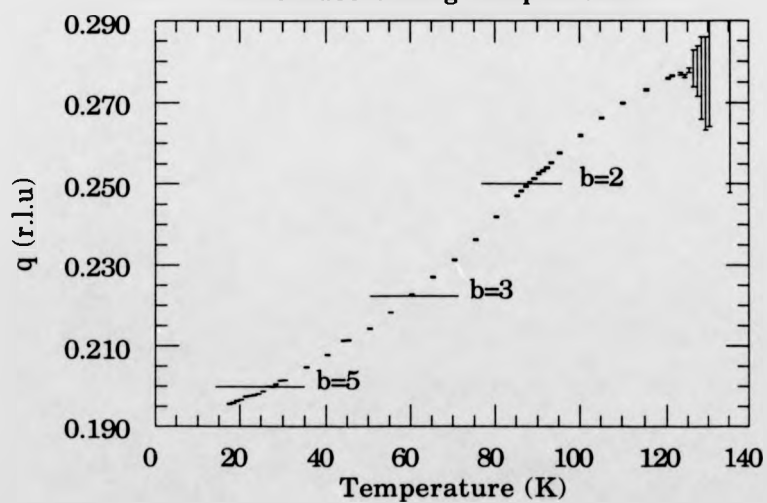
6.2.2 Neutron Scattering Results

The data described here was collected on the D10 diffractometer at the I.L.L.. The crystal was mounted with the a* and c* axes in the scattering plane. The energy analyser was used set to zero energy transfer, and no collimation was used.

From $(10l)$ and $(00l)$ scans performed between 135K and 17K the thermal evolution of $\mathbf{q}$ was determined (fig.6.43). The initial value is close to that of Ho at 0.275, however $\mathbf{q}$ evolves slowly and at 26K it is equal to $\frac{1}{5}$, considerably short of the commensurate value of $\frac{1}{6}$ adopted in the conical phase of Ho. The most striking feature of these data is that at the transition to what was assumed to be a conical phase $\mathbf{q}$ continues without any evidence of a lock-in or inflection.

The only high symmetry structures which could possibly be assumed are the b=2 structure, which appears at 87K coincident with the anomalies in C_{44} and α_{44}, and the b=3 structure and the b=5 structure, which could be coincident with the transition at Tc.

The intensity data (figs. 6.44 and 6.45) are consistent with a basal plane helix existing from 126K down to approximately 25K whereupon there appear to be a modest increasing in the nuclear peaks (101) and (100) indicative of the development of ferromagnetic moment along the c-axis. Because only two reflections which provide information on the c-axis component of the magnetisation have been measured a detailed determination of the magnetic structure is not possible, However, data analysis based on this limited data set has shown some evidence of a c-axis modulated moment.

Fig. 6.44 Peak Intensity vs. Temperature for the (100) peak and Primary Satellite
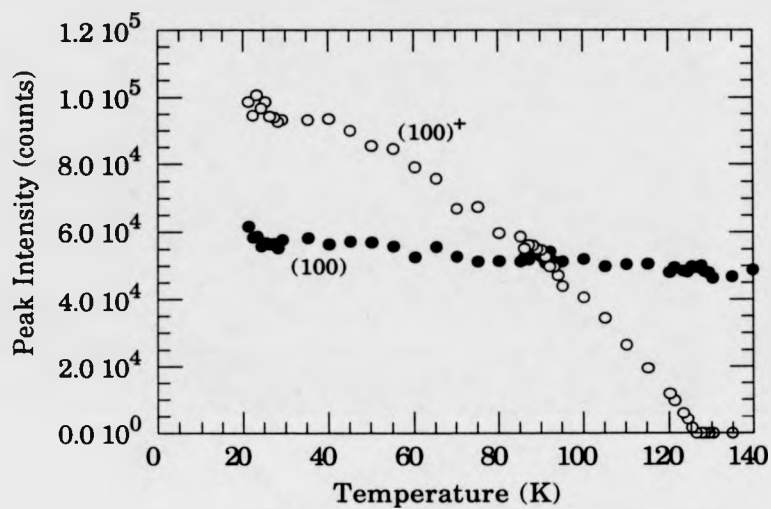
Fig. 6.45 Intensity of the (002) peak and primary satellite vs. decreasing temperature.
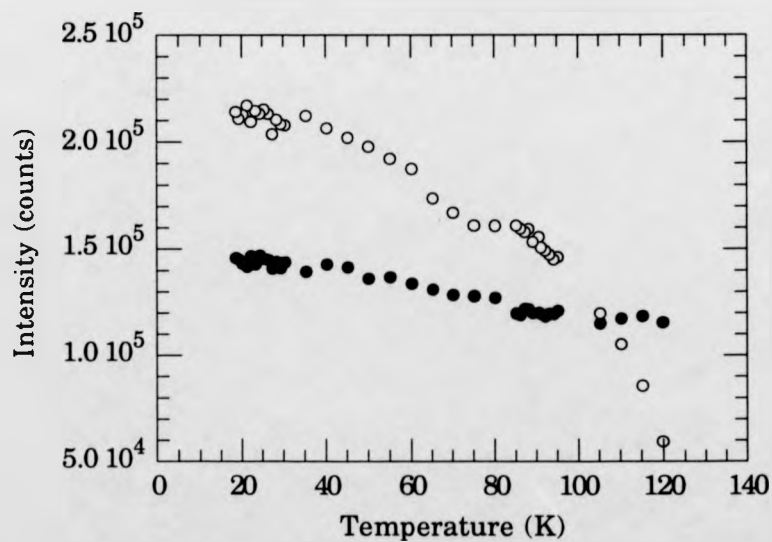
6.2.3 Discussion and Conclusions from the $Ho_{90}Er_{10}$ data.

These neutron scattering data were collected in time remaining from a previous experiment and as such are not as comprehensive as would have been possible if more time were available. A more thorough investigation is required, particularly in the conical phase. Such an experiment is planned for early 1992 at the Risø reactor in Denmark.

The $(10l)$ data is remarkable in that no higher order peaks were visible apart from $2\mathbf{q}$, which may be caused by multiple scattering. However, the proximity of $\mathbf{q}$ to $\frac{1}{5}$ throughout the intermediated phase means that higher order peaks would be obscured by the primary satellites and $2\mathbf{q}$ reflections. Third and fifth order peaks were observed on $(00l)$ scans.

The only high symmetry structure which showed any coupling to the ultrasonic elastic constants was that corresponding to b=2. The anomaly in C_{44} observed at 89K is identical to that observed in Ho at the temperature corresponding to the same values of $\mathbf{q}$ and b, thus, reinforcing the argument that the anomalous behaviour arises as a result of the formation of the b=2 structure. However, it is still not clear why the coupling, particularly to α_{44}, should be so great for the b=2 structure, bearing in mind that α_{44} was not seen to couple to any other high order commensurate structures.

The addition of 10% Er into Ho has the effect of reducing the Néel temperature and increasing the Curie temperature as found by Bozorth and Gambino. The thermal evolution of $\mathbf{q}$ is considerably slower than that displayed by pure Ho and continues, uninterrupted, as the conical phase is entered.

References

Ali N., Willis F., Phys. Rev. B 42 10 6820 (1990).

Åstrom H.U., Benediktsson G. J.Phys Condens. Matter 1 4381 (1989).

Åstrom H.U., Chen D-X, Benediktsson G., Rao K. J.Phys. Condens.
Matter 2 3349 (1990).

Atoji M. Solid State Commun. 14 1047 (1974).

Bak P. Rep. Prog. Phys 45 587 (1982).

Bates S., Patterson C., McIntyre G.J., Palmer S.B., Mayer A., Cowley R.A.,
Melville R.J., J. Phys. C: Solis State Phys. 21 4125 (1988).

Bozorth R.M., Gambino R.J., Phys. Rev. 147 487 (1966).

Burger J.P., Vajda P., Daou J.N., Chouteau G. J.Phys F Met. Phys. 16
1275 (1986).

Cable J.W., Wollan E.O. Koehler W.C. Wilkinson M.K. Phys. Rev. 140 6A
1896 (1965).

Cowley R.A., Bates S. J.Phys. C Solid State Phys. 21 4113 (1988).

Cowley R.A. reported in Jensen J. and Mackintosh A.R., "Rare Earth
Magnetism, Structures and Excitations", Oxford Science
Publications, (1991).

Felcher G.P., Lander G.H., Arai T., Phys. Rev. B 13 7 (1976).

Gibbs D., Bohr J., Axe J.D., Moncton D.E., D'Amico K.L. Phys. Rev. B 34
11 8182 (1986).

Gibbs D., Moncton D.E., D'Amico K.L., Bohr J., Grier B.H. Phys. Rev.
Letts. 55 234 (1985).

Habenschuss M., Stassis C., Sinha S.K. Deckman H.W., Spedding F.H.
Phys. Rev. B 10 3 1020 (1974).

Howard B.K., Bohr J., Physica Scripta T39 96 (1991).

Jensen J. J.Phys F Metal Phys 4 1065 (1974).

Jensen J. J.Phys F Metal Phys 6 6 1145 (1976).

Jiles D.C., Palmer S.B., J.Phys. F: Metal Phys. 11 45 (1981).

Kittel C., Phys. Rev. 110 836 (1958).

Lee M.C., Treder R.A., Levy M., J. Phys. Chem. Solids 36 1281 (1975).

Levy P.M. Phys. Rev. 177 509 (1971).

Lüthi B., Aplied Phys. Letts. 8 5 107 (1966).

Matthews H.L., LeCraw R.C., Phys. Rev. Letts. 8 10 397 (1962).

McMorrow D.F, personal communication (1991).

Melcher R.L., Phys. Rev. Letts. 25 1201 (1970).

Miwa H., Yosida K. Prog. Theo. Phys. 26 5 693 (1961).

Nicklow R.M., Wakabayashi N. Wilkinson M.K., Reed R.E. Phys. Rev.
        Lett. 27 334 (1971).

Nourtier C., J. de Physique 34 57 (1973).

du Plessis P. de V. J.Phys. F: Metal Phys. 6 873 (1976).

Schlömann E. J.Appl. Phys. 31 1647 (1960).

Schmitzer C., Hilsher G., Vajda P., Doon J.W. J.Phys F Met. Phys 17 865
        (1987).

Sherrington D. J.Phys C Solid State Phys. 6 1037 (1973).

Southern B.W., Gooding D.A., Phys. Rev. B 7 1 534 (1973).

Truell R., Elbaum C., Chick B.B., "Ultrasonic Methods in Solid State
        Physics", Academic Press, New York (1969)

Vigren D.T. Solid State Commun. 18 1599 (1976).

Chapter 7

The Magnetic Structure of Erbium in an Applied Magnetic Field: Stabilising the Devil's Staircase.

Introduction

In the preceding chapter, the magnetic structure of erbium in zero field has been described in terms of a spin-slip model in which commensurate structures, made up of combinations of groups of three and four atomic layers (triplets and quartets), arise as **q** evolves with temperature. Three structures which exhibited a net ferromagnetic moment were identified (b=7, b=11 and b=23). These are the structures which are made up of an odd number of quartets to triplets. The latter two showed some evidence of a lock-in of q over a temperature range of no more than 2K, because the magnetostrictive energy, which plays a more important rôle at lower temperatures, stabilises structures with a net ferromagnetic moment.

The application of a magnetic field along the c-axis would be expected to stabilise any structures which have a net ferromagnetic moment along the c-axis and in doing so induce a more complete devil's staircase than was seen at zero field. Previous magnetisation measurements (Flippen, 1964 and Feron, 1970) and ultrasound measurement (Jiles, 1981 and DuPlessis, 1976) indicates that the "elliptical structure" referred to in chapter 6 collapses rapidly to a c-axis

137

ferromagnetic structure without adopting any intermediate structures, with critical fields ranging from less than 0.1T at 20K to approximately 1.5T at 50K. However, it should perhaps be mentioned at this point that some features of the isothermal measurements of Jiles may be interpreted as arising from the existence of an intermediate step in the magnetisation. The magnetisation data of Gama and Fóglio (1988) show a less steep transition from the antiferromagnetic to the ferromagnetic structure than that observed by Féron, but this may be attributed to demagnetisation effects since the sample was not elliptical. One point, which is probably only of academic interest, is the step observed in their calculated magnetisation plot at 40K. This step is probably of little significance because the model for the calculation only allowed for an eight layer structure, however, similar anomalies have been observed in the measurements of C_{11} and C_{33} included in the paper by Gama and Fóglio, and in the magnetostriction data of Rhyne and Legvold (1965). Both features occur above the critical field derived from magnetisation measurements, indicating a transition within the ferro-cone phase.

The recent neutron scattering data of Cowley et al (1991) on Ho showed that the application of a c-axis field caused q to lock in to commensurate structures. It is remarkable that a field applied perpendicular to the plane containing the moments should stabilise these structures. Although the magnetic structures of erbium and holmium are different these results raise the possibility that a c-axis field may also stabilise those commensurate structures that do not have net ferromagnetic moments, ie those with an even number of quartets to triplets. The cone phase may also be liable to form locked-in structures on the same basis.

Ultrasound measurements have been performed with fields of between 0 and 1.5T applied along the c-axis, with a view to drawing up an H-T phase diagram for erbium which will map the evolution of

commensurate structures with field and temperature. The interpretation of the ultrasound data is complicated by the difficulty in discriminating between two different commensurate structures, and the necessarily qualitative interpretation of the ultrasound data. Consequently the phase diagram derived on the basis of the measurement described here is tentative in nature. It should provide initial information which would make for a more efficient neutron study. The phase diagram will be discussed in the light of the neutron scattering data of Lin et al (1991) which was presented at ICM91 alongside the present work.

7.1 Experimental Details

The sample used for these measurements is the same as that used in the previous chapter. The ideal sample shape for measurements performed in a magnetic field would be an ellipsoid which would overcome demagnetisation problems, however, this is clearly impossible for ultrasound measurements where samples with parallel sides are essential. No magnetisation data is available for this sample but demagnetisation corrections have been estimated using the graphical method of Osborne (1945) and the magnetisation data of Féron and are presented in Appendix C.

The measurement techniques employed were as described in chapter 3. Measurements were made of C_{33}, α_{33}, C_{44}, α_{44} and C_{11}. Shear waves propagating in the basal plane with the polarisation parallel to the c-axis, and shear waves propagating parallel to the c-axis were used to obtain C_{44} and α_{44}. However, the c-axis propagating mode suffered from the high attenuation experienced at zero field. This effect increased as the magnetic field was applied, making measurements at high field difficult.

Consequently only the data collected with the shear wave propagating in the basal plane are presented here, however, the two modes do not produce contradictory results. The attenuation of the signal was high particularly in the ferro-cone regions and the nature of the calculation of the attenuation (by using only two echoes) means that the α_{44} data are less reliable at higher fields.

The longitudinal wave propagated along the c-axis produced good echo trains throughout the temperature and magnetic field range considered allowing both C_{33} and α_{33} to be measured reliably.

Measurements of C_{11} were hampered by the softness of this mode propagated perpendicular to the plane of magnetisation, and the difficulty of bonding to the face which undergoes greatest magnetostriction. On cooling below 52K the echo train decayed into the noise. Some measurements were made on warming from the ferro-cone region, but the echo train usually died away at approximately 30K. Only those measurement which were reliably repeated are included.

All measurements were made at constant fields with the temperature sweeping at the lowest possible rate of approximately 0.5Kmin^{-1} between 50K and 10K, in the higher temperature phase the sweep rate was normally twice that speed. Because of the high hysteresis in $\mathbf{q}$ all data presented here were collected while cooling, although the salient points are the same for measurements made whilst increasing temperature.

The coupling of the elastic constants to the three magnetic phases and the commensurate structures has been discussed in the previous chapter. Only the effects of locked in phases on α_{33} have not been covered and they are considered in section 7.3.

7.2 C_{33} and α_{33}

In zero field C_{33} couples to the 7/2 (b=7) structure, the formation of the 1/4 structure and the T_N (85K), T_M(52K) and T_C(18K) phase transitions. A small inflection was observed at 33K which may be attributed to the formation of the 4/15 (b=15) structure. A shoulder in the hardening of C_{33} as the T_C transition is approached revealed either the lock-in to the $\frac{1}{4}$ structure or the b=23 structure, and a small softening at 48K coincided with the b=7 $\left(\frac{7}{2}\right)$ structure. The attenuation coefficient, α_{33}, showed critical peaks at the T_N, T_M and T_C phase transitions.

The effects of a field applied along the c-axis on C_{33} are dramatically illustrated by the waterfall plot (fig7.1) in which successive scans are displaced by 3K and 0.02 (arbitrary units). The step like feature which becomes more pronounced as the field is increased is characteristic of a ΔE effect (DeKlerk, 1958. for example) which is observed in unsaturated ferromagnetic samples as energy is lost from the ultrasound wave due to the movement of Bloch domain walls. The ΔE usually occurs when the ultrasound wave is propagated perpendicular to the applied field direction and hence the 180° Bloch walls. In this case the dramatic softening is probably the result of the formation of a ferro-cone structure which is soft in comparison to the antiferromagnetic structures, as discussed in the previous chapter. If this is the case one may infer, just from figure 7.1, that two different cone structures exist below T_C. In order to discuss smaller effects, each measurement must be considered individually. Temperatures corresponding to anomalies in the data will be referred to as T_i where the subscript i corresponds to the transition, or the spin-slip distance of the commensurate structure. For example, T_{C1} represents the temperature of the highest temperature transition to a ferro-cone structure. Where a
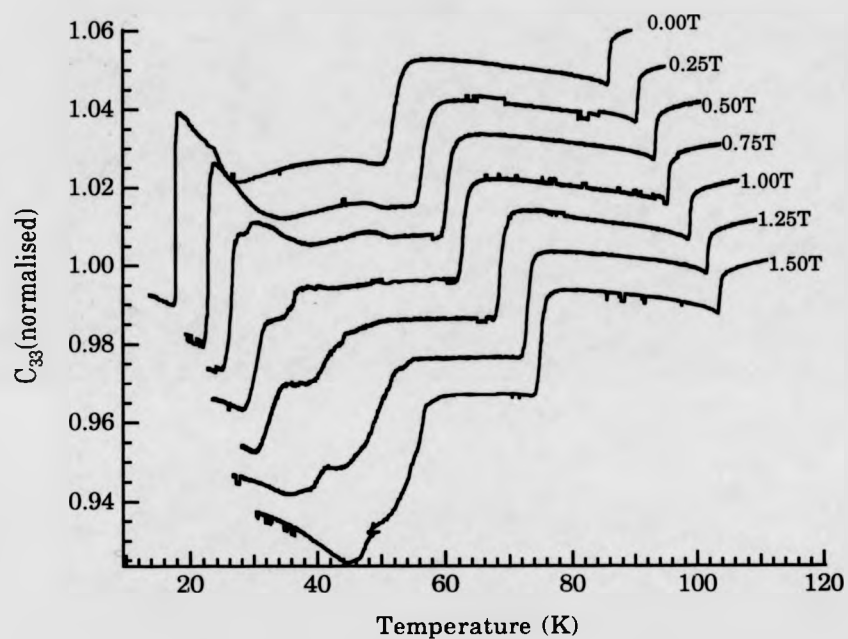
Fig. 7.1 C_{33} vs. tempertaure with applied field varied from0.0T to 1.5T.
The data were collected with decreasing temperature. The
scale corresponds to the 0T data, suceeding measurements
are offset by 3K and 0.02 (arbitrary units).

structure is assumed to lock-in, the lower temperature limit of the phase will be indicated with a single prime, the high temperature limit with a double prime, thus the b=23 phase is locked in between $T_{23''}$ and $T_{23'}$.

With a small field of 0.25T applied along the c-axis, the behaviour of C_{33} (fig.7.2) is very much the same as that in zero field. The anomaly associated with the 2/7 phase is observed at 47K as opposed to 48K in zero field. The region between the sharp fall in C_{33} which corresponds to the development of a basal plane component of the magnetisation at T_M and this anomaly appears as a plateau which hints at a lock in of the 2/7 phase over this region. The continuous hardening associated with the squaring up of the modulation is still seen, however the change of gradient which corresponded to the formation of the 1/4 structure or the b=23 structure at 24K is far less distinct than it was in zero field. The transition at Tc appears to be slightly less dramatic and there is a suggestion of a very small step-like feature immediately prior to the transition. For reasons which will become obvious later the transition to the $\frac{5}{21}$ locked in cone phase will be referred to as T_{C3}. The attenuation data (fig. 7.3) exhibits the same critical behaviour at the principle phase transitions as at zero field, the peak associated with T_M is a little broader.

With a field of 0.5T (fig. 7.4) the departure from the zero field behaviour is much more apparent. No features are observed which were not present on the data at 0.25T, however, the step-like feature at 20K has become more apparent and three transitions may be identified; T_{C1}, the start of the flat region, T_{C2}, the low temperature limit of this region and T_{C3}, the onset of the $\frac{5}{21}$ cone, and are indicated on figure 7.4. The step probably corresponds to the formation of a ferro-cone structure, the relative softening depending on the divergence of the moments from the c-axis. Allowing for demagnetisation corrections, the formation of a cone phase in the region is

142

Fig. 7.2 C_{33} vs. temperatrure at 0.25T.
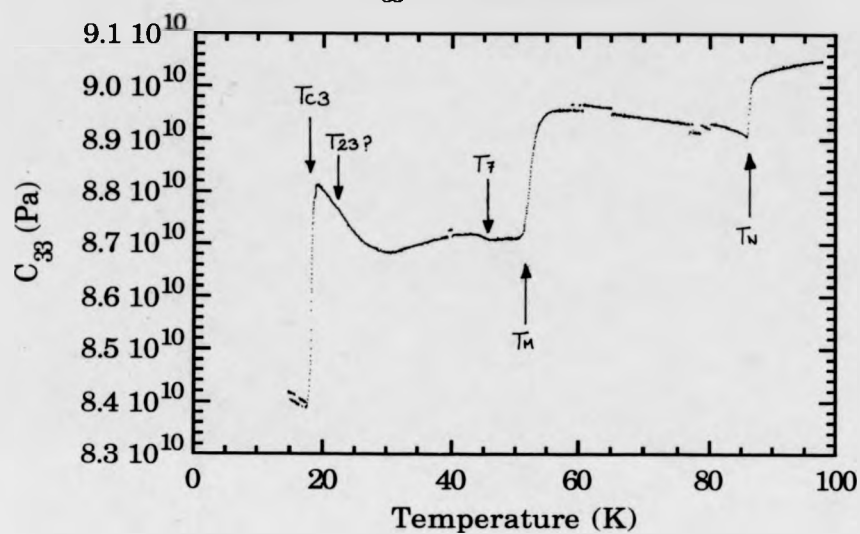
Fig. 7.3 α_{33} vs. temperature at 0.25T.
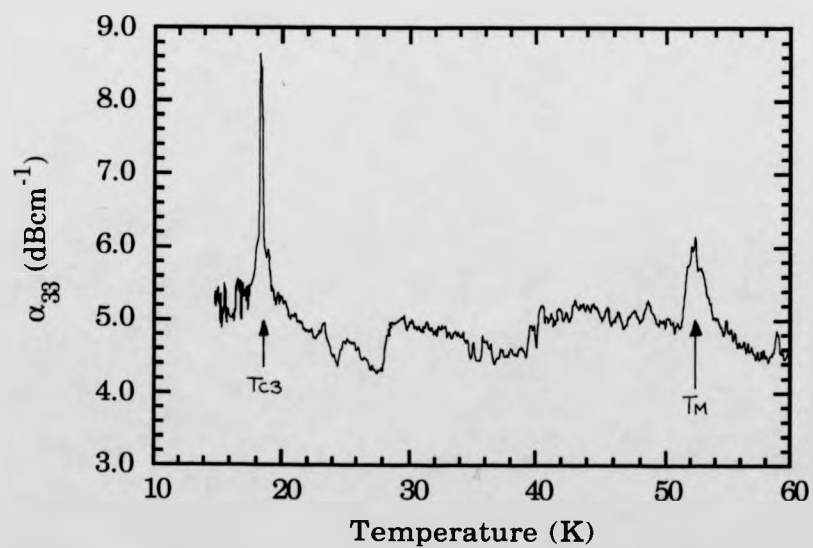
Fig. 7.4 C_{33} vs. temperature at 0.5T.
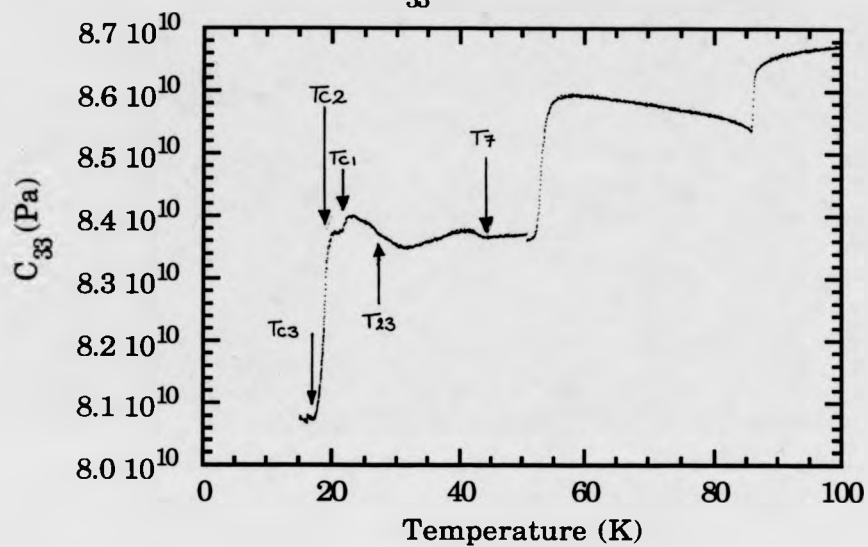
Fig. 7.5 α_{33} vs. temperature at 0.5T
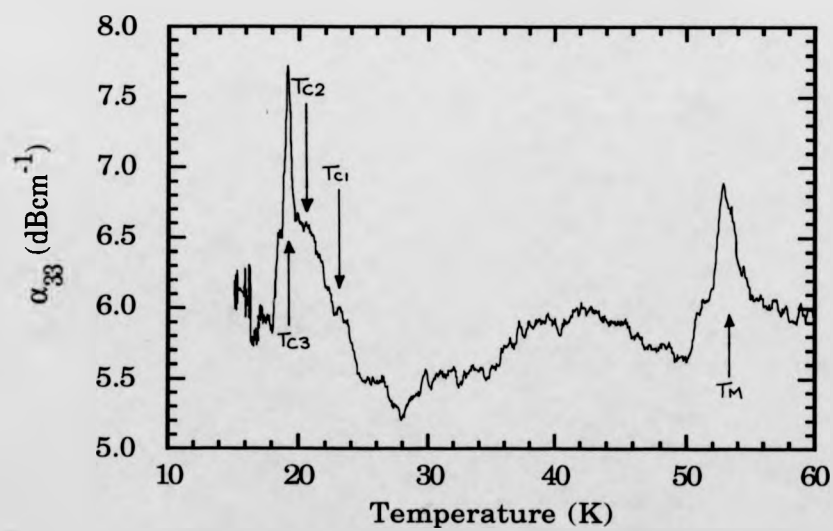
in reasonably good agreement with the critical field measured by Féron. The attenuation data (fig. 7.5) show critical peaks at T_M at 53K and at T_{C3} at 19K. Above T_{C3} α_{33} shows a broad feature coincident with the small step in C_{33} which may be attributed to the transitions at T_{C2} and T_{C1}. The 2/7 anomaly has moved to 44K with the flat region becoming more clearly visible, reinforcing the view that the 2/7 phase has locked in in this region.

The destruction of the 1/4 phase appears to be complete by 0.75T with no hardening prior to C_{33} (fig. 7.6). The transition to the cone structure T_{C1} takes place at 26K with a small anomaly visible just above T_{C1} which may constitute the first evidence of a locked-in phase in the intermediate region, possibly b=23. The attenuation data (fig. 7.7) displays peaks at 26K, 24K and 20K, corresponding to T_{C1}, T_{C2} and T_{C3} respectively. Less distinct features are visible at 29K and 28K, providing supporting evidence for the locked-in elliptical structure. They have been tentatively labelled $T_{23''}$ and $T_{23'}$. The broad regions between peaks may arise as a result of $\mathbf{q}$ being locked-in in this region. The mechanism which produces an increase in the attenuation at these regions will be discussed in the next section.

As the field is increased to 1.0T and 1.25T the measurements display the same features, the 2/7 region continues to grow, and the region between T_{C1} and T_{C2} becomes increasingly deep. The C_{33} and α_{33} data collected at 1.0T are presented in figures 7.8 and 7.9 respectively. The peak in α_{33} at T_{C1} was so high as to cause a temporary loss of signal, which explains the discontinuities in the measurements of C_{33} and α_{33}. With a field of 1.25T there is a suggestion of an additional phase above T_{C1} in the C_{33} data (fig. 7.10). The two transitions are tentatively indicated $T_{15''}$ and $T_{15'}$. While the α_{33} data (fig.7.11) show a broad peak in the attenuation around 35K, suggesting that two or three transitions take place in the region between 38K and 31K. The region which is likely to correspond to the locked-in b=15 structure is indicated.

143

Fig. 7.6 C_{33} vs. temperature at 0.75T.
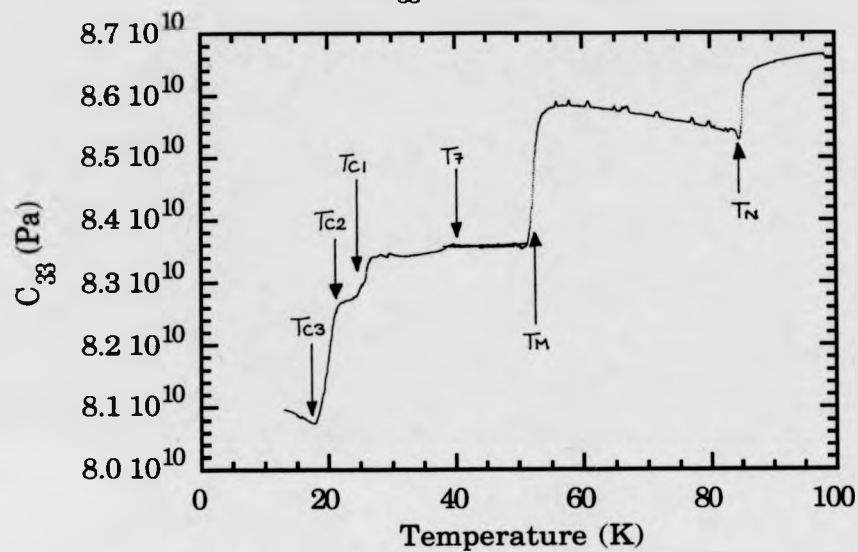
Fig. 7.7 α_{33} vs. temperature at 0.75T.
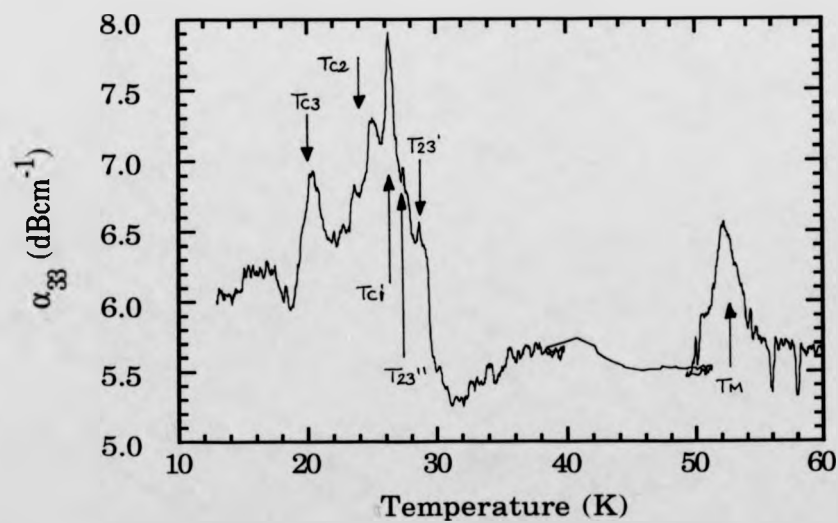
Fig. 7.8 C_{33} vs. temperature at 1.0T.
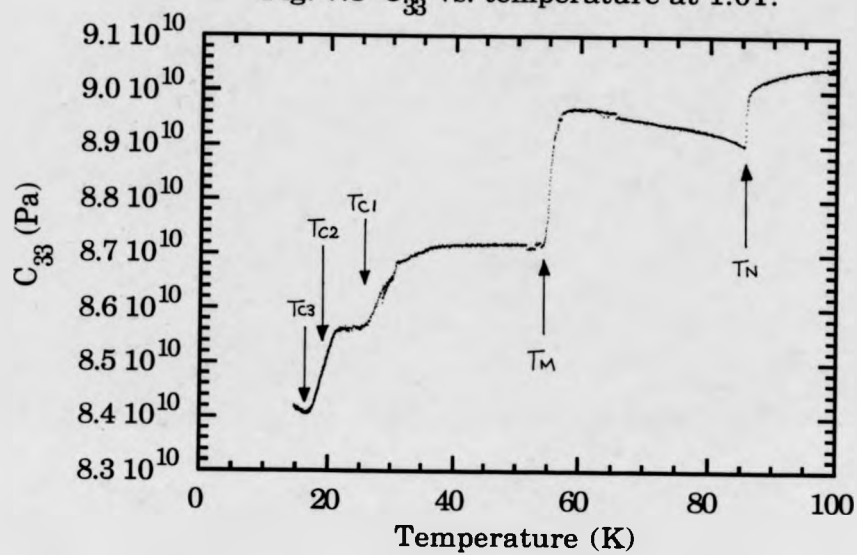
Fig. 7.9 α_{33} vs. temperature at 1.0T
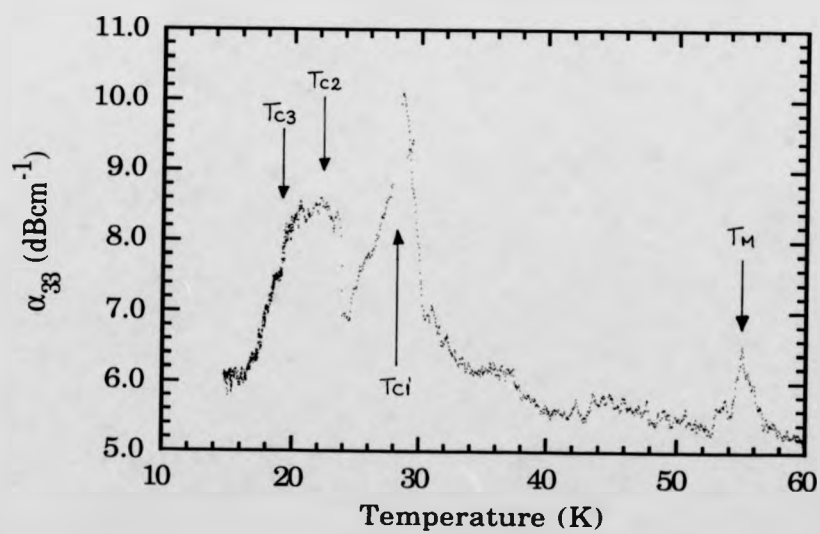
Fig. 7.10 C_{33} vs. temperature at 1.25T
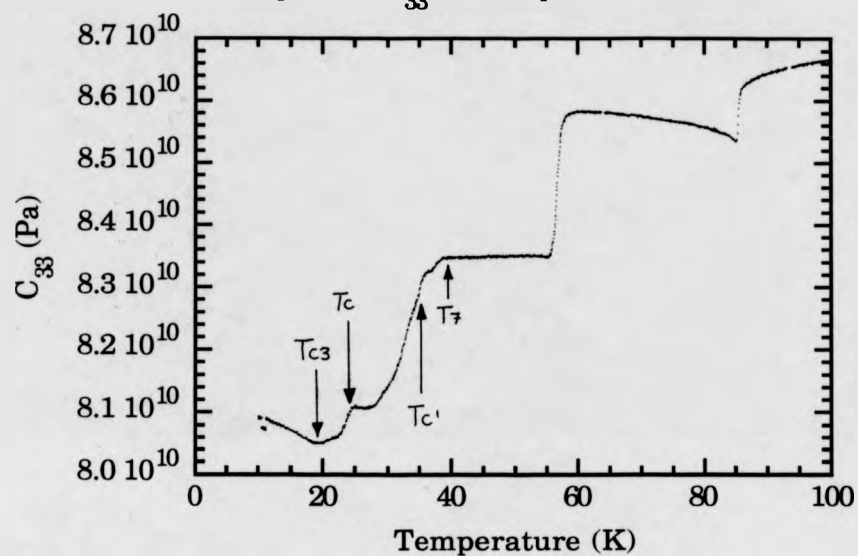
Fig. 7.11 α_{33} vs. temperature at 1.25T.
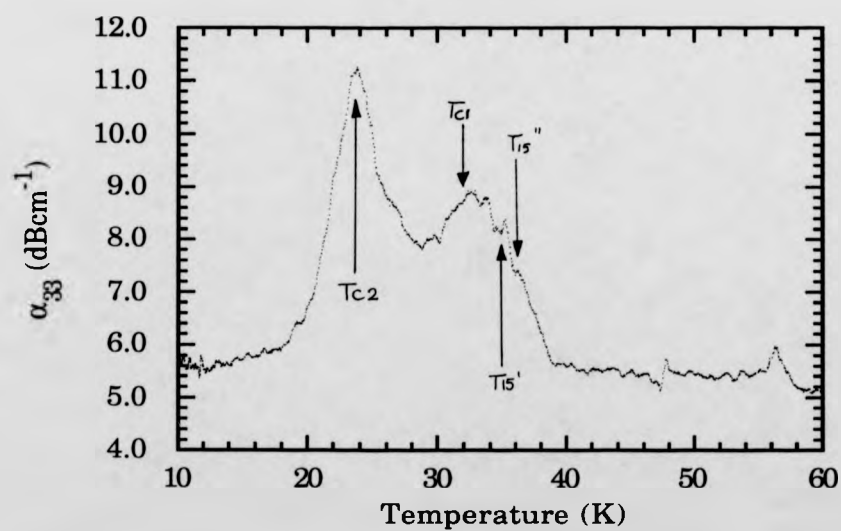
At 1.5T the data appear greatly simplified. C_{33} (fig. 7.12) shows that T_{C3} has increased to 25K, with T_{C2} and T_{C1} at 28K and 38K respectively. The attenuation data at 1.5T (fig.7.13) show large peaks at 36K and at 26K, possibly arising from a lock-in of q between T_{C1} and T_{C2}.

The anomalies and transitions identified in the C_{33} and α_{33} data are summarised in tables 7.1 and 7.2. A tentative partial phase diagram has been drawn based on these measurements (fig. 7.14) allowing the identification of the critical field of the ellipsoidal structure. However, they supply little evidence to support the existence of locked in commensurate structures. What evidence there is, is supplied by the peaks in α_{33} and the small features in C_{33} immediately prior to T_{C1} which provide some evidence for the existence of locked in 6/23 and 4/15 phases. The evidence for the existence of the squared up 1/4 phase up to about 0.5T is supplied by the stiffening of the elastic constant, however, the distinct step observed at zero field is not clear. In fact the squaring up of the modulation as the eight layer structure is approached may never actually be achieved due to the onset of the cone structure. The most interesting feature of the phase diagram is the existence of what appear to be three cone structures, two of which (the low temperature 5/21 cone below T_{C3} and the higher temperature cone between T_{C2} and T_{C1}) show evidence of a lock-in in q. A reasonably reliable way of confirming that these phases are ferro-cone structures is to calculate the critical fields and compare them to other magnetisation measurements. This has been done, and the results will be presented after the other ultrasound data has been discussed.

144

Fig. 7.12 C_{33} vs. temperature at 1.5T.
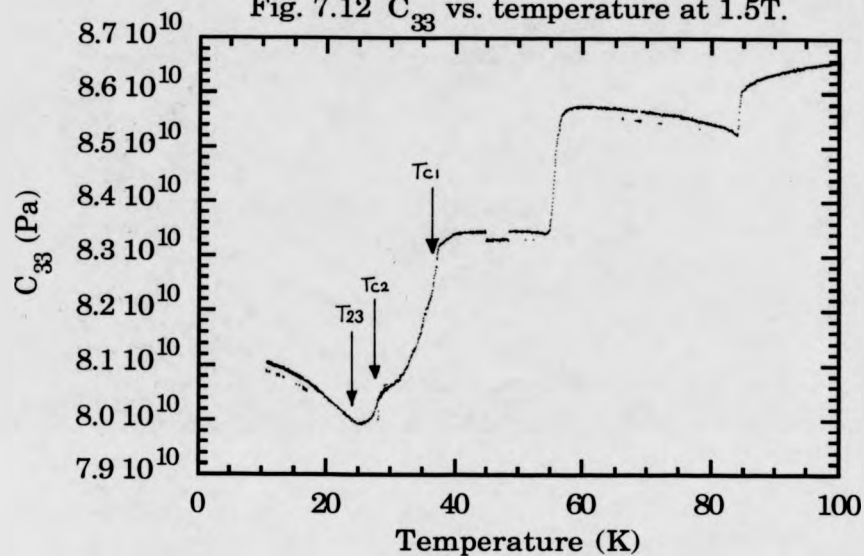
Fig. 7.13 α_{33} vs. temperature at 1.5T.
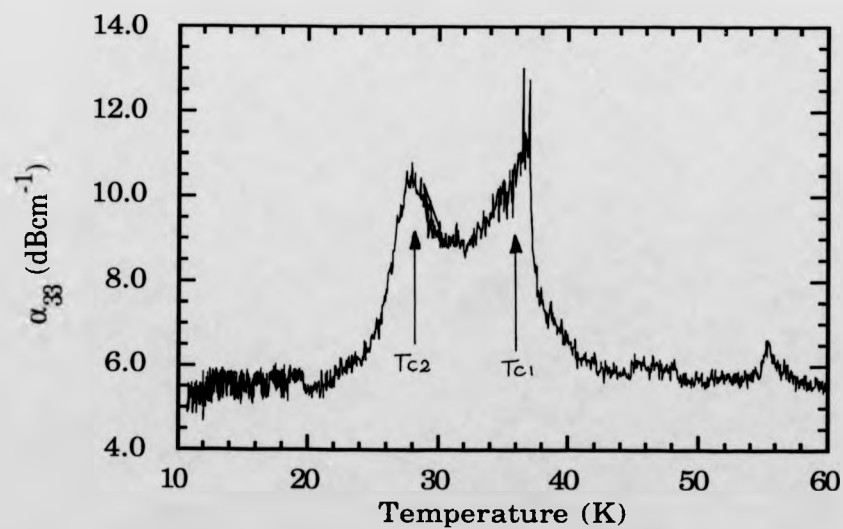
Table 7.1 Anomalies arising in C_{33} as a result of an applied field parallel to the c-axis

Field (T)	T_{C3}	T_{C2}	T_{C1}	$T_{23'}$	$T_{23''}$	$T_{15'}$	$T_{15''}$	T_{11}	T_7	T_M
0.00	18			24.5			33		48	52
0.25	18			24?					47	52
0.50	19	21	22						45	53
0.75	19	21	26		27?				40	53
1.00	19	21	28							55
1.25	20	24	35				36?		39	55
1.50	25	27	38						40	55

Table 7.2 Anomalies arising in α_{33} as a result of an applied field parallel to the c-axis

Field (T)	T_{C3}	T_{C2}	T_{C1}	$T_{23'}$	$T_{23''}$	$T_{15'}$	$T_{15''}$	T_{11}	T_7	T_M
0.00	18									52
0.25	19									52
0.50	20	21	23							53
0.75	20	23?	26	27	29					53
1.00	19	22	33							55
1.25	19	25	32			34	36?			55
1.50	25	27	38							56
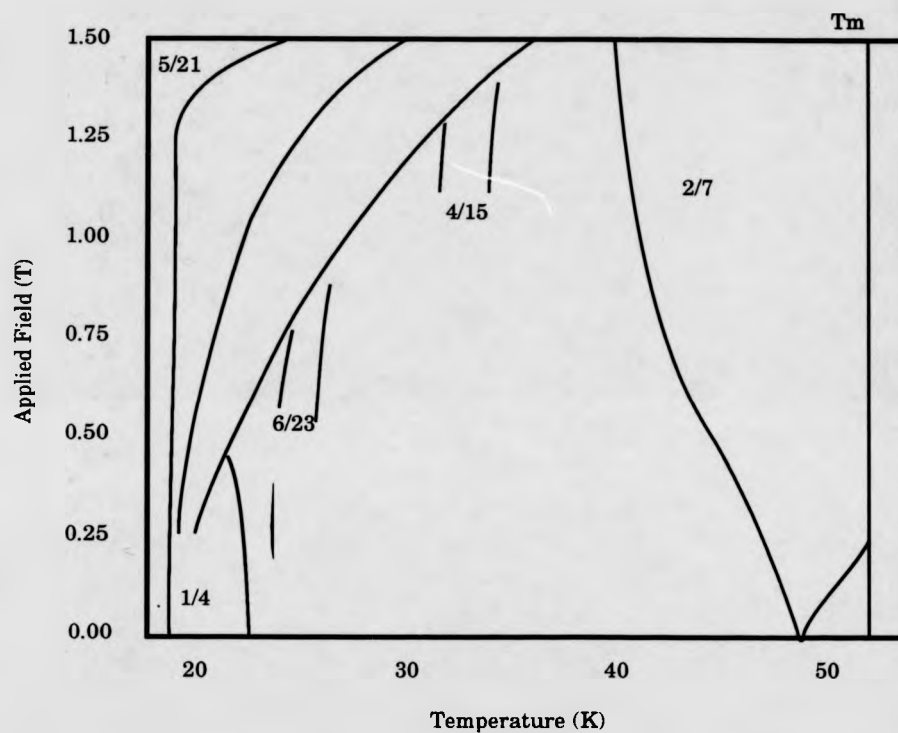
Fig. 7.14 The applied field-temperature phase diagram of Er.
constructed from measurements of C_{33} and α_{33}.

7.3 Commensurate Phases and α_{33}

The peaks in the attenuation of a compressional wave propagated along the c-axis arising from order-order and order-disorder transitions have been discused in the chapter 3. The case for the transitions between commensurate and incommensurate regions is similar in that the attenuation arises as a result of the modulation of the exchange by the longitudinal strain.

Tachiki et al (1968) have studied the interaction of the compressional wave with a helical antiferromagnet. Their argument is just as valid for the elliptical structure, since it is based on the renormalisation of the exchange energy as a result of the ultrasonic strain and does not consider anisotropic contributions. If we consider a length of the sample shorter than the ultrasonic wavelength we may consider, as we have done in chapter 3, the ultrasonic wave as an ultrasonic strain field. Under the influence of this strain the lattice is deformed, the conduction band is distorted, and the conduction electron will assume a new configuration which is stable with respect to the new distorted conduction band. The relaxation time for the process is assumed to be short in comparison to the time for the passage of the ultrasonic pulse. The overall result is a small change in q, accompanying the passage of the ultrasound wave. What we have in the case of a locked in commensurate structure is a situation in which q is clamped by the magnetoelastic energy and when a magnetic field is applied, the Zeeman energy.

Quoting Tachiki's expression for the exchange energy with the lattice under the influence of strain ε

$$E_{ex} = NS^2 \left(\frac{1}{2} \frac{\partial^2 J}{\partial q^2} (\Delta q)^2 + \frac{d^2 J}{dq d\varepsilon} (\Delta q)\varepsilon + \frac{1}{2} \frac{d^2 J}{d\varepsilon^2} \varepsilon^2 \right)$$

145

where N is the total number of spins and J and S have their usual meanings.

Clearly, since $\frac{\partial^2 J}{\partial \varepsilon^2}$ is positive, the exchange energy will be increased by the strain and in order to compensate $\mathbf{q}$ is altered. If $\mathbf{q}$ is clamped in some way the exchange energy cannot be dissipated in this manner. Consequently, in the case of the locked in commensurate structures, the ultrasound strain increases the exchange energy until it overcomes the magnetostrictive and Zeeman energies and adopts a new configuration, thus extracting energy from the ultrasound wave. The amount of energy absorbed from the ultrasound wave is related to the magnetostrictive and Zeeman energies stabilising the structure and inherently the stability of the commensurate structure. At the onset of the commensurate phase, one magnon-one phonon soft mode behaviour would be expected similar to that at an order-order transition.

The fact that the 2/7 phase does not show a perceptible increase in ultrasonic attenuation, and the absence of strong coupling to α_{33} at low fields suggest that the magnitude of the effects depend strongly on the magnetostrictive energy, which is more significant at lower temperatures, and that the commensurate structures are less stable at lower fields.

7.4 C_{44} and α_{44}

In zero field, the C_{44} and α_{44} measurements were the most useful in identifying the position of commensurate structures due to the tendency of the shear strain to follow the cone and elliptical structure. With the application of a magnetic field the temperature dependence of C_{44} attains

146

where N is the total number of spins and J and S have their usual meanings.

Clearly, since $\frac{\partial^2 J}{\partial e^2}$ is positive, the exchange energy will be increased by the strain and in order to compensate $\mathbf{q}$ is altered. If $\mathbf{q}$ is clamped in some way the exchange energy cannot be dissipated in this manner. Consequently, in the case of the locked in commensurate structures, the ultrasound strain increases the exchange energy until it overcomes the magnetostrictive and Zeeman energies and adopts a new configuration, thus extracting energy from the ultrasound wave. The amount of energy absorbed from the ultrasound wave is related to the magnetostrictive and Zeeman energies stabilising the structure and inherently the stability of the commensurate structure. At the onset of the commensurate phase, one magnon-one phonon soft mode behaviour would be expected similar to that at an order-order transition.

The fact that the 2/7 phase does not show a perceptible increase in ultrasonic attenuation, and the absence of strong coupling to α_{33} at low fields suggest that the magnitude of the effects depend strongly on the magnetostrictive energy, which is more significant at lower temperatures, and that the commensurate structures are less stable at lower fields.

7.4 C_{44} and α_{44}

In zero field, the C_{44} and α_{44} measurements were the most useful in identifying the position of commensurate structures due to the tendency of the shear strain to follow the cone and elliptical structure. With the application of a magnetic field the temperature dependence of C_{44} attains

146

new structure, but attenuation is very high in the conical phase and overall the attenuation is greater making reliable measurements difficult. The rapid increase in α_{44} prior to T_C in the zero field data may be attributed to the onset of the locked in $\frac{1}{4}$ structure, however, the possibility that it corresponds to the development of the moments out of the a-c plane has been discussed in the previous chapter. While some ambiguity remains, this feature will produce inevitable confusion in the interpretation of the ultrasound data in a magnetic field.

With a small field of 0.25T the C_{44} data (fig. 7.15) shows little difference from that at zero field. There is some evidence of small dips at 42K and 33K which may correspond to the b=11 and b=15 structures. The coupling to the b=11 structure is the first coupling of the ultrasound to a commensurate structure which does not have a net ferromagnetic moment. Similar features are also visible at 25K and 28K, possibly corresponding to the transitions associated with the b=23 structure. The signal became unmeasurably small below 23K. Small changes in gradient are more difficult to identify at lower temperatures and are more easy noted in the attenuation data (fig.7.16). In zero field, only one peak was visible at 24K which corresponds to the lower temperature transition from the b=23 lock in to an incommensurate region. With the magnetic field applied three clear peaks at 24K, 25K 28K and two less distinct peaks at 30K and 34K are visible. The peak at 28K may herald the onset of the b=23 structure, with one of the lower peaks indicating the lower temperature limit of this phase. The extra peak is difficult to interpret and may arise from the formation of the b-19 structure. The broad features at 30K and 34K may possibly arise from the presence of the b=15 structure. The high attenuation at 23K observed at room temperature is also observed with a field of 0.25T. Whether this high

Fig. 7.15 C_{44} vs.temperature at 0.25T
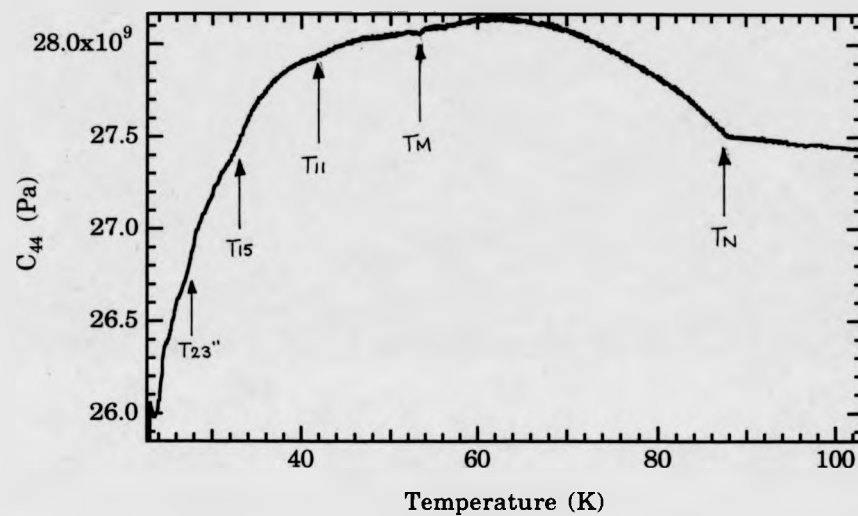
Fig.7.16 α_{44} vs. temperature at 0.25T.
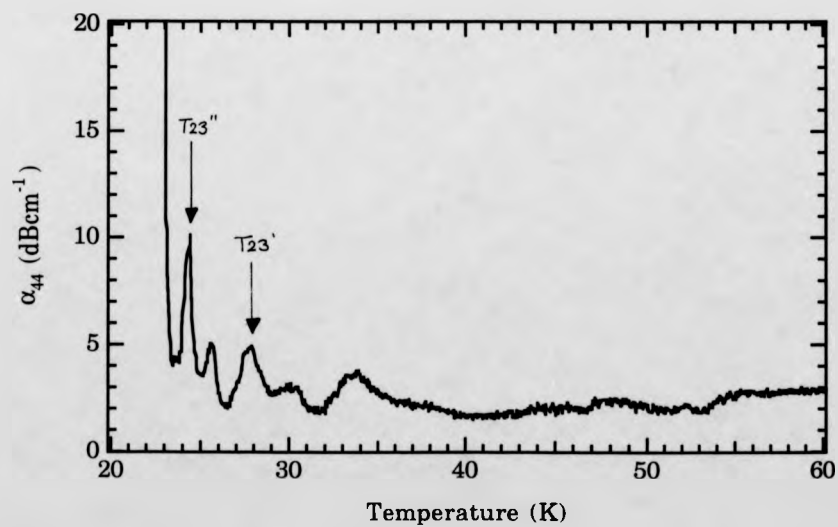
attenuation is due to the formation of a cone structure, or the tendency of the moment to fall out of the a-c plane is not clear.

At 0.5T (figs. 7.17 and 7.18) the situation appears to be less complicated. C_{44} exhibits anomalies which correspond to the b=11, b=15 and b=23 structures as indicated. A peak in α_{44} corresponds to the anomaly at $T_{23"}$ in C_{44}. No other distinct features are displayed by α_{44} before the attenuation becomes prohibitively large at 23K. A small dip at 42K corresponds to the formation of the b=11 structure.

With a field of 0.75T the effect of the field on C_{44} (fig. 7.19) is more dramatic and the attenuation of the signal at low temperatures is so large as to make the relative measurements unreliable. The small dip observed at 0.5T associated with the b=11 structure is now considerably bigger. Anomalies at 31K and 29K are also visible. The attenuation data (fig. 7.20) show a peak at 40K associated with T_{11}. An unusual feature is displayed between 32K and 28K, with the attenuation initially appearing to reduce prior to a large increase. This feature has been tentatively attributed to the locked in b=15 phase.

At 1.0T (figs. 7.21 and 7.22) the echo trace died away into the noise between 24 and 23K but the signal reappeared and on one occasion measurements were possible down to 12K. The dip at 37K corresponding to b=11 is now accompanied by another at 32K which may be due to the increasing stability of the b=15 structure which may persist down to another anomaly at 27K. The low signal level is reflected in the scatter of the α_{44} data. The unusual feature which was observed at 0.75T appears to be considerably broader. At 24K the structure appears to undergo the transition to the cone producing a large critical peak in α_{44}. The softness of the region between 23K and 22K relative to that below 18K suggests that the two cone phases have different structures.

Fig. 7.17 C_{44} vs temperature at 0.5T.
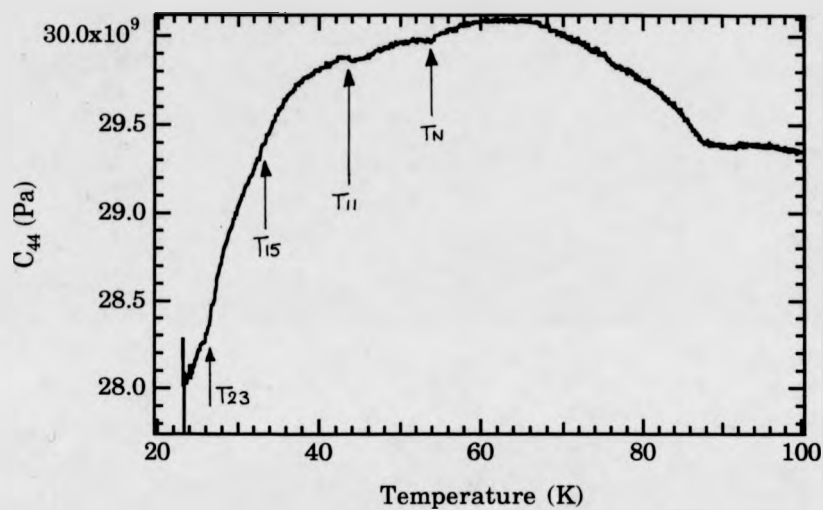
Fig. 7.18 α_{44} vs. temperature at 0.5T.

Fig. 7.19 C_{44} vs. temperature at 0.75T.
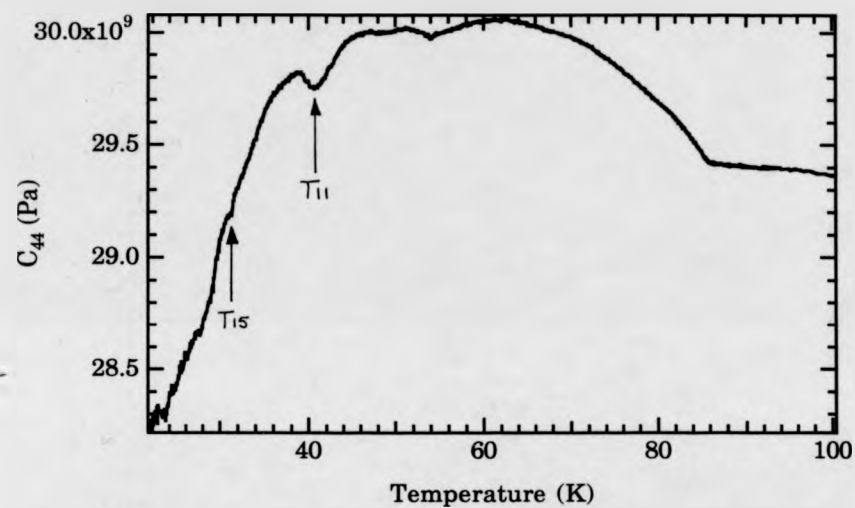
Fig. 7.20 α_{44} vs. temperature at 0.75T.
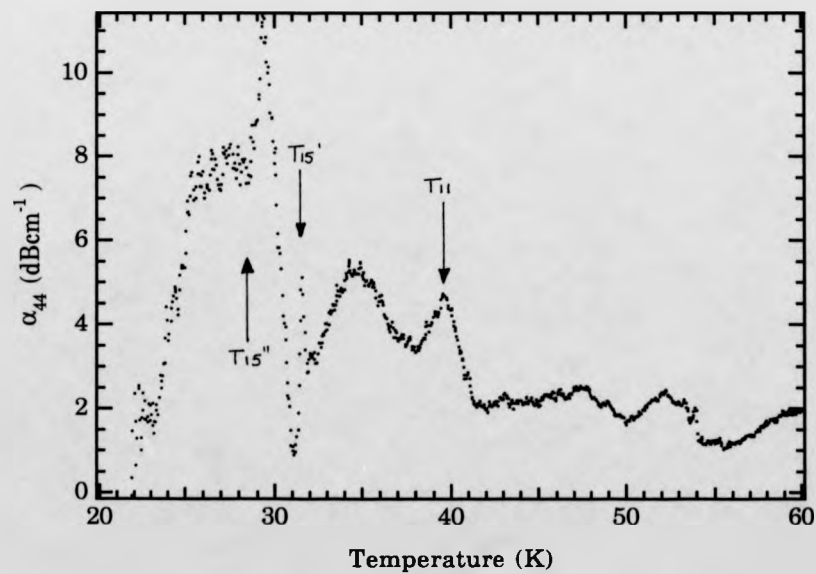
Fig. 7.21 C_{44} vs. temperature at 1.0T.
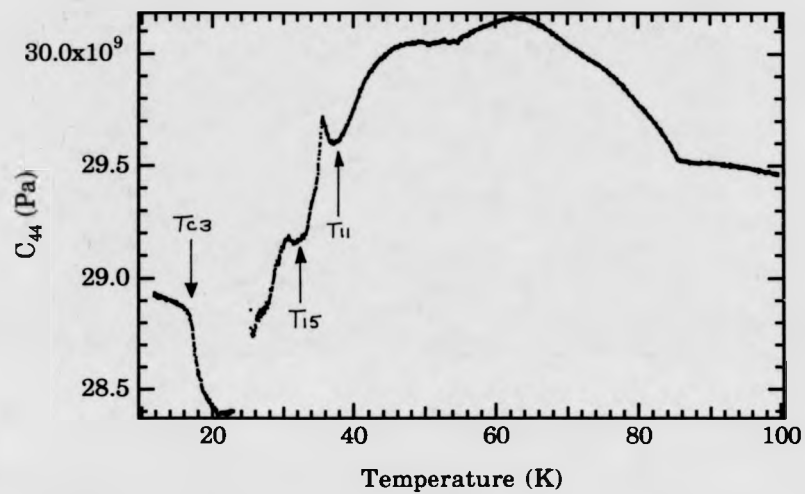
Fig. 7.22 α_{44} vs. temperature at 1.0T.
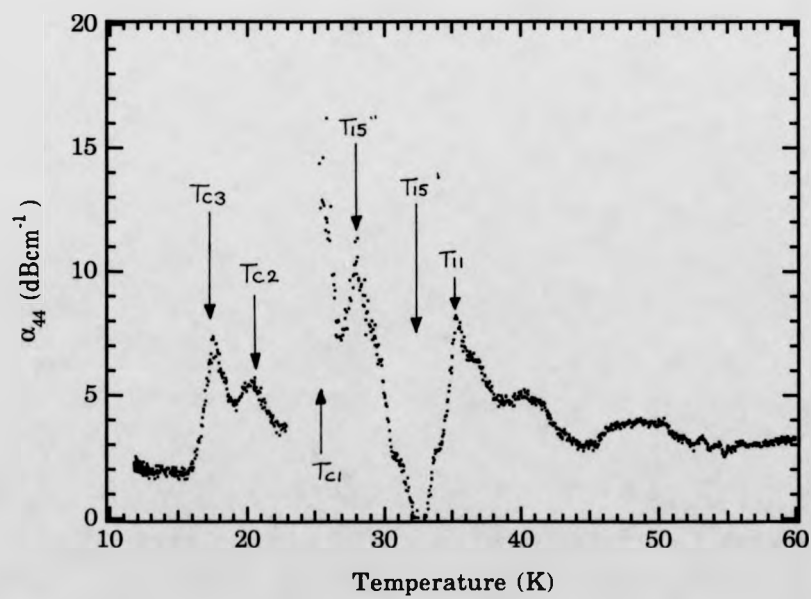
The encroaching cone phase limited measurements at 1.25T (figs. 7.23 and 7.24) to above 27K. Anomalous behaviour corresponding to the existence of the b=15 and b=11 structures was observed as indicated on the figure. Again a large peak in α_{44} accompanies T_{C1} this time at 32K. The dramatic reduction in α_{44} and subsequent increase which has so far been attributed to the b=15 phase is still observed.

At 1.5T (fig. 7.25) the sharp dip at T11 has become less distinct which would be expected with the b=11 and b=15 phases effectively squeezed out by the growing b=7 phase and the ferro-cone phases. The ferro-cone transitions are indicated.

On the basis of the C_{44} and α_{44} measurements the partial phase diagram (fig.7.26) has been constructed. More information is available about the lower temperature structures than from the longitudinal wave data and there is good agreement between both phase diagrams, however several ambiguities still exist. The high value of α_{44} in the cone phases has hampered a thorough investigation of this region, however, measurements at 1.5T suggest an additional phase within the lower temperature cone region. The difference in the position of the initial transition to the ferro-cone structure between the shear wave and the longitudinal wave phase diagrams is probably because the transition point on the C_{33} data was assumed to be the start of the softening, whereas the peak in α_{44} was assumed to be the transition point in the shear wave data.

7.5 C_{11}

The C_{11} mode, a longitudinal wave propagated across the basal plane, is notoriously difficult to measure due to bonding problems, but even more difficult when the moments are confined to a plane perpendicular to

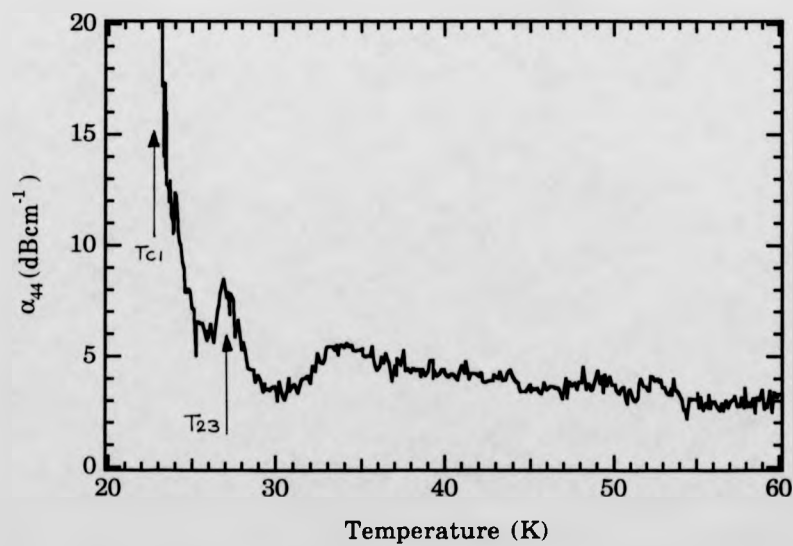Fig. 7.23 C_{44} vs. temperature at 1.25T
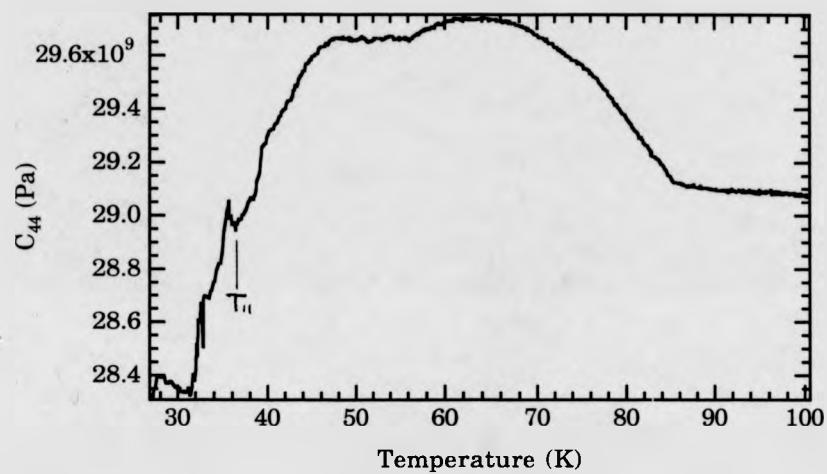
Fig. 7.24 α_{44} vs. temperature at 1.25T

Fig. 7.25 C_{44} vs. temperature at 1.5T.

Table 7.3 Anomalies arising in C_{44} as a result of an applied field parallel to the c-axis

Field (T)	T_{C3}	T_{C2}	T_{C1}	$T_{23'}$	$T_{23''}$	$T_{15'}$	$T_{15''}$	T_{11}	T_7	T_M
0.00			23?	24	27					52
0.25			23	25	26	33	33	42		53
0.50			23		26	33		44		53
0.75			22			27	31	41		54
1.00	18					31	33	38		55
1.25		28	32					36		54
1.50	28	30	34					38		55

Table 7.4 Anomalies arising in α_{44} as a result of an applied field parallel to the c-axis

Field (T)	T_{C3}	T_{C2}	T_{C1}	$T_{23'}$	$T_{23''}$	$T_{15'}$	$T_{15''}$	T_{11}	T_7	T_M
0.00				24						
0.25			23	25	28					
0.50			23		26					
0.75						28	32	41		
1.00	18	20	23			28	33	38		
1.25		28	32			36	37	39		
1.50										

Fig. 7.26 The applied field-temperature phase diagram of Er, constructed from measurements of C_{44} and α_{44}.

the propagation direction, as they are in the intermediate phase of erbium. The only measurements which were possible were those performed while warming from the cone phase and they met with only limited success, the signal usually disappearing at Tc. However at 0.5T measurements were possible up to approximately 30K, possibly due to the more gentle transition at T_C.

Figures 7.27 and 7.28 provide some illustration of the problems with this measurement, the high level of noise arising as a result of the weak signal. Two dips are clearly visible in C_{11}, which, taking into account the hysteresis of the order of 2K correspond to the formation the higher temperature cone, and the 6/23 structure. The absence of strong coupling to the lower temperature cones is not understood. Since the wave is propagating perpendicular to the magnetisation C_{11} would show ΔE type effects on the formation of a ferromagnetic structure, which is not saturated however, a similar softening may be explained in terms of the additional symmetry elements arising from the formation of commensurate structures which display a net ferrmomagnetic moment.

The attenuation data also show very pronounced features at 22K and between 28K and 30K. The low signal level is such that the other structure visible in α_{11} cannot be regarded as reliable.

7.6 Discussion and Conclusions

By combining the C_{33}, α_{33}, C_{44} and α_{44} data the tentative applied field- temperature phase diagram (fig7.29) has been drawn. The most outstanding ambiguity is the nature of the three phases which have been referred to as cones. The lower temperature phase which is stable at zero field appears to remain intact right up to 1.5T in good agreement with the

Fig. 7.27 C_{11} vs. temperature at 0.5T.
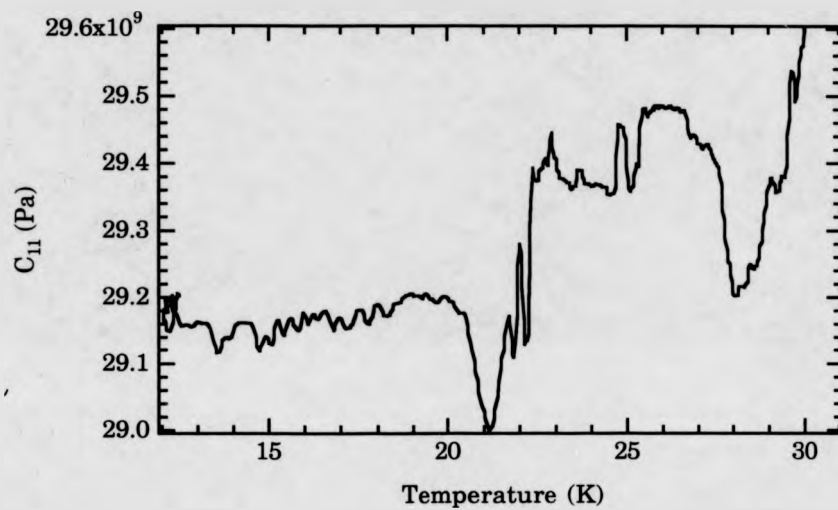
Fig. 7.28 α_{11} vs. temperature at 0.5T.
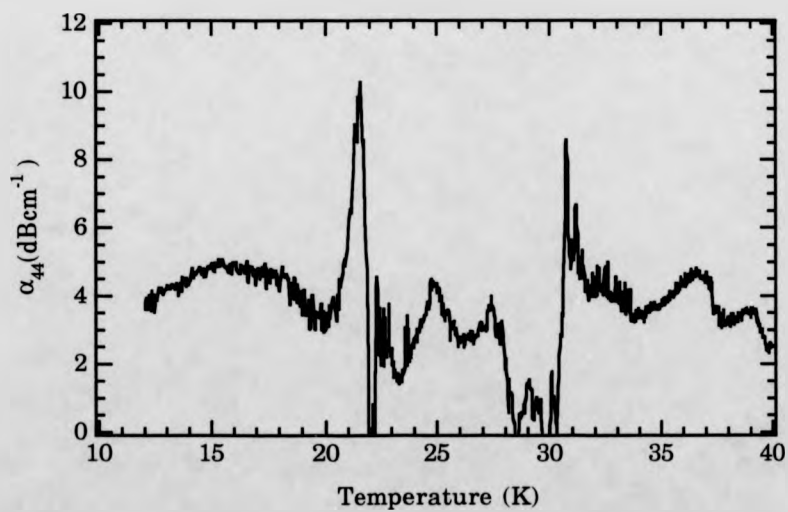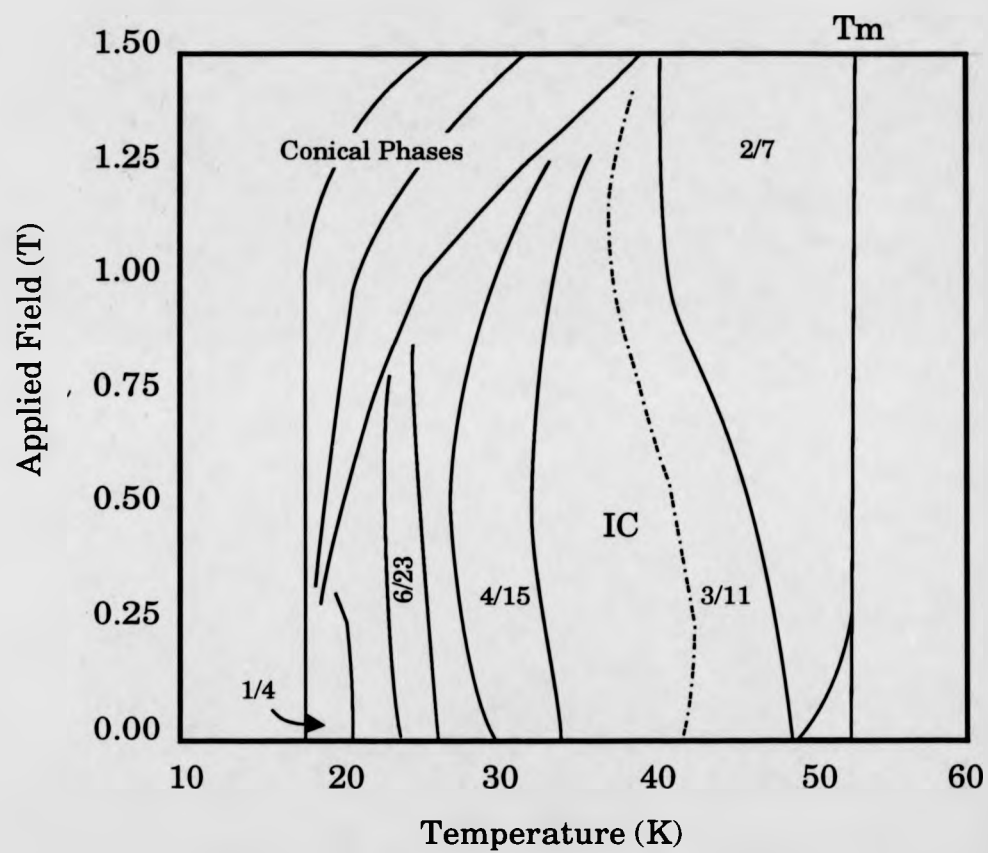
Fig. 7.29 The applied field-temperature phase diagram of Er.

measurements of Bozorth (1972). The other two cone phase are more difficult to understand. By comparing the critical field for the onset of each phase with magnetisation measurements we can deduce which of the transitions is actually the transition to the ferromagnetic cone. The graph of the critical temperatures in comparison to the data of Féron (fig7.30) clearly shows, even within the considerable doubt arising from the estimated demagnetisation factor, that it is the higher temperature transition which corresponds to the onset of ferromagnetism established by the magnetisation measurements.

This ultrasound phase diagram appears to be in broad agreement with that of Lin produced on the basis of neutron diffraction data. The stability of the 2/7 phase is similar. The most obvious difference is the stability of the 6/23 structure on our phase diagram. At 0.5T Lin observed a lock in at 4/15 but not at 6/23. However, there does appear to be a great deal of sample dependence of the evolution of q and cooling rates and thermal history are also likely to play an important role. In zero field Lin has not observed a lock in to q=6/23 but to q=5/19 apparently contradicting the neutron data presented in the previous chapter.

At 1.5T Lin observed q reducing continuously from 2/7, at the transition to the cone structure, down to the 5/21 cone, however, an inflection was observed at q=1/4 and measurements at higher field revealed a cone structure locked into 1/4. Thus the three cone phases observed in the ultrasound data may be a locked in 1/4 cone, an intermediate incommensurate cone and the low temperature 5/21 cone.

The 1/4 cone structure is not commensurate with respect to either the basal plane or c-axis structure and its observation by neutron diffraction is surprising.

The identification of the commensurate regions from the ultrasound data has been qualatative and has assumed that only those structure which

Fig . 7.30. Critical Fields for the conical phases of Er for comparison of the ultrasound data presented in this work with the magnetisation data of Féron (1969).
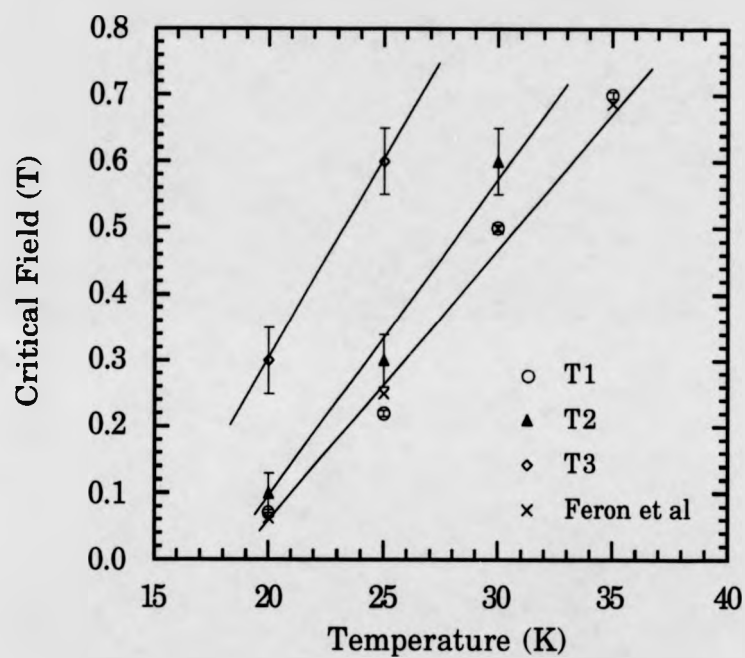
were stable at zero field will form locked-in structures on the application of a field. the possibility remains of other structures such as b=19 or even b=27 structures becoming stable albeit over very limited temperature ranges. Another possibility is that structure akin to helifans (Jensen and Mackintosh, 1990) may develop in which combinations of quartets and triplets which were not stable in the absence of an applied field may develop.

Clearly, further neutron experimental work is required to improve our understanding of the applied field behaviour of Er. Dr Lin and co-workers are awaiting delivery of a high purity sample on which to continue their study. Our own work is hampered by the inavailability of the I.L.L.. The single crystal diffractometer (SXD) at ISIS has been shown to produce promising results when used to monitor the high order peaks exhibited by Ho in the helical phase (Stirling et al, (1990) and if suitable sample environment is available may provide an alternative to D10.

References

Cowley R.A., Jehan D.A., McMorrow D.F., McIntyre G.J., Phys. Rev. Letts. 66 1521 (1991).

DuPlessis P deV J. Phys. F: Metal Phys. 6 873 (1976).

Féron J.L., Hug G., Pauthenet R., Z. Angew (Math.) Phys. 30 61 (1970).

Flippen R.B., J. Appl. Phs. 35, 1047 (1964).

Gama S., Fóglio M.E., Phys. Rev. B 37 2123 (1988).

Jensen J., Machintosh A.R., Phys. Rev. Letts. 64 22 2699 (1990).

Jiles D.C., Palmer S.B., J. Phys. F: Metal Phys. 11 45 (1981).

Lin H., Collins M.F., Holden T.M., Wei W., ICM91 to be published in J. Magn. Magn. Mats. (1991).

Osborne J.A., Phys. Rev. 67 351 (1945).

Rhyne J.J., Legvold S., Phys. Rev. 140 A2143 (1965).

Stirling W.G., Tang C.C., Haycock P.W., Wilson C.C., ISIS Experimental Report SXD/89-1/16 (1990).

Tachiki M., Levy M., Kagiwada R., Lee M.C., Phys. Rev. Letts 21 16 1193 (1968).

Chapter 8

Discussion, Conclusions and Further Work.

The magnetic properties of the Gd-Lu alloy system and those exhibited by erbium and holmium-erbium represent two quite diverse facets of rare earth magnetism. In the former, the ordering is dictated solely by two-ion effects, in the latter competition between two-ion and single ion interactions give rise to the complex behaviour. Consequently, it is difficult to draw an overall conclusion to the work presented here.

An automated ultrasound measurement system has produced elastic constant data with good point to point precision which has allowed the delineation of magnetic phases thereby increasing the efficiency of neutron scattering experiments where time is at a premium. In addition, ultrasound data has revealed unusual features which are not immediately apparent from neutron scattering data, such as high order commensurate structures in Ho, Er and Ho-Er. However, there is still room for improvement of the automated system as it stands. The use of a more powerful pulse generator will allow measurements throughout attenuating phases of magnetic systems, and in materials which have proved difficult to measure so far, such as superconducting polycrystals. An improvement on the point to point precision may be achieved by

adopting a cepstral technique (Gericke O.R., 1990), however, with a considerable loss of speed. The current method for the calculation of the attenuation coefficient has proved satisfactory for the identification of phase transitions, however, a more reliable technique involving the fitting of an exponential function to the decaying echo train would undoubtedly improve the quality of the data collected. At present the digitised waveform of (usually) two echoes is read into the computer for analysis, and the adaptation of the program to perform a fit to a longer echo train would be reasonably straight forward.

New detail has been added to the phase diagram of the Gd-Lu alloy system, which has been shown to be very similar to that of Gd-Y. The principle areas of interest remain the ferro-I region, and the HAF-canted ferro transition where the turn angle is seen to tend to zero at the transition. From this work and previous work it is clear that the transition comes about via the growth of domain walls, however, it is still not clear why an out of plane component of the magnetisation should develop.

Further work should be directed at providing a more thorough understanding of the ferro-I region and the HAF-canted ferro transition. The Ferro-I region in Gd-Lu is very small, and it is clear that an intensive investigation of both points would be best performed in Gd-Y. The Gd-Y system has been very thoroughly studied in zero field by Bates (1985) and Melville (1989). Further investigation would involve neutron investigations of the systems in an applied magnetic field, and ultrasound and neutron scattering studies of samples under a stress, as outlined in chapter 5.

The spin-slip structure for the c-axis component of erbium of Gibbs et al (1986) has been shown to provide a good explanation for the anomalous behaviour of the ultrasonic elastic constants. Those

commensurate structures which exhibit a net ferromagnetic moment are stabilised by the magnetoelastic energy and are seen to lock in over temperature ranges of up to 2K in good agreement with the X-ray scattering work of Gibbs. Several unusual features have been observed in both the ultrasound and neutron scattering data, which may be interpreted as the development of a circular distribution of the magnetisation on the basal plane, prior to the lock-in to an eight layer structure, leading to the formation of a structure similar to an alternating cone structure. As the eight layer structure is adopted the inter-layer equivalence of the HCP structure is lifted. A considerable amount of attention is being directed to producing a comprehensive model for the magnetic structure of Er, making full use of the large amount of data which has already been collected using both X-ray and neutron scattering techniques.

Ultrasound data collected on a single crystal $Ho_{90}Er_{10}$ alloy, and the results of an initial neutron scattering investigation, indicates that it exhibits magnetic behaviour similar to that of pure Ho. Several of the higher order commensurate structures observed in pure Ho are also observed in the alloy, however, the propagation vector is shown to develop considerably more slowly with temperature. At the transition to the ferro-cone phase the propagation vector continues to evolve, showing no tendency to lock in above 17K. The limited amount of neutron diffraction data collected to date shows some suggestion of a c-axis modulated moment.

Measurement of the ultrasound elastic constants, and the attenuation coefficient have allowed the construction of a tentative applied field-temperature phase diagram for erbium. The phase diagram shows that a c-axis magnetic field stabilises those commensurate structures with a net ferromagnetic moment, in broad agreement with recent

neutron diffraction data (Lin, 1991). There is also evidence of two distinct conical phases in addition to the phase which is stable in zero field below 18K. The neutron data of Lin et al (1991) suggest that this phase has a propagation vector stable at q= $\frac{1}{4}$. A propagation vector which is not commensurate with the basal plane symmetry reminiscent of the devil's staircase observed in Ho by Cowley et al (1990). Further neutron investigations of the H-T phase diagram of erbium are underway. Measurements of the elastic constants of Ho with a magnetic field applied along the c-axis will be performed as soon as a magnet capable of producing a field of 3T becomes available.

If an overall conclusion can be drawn from a diverse thesis such as this, it is to reconfirm the complementarity of macroscopic techniques, such as ultrasonic and resistivity measurements, to microscopic techniques, principally neutron scattering, for the study of magnetic systems. Rare earth magnetism continues to pose many difficult questions, for which the answers will only be attained as sample quality, measurement techniques and theoretical understanding improve.

References

Bates S., PhD thesis, Hull University (1985).

Cowley R.A., Jehan D.A., McMorrow D.F., McIntyre G.J., Phys. Rev. Letts. 66 1521 (1991).

Gericke O.R., pp27 in "Advances in Non-Destructuive Testing, Vol 15", McGonnagle W.J., Gordon Breach (1990).

Gibbs D., Bohr J., Axe J.D., Moncton D.E., D'Amico K.L., Phys. Rev. B 34 11 9192 (1986).

Lin H., Collins M.F., Holden T.M., Wei W., ICM91 to be published in J. Magn. Magn. Mats. (1991).

Melville R.J., PhD. thesis, University of Warwick (1989).

Appendix A

Magnetic and Nuclear Extinction Corrections

For a type I crystal (where the extinction is dominated by the mosaic spread) the secondary extinction may be calculated using Becker and Coppens (1974) improvement of Zachariasens equation

$$Y_S = \left((1 + 2x + \frac{A(\theta)x^2}{1 + B(\theta)x}) \right)^{-\frac{1}{2}}$$

where

$$x = \frac{2}{3} Q \, \alpha \, \overline{T}$$

with

$$Q = \left| \frac{F}{V(\text{Å})} \right|^2 \frac{\lambda^3(\text{Å})}{\sin 2\theta} \, .$$

The parameter α is a function of the mosaic spread of the crystal, which, if we assume the spread to be Gaussian may be written

$$\alpha = \sqrt{2}g \qquad \text{where} \qquad g = \frac{1}{2\sqrt{\pi\eta}}$$

and η is the mosaic spread in radians. $\overline{T}$ is the mean path length through the crystal in cm. Both η and $\overline{T}$ are calculated in the UPPALS and DATAP programs. The parameters A and B are numerically derived by Becker and Coppens, however, the higher order terms may be omitted for values of Y of 0.4 or more as is the case in this work.

If we assume that the magnetic domains are a similar size to the mosaic blocks, the extinction arising from nuclear and ferromagnetic

159

contributions may be calculated by considering the change in the extinction with the increase in scattering and using the magnetic equivalent of x, x_{mag}.

$$x_{mag} = \frac{2}{3} Q_{mag} \, \alpha \, \overline{T}$$

where

$$Q_{mag} = \left| \frac{pqG_{hkl}}{V(\text{Å})} \right|^2 \frac{\lambda^3(\text{Å})}{\sin 2\theta}$$

thus

$$\frac{F_m{}^2}{F_n{}^2} = \frac{x_{mag}}{x}.$$

$$\frac{dY}{dx_{mag}} = -(1+2x)^{\frac{3}{2}}$$

consequently the total extinction Y_{m+n} may be written

$$Y_{m+n} = Y_n + \frac{dY}{dx_{mag}} \, x_{mag}.$$

The corrected normalised structure factors are given by

$$\frac{F_m{}^2}{F_n{}^2} = \frac{I_{m+n}\left(\dfrac{Y_n}{Y_{m+n}}\right) - I_n}{I_n}.$$

With this equation rewritten in terms of x_{mag} as shown below, it may be solved iteratively using the Newton-Raphson method.

$$f(x_{mag}) = \frac{I_{m+n}Y_n}{I_n(Y_n - (1+2x_{mag})^{\frac{3}{2}} x_{mag})} - 1 - \frac{x_{mag}}{x} = 0$$

Appendix B

The COREX, Extinction Corrections Program

The COREX program is a straightforward implementation of the extinction correction method described in appendix A and is included not because it is deemed to be of great worth, but in the hope that it may save others unnecessary time and effort. It is run on the Micro-Vax in the Department of Physics at the University of Warwick.

Input data is in the form of a .COL file produced by the I.L.L. program ADV. A simple program called FILSRT sorts these data by hkl into new files for each reflection containing numor, h, k, l, intensity and temperature. A parameter file named COREX.PAR contains the necesary parameters for the program including the input and output filenames. An example of COREX.PAR is given below before the listing of COREX.FOR.

Example of a COREX.PAR parameter file

```
10000  0.00001      :Maximum Iterations, Tolerance
0.463 0.48          :Nuclear Extinction, Wavelength (Å)
1.0218 4            :b(x10^{12}cm),G
64.4084 4.79        :Unit Cell Volume (Å^3), θ(°)
0.2268 4.208e-5     :T̄(cm), η (rads.)
g1235d.col          :Input Filename
g1235d.exc          :Output Filename
2700                :Nuclear Intensity for Normalisation
```

161

COREX.FOR

```
C          **********************************************************
C          *                                                        *
C          *    Magnetic Extinction Correction Program   Version 3  *
C          *                                                        *
C          *    RSE                                        21/8/91   *
C          *                                                        *
C          **********************************************************
C
C
C          **********************************************************
C          Declaration of Variables
C          All variables have been given meaningful names where possible
C          F and FDERIV are the values of the function and its derivative
C          respectively, XN is the value of XMAG for the next iteration.
C          FIL and OFIL are the input and output data files respectively.
           INTEGER MAXIT,NUMOR,H,K,L
           REAL*8 YN,TOL,B,G,VOL,LAMBDA,THETA,ETA,TBAR,Q
           REAL*8 XN,XMAG,XNUC,ITOT,INUC,F,FDERIV,FSQNOR
           CHARACTER*50 FIL,OFIL
C          **********************************************************
C
C          **********************************************************
C          *                  MAIN PROGRAM                          *
C          **********************************************************
C
           CALL INIT(TOL,MAXIT,YN,INUC,FIL,OFIL,XNUC)
               OPEN(UNIT=25,FILE=OFIL,STATUS='NEW')
               OPEN(UNIT=20,FILE=FIL,STATUS='OLD')
50             READ (20,*,END=250) NUMOR,H,K,L,ITOT,TEMP
                   XMAG=((ITOT-INUC)/INUC)*XNUC
                   DO 100 I = 1,MAXIT
                       CALL FN(ITOT,INUC,YN,XMAG,XNUC,F,FDERIV)
                       XN=XMAG-(F/FDERIV)
                       IF (ABS(XN-XMAG).LT.TOL) GOTO 110
                       XMAG=XN
100                CONTINUE
                   PRINT* ,'NO CONVERGENCE' ,NUMOR, TEMP
110                FSQNOR=(XMAG/XNUC)
                   CALL DATOUT(NUMOR,FSQNOR,H,K,L,TEMP)
               GOTO 50
250            CLOSE (20)
               CLOSE (25)
           END
C
C          **********************************************************
C          *                  SUBROUTINE INIT                       *
C          **********************************************************
C          Introduces initial values and constants
           SUBROUTINE INIT(TOL,MAXIT,YN,INUC,FIL,OFIL,XNUC)
           REAL*8 YN,TOL,INUC,B,G,VOL,LAMBDA,THETA,ETA,TBAR,Q
           CHARACTER FIL*50,OFIL*50
               OPEN (UNIT=10,FILE='COREX.PAR',STATUS='OLD')
               READ (10,*) MAXIT,TOL
               READ (10,*) YN, LAMBDA
               READ (10,*) B, G
               READ (10,*) VOL, THETA
               READ (10,*) TBAR, ETA
               READ (10,32) FIL
               READ (10,32) OFIL
32             FORMAT (A50)
```

```
                      READ (10,*) INUC
                      Q=(((G*B)/VOL)**2)*(LAMBDA**3)/SIN(2*THETA*3.14159/180)
                      XNUC=(2**0.5/(3*(3.14159*ETA)**0.5))*TBAR*Q
                      PRINT* ,YN, TOL, MAXIT, FIL, OFIL, INUC,XNUC,Q
                      CLOSE (10)
              RETURN
              END
C
C
C             ****************************************************************
C             *                      SUBROUTINE FN                          *
C             ****************************************************************
C             Calculates F and FDERIV
              SUBROUTINE FN(ITOT,INUC,YN,XMAG,XNUC,F,FDERIV)
              REAL*8 ITOT,INUC,X,F,FDERIV
                      F=(ITOT*YN/INUC)/(YN-(((1+(2*XMAG))**(-3/2))*XMAG))
      *-1-(XMAG/XNUC)
                      FDERIV=(ITOT*YN/INUC)/((YN-(1+(2*XMAG))**(-3/2)*XMAG)
      ***2)*((XMAG**(-2/3)+(2*XMAG)**(1/3))**(-5/2))*(XMAG**(-2/3)-XM
      *AG**(-5/3))-(1/INUC)
              RETURN
              END
C
C             ****************************************************************
C             *                      SUBROUTINE DATOUT                      *
C             ****************************************************************
C             Writes corrected normalised structure factors to OFIL
              SUBROUTINE DATOUT(NUMOR,FSQNOR,H,K,L,TEMP)
              INTEGER NUMOR,H,K,L
                          WRITE (25,35) NUMOR,H,K,L,TEMP,FSQNOR
35                          FORMAT (I8,I4,I4,I4,F10.4,F13.8)
              RETURN
              END
```

Appendix C

Demagnetisation Corrections for Er.

The internal field B_i arising from an external field B_{oi} applied along the direction i is given by

$$B_i = B_{oi} - \frac{N_i}{4\pi}M_i$$

where N_i is the demagnetisation factor and M_i is the manetisation of the sample in $JT^{-1}M^{-3}$.

No magnetisation was available for the single crystal of erbium used in the magnetic field study described in chapter 7. Consequently, N_c had to be estimated using the graphical technique of Osborne (1945), which yielded a value of $N_c = 4.33$.

Using the magnetisation data of Féron (1969) the graph of internal field vs applied field (fig. AC.1) was constructed.

References

Féron J.L., Hug G. and Pauthenet R., Z. Angew (Math.) Phys. 30 61 (1969).

Osborne J.A., Phys. Rev. 67 11&12 351 (1945).

Fig AC.1 Applied Field vs. Internal Field for Er
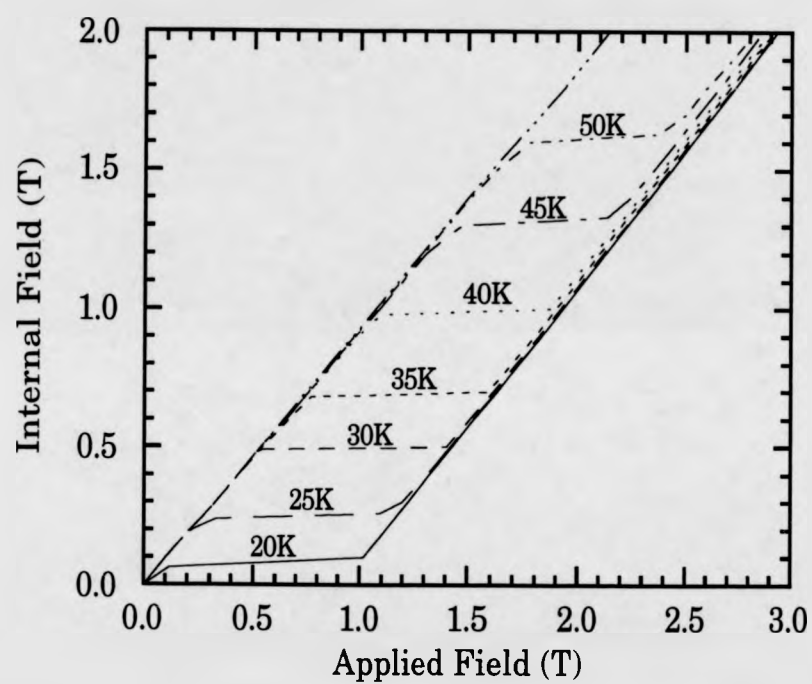
Publications Arising From this Work.

"The Magnetic Phase Diagram of the Gd-Lu Alloy System",

R.S.Eccleston, A.R.Griffiths, M.L.Vrtis, G.J.McIntyre, D.Fort and
S.B.Palmer, Physica B 174 33 (1991).

"Ultrasound Investigation of the Magnetic Structure of Er in an Applied
Magnetic Field",

R.S.Eccleston and S.B.Palmer, accepted for publication in J. Magn.
Magn. Mater. (1991).

"Gd-Lu in an Applied Magnetic Field",

R.S.Eccleston and S.B.Palmer, accepted for publication in J. Magn.
Magn. Mater. (1991).

"Automated Measurement of Ultrasound Velocity and Attenuation",

M.Salgeiro da Silva, R.S.Eccleston, J.Bessa Sousa and S.B.Palmer.
submitted for publication in Ultrasonics.

Magnetic Properties of Gd-Lu Alloys, Er and a Ho$_{90}$Er$_{10}$ Alloy.

TITLE ......

AUTHOR ....

Roger Soulsby Eccleston

DEGREE ....

University of Warwick.

AWARDING BODY

DATE ....

December 1991.

THESIS

NUMBER ....

THIS THESIS HAS BEEN MICROFILMED EXACTLY AS RECEIVED

cms	1	2	3	4	5	6	REDUCTION X	12
							CAMERA	3
							No. of pages	